MICROSTRUCTURE AND THERMO-MECHANICAL PROPERTIES OF GRADIENT NICKEL ALLOYS

by

Jie Ding

A Dissertation

Submitted to the Faculty of Purdue University

In Partial Fulfillment of the Requirements for the degree of

Doctor of Philosophy

School of Materials Engineering

West Lafayette, Indiana

May 2020

THE PURDUE UNIVERSITY GRADUATE SCHOOL
STATEMENT OF COMMITTEE APPROVAL

Dr. Xinghang Zhang, Chair
School of Materials Engineering

Dr. Carol Handwerker
School of Materials Engineering

Dr. Kevin Trumble
School of Materials Engineering

Dr. Haiyan Wang
School of Materials Engineering
School of Electrical and Computer Engineering

Approved by:
Dr. David Bahr

Dedicated to my wife: Yingqiao He

ACKNOWLEDGMENTS

First, I must thank my advisor and defense committee chair, Prof. Xinghang Zhang for his kind encouragement and instructive guidance in the last 5 years. His insightful discussion, patience in explaining science and critical thinking have enlightened me on how to become an independent researcher. I also thank my committee members, Prof. Carol Handwerker, Prof. Kevin Trumble, and Prof. Haiyan Wang for their guidance and precious suggestions that improved the quality of this thesis. Additional thanks are given to Prof. Wang for the use of her laboratory facilities. I am also grateful to Prof. Yashashree Kulkarni and her student Ms. Dajla Neffati for their great help in MD simulations.

I greatly appreciate my friends and coworkers in Prof. Zhang's group at Purdue University, Dr. Sichuang Xue, Dr. Qiang Li, Ruizhe Su, Yifan Zhang, Zhongxia Shang, Jeahun Cho, Tongjun Niu, Tianyi Sun, Nicholas Richter, Bo Yang, Benjamin Thomas Stegman, and other friends in Prof. Wang's group including Dr. Xingyao Gao, Dr. Zhimin Qi, Dr.Xin Sun, Xuejing Wang, Juncheng Liu, Bruce Zhang, Di Zhang etc. I also want to thank our previous group members, Dr. Zhe Fan, Dr. Jin Li, Dr. Jie Jian, Dr. Jijie Huang, Dr. Han Wang and Dr. Cuncai Fan. Many thanks for their companionship and help during my PhD study. I want to give extra thanks to Dr. Jin Li for his encouragement and great help when I was in trouble.

I also appreciate the great help from the staff of School of Materials Engineering, including Vicki Cline, Rosemary Son, Stacey Coar, Shannon Heidrich, Jameson Root, Lisa Stacy, Timothy Vanmeter, Darren Pauly and Aury Ku Blanco.

I acknowledge the Life Science Microscopy Facility and Birck Nanotechnology Center at Purdue University. I also acknowledge the financial support from Petroleum Research Funds (PRF) and Department of Energy, office of Nuclear energy (DE-NE).

I would express my deepest gratitude to my parents and wife for their continued and unwavering support. I would never have the courage to keep going without their understanding and encouragement.

TABLE OF CONTENTS

LIST OF TABLES

LIST OF FIGURES

ABSTRACT

Gradient structured (GS) metallic materials have shown unique properties including the synergy of high strength and good ductility, improved fatigue and wear/friction resistance etc. One of the severe surface modification technique, surface mechanical grinding treatment (SMGT), has been proven an effective method for the generation of gradient structures in metallic materials. Most of Ni-based superalloys are precipitation strengthened and with an extraordinary combination of high strength, ductility and resistance to oxidation at high temperatures. The precipitation behaviors of these materials are sensitive to their initial microstructures. This thesis focuses on the microstructure evolution and mechanical behaviors of two types of gradient Ni alloys.

GS Hastelloy C-22HS and Inconel 718 (IN718) Ni-based superalloys were fabricated through the SMGT technique. The gradient structures consist of nanograined (NG) or nanolaminate (NL) surface layer and the subsurface layers with deformation twins. *In situ* compression test results reveal that intergranular back stress may contributes to the high work hardening capability of the GS C-22HS alloy. Mo-rich thick grain boundaries (GBs) formed in the gradient C-22HS samples after heat treatment. *In situ* micropillar compression studies coupled with molecular dynamics (MD) simulations reveal that the Mo-rich thick GBs are stronger barriers than conventional thin GBs to the transmission of dislocations, leading to significant strengthening. Furthermore, the formation of thick GBs also contributes to the improvement of thermal stability of nanograins in the C-22HS alloys. The gradient microstructures in the IN718 alloy changed the precipitation behavior and thermal stability of nanograins in the alloy. The studies on precipitation behaviors of GS IN718 alloy reveal that η phase formed in the severely deformed surface NG layer after annealing at 700 ^{o}C. Thermal stability studies show that NG IN718 alloy with grain sizes smaller than the critical value of ~ 40 nm is thermally more stable than their coarse-grained counterpart. The underlying mechanisms of strengthening and improved thermal stability of the gradient Ni-based superalloys are discussed based on transmission electron microscopy studies and MD simulations. This work suggests that tailoring the gradient microstructures may lead to the discovery of metallic materials with novel mechanical and thermodynamic properties.

CHAPTER 1. INTRODUCTION

1.1 Challenges in processing bulk high strength and ductile metallic materials

Extensive investigations into metallic materials over the last several decades indicate that high strength can be accomplished via the reduction of grain sizes from the micrometer scale to the ultrafine (100-1,000 nm) or nanoscale (< 100 nm) [1–6]. The strength of fine-grained materials often follows the classical Hall-Petch relationship [7,8]:

$$\sigma = \sigma_0 + k \cdot d^{-1/2} \qquad \text{Equation 1.1}$$

where σ_0 represents the yield strength at large grain size, k represents the resistance of grain boundaries to the transmission of dislocations, d represents the average grain size.

The traditional grain refinement method is based on cold working followed by recrystallization at high temperatures, or by introducing new grains directly during hot working through dynamic recrystallization [9]. The grain size derived from these traditional heat treatment techniques is usually limited to a few microns.

Over the last decades, another technique, severe plastic deformation (SPD), has been applied extensively for the fabrication of submicron to even nanograined (NG) metals and alloys [2,5,10–34]. Several types of SPD techniques have been invented in the last decades, including equal channel angular compressing (ECAP) [17,24,25,30,31,34–39], high pressure torsion (HPT) [18,27,40–45], accumulative roll bonding (ARB) [12,22,46], and many other variants of SPD techniques [22,47]. Fig.1.1 shows the schematics illustrating the operation principle of these three techniques and the corresponding transmission electron microscopy (TEM) micrographs of the processed samples [12,22,46–49]. It shows that the grain size of the processed samples is in the ultrafine grained (UFG) range (100-1,000 nm). The introduction of NG structures is usually accompanied with high strain/strain rate and/or lower processing temperatures.

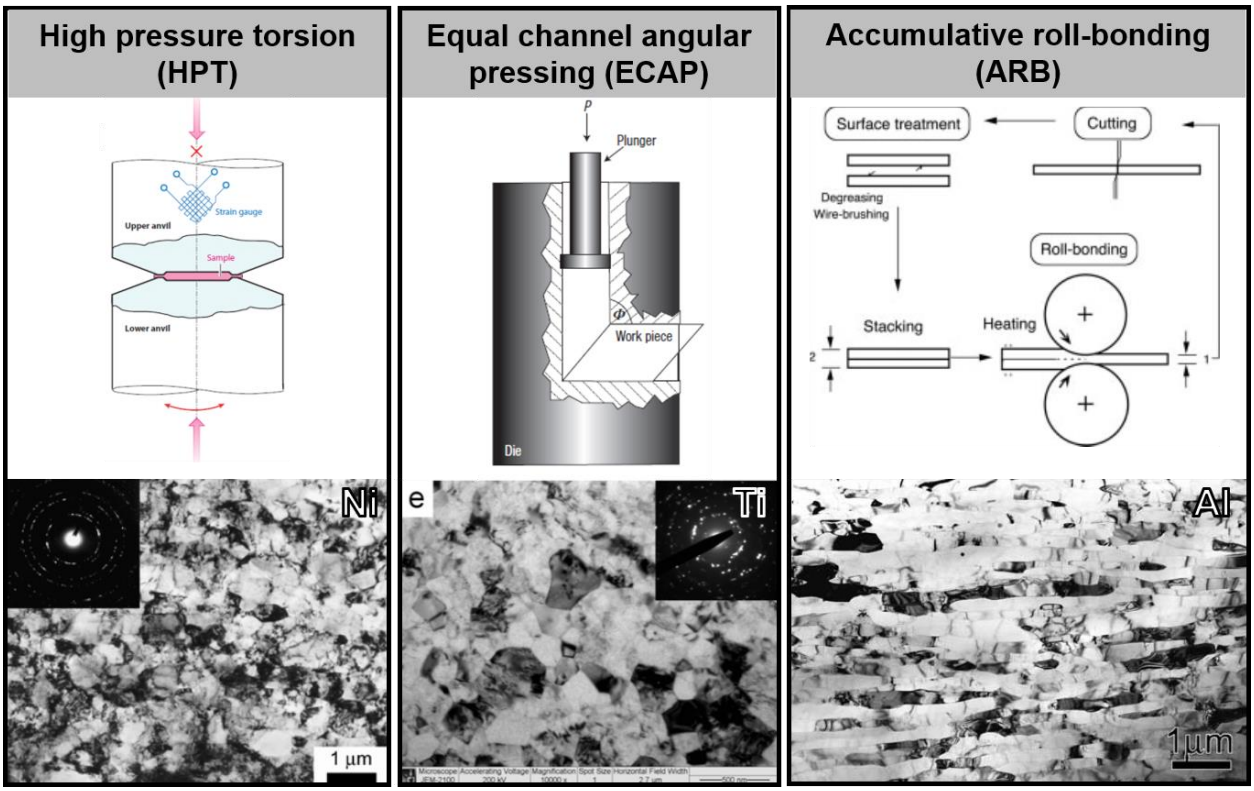

Figure 1.1 Widely used SPD techniques for the fabrication of nanograined metallic materials and the corresponding TEM micrographs of processed samples [12,22,46–49].

UFG and NG metals can be several times stronger than their conventional CG counterparts [50–58]. In literature, the ultimate tensile strength (UTS) of nanocrystalline (NC) copper fabricated by in-situ consolidation can reach up to 1.1GPa, almost comparable with that of commercial steels [52]. The UTS of NG Ti fabricated by HPT was reported to be more than 1.2 GPa, which was comparable to Ti alloys [59]. However, these UFG and NG materials are usually brittle and exhibit a limited tensile ductility when deformed under tension. The poor tensile ductility is a roadblock that hinders the practical applications of UFG and NG metallic materials [10,53,54,60–62]. Fig.1.2 shows the tensile behaviors of Cu-15 at.% Al alloy fabricated by HPT and 316L stainless steel prepared by ECAP when comparing with their CG counterparts [63]. The UTS of SPD sample is much stronger than that of CG one, while the uniform elongation of specimens decreases drastically after grain refinement in both cases. The limited tensile ductility appears because of the absence of strain hardening in nanograins and the suppression of conventional deformation mechanisms, such as dislocation slip and multiplications, while other deformation mechanisms,

like grain boundary sliding, are not yet activated to accommodate plastic strain [64–70]. Hence, stress becomes localized and early necking takes place immediately after yielding.

Furthermore, according to Considère's criterion [65], necking occurs when

$$(\frac{\partial\sigma}{\partial\varepsilon})_{\dot{\varepsilon}} < \sigma \qquad \text{Equation 1.2}$$

where the left term represents the work hardening rate of sample at a certain strain rate $\dot{\varepsilon}$, and right term is the corresponding flow stress. To maintain a high ductility, a higher strain hardening rate is required to surpass flow stress for NG or UFG metals with higher strength than their weaker counterparts. It appears that ductility is inevitably compromised once a metallic material is strengthened by grain refinement [71].

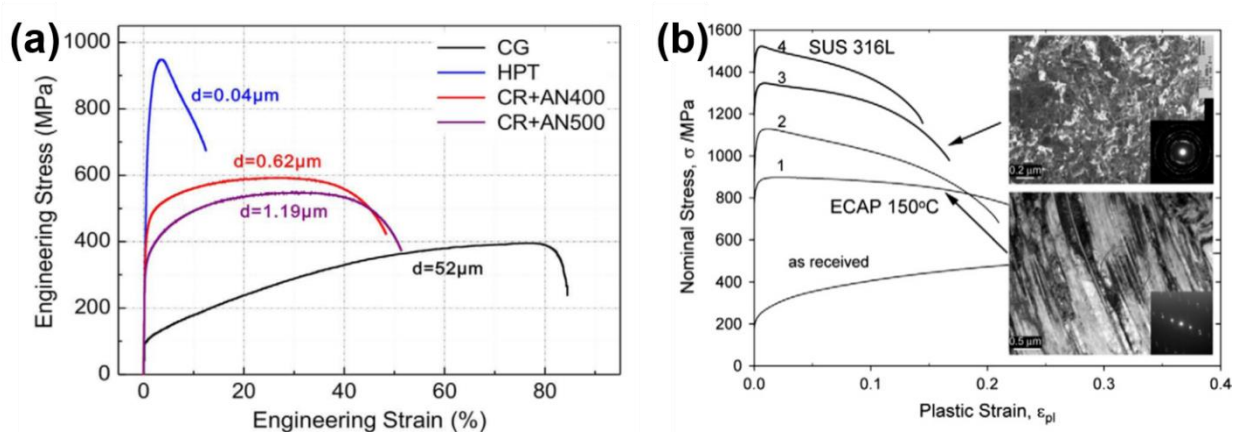

Figure 1.2 The accomplishment of high strength at the cost of ductility in (a) Cu-15 at% Al alloy [72] and (b) 316L stainless steel after grain refinement [63].

1.2. Introduction of gradient structured (GS) metals

Does it mean that limited ductility is intrinsic to NG metals? One of the most common phenomena that contradicts this assumption is that NG metals can be compressed to a higher strain level or rolling as long as the cracking can be suppressed [73,74]. Meanwhile, dimples features have also been captured on the fracture surface of electrodeposited nanocrystalline Ni, indicating the existence of ductile fracture mechanisms [75–77]. These evidences illustrate that grain refinement does not necessarily lead to the absence of ductility. Some strategies have been proposed and several success stories have been reported [56,68,74,78–80]. For instance, by creating a bimodal structure consisting of nanoscale and micron size grains, strain hardening is

achievable [81]. Other strategies include the introduction of nanotwins [55], transformation induced plasticity (TRIP) and twinning induced plasticity (TWIP) etc. [56,82,83]. Xiang et al. [78] and Lu et al. [84] revealed that, well-bonded copper thin films on polymer substrate can be strained up to 10% when the strain localization is retarded by the substrates, which means a ductile core or substrate is favorable for the suppression of strain localization. Similar strategy has been proposed by Ma [83]. Consequently, the idea of processing an architecture that consists of NG outer layer and CG inner core naturally rises. This architecture further triggered the design of gradient structured (GS) metals, which has been proven an effective way to improve the mechanical behaviors of metal with nanoscale or ultrafine grain sizes [85–100].

The grain size of GS naterails varying from nanometer scale to micrometer scale [86,94]. Fig.1.3a schematically illustrates an example of cross-section microstructure of GS materials, in which the structure has been divided into four layers: the topmost NG or nanolaminated (NL) layer; the UFG or ultrafine-laminated (UFL) layer; the severely deformed CG layer; and the untreated CG core. Fig.1.3b shows a scanning electron microscopy (SEM) micrograph of the GS layer of copper that was prepared by surface mechanical grinding treatment (SMGT) [101]. The corresponding TEM micrographs (Fig.1.3c-e) at position B, C and D also reveal that the average grain size in the position B (close to the surface) is less than 100 nm (in Fig.1.3c), which is referred to as the NG layer. While the average grain size at position D is larger than 100 nm (in Fig.1.3e), corresponding to the UFG region according to foregoing definition.

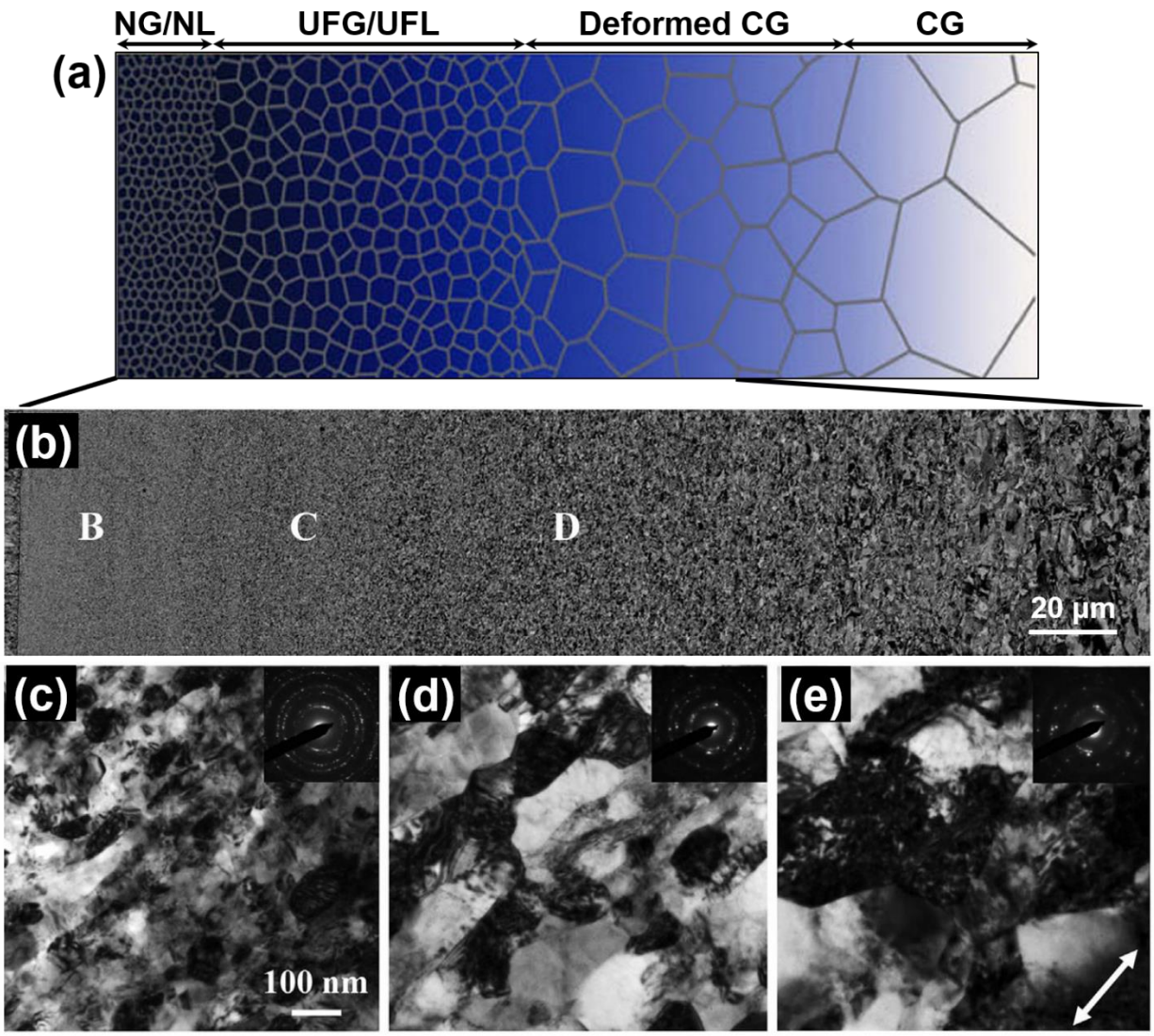

Figure 1.3 (a) Schematic showing the microstructure of GS metallic materials. (b) SEM micrograph showing the microstructure evolution of the GS Cu fabricated by SMGT. (c-e) The corresponding TEM micrographs showing the grain size variation at the position B, C and D in (b) [101].

Plastic deformation is an effective approach for grain refinement [5,102]. To synthesize such a GS metal with NG surface layer, several surface modification techniques have been invented, including surface mechanical attrition treatment (SMAT) [82,86–88], SMGT [85,94] and surface mechanical rolling treatment (SMRT) [92] etc. Fig.1.4 schematically illustrated the operation principles of these commonly used techniques for fabrication of gradient structures [88,94,103]. As shown schematically, SMAT process is suitable for the fabrication of GS metal plates, while the other two are suitable for cylinder specimens. The deformation depth after treatment varies

based on different techniques and experimental parameters. Consequently, the microstructures of GS metals differ slightly among various experiment setups. But the overall tendency for microstructure evolutions of gradient structures along the depth direction is similar.

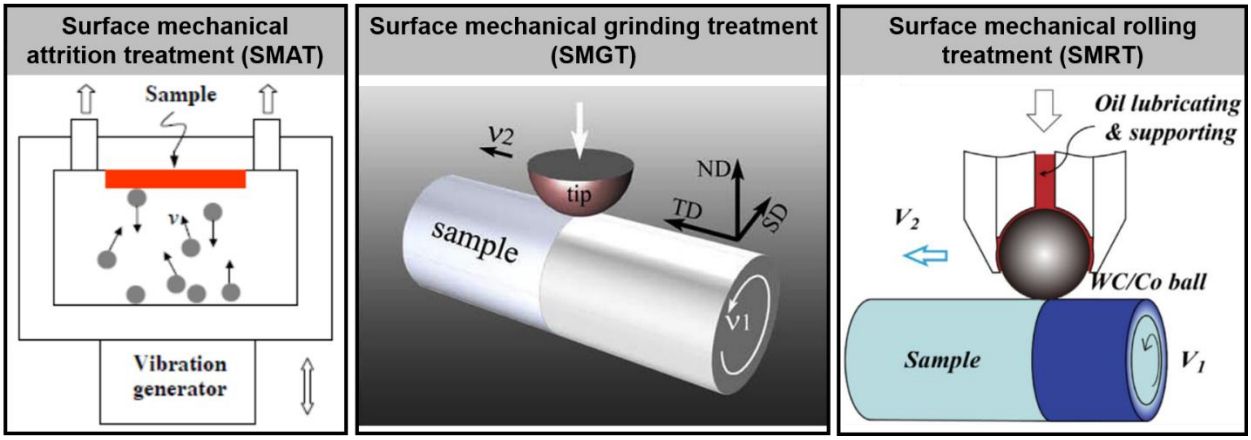

Figure 1.4 Three commonly used techniques for the fabrication of GS metals [88, 94, 103].

Previous research works have shown that the formation of such gradient may significantly improve mechanical properties of metallic materials [85,86,95]. For instance, Fang et al. [85] found that the NG Cu surface layer in the GS Cu (processed by using SMGT approach) has 10 times higher tensile strength than that of its CG counterpart but has poor ductility, whereas the yield strength of the GS copper is two times higher that of the CG ones without sacrificing tensile plasticity as shown in Fig.1.5a. In Fig.1.5b, a GS interstitial free (IF) iron sample fabricated by Wu et al. [86] by SMAT exhibited a several times higher yield strength than the untreated ones. In addition, Huang et al. [103] found that the GS surface layer on AISI 316L stainless steel specimens fabricated by SMRT dramatically improved the fatigue resistance. These results have shown that introducing gradient structure is a promising strategy for the development of metals with a synergy of high strength and good tensile ductility.

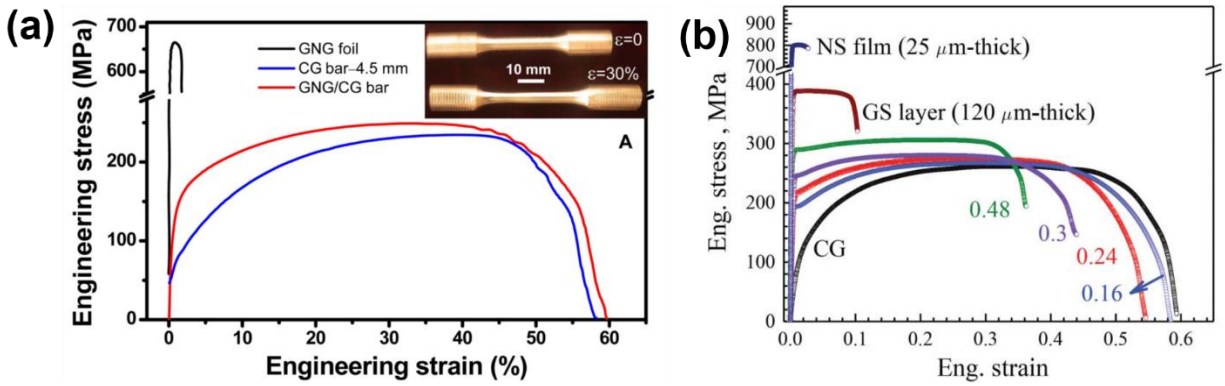

Figure 1.5 The stress-strain curves of (a) SMGT Cu and (b) SMAT IF Fe showing the synergy of high strength and good ductility of GS metals [85,86].

1.3. Microstructure evolution of gradient structured metals

The microstructure evolution of GS materials synthesized by various techniques has been investigated by researchers using SEM, TEM and electron back scattered diffraction (EBSD) [85,86,93,94]. Grain refinement of metallic materials by plastic deformation is generally governed by the formation of different boundaries, like dislocation cells, twin boundaries (TBs), low angle grain boundaries (LAGBs) and high angle grain boundaries (HAGBs) [94]. Dislocation activities and deformation twinning are closely related to the stress and stain states. Generally, the distribution of stress and strain along the depth direction during severe surface plastic deformation process varies. Consequently, the microstructure of GS materials evolves accordingly. The characteristics of microstructure of each layer will be discussed in the following sections and schematically illustrated in Fig.1.6. As shown in the schematic, with the decreases of distance away from treated surface, both strain gradient (χ) and strain rate (γ) increase drastically (in different unit and magnitude, the unit of strain gradient and strain rate is μm^{-1} and s^{-1}, respectively), especially in the surface NG/NL layer region, which is vital for the formation of NG/NL structure.

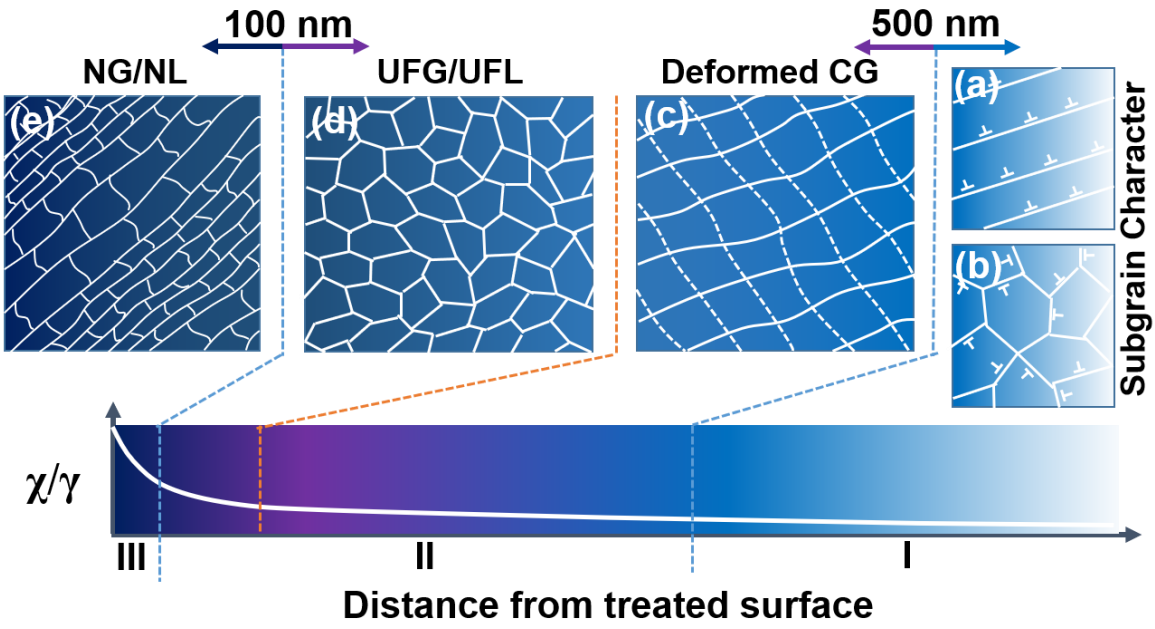

Figure 1.6 Schematic microstructure, strain gradient (χ) and strain rate (γ) evolution of GS materials. (NG: nanograined, NL: nanolaminated, UFG: ultra-fine grained, UFL: ultra-fine laminated, CG: coarse grained)

1.3.1 Microstructure evolution in the deformed CG layer

Deformed CG layer refers to the one far away from the treated surface, as denoted in Fig.1.6 (region I). As the curve that illustrates the evolution of strain gradient (χ) or strain rate (γ) along the depth direction in Fig.1.6 shows, the strain and strain rate in deformed CG layer is low (the evolution of χ and γ behaves similarly in different magnitude). Sub-grain structures are formed in original coarse grains by dislocation activities after deformation. There are two main mechanisms for the accommodation of plastic deformation: dislocation slip and deformation twinning [87,90]. For metals with high stacking fault energies (SFEs), dislocation slip is the favorable mechanism [104,105]. While for metals with low SFEs, deformation twinning plays a dominant role [97]. In literature, for metals with low or medium SFEs like nickel, strain is usually accommodated by forming planar dislocation arrays and grids or mechanical twins [97,99]. This type of dislocation configuration can be caused by the relatively low SFE that hinders the cross slip of partial dislocations and causes dislocations to arrange along their favorable slip planes [97].

For metals with medium to high SFE, deformation twinning is hindered, dislocation cells or walls are formed for accommodation of strain [104,105]. The formation of these sub-grain

structures is believed to be associated with the transformation from cellular structure to granular structure when the density of dislocation reaches a critical value, accompanied by the annihilation of dislocations with opposite Burgers vectors [2]. Fig.1.7 shows two experimental observations of dislocation cells of copper with medium SFE (Fig.1.7a) [105] and aluminum with high SFE (Fig.1.7b) [104] that were fabricated by SMGT. However, SFE is not the only factors that determine which mechanisms (deformation twinning and dislocation cell) dominate the accommodation of plastic strains during deformation. Deformation twinning was observed in metallic materials with medium SFE like copper and even in metals with high SFE like titanium when the applied strain rate is high enough [92,105].

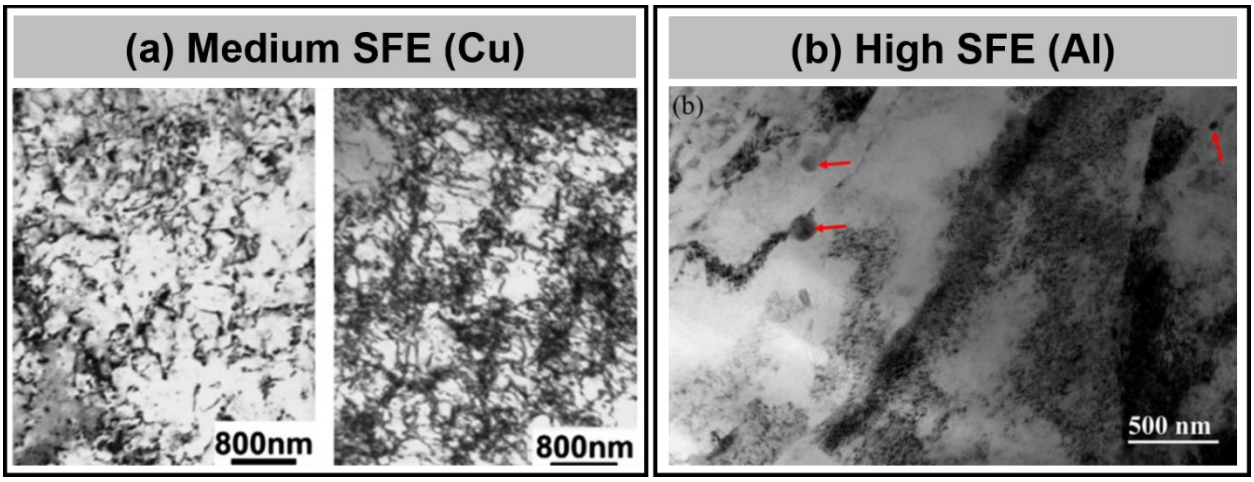

Figure 1.7 TEM micrographs of the severely deformed layer of (a) Cu with medium SFE and (b) Al with high SFE revealing the dislocation cell structures [104,105].

1.3.2 Microstructure evolution in the UFG/UFL layer

With decreases of depth away from treated surface, both strain gradient and strain rate increase. In the deep region of the GS materials (region II in Fig.1.6), plastic deformation induces the formation of UFG and UFL structures. Researches show that the strain level and strain rate in this layer are almost comparable to that in bulk metals fabricated by plastic deformation like cold rolling, torsion and HPT etc. [94], which results in the formation of nanoscale deformation twins and dislocation cell/wall structures. These preformed nanotwins or dislocation structures will eventually transform the original coarse grain into UFG or UFL structure through twin-twin, twin-dislocation or dislocation-dislocation interactions.

For the metals with preformed nanotwins, there are four different mechanisms for the grian refinement [106]: (1) For metals with low SFEs, the driving force for deformation twins to overcome the barriers of preexisting TB is relatively low. Then intersection of twins from different slip planes takes place, which can divide the original coarse grain into rhomboid blocks with high angle orientation [97,106]. The schematics and corresponding experimental TEM observations in Fig.1.8a and b illustrated the interaction process. The rhomboid blocks resulted from twin-twin intersection are clearly observed in the 304 stainless steel fabricated by SMAT in Fig.1.8b [97]. (2), In general cases, manipulation and interaction of dislocations dominate the accommodation of plastic strain. Dislocations accumulate within twin layers and arrange themselves into interconnecting boundaries for minimization of strain energy, and further separate twin layers into finer blocks [97,103]. When the energy needed for the activation of secondary deformation twin that penetrate through the primary TB is too high for metals with relative low SFE, or the deformation strain rate is high enough for metals with relative high SFE, the dislocation wall arrangement between deformation twin lamella will play the key role in accommodating plastic strain. (3) If the orientation of shear stress is favorable for the formation of secondary twins, refinement of twin layers is feasible via subdividing the lamellae into prismatic blocks by secondary twins. The experimental observation of this mechanism is similar with what we find in case (1), as shown in Fig.1.8. (4) When strain hardening becomes difficult within twin layers, shear banding occurs to accommodate plastic strain. Equiaxed nanograins form within shear bands as the twin boundaries are severally twisted under localized strain.

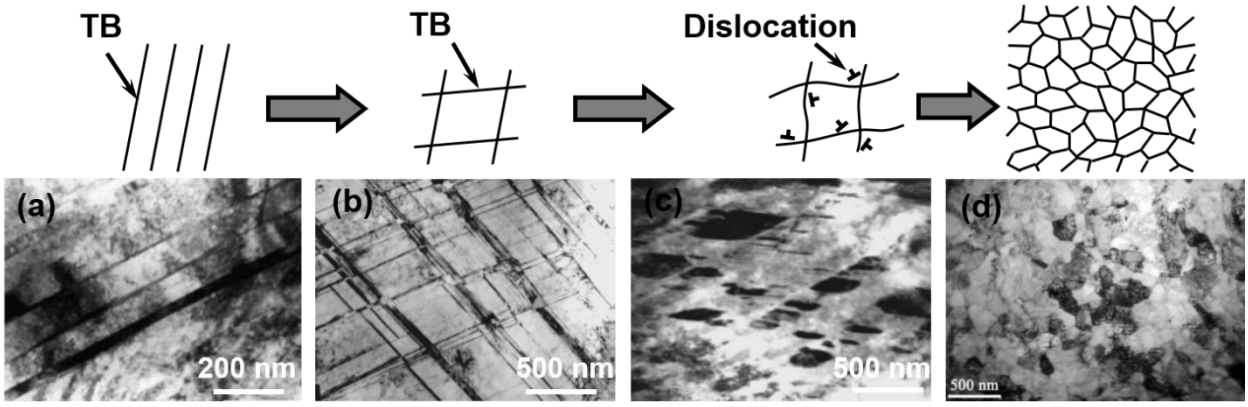

Figure 1.8 Schematics and corresponding TEM micrographs revealing the microstructure evolution in the UFG/UFL layer of metals with low SFE. (a) Deformation twins in the SMAT 316L stainless steel [107], (b) twin-twin intersection in SMAT 304 stainless steel [108], (c) twin dislocation interaction in SMAT 304 stainless steel [108], and (d) UFG structures formed in the SMRT 316L stainless steel [103].

While for metals with medium to high SFE, or when the strain rate is not high enough to activate nanotwins in original coarse grains, dislocation activities will dominate the accommodation of plastic strain during deformation [94,95,105,109]. Fig.1.9 and Fig.1.10 schematically illustrated and experimentally verified the evolution of microstructure during deformation for these scenarios. Under a certain level of deformation strain, dislocation activities result in the formation of dislocation tangles (DT) or dense dislocation walls (DDW) (Fig.1.9a and Fig.1.10a). The further increasing of both strain and strain rate lead to dislocation annihilation and rearrangement of both DDW and DT to minimize the system energy, forming subgrains with small orientation angles, as illustrated in Fig.1.9b and Fig.1.10b.

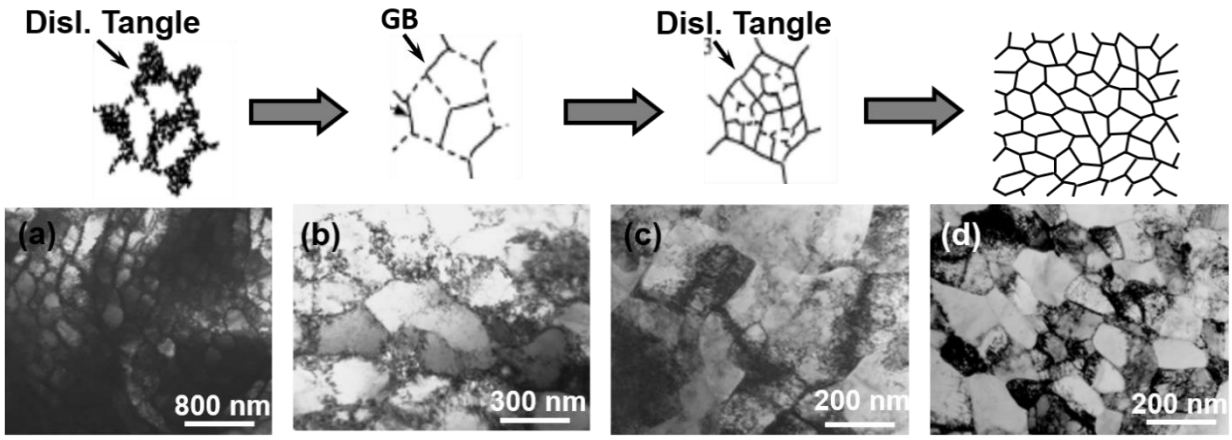

Figure 1.9 Schematic and corresponding TEM micrographs revealing the microstructure evolution in the UFG layer of metals with medium/high SEF. (a) the formation of DTs [105], (b) transformation of DTs into subgrains with small orientation angle [105], and (c) evolution of subgrains to grains with HAGBs and the formation of sub DTs within new grains under further straining in SMAT Cu [105]. (d) the UFG structured formed in SMAT IF Fe sample [95].

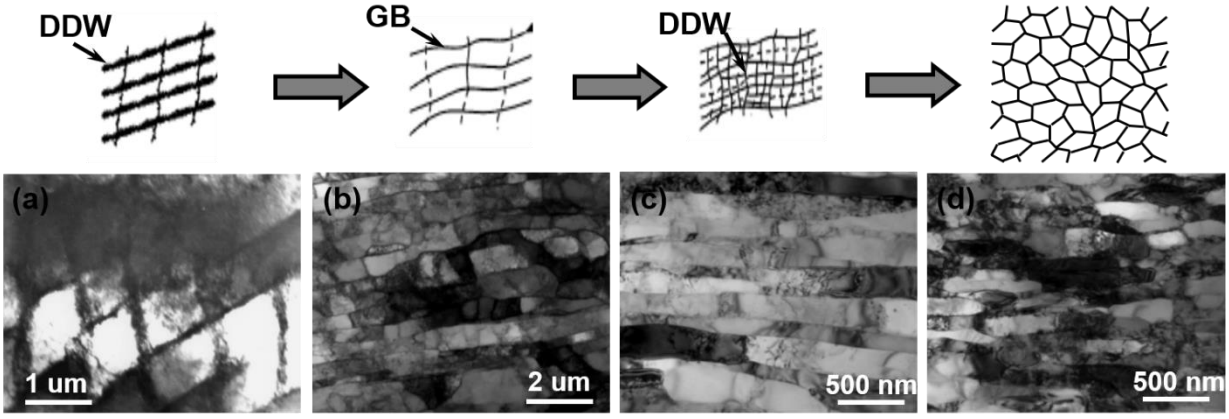

Figure 1.10 Schematic and corresponding TEM micrographs revealing the microstructure evolution in the UFL layer of metals with medium/high SEF. (a) the formation of DDW in SMAT Fe sample [109]. (b) the formation of subgrains that evolves from DDW [94], (c) the transformation of LAGB to HAGB and formation of sub DDW within lamella [94], and (d) the formation of UFL structures in SMGT Ni sample [94].

Upon the formation of subgrains, either through deformation twinning or dislocation cell forming mechanisms, the subsequent evolution process is governed by the interaction of dislocations with subgrain boundaries under further straining. To accommodate more dislocations, UFL or UFG structure is formed by further refining subgrains. The reduction of boundary spacing is accomplished by the split of single lamellae into two parallel ones or by the formation of even

smaller scaled DDW and DT structures, as Fig.1.8c, Fig.1.9c and Fig.1.10c illustrated. During this process, the continuous accumulation of dislocations into the boundaries leads to the increase of misorientation angle between two adjacent crystallites, which results in the subdivision of original subgrains/lamellea and the evolution of structure, i.e., increase of fraction of HAGBs and decrease of subgrain size and lamellae space [103].

The UFG layers generally have comparable or even smaller lamellae spacing and higher fraction of HAGBs and smaller aspect ratios than UFL layers [94]. The formation of UFG layers are believed to associate with the generation of more transversal dislocation walls within each lamella. The interaction of new formed dislocations with the transversal boundaries leads to the transformation of LAGBs to HAGBs. Meanwhile, owing to the smaller grain size, the annihilation of dislocations is promoted [94]. The temperature rises during deformation and the migration of triple junctions also favor the removal process of defects inside nanoscale structures. Dynamic equilibrium is reached when the defects removal process accelerated by increasing plastic strain reaches a certain level that may offset by the dislocation generation. In this case, saturated UFG microstructure, in which the characteristics of grains like morphologies, grain size and orientation don't even change with higher strain, is formed [22]. In literature [22,88,94], such a saturated structure features 100-200 nm in grain size and 70-80% of HAGBs as the strain level ranges from 10 to 25 and strain rate reaches up to 10^2-10^3/s.

1.3.3 Grain refinement in NG/NL layer

The strain and strain rate imposed in the UFG/UFL layer region that is comparable with conventional SPD techniques resulted in a saturated grain size of ~100-200 nm [94]. Hence, even higher strain and strain rate level are required for the formation of NG/NL structure with finer grain size. Previous studies reveal that the outmost layer of GS materials prepared by SMGT undergoes a larger strain (25-60), higher strain rate (10^3-10^4/s) and gradient (0.3-0.6/μm) than that in the deeper UFG layer [94]. It is well known that higher strain rate will contributes to the dislocations generation and suppresses the annihilation of dislocations, which promotes grain refinement before LAGBs transform to HAGBs [94,105]. Meanwhile, geometrically necessary dislocations (GND) are required to maintain the crystal continuity. The density of GND (ρ_G) can be calculated by $\rho_G = \frac{4\chi}{\sqrt{3}b}$, where b represents the Burgers vector of the material and χ is the strain

gradient [94,110]. The strain gradient of 0.3-0.6/μm corresponds to an approximate ρ_G = 5-10 × $10^{15}/m^2$. As a result, the presence of high strain rate and strain gradient significantly promotes the accumulation of dislocations that is favorable for the formation of LAGBs. To accommodate these dislocations, more dislocation boundaries form. These dislocation boundaries may further transform to LAGBs and eventually refine UFG/UFL structures into NG/NL structures. Fig.1.11 shows the microstructure of NG/NL formed in Cu [105] (Fig.1.11a), Ni [94] (Fig.1.11b) and Al [111] (Fig.1.11c). It reveals that dislocations and deformation twins are coexist within the grains of both Cu and Ni. These nanotwins and dislocations will eventually fine the grain into even smaller size with further straining.

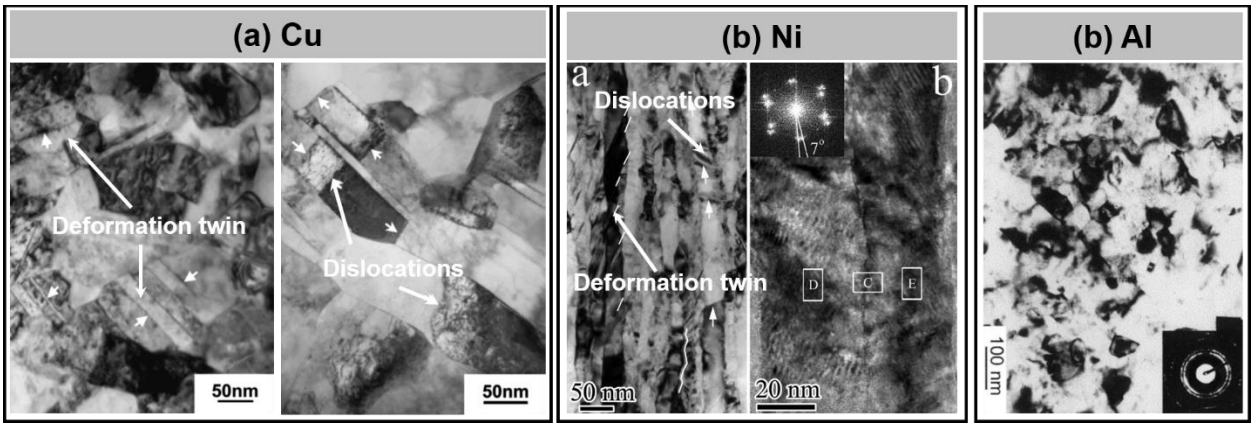

Figure 1.11 TEM micrographs showing the sub-microstructure of NG/NL layer(a) Cu [105], (b) Ni [94] and (c) Al [111].

1.4. Mechanical behavior of GS metals

GS materials exhibit excellent mechanical properties [85,86]. Fig.1.5 shows two examples about GS metals that inherit both the strength of surface NG layer and ductility of inner CG core. The synergized strength and ductility are believed to be attributed to the back stress strengthening and work hardening, or mechanically induced nanograin coarsening [85,86,93,101]. These two mechanisms that contribute to high strength and good ductility (or high strain hardening) of GS materials will be discussed in detail separately.

1.4.1 Strengthening effect of gradient structured metals

As Fig.1.5 shows, both CG IF steels and copper possessed several times smaller yield strength than their freestanding GS (or NG) counterparts. But the combination of soft CG substrates and hard GS surface layer leads to a doubled or even tripled strength (~2.0 and ~2.6 times than the CG copper and IF steels, respectively), which is related to the mechanical incompatibility of deformation behavior of this heterogeneous structure [86,93,95]. As shown in Fig.1.12a, the black curve and red curve represent the tensile strain behavior of CG IF Fe specimen and GS IF Fe specimen with 24% volume fraction of gradient structure layer, respectively [86]. The green curve represents the calculated engineering stress-strain curve according to rule of mixture (ROM). It clearly reveals that the flow stress of GS sample is much higher than the calculated value. Fig.1.12b shows the evolution of yielding strength of GS IF Fe sample with various volume fraction of gradient structure layers (red), the calculated strength using classical (blue) and modified (green) ROM. It also verifies the synergetic strengthening effect of GS layer. The stress-strain curves in Fig.1.12c reveal that the yielding strength decreases gradually with the increases of the thickness of removed surface gradient structure layers, which implies that surface gradient structures dominate the strengthening effect of GS metals.

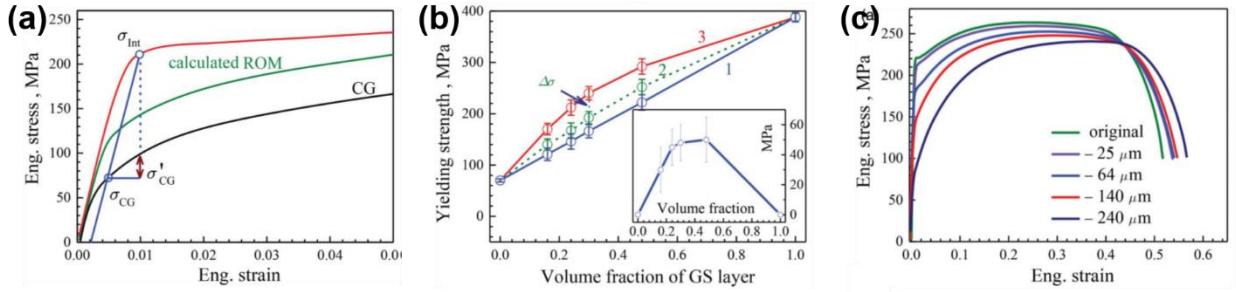

Figure 1.12 The synergetic strengthening effect of GS IF Fe sample [86]. (a) Stress-strain curves showing the synergetic strengthening effect of GS specimens beyond the role of mixture (ROM). (b) Yield strength evolution with the increase of volume fraction of GS layer. (c) Stress strain curves of the specimens with different volume fraction of GS.

Where does the synergetic strengthening effect of GS metals comes from? During the early stage of uniaxial tensile tests of GS materials when tensile stress is higher than the yield strength of CG core but lower than that of GS layer, the CG core deforms plastically, while the GS layer deforms elastically. Wu et al. [86] measured the Vickers hardness difference of SMAT IF steels along the depth direction before and after 1% tensile strain. They found that there is no hardness

change for the surface GS layers, indicating an elastic behavior of this layer. The finite element modeling results (as Fig.1.13 shows) also verified that [112]. At the early stage of uniaxial tensile tests, the surface NG layers undergo a limited tensile strain while the CG core is deformed at larger strain (Fig.1.13c). The apparent Poisson's ratio of the plastically deformed core is 0.5, while that of the elastically deformed GS layer is around 0.3, which means the central CG core shrinks more faster than the GS layer [86]. However, the deformation of the core is restricted by the hard surface layer for the sake of strain continuity. This deformation incompatibility results in a strain gradient near the interface of CG core and GS surface layer, and further triggers the accumulation of GNDs [110,113]. The pileup of GNDs along the GS/CG interface further causes back stress. Back stress has been proven an important factor that affects the strengthening and strain hardening [71,93]. It can reduce the effective shear stress required for the slip of mobile dislocations, which means higher stress is required for the activation of dislocation slip in the presence of back stress [93,110,112]. Meanwhile, the constraint of GS surface layer to CG core also results in a compressive stress in outer GS layer and a tensile stress in inner CG core, which transforms the original uniaxial stress state into a two-dimensional one. This stress gradient formed between surface GS layer and inner CG core has been proven effective in increasing yield stress in the form: $\tau' = \frac{\tau_Y}{1-\delta L_{obs}/4}$, where δ is the stress gradient, τ_Y is the yield strength when $\delta = 0$, and L_{obs} is the obstacle distance for dislocation slip [94]. In summary, the synergy of back stress strengthening and stress gradient strengthening leads to the high strength of GS materials.

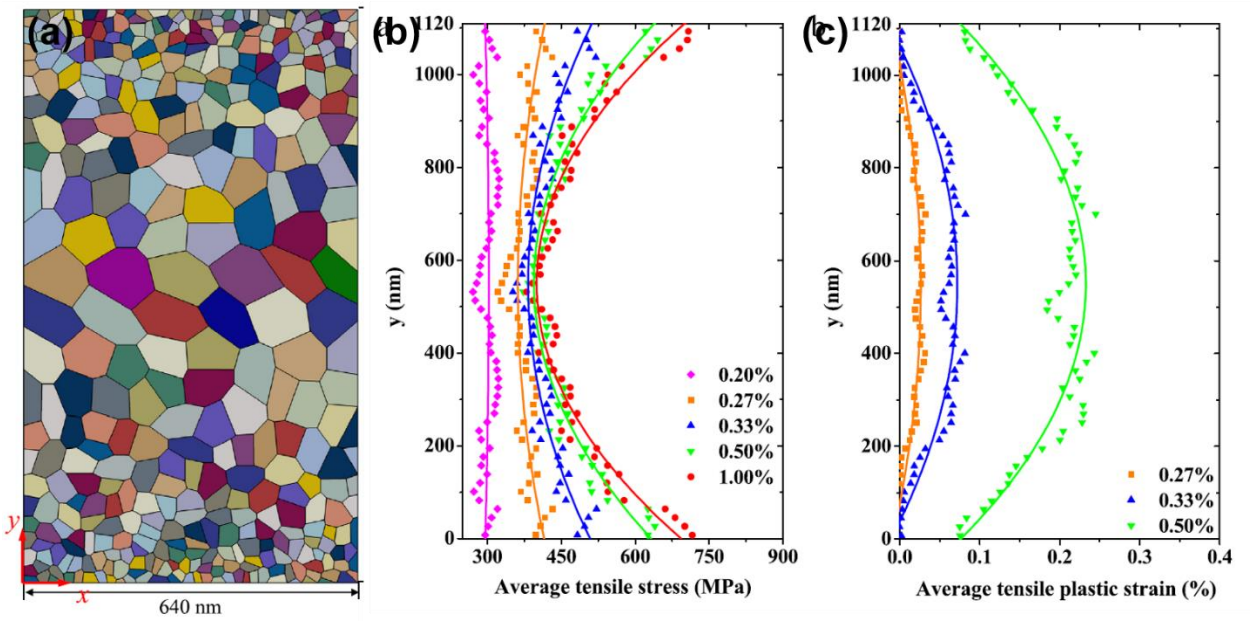

Figure 1.13 (a) Crystal plasticity finite element model of gradient structured Cu. (b and c) The evolution of average tensile stress and tensile plastic strain along the thickness direction [112].

1.4.2 Strain hardening effect of gradient structured metals

Except the significant yield strength increment, the good ductility of GS metals almost comparable with their CG counterparts is another benefit of it. There are two mechanisms have been proposed for the good plasticity or high strain hardening, i.e., back stress hardening [86,93] and mechanically induced surface nanograin coarsening [85,101]. These two mechanisms will be discussed below separately.

With the increase of tensile strain, the tensile stress increases at a much higher rate in GS surface layer than in the CG core, as suggested by the finite element modeling studies (in Fig.1.13b) show [112]. When the tensile stress in outer GS layer exceeds its yield strength, necking is about to takes place due to its limited strain hardening [95]. During this process, the tangled high-density dislocations in the interior and boundary area of nanograins are wiped out. Wu et al. [95] have identified this annihilation process in GS IF steels by measuring the density of mobile dislocation density through stress relaxation tests. The ratio ($Re = \rho_m/\rho_{m0}$) experienced a sharp drop when the strain increased from 0.008 (soon after yielding) to 0.015 (necking point of NS surface layer), and corresponding TEM results also verified this transformation process.

However, when the strain reaches the necking point of surface GS layer, the lateral shrinkage of surface GS layer is constrained by the stable inner CG core. Similar to the situation in the early stage of tensile tests, this constraint also leads to a strain gradient near the GS/CG interface. Meanwhile, due to the necking instability of surface GS layer, the lateral stress of the surface layer transits from compression to tension, while the transition in the inner CG core takes place in opposite direction [86,95]. The stress state transition also facilitates the increase of strain gradient [93]. As a result, the strain gradient caused by deformation incompatibility and stress state transition between GS and CG layer result in the accumulation of GNDs along the GS/CG interface. The depletion of dislocations in prior stage also provides more space for the accumulation of GNDs. The pileup of GNDs further cause back stress that is against the applied stress [93]. Back stress can be measured experimentally from loading-unloading tests. Fig.1.14a shows the schematic of the hysteresis loop for the measurement of back stress. Detailed description of each stress and strain labeled in the schematic can be found in the literature [93]. The corresponding back stress σ_b can be calculated using the following equation:

$$\sigma_b = \frac{\sigma_r+\sigma_u}{2} \qquad \text{Equation 1.3}$$

Fig.1.14b shows the evolution of back stress of GS IF steels calculated using the hysteresis loop of loading-unloading tests with increasing unloading strain. Fig.1.14c represents the corresponding back stress hardening (solid curve) [93]. It's apparent that the high θ of GS IF steels (especially to the θ up-turn just after the necking of surface layer) is attributed to the back stress strain hardening.

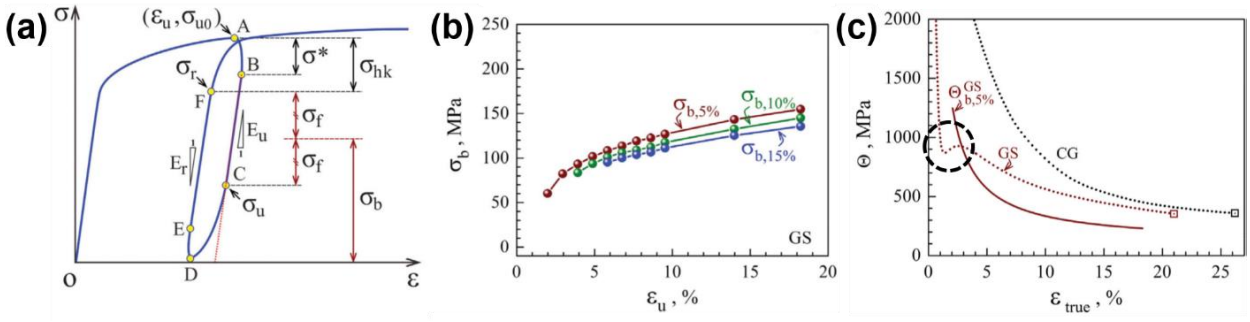

Figure 1.14 (a) The schematic of the hysteresis loop for the measurement of back stress. (b) Back stress evolution with increasing of unloading strain of GS IF Fe. (c) The back stress strain hardening in GS IF Fe [93].

For GS materials, the ductility improvement originating from mechanically induced nanograin coarsening has only been reported in SMGTed copper [85,101], even though grain growth of several NG materials under indentation, tension and compression has been observed [114–116]. The microstructure evolution of SMGTed GS copper under tension reveals the grain coarsening process (see Fig.1.15) [85]. As Fig.1.15c shows, after 127% of true strain (ε_T), the grain size increased from original 20 nm to 280 nm, and the dislocation density in coarsened grains is rather low (as the TEM image of Fig.1.15d shows), which precluded the deformation mechanism of dislocation slip during tension tests. It is reasonably believed that the grain coarsening in this case contributed to the grain boundary migration. Both experimental observations and molecular dynamic simulations have proven that, among the possible grain boundary-based mechanisms, the grain boundary migration is the dominant one that contribute to the grain coarsening [117]. In literature [118], when the grain size ranges from 1 μm to 10 nm, the movement of dislocations is mostly restricted to slip planes, above which the dislocation activities play roles and below which the grain boundary activities dominant. In addition, this grain coarsening process has been found not only stress driven, but also strongly dependent with temperature and strain rate. Elevated temperature and reduced strain rate favor the coarsening process [101]. In summary. The mechanically induced grain coarsening in GS copper, although reducing the strength of it to some extent owing to "strain softening" (not discussed in this thesis), enabled it to accommodate more plastic strain and exhibited an excellent ductility.

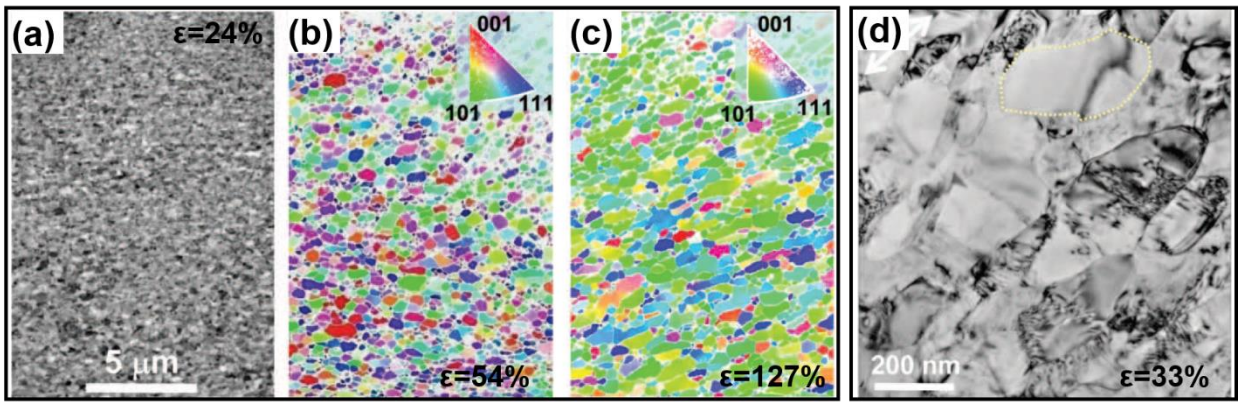

Figure 1.15 (a-c) SEM and EBSD micrographs showing the grain coarsening phenomenon of the surface NG layer of GS Cu. (d) TEM micrograph reveals that dislocations have been wiped out after grain coarsening [85].

1.5. Other properties improvements of gradient structured metals

Except the studies about the synergy of high strength and good ductility of GS metallic materials, investigations about the effect of gradient structure to the other properties of metals have also been performed by researchers.

1.5.1 Friction resistance of gradient structured metals

Lowering the coefficient of friction (COF) of metallic materials under sliding is critical for improving reliability of metal components in technical application [119–121]. The frictional contact between metals, or metals and other harder materials like ceramics, usually leads to surface roughening by microcracking or folding, and the formation of nanostructured tribolayers after repeated sliding on the roughened wear surface [122–126]. The delamination of hard tribolayers and the further roughening during sliding lead to a high COF of metals [127]. Grain refinement has been proven effective in lowering the COF at low sliding speed and force as it hardens metals significantly [128–131]. However, the reduction of COF in nanograined metals is absent in high sliding speed and force due to the strain localization of nanograins with limited plastic deformation capability [64,132]. The mechanical instability of nanograined metals and their tendency of delamination contribute to the absence of lower COF when sliding with high speed and/or force [64,128]. Hence, increasing the stability of subsurface layer to accommodate the sliding-induced plastic deformation and hinder surface roughening and delamination is essential for lowering the COF of metals with nanograined surface layer. Introducing gradient structure with nanograined hard surface layer and gradually softened subsurface layers into metals is therefore a promising strategy.

Chen et al. [126,133] investigated the influence of gradient nanograined surface layer to the friction and wear reduction of both pure copper and copper alloys. As shown in Fig.1.16a, a gradient nanograined layer was fabricated in the copper sample by means of SMGT. The comparison of COF of CG, nanograined and GS copper samples with various sliding numbers and sliding load are plotted in Fig.1.16b and c, respectively. It reveals that the COF of GS sample remains steady at the value of 0.37, in contrast to that of CG (0.74) and NG (0.67) sample. The COF of GS sample just slightly changed from 0.35 to 0.40 with the sliding load increased from 10 to 50 N, whereas those of the CG and NG sample remain higher than 0.60 at the same condition,

as shown in Fig.1.16c. The post-sliding microstructure analyses (as shown in Fig.1.16d) confirm the grain coarsening and dynamic recrystallization (DRX) in the subsurface UFG region. The plastic deformation during sliding was accommodated by the nanograined structures and the localized deformation was suppressed, leading to a much lower COF of the GS sample. Similar phenomenon has been reported in GS Cu-Ag alloy by SMGT [127]. The COF of Cu-Ag alloy decreased from 0.64 in CG sample to 0.29 in GS sample, which is attributed to the fact that stable gradient nanograined structure accommodated the plastic deformation during sliding.

In summary, the NG surface layer of gradient structure with high strength improved the COF of metals, while the subsurface layer with relatively better strain hardening properties accommodated the plastic deformation during sliding, which eliminated the strain localization and the subsequent delamination of nanograined tribolayer, leading to a significantly improved friction resistance of metallic materials [126,127,133]. The microstructure stability of outmost NG surface layer plays an important role as grain coarsening during sliding is expected to diminish the enhancement effect of gradient structure to the friction resistance of metals.

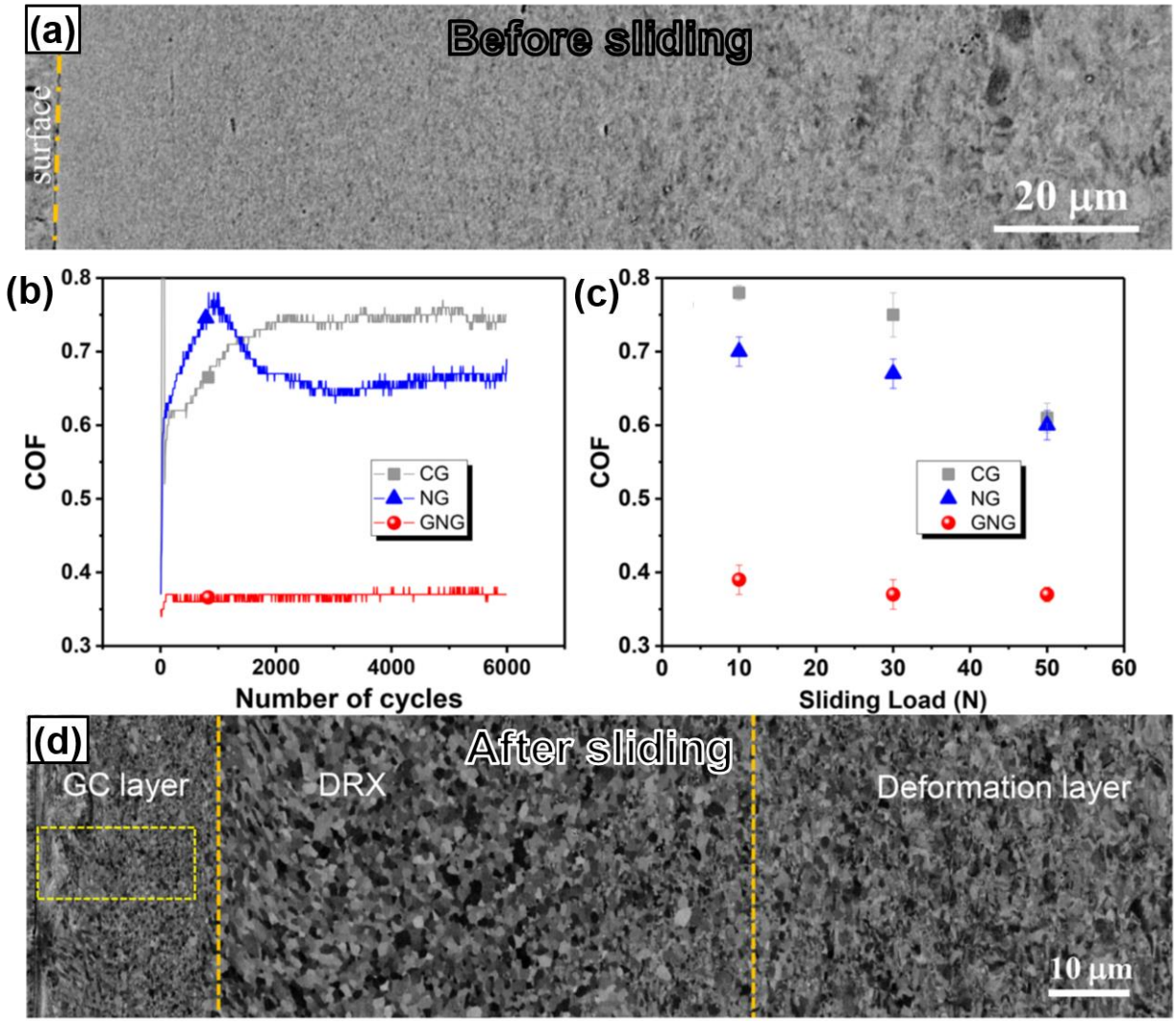

Figure 1.16 (a) SEM image of the gradient nanograined layer of pure copper. Variation of COF with (b) sliding cycles and (c) applied load of CG, NG and GS copper. (d) SEM image of the subsurface layer in the gradient nanograined copper specimens after sliding tests [133].

1.5.2 Fatigue resistance of gradient structured metals

Fatigue resistance is another quality that determines the reliability of metals since most of metallic components are under cyclic loading condition. The effect of gradient nanostructure to the fatigue performance of metallic materials has also been investigated by researchers extensively [134–144]. Prior researchers have concluded that grain refinement is beneficial to the improvement of fatigue properties [103]. However, the fatigue endurance of metals with finer grain size is generally decreased comparing with their CG counterparts under the cyclic loading condition with

higher strain amplitude or under strain-controlled loading model. This is related to the fact that the crack propagation rate in metals with refined grains is much larger owing to the lack of ductility [103,145].

Since the fatigue fracture usually initiated from the metal surface and subsequently propagated into the interior, we may expect an enhanced fatigue resistance of metals by introducing compressive residual stress or fine-grained layer with higher strength on the outmost layer. Conventional techniques like shot peening and laser shot peening therefore have been applied for the improvement of fatigue properties of metals for this sake [134,137,140]. Shiozawa et al. [143] studied the fatigue resistance of high-C-Cr bearing steel fabricated by shot penning. They found that microcracks activated from the surface of untreated specimens, in contrast to the cracks initiated from the subsurface layer of shot-penned specimens. The fatigue life of the processed specimens increased under the high stress amplitude and low number of cycles conditions. While for the condition of low stress amplitude and long cyclic period, the difference in fatigue life between shot-peened and untreated specimens was negligible. The low cycle fatigue performance of AA7075 aluminum specimen with surface gradient structure processed by ultrasonic shot peening was investigated by Pandey et al. [140]. Significant low cyclic fatigue life improvement was observed in the treated specimen after 180 s ultrasonic shot peening. Whereas increasing the treatment duration to 300 s led to a reduced fatigue life. Pandey et al. attributed the enhancement of fatigue life to increased resistance of treated specimens against fatigue crack initiation. Besides, decreased fatigue crack growth rate and plastic strain amplitude have also been observed in AISI 304 stainless steel after shot peening or deep rolling by Altenberger et al. [142]. However, the improvement of fatigue resistance of the above listed metals processed by conventional surface modification techniques only occurs under stress-controlled cyclic loading mode, and the strain amplitude applied was relatively low. This phenomenon may be attributed to the relatively thin surface layer with high hardness.

The gradient structures introduced by novel surface modification techniques like SMAT, SMGT, SMRT etc. have been proven more effective than conventional approaches in the enhancement of fatigue endurance of metals [103]. Huang et al. [103] studied the fatigue behavior of GS 316L stainless steel processed by means of SMRT. Fig.1.17a shows the gradient structures formed after SMRT. The depth of deformed area is measured to be larger than 500 μm, much thicker than those were introduced by conventional metal surface modification methods. The TEM

micrographs in Fig.1.17b-d show the microstructure in different depth. The mean grain size of outmost nanograined layer (in Fig.1.17b) is approximately 30 nm. The dominated structure at the depth of ~ 270 μm is high-density DTs with average twin thickness of ~ 25 nm (in Fig.1.17d). The comparison of S-N curves of GS specimens with gauge diameter of 6 mm (refers to SMRT-6, the volume fraction of gradient layer is estimated to be ~ 46%) and of 3 mm (refers to SMRT-3, the volume fraction of gradient layer is estimated to be ~ 78%), and their CG counterparts is plotted in Fig.1.17e. It clearly reveals that fatigue limits of the 316L stainless steel increased significantly from 180 MPa to 320 MPa for SMRT-6 specimen, and further increased to 420 MPa for SMRT-3 specimen. The fatigue ratio (the ratio of fatigue limits and ultimate tensile strength) of SMRTed specimens is significantly elevated. The authors attributed the enhancement of fatigue resistance of SMRTed specimens to the increase of both fatigue strength exponent and coefficient. The initiation of crack was suppressed by the nanograined top surface layer with high strength, as shown in Fig.1.17b. Meanwhile, the plastic strain amplitude was accommodated by the gradient layer of SMRTed 316L specimens by reducing the strain localization. The combination of suppressed initiation of cracks and diminished plastic strain amplitude resulted in the significantly enhanced fatigue properties. However, the influence of compressive residual stress of gradient layer to the enhancement of fatigue resistance was measured to be negligible in their study [103].

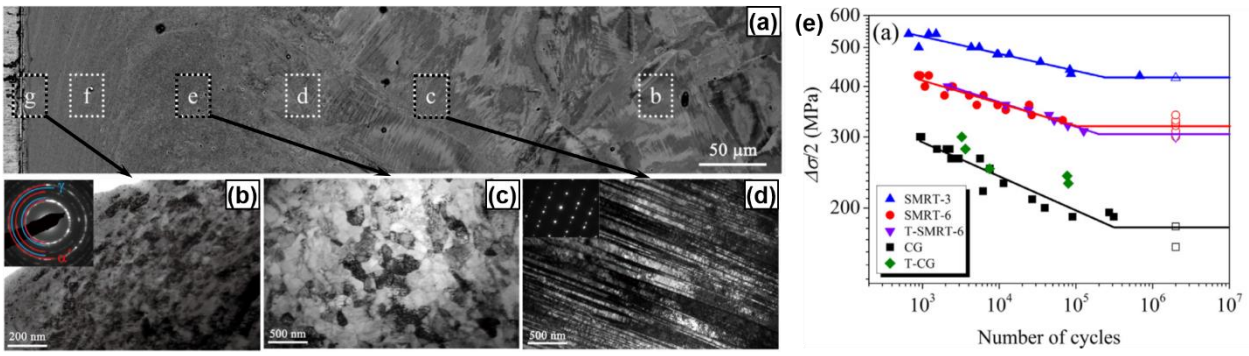

Figure 1.17 (a) SEM image of the gradient structure formed in AISI 316L stainless steel by SMRT. TEM images showing the (b) NG, (c) UFG and (d) deformation-twinned structures of the gradient layer, (e) Comparison of S-N curves of different AISI 316L specimens [103].

Similar study on the fatigue life improvement of GS 316L stainless steel was performed by Roland et al. [107] as well. In their study, the gradient structure was generated by means of SMAT, by which the plastic deformation depth of the sample (~ 200 μm) was thinner than that was

processed by SMGT (~ 500 μm). However, the average grain size of the outmost nanograined layer (~ 20 nm) was even smaller. Traction compression fatigue tests results reveal that the fatigue limits increased from ~ 300 MPa for CG sample to ~ 380 MPa for SMAT sample. The fatigue limit is slightly lower than that for SMGT 316L sample (~ 420 MPa), which may be attributed to the much shallow penetration depth. The NG surface layer with high density of defects impeded the movement of dislocations and hindered the initiation of cracks. However, the authors believed that the compressive residual stress is critical to the enhancement of fatigue resistance as high compressive residual stress formed in the gradient layer servers as an obstacle for the propagation of cracks, contradict to that was reported in SMRT 316L specimen [103]. The suppressed crack nucleation and propagation led to the lifetime and fatigue strength increments. In their study, Roland et al. also found that annealing the SMAT specimen at 400 ^{o}C, albite the compressive residual stress was relaxed at this condition, can further improve the fatigue properties (fatigue limits increased to ~ 400 MPa). The combination of strain hardening, straining induced phase transformation and the stable NG surface layer was contributed to the improved fatigue resistance [107]. Huang et al. [136] studied the influence of gradient structure of martensitic stainless steel (Z5CND16-4) fabricated by SMGT to the fatigue resistance and reported similar behavior. The introduction of gradient layer increased the fatigue limit from 300 MPa for CG specimen to 415 MPa. Post-annealing treatment at 450 ^{o}C for the SMGT specimen further increased the fatigue limit to 440 MPa.

Except for the studies about fatigue resistance improvement of GS stainless steels, works on other metallic materials like copper and twinning-induced plasticity (TWIP) steels have also been performed [138,144]. The study on the improved fatigue performance of GS copper processed by means of SMGT was investigated by Yang et al. [144]. The introduction of a GS layer with thickness of ~ 500 – 700 μm significantly improved the fatigue strength of copper from 56 MPa to 98 MPa. The corresponding fatigue life of GS copper was more than 14 times of that of the CG ones at the low-cycle-fatigue regime with the stress amplitude of 140 MPa. The gradient layer improved the fatigue strength and suppressed the nucleation of microcracks, resulting in the enhanced fatigue resistance. However, the microstructure analyses of the fatigue fractured specimen reveal grain coarsening in the top region of the GS layer. The cracks were initiated and propagated from these CG region of surface NG layer during cyclic loading and led to failure. It

implies that the stability of surface NG layer is critical to the improvement of fatigue resistance of GS metals, consistent with other works.

The studies on strain-controlled fatigue properties of metals are scarce Shao et al. [138] investigated the strain-controlled low-cycle fatigue performance of GS Fe-18Mn-0.6C TWIP steel processed by 180^{o} torsion with subsequent annealing treatment at 700 ^{o}C for 10 mins. The grain refinement efficiency of torsion is much lower than the other severely plastic deformed surface modification techniques, but graded size distribution was successfully introduced. The low-cycle fatigue tests of as received CG specimens, finer-grained (FG) specimens, and GS specimens reveal that GS specimens exhibit better fatigue performance than both CG and FG specimens at high strain amplitude ($\Delta\varepsilon/2 > 0.6\%$), although the fatigue life GS specimens at lower amplitude ($\Delta\varepsilon/2 < 0.4\%$) is slightly lower than that of FG specimen. Meanwhile, the GS specimen presents better fatigue resistance than FG and CG specimens. Similarly, the FG surface layer suppressed the initiation of cracks along shear bands. However, the prevailing GNDs formed in the gradient layer of TWIP steel in their story provide extra cyclic stress besides SSDs, further enhancing the fatigue strength. The effects of GNDs to the improvement of fatigue resistance was rarely be considered in other works. Besides, the hardening effects of GNDs contribute to extra strain hardening in the subsurface layer of gradient structure than in the outmost layer of specimen after fatigue tests, forming a structure consists of a hard core and soft shell. This structure is beneficial for surface stress relaxation and further prolongs the time for crack nucleation from the outmost layer.

Previous studies focus on the metals with negatively graded strength, i.e. the strength/hardness decreases from surface to center of specimen. Ma et al. [141] investigated the enhanced fatigue resistance of 304 austenitic steels with both positively and negatively graded strength. The gradient structure was introduced by pre-torsion treatment. The fatigue tests reveal, not surprisingly, that the GS samples present better fatigue performance than the corresponding gradient-free samples. The comparison of two GS specimens shows that the sample with negative strength gradient exhibits better crack nucleation resistance, whereas positive gradient is more effective at suppressing grain propagation. Both the experimental results and corresponding finite-element simulations show that the plastic zone at the tip of crack-like notch of negatively graded specimen is the smallest when comparing with other samples, which explains the longest crack initiation live. The positively graded specimen presents the most homogenous stress field at the tip position. Once crack is initiated, the plastic zone and stress concentration at the tip of cracks of

positively graded specimen are smaller than the negatively graded and CG counterpart, leading to a slower crack propagation rate.

In summary, the introduction of gradient layer into the metal surface significantly enhanced the fatigue properties of metals [135,136,144]. The factors that determine the enhancement efficiency include the strength gradient direction (positive or negative), the stability of surface layer with high strength, the relaxation of surface compressive stress (by annealing) and the degree of the gradient of strength, etc. More studies, especially the simulation studies that modeling the fatigue behaviors are expected for the fundamental understanding and application of gradient structure to the improvement of fatigue performance.

1.5.3 Thermal stability of gradient structured metals

As mentioned in Sec. 1.3, the grain refinement efficiency of SMGT is much higher than other conventional SPD techniques like HPT, ECAP etc.[94]. The mean grain size of outmost surface layer of SMGT metals can be refined to ~ 20 nm, whereas the reported finest grain size of metals that were processed by conventional SPD methods was around 100 nm. Intuitively, finer grains of SMGT samples are usually more susceptible to grain coarsening than relative larger grains of other SPD samples at high temperatures [146,147]. However, the special grain morphology and grain boundary structures of nanograins of SMGT samples enabled the extraordinary thermal stability of surface NG layer.

Two-dimensional nanometer-scaled laminated microstructures were introduced in the outmost layer of pure Ni by Liu et al. using DMGT technique [99], as shown in Fig.1.18a. The laminated structures are typical microstructure of surface layer of GS metals by SMGT under shear stress, which have been observed in many other SMGT metals like copper, stainless steel and nickel-based alloys, etc. [85,103]. Both NG and NL structures are observed in Fig.1.18a. After annealing the sample at 500 ^{o}C for 1 hour, the original NG structures coarsened to micrometer-scaled equiaxed grains, as shown in Fig.1.18b. However, the morphologies of NL structures that were sandwiched between NG layers retained.

The grain coarsening behavior of NC metals can be examined by looking at the GB velocity (v) [148,149]:

$$v = M_{gb} \cdot \gamma_{gb} \cdot \kappa \qquad \text{Equation 1.4}$$

where M_{gb} represents the GB mobility, γ_{gb} is the GB energy and κ is the local boundary curvature. It implies that the grain coarsening of NC materials is controlled by both kinetic [150,151] and thermodynamic [152,153] components. Detailed TEM analyses reveal that most of grain boundaries in NL structures are LAGBs. The low excess energy (smaller value of γ_{gb}) and mobility of LAGBs (smaller value of M_{gb}) compared with HAGBs lower the velocity of grain boundaries, leading to the high thermal stability. The laminated morphology of NL structure may contributed to the enhanced thermal stability, i.e., the extremely large radius of 2-dimensinal lamellar can reduces the capillary force for grain boundary movement (smaller value of k); the orientation pinning effect of and suppressed recrystallization nucleation kinetics (smaller value of M_{gb}) by the laminated structures may also contribute to the improved thermal stability [99].

The follow-up study on the thermal stability of GS pure Ni and Cu that were processed by SMGT was performed by Zhou et al. [154]. The difference is that liquid nitrogen rather than cooling oil was used as cooling medium. The gradient structure formed in pure Ni after SMGT is presented in Fig.1.18c. Detailed TEM observation of surface NG region in Fig.1.18e shows that nanograins with an aspect ratio of ~ 2.0, rather than nanolamellae with larger aspect ratio, formed after SMGT. LAGBs were formed (though no relevant data was provided in the literature), similar to the NL structure in previous story [99]. The benefits of laminate morphology to the enhancement of thermal stability should be absent, or at least be diminished, in this follow up study. Deteriorated thermal stability is therefore be expected. However, after annealing the sample at 600 ^{o}C for 30 mins, as shown in Fig.1.18d and Fig.1.18f. the NG layer remains stable without any grain coarsening, in contrast to the obvious grain growth in the sublayer. The comparison of grain size of surface NG region before and after annealing in Fig.1.18g also verifies the observation. The instability temperature, or grain-coarsening temperature of nanograins (above which apparent grain coarsening occurs after 30 mins annealing) as the function of initial grain size is plotted in Fig.1.18h. It reveals that the grains below a critical size (~ 90 nm for Ni in Fig.1.18h and ~ 70 nm for Cu) present extraordinary thermal stability. The measured instability temperatures of Ni and Cu rise up to ~ $0.68T_m$ (the equilibrium melting temperature in K) and ~ $0.45\ T_m$, respectively.

Zhou et al. [154] attributed the extraordinary thermal stability of NG Ni and Cu with grain size smaller than the critical value to grain boundary energy drop and grain boundary relaxation. The grain boundary excess energy was reduced from ~ 0.52 ± 0.03 J/m^2 to 0.23-0.27 J/m^2 when the grain size refined from ~ 125 nm to ~ 50 nm, resulting in the enhanced thermal stability of

nanograins below critical size. The grain boundary excess energy drop may stem from the fact that the plastic deformation of topmost surface layer during SMGT is accommodated by the formation of SFs and/or nanotwins in low-energy configuration. Meanwhile, the grain boundary relaxation also contributes to the grain boundary energy drop. Grain boundary relaxation during plastic deformation can transforms the grain boundary structure into a lower energy state through grain boundary dissociation, which takes place by emission of stacking faults from grain boundaries. Meanwhile, the formation of nanotwins is also believed to lower the grain boundary energy state. In contrast, the NG structures produced by other techniques like inert gas condensation generally exhibit poor thermal stability due to the high energy state of grain boundaries [155].

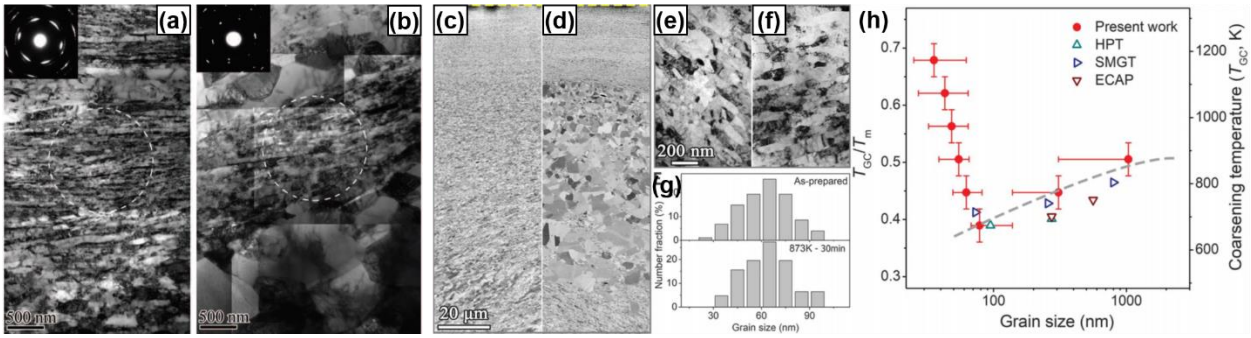

Figure 1.18 Thermal stability of nanostructured Ni layer processed by SMGT [99,154]. TEM micrographs showing the microstructure of NL Ni layer (b) before and (c) after annealing at 500 ^{o}C for 1 hour. SEM images of (a) as-processed GS Ni sample that was processed by SMGT using liquid nitrogen as cooling solvent and (b) the sample after annealing at 600 ^{o}C for 30 mins. TEM images of the nanograins of (c) as-processed sample and (f) the sample after 600 ^{o}C annealing. (g) Grain size distribution of as processed and 600 ^{o}C annealed specimens. (h) Grain coarsening temperature as a function of average grain size in GS Ni.

In summary, the nanostructures formed in the topmost layer of gradient structure that was processed by SMGT present unique grain morphology and possess lower grain boundary energy state compared with other nanostructured metals, leading to the significantly enhanced thermal stability. The formation of these structures is closely related to the high strain rate and gradient, and the shear deformation during SMGT [99,154].

1.6. Nickel-based superalloys

1.6.1 Microstructure and precipitation behavior of nickel-based superalloys

Nickel-based superalloys exhibit extraordinary combination of high strength, ductility and oxidation resistance at high temperatures [156,157]. The application of these type of metallic materials is mainly in the combustor and turbine section of the engine where extremely high temperature maintained during operation. Except the applications in heat engine, the nickel-based alloys are also widely used in the oil and gas industry, nuclear power plant, military electric motors, chemical processing vessels, petrochemical equipment and heat exchange tube etc. [156,158].

The extraordinary performance of nickel-based alloys is mainly attributed to the combination of high phase stability of FCC structured γ matrix and the capability to be strengthened by a variety of methods [158]. The processing methods of nickel-based alloys depend on the intend applications as the cooling schemes is essential for the control of grain structures, which further determine the high temperature performance of the alloys. For instance, grain boundaries usually be damage first at elevated temperatures. Hence, the components in the early stage of jet engine where operating temperature is the highest are typically single crystallized. However, the components in the later (lower operating temperature) stage of jet engine are manufactured by polycrystalline alloys [158]. There are four major forms of nickel-based alloys [159]: i) billets formed from forged or rolled conventionally cast ingots; ii) directionally solidified alloys with polycrystalline structures; iii) single-crystal alloys; iv) powder metallurgy processed alloys used in jet engine disks. Although nickel is the major component, most of nickel-based alloys contain up to almost 40 wt.% of five to ten kinds of other alloying elements. Table 1.1 listed the chemical composition of several typical nickel alloys [158–160].

Table 1.1 Chemical compositions of commercial nickel-based alloys (wt.%, balanced by Ni) [158–160]

Alloys	Elements													
	Al	Ti	Zr	Fe	Co	Cr	Nb	Mo	W	Ta	Hf	Re	C	B
Commercial cast and wrought alloys														
IN 718	0.5	0.9	-	18.5	-	19.0	5.1	3.0	-	-	-	-	-	0.02
IN 713LC	5.9	0.6	0.1	-	-	12.0	2.0	4.5	-	-	-	-	0.05	0.01
Waspaloy	1.3	3.0	-	1.0	13.5	19.5	-	4.3	-	-	-	-	0.08	0.006
C-22HS	0.5	-	-	2.0	1.0	21.0	-	17.0	1.0	-	-	-	0.01	-
C1023	4.2	3.6	-	-	10.0	15.1	-	8.5	-	-	-	-	0.16	0.01
Rene’ 80	3.0	5.0	0.03	-	9.5	14.0	-	4.0	4.0	-	-	-	0.17	0.02
Directionally solidified alloys														
IN792	3.4	4.0	0.06	-	9.0	12.6	-	1.9	4.3	4.3	1.00	-	0.09	0.02
GTD111	3.0	4.9	-	-	9.5	14.0	-	1.5	3.8	2.8	-	-	0.1	0.01
Single-crystal alloys														
Rene’ N4	4.2	3.5	-	-	7.5	9.8	0.5	1.5	6.0	4.8	0.15	-	0.05	0.00
Rene’ N5	6.2	-	-	-	7.5	7.0	-	1.5	5.0	6.5	0.15	3.0	0.05	0.00
Rene’ N6	5.8	-	-	-	12.5	4.2	-	1.4	6.0	7.2	0.15	5.4	0.05	0.00
CMSX-3	5.6	1.0	-	-	5.0	8.0	-	0.6	8.0	6.0	0.10	-	-	-
CMSX-4	5.6	1.0	-	-	9.0	6.5	-	0.6	6.0	6.5	0.10	3.0	-	-
CMSX-10	5.7	0.2	-	-	3.0	2.0	0.1	0.4	5.0	8.0	0.03	6.0	-	-
PWA 1484	5.6	-	-	-	10.0	5.0	-	2.0	6.0	9.0	0.10	3.0	-	-
Powder-processed alloys														
Rene’95	3.5	2.5	0.05	-	8.0	13.0	3.5	3.5	3.5	-	-	-	0.065	0.013
N18	4.4	4.4	0.03	-	15.6	11.2	-	6.5	-	-	0.5	-	0.02	0.15
IN100	4.9	4.3	0.07	-	18.4	12.4	-	3.2	-	-	-	-	0.07	0.02

Table 1.2 The alloying elements effects of commercial nickel-based alloys [158,159,163].

Elements	Effects
Al	γ' phase former, improve oxidation and hot corrosion resistance
Ti	γ' phase former, tailor the stacking fault energy
Zr	Inhibit grain boundaries sliding
Fe	Solid solution strengthener
Co	Solid solution strengthener, increase the solvent temperature of γ' phase
Cr	Solid-solution strengthener, M_7C_3 and $M_{23}C_6$ carbides former, improve oxidation and hot corrosion resistance
Nb	γ" phase former, MC and M_6C carbides former
Mo	Solid solution strengthener, MC, $M_{23}C_6$ and M_6C carbides former
W	Solid solution strengthener, MC, $M_{23}C_6$ and M_6C carbides former
Ta	Solid solution strengthener, MC carbide former, improve creep properties
Hf	Solid solution strengthener, improve castablity, control the shapes of carbides
Re	Solid-solution strengthener, retard γ’ coarsening
C	M(C,N) carbonitrides former, grain-boundary strengthener
B	Grain-boundary strengthener, improve creep properties and rupture strength
N	M(C,N) carbonitrides former

As listed in the table 1.1, nickel-based alloys have complex chemistry. Various amount and combination of alloying elements are added to the FCC structured matrix to achieve desired microstructure and mechanical properties. For instance, the addition of Al and Nb would tend to form the major strengthening precipitates: γ' and γ" phases [161,162]. Ti element substitutes the Al site of γ' phase and correspondingly increase the fraction of γ' precipitates. Besides, the SFE of the alloy decreased with the increasing of Ti concentration [159]. Mo presents in both γ matrix and γ' phase, and determines the relative mismatch between them [159]. Cr mainly solute in γ matrix and confers oxidation and corrosion resistance [158,159]. The addition of Zr may segregates to grain boundaries and inhibit the grain boundaries sliding at high temperatures. the other elements like Mo, Ta, W and Re are added for solid solution strengthening and to increase the concentration of γ' and γ" phase. Besides, the B, C and Hf contribute to the formation of borides or carbides that are usually decorated along grain boundaries [158,159]. The effect of typical alloying elements of nickel-based alloys are listed in table 1.2 [158,159,163].

Most of nickel-based alloys are precipitation strengthened. There are several kinds of precipitates with various crystal structures and chemical compositions tend to form after heat treatment. Prior studies suggest that the initial thermal history of the alloys and the subsequent ageing conditions under which these alloys are processed significantly influence the size, shape, distribution and volume fraction of precipitates and, consequently, resulting in different high temperature performance [164–176]. The most commonly encountered precipitates in nickel-based alloys including γ', γ", δ, η, β, carbides and Laves phase etc. [159,168]. Detailed information about some of these precipitates will be presented in the following section.

The extraordinary high temperature strength of nickel-based alloys can largely be attributed to the γ' and γ" phases that coherently distributed in face-centered-cubic (FCC) γ matrix [177–192]. The strengthening of these two phases are originated from three folders [193]: i) the intrinsic strength of γ' and γ" phases, ii) the coherency strain that related to lattice misfit between the coherent or semi-coherent γ/γ' and γ/γ" interfaces and iii) the anti-phase boundary energy, which is proportional to the energy required for a dislocation to glide through. The coherent strain hardening derived from lattice mismatch is the dominant strengthening mechanism for theses alloys at peak aged condition.

The γ' precipitate has a nominal composition of Ni_3Al with an ordered $L1_2$ (FCC) structure, as shown in Fig.1.19a, where Al occupies the cubes corners while Ni locates at the centers of cube faces [159]. There are equivalent three Ni atoms and one Al atoms in one cube. However, other alloying elements like Ti and Nb tend to substitute the Al site and vary the chemical composition of γ' phase in different alloys and, consequently, leading to a different lattice mismatch between γ' and matrix. The lattice mismatch (δ) between precipitates and matrix is critical in strengthening and can be quantitatively defined as [159]:

$$\delta = \left|\frac{a_{\gamma\prime} - a_{\gamma}}{\bar{a}}\right| \qquad \text{Equation 1.5}$$

where $a_{\gamma'}$ and a_{γ} represent the lattice spacing of a certain lattice plane of γ' and γ phase, respectively, and $\bar{a}$ represents the average value of $a_{\gamma'}$ and a_{γ}. Typically, the substitution of other elements to Al tailors the mismatch parameter of nickel-based alloy from almost zero (in Waspaloy superalloy) to ~ 0.5% [159]. The lattice mismatch (or misfit) between precipitates and matrix not only influences the mechanical properties by triggering the initial internal stress, but also tailors the shape of precipitates. Generally, the growing of precipitates is anisotropic to meet the requirement of lowest free energy. The strain energy associated with the coherency straining of the lattice during precipitation growth has a minimum value along the directions that have the lowest elastic modulus, i.e, the <001> direction for γ' precipitates. The {001} planes of γ' precipitates therefore possess the lowest strain energy. Consequently, the γ' phases are usually spherical in shape when the diameters are small. With the increasing of precipitate size, a flat γ/γ' interface parallel to <001> direction is preferentially formed, leading to the formation of cuboidal γ' precipitates. Besides, the precipitation and growth of γ' phase is sensitive to the cooling rate. Faster cooling rate usually results in a uniformly distributed size of γ' phase [159,194].

The other primary precipitate of nickel-based alloys that induces strengthening is γ" phase with a nominal composition of Ni_3Nb. The γ" phase has a DO_{22} (body-centered-tetragonal, BCT) structure as shown in Fig.1.19a [159]. Similarly, other elements like Al and Ti tend to substitute the Nb sites. Comparing the structure of γ' and γ" precipitates, their lattice parameter, a, is almost identical, whereas the parameter, c, of γ" phase is almost twice of that of γ' phase, by which γ" is named. The crystal structure relationship between tetragonal γ" phase and FCC γ matrix are as follow [191]:

$(011)_{\gamma"}||\{001\}_{\gamma}$, and $\langle 100\rangle_{\gamma"}||\langle 100\rangle_{\gamma}$.

However, the lattice mismatch parameters of γ"/ γ interface is anisotropic. Slama et al. [191] and Cozar et al. [195] studied the mismatch parameter of IN718 alloys and concluded that the lattice mismatch along <100> γ" and <010> γ" directions is less than 1%, whereas that along the <001> γ" direction is as high as 3%. The formation of coherent interface between precipitates and matrix is only possible when the coherency deformation is less than 1%, which implies that γ" phases tend to growth toward the <100> γ" and <010> γ" directions rather than the <001> γ" direction, leading to the formation of disk-shaped γ" phase that lies parallel to the {001} planes of γ matrix [191]. The coherency of γ"/ γ interface diminishes with the increasing size of γ" phase and vanishes after a critical value. This critical size of γ" phase varies in different alloys and usually in the range of several tens of nanometers [191].

According to the effects of different alloying additions (as shown in Table 1.2) and the differences between the nominal composition of γ' and γ" precipitates, the precipitation of these two phases is usually takes place independently with respect to each other [185]. For nickel-based alloys that contain both γ' phase former elements (Al and Ti) and γ" phase former elements (Nb), both γ' and γ" precipitates are observed. The EDS maps of a commercial Inconel 718 (IN718) nickel-based alloy in Fig.1.19b reveals that the Al and Nb elements enriched in γ' and γ" phases, respectively [176]. The γ' phases are still spherical in shape with small size, whereas the γ" phases are in disk shape. The TEM micrograph in Fig.1.19c also shows the co-precipitation of γ' and γ" phase in IN718 alloy after ageing at 800 ^{o}C for 6 hours [196]. The corresponding SAD patterns of γ' phase in Fig.1.19d and γ" precipitates in Fig.1.19e reveal the crystal structure relationship difference of these two phases with the γ matrix. The precipitation sequence of γ' and γ" phase is controlled by the ratios of Al + Ti to Nb of the alloys. Prior studies found that precipitation of γ' phase is more favored compared to γ" phase when the composition ratio of Al+Ti/Nb increases.

When this ratio exceeds about 0.9, a “compact morphology” in which the cuboidal shaped γ’ phases are coated on all six faces with γ” phases appears. The nucleation and growth of precipitates with this compact morphology are sluggish than those precipitated independently, resulting in an enhanced microstructural stability of the alloys.

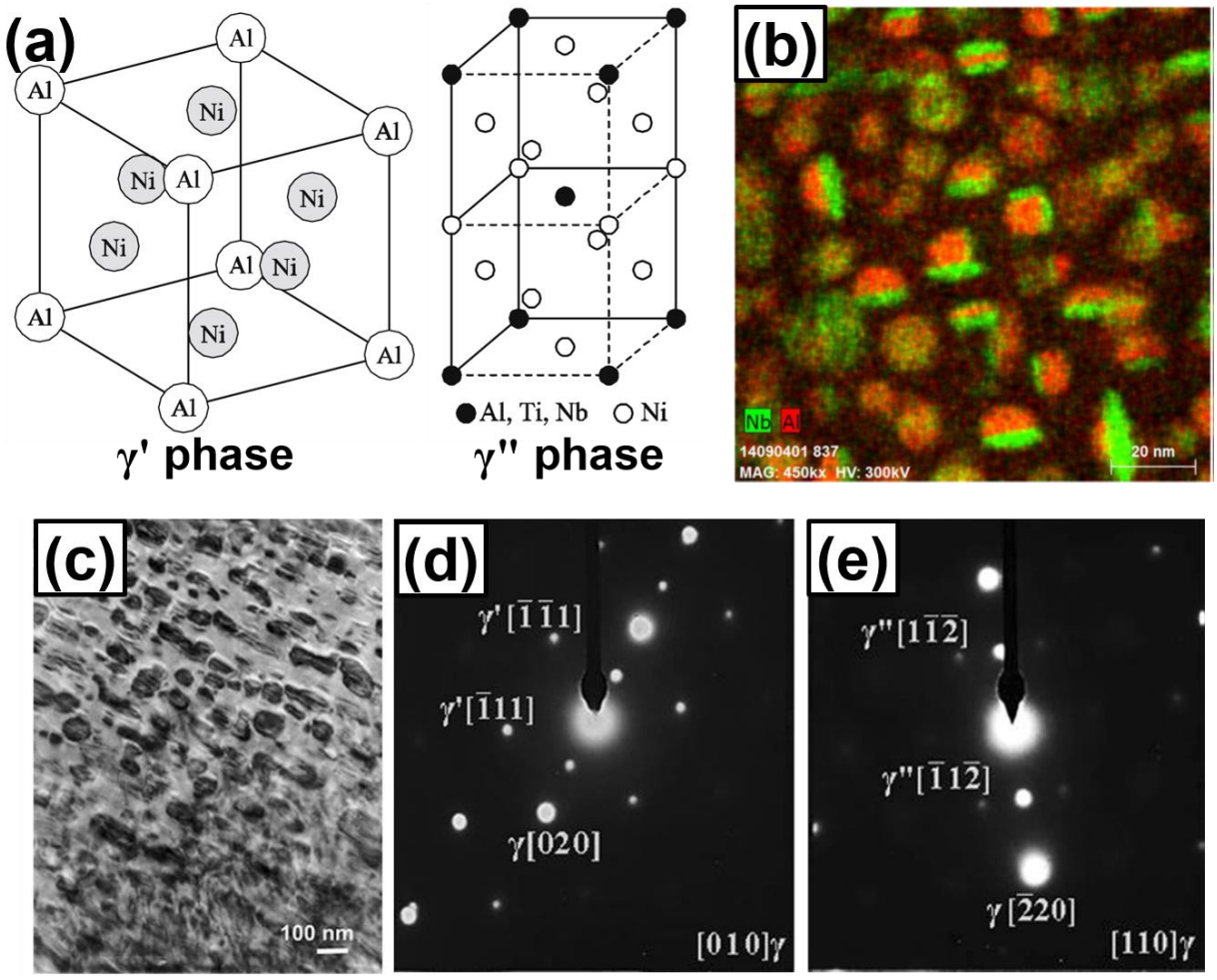

Figure 1.19 (a) Crystal structure of γ’ and γ” precipitates [159]. (b) EDS map of a commercial IN718 nickel-base alloy showing the partition of Al and Nb to γ’ and γ” precipitates, respectively [176]. (c) BF TEM micrograph showing the precipitation of γ’ and γ” phase in IN718 after ageing at 800 ^{o}C for 6 hours. The corresponding SAD pattern for (d) γ’ and (e) γ” phases [196].

The solvus temperature of γ’ and γ” precipitates is around 900 ^{o}C. At the temperatures above 900 ^{o}C or on prolonged exposure at lower temperatures, other kinds of precipitates, like δ and η phases formed [162,197–203]. The γ” phases are metastable and transform to equilibrium stable δ phases if the alloy is kept between 700 – 900 ^{o}C [179]. At the aging temperature higher

than 900 °C, δ phases precipitate directly from the grain boundaries. The δ phase has $D0_a$ orthorhombic crystal structure (Fig.1.20a) and the same nominal composition with γ" phase (Ni_3Nb). Other elements like Al and Ti has been often found to substitute the Nb site, tailoring the chemical composition and lattice parameter of δ phase in different alloys [204]. The orientation relationship between δ precipitates and γ phase has been studied by researchers in several systems and can be expressed as follows [205]:

$\{111\}_\gamma||(010)_\delta$, and $\langle 110\rangle_\gamma||\langle 100\rangle_\delta$.

The orthorhombic structure of δ phase comprises of near-hexagonal stacking layer along the b-direction with an ABAB-type stacking sequence perpendicular to the habit $(111)_\gamma$ plane. The mismatch parameter between δ phase and matrix are also anisotropic. For instance, in commercial IN718 alloy, the lattice mismatch between the {010} planes of δ phase and {111} planes of γ matrix is ~ 0.54% along $[100]_\delta$ direction and ~2.38% along the $[001]_\delta$ direction. Fig.1.20b shows the TEM micrograph of the typical plate-like morphology of δ precipitates with extremely high aspect ratio [206].

Another type of precipitate with plate-like morphology that has been observed in nickel-based alloys is η phase. The nominal chemical composition of η phase with $D0_{24}$ hexagonal crystal structure is Ni_3Ti, as shown in Fig.1.20a [205,207]. The site of Ti can be substituted by other elements like Al, Nb etc., resulting in the formation of η phase with different chemical compositions. For instance, the η phase formed in Allvas 718 Plus nickel-based alloys has the chemical composition of Ni_6AlNb [205]. The investigations about the orientation relationships between η phase and matrix reveals that it follows the Blackburn orientation relationship [205]:

$\{\bar{1}\bar{1}1\}_\gamma||\{0001\}_\eta$, and $\langle 011\rangle_\gamma||\langle 2110\rangle_\eta$, $\langle 112\rangle_\gamma||\langle 0\bar{1}10\rangle_\eta$.

Unlike the anisotropy of lattice mismatch along different direction of δ phase, the lattice mismatch between the {0001} basal plane of η phase and {111} planes of matrix along the <011>γ direction is ~ 0.98%, whilst that along the <112>γ direction is ~ 0.95% in Allvas 718 Plus alloy [207]. Fig.1.20c shows the TEM micrograph of typical η phase with plate-like morphology.

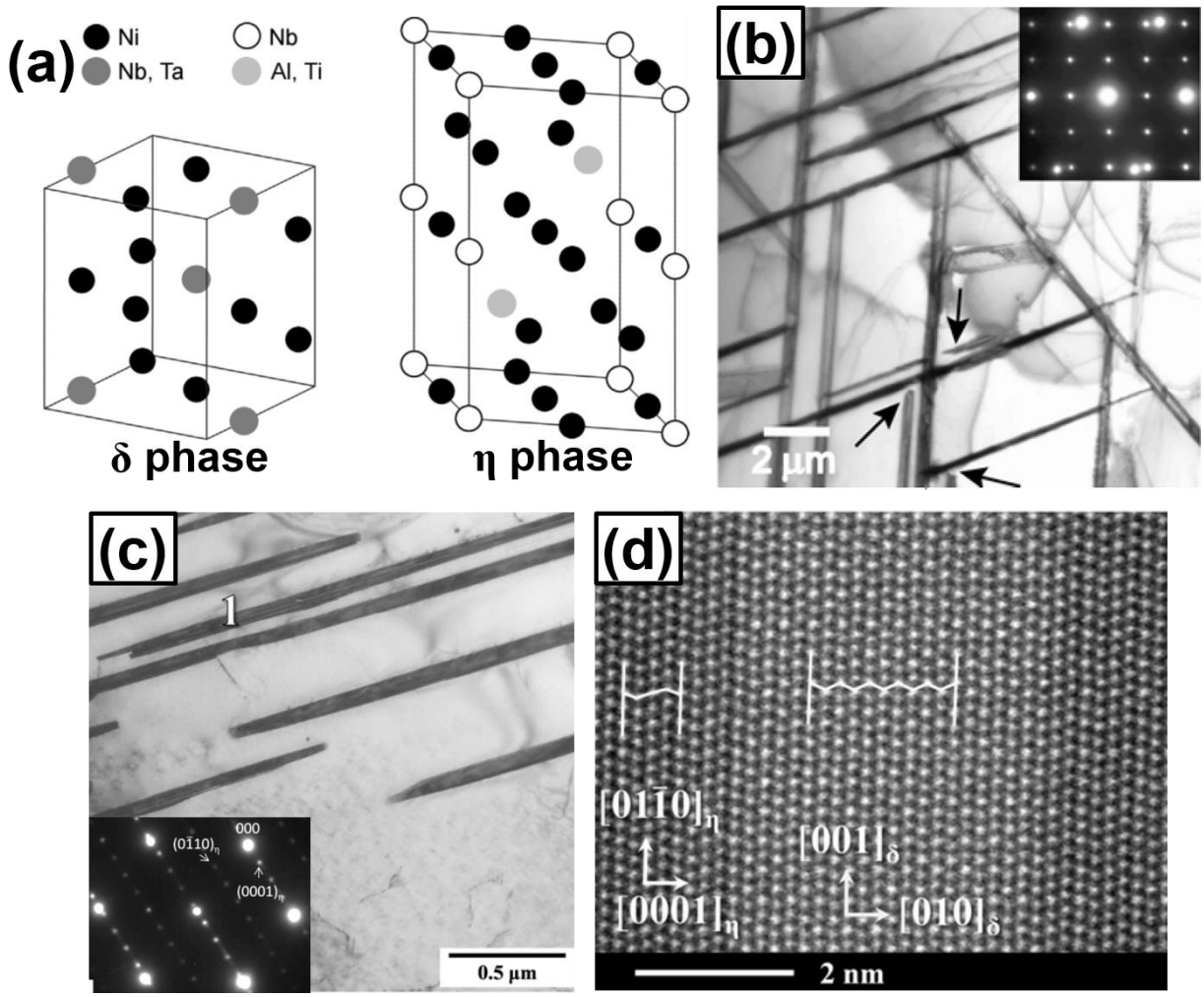

Figure 1.20 (a) Crystal structures of both δ and η precipitates [208]. BF TEM micrographs of (b) δ precipitates [206] and (c) η precipitates. Inset is the corresponding SAD patterns. (d) HRTEM micrograph showing the stacking sequence of δ (ABABA-type) and η (ABACA-type) precipitates [205].

Despite the difference in chemical composition, the crystal structures of δ and η precipitates are similar. The structure of η precipitates comprises the stacking layers along the c direction with an ABAC-type sequence perpendicular to the habit $(111)_\gamma$ plane. Compared with the ABAB-type stacking sequence of δ phase, the only difference lies in the presence of a C-layer than a B-layer in η phase [207]. Therefore, a fully coherent interface between the close-paced plane of these two phases can form. Pickering et al. [205] and Messé et al. [207] have found the presence of both hexagonal structured η phase and orthorhombic structured δ phase in one large precipitate. As shown in the HRTEM micrograph in Fig.1.20d, the interface between the close-packed {0001}

plane of η phase (left) and {010} plane of δ phase (right) is fully coherent in Allvas 718 Plus alloys after annealing at 840 ^{o}C for 4 hours. The precipitation of δ and η phases appears first at random grain boundaries that serve as diffusion path for alloying elements, then followed by twin boundaries, and at long time intragranularly [205]. There are two growth mechanisms have been reported for the precipitation of δ and η phases, i.e., by i) discontinuous precipitation or ii) diffusion of alloying elements and by the transformation of γ' phase (for η phase) or γ" phase (for δ phase). The phase transformation involves structure changes, from $D0_{22}$ (γ") to $D0_a$ (δ) or $L1_2$ (γ') to $D0_{24}$ (η), which requires higher activation energy. For discontinuous precipitation, there are three types of reaction have been summarized as follows [209]:

Type 1: α' → α + β

Type 2: α' + ε → α + ε

Type 3: α' + ε → α + θ

where α' represent the single-phase supersaturated matrix, α is the solute depleted phase after reaction, β and θ are the stable precipitates formed, and ε is the prior coherent matrix precipitate. The precipitation of δ and η phase fit well with type 3 of discontinuous precipitation, where α is the FCC structured γ matrix, ε refers to the coherent precipitates of γ' or γ" and θ corresponds to the stable δ and η phases. Discontinuous precipitation usually results in a serrated grain boundaries, similar phenomena have been reported in many nickel-based alloys [205,207,210].

γ', γ", δ and η phases are the primary precipitates that control the properties of nickel-based alloys. The precipitation behaviors, including the type, size, shape, morphology and volume fraction of precipitates are determined by the chemical composition and thermomechanical history of the alloys. The precipitation behaviors of nickel-based alloys are determined by the alloying elements [208]. For instance, Al, Ti, Nb and Ta are found to promote the precipitation of γ' and γ" phases. Whereas excess level of Ti addition is beneficial to the precipitation of η phases. Excessive level of Ta and Nb will promote the precipitation of δ phases. Antonov et al. [208] systematically investigated the thermal stability and compositional dependence on alloying elements in several γ'-γ"-δ-η Ni-base superalloys. They concluded that if the chemical compositional ratio of Al/(Nb+Ta+Ti) smaller than 0.85, the precipitation of δ and η phases dominates, whilst a velue greater than 0.85 usually suggesting the precipitation of γ' phase. The precipitation of δ and η phases is also controlled by the addition of alloying elements. The combinations of different type, size, morphology and volume fraction of precipitates yield different types of nickel-based alloys.

Hence, alloys that meet different demands of service conditions can therefore be designed by optimizing the chemical composition of them.

Except the precipitates mentioned above, several other kinds of precipitates also play an important role in the performance of nickel-based alloys at high temperatures. Carbides are one of the primary precipitates and the role of it to the properties of nickel-based superalloys are complex [211,212]. There are three kinds of carbides in nickel-based alloy: MC, $M_{23}C_6$ and M_6C. MC carbides form when the segregated C react with Mo, Ti and Cr during solidification. They are mostly in discrete blocky shape and distribute in both intergranular and intragranular positions. MC carbides have NaCl structures and tend to degenerate to secondary carbides at high temperatures. $M_{23}C_6$ carbides usually precipitate at intermediate temperatures between 760 - 980 ^oC with irregular shape intergranularly. Specifically, these carbides tend to precipitate from HAGBs with high interface energy. They can precipitate directly from the γ matrix, or through the reaction of [211]:

$MC + \gamma \rightarrow M_{23}C_6 + \gamma'$

$M_{23}C_6$ carbides have a complex cubic structure that is similar with the structure of σ precipitates. Therefore, the degradation of σ precipitates also leads to the formation of $M_{23}C_6$ through the eutectoid reaction of:

$\sigma + C \rightarrow M_{23}C_6 + \gamma$

As for M_6C carbides, they are more thermodynamically stable than $M_{23}C_6$ carbides. M_6C carbides present both in intergranular and intragranular positions through the reaction of:

$MC + \gamma \rightarrow M_6C + \gamma'$

similar to the precipitation of $M_{23}C_6$ carbide. The difference is that M_6C formed at higher temperatures than $M_{23}C_6$ when the amount of Mo and W is between 6 – 8 wt.% [211].

The precipitation of other phases like Laves phase, μ phase, β phase, P phase and Pt_2Mo-type long range ordered Ni_2Mo or $Ni_2(Cr,Mo)$ phase etc. have been extensively investigated by researchers as well [158,213–215]. The formation of these precipitates determines the performance of nickel-based alloys at elevated temperatures, such as the strength, creep strength, oxidation and corrosion resistance etc. Mechanical behavior is the focus of this project and a brief summary of microstructure-mechanical properties relation of nickel alloys will be presented in the following section.

1.6.2 Microstructure-mechanical properties relation of nickel-based alloys

As aforementioned, mechanical behaviors of nickel alloys are a strong function of microstructures [179,180,191,192]. Tensile strength, creep strength, thermo mechanical fatigue properties and cyclic crack growth are of primary interests. The limitation of any of these four properties determines the overall performance of the alloy.

The high strength or hardness of nickel-based alloys is mainly determined by the precipitation of ordered γ' and γ" phases [161,193,216]. While a dislocation glide through a precipitate particle that grow coherently with matrix, the strengthening of the alloy can arise due to several mechanisms like coherency strain hardening, order hardening, modulus hardening and stacking faults hardening etc. [193,216]. For nickel-based alloys, prior studies suggest that the first two are the primary strengthening mechanisms and the contribution of the rest are negligible. The factors that influence the strengthening effect including the size, shape, density and morphology of γ' and γ" phases. Generally, the increased volume fraction of ordered precipitates contributes to the improvement in strength, but comes at the expense of processing capability or environment resistance as tailoring of chemical composition of the alloys is required. Yan et al. [217] also found that a critical value of γ' precipitates exist for the optimization of yield strength of IN740H alloys. Fig. 1.21a and b show the blockage effect of γ' precipitates to the movement of stacking faults and dislocations in the γ matrix channel of the single crystalline nickel-based alloy after tensile tests at room temperatures and 900 ^{o}C, leading to the strengthening of the alloy [218].

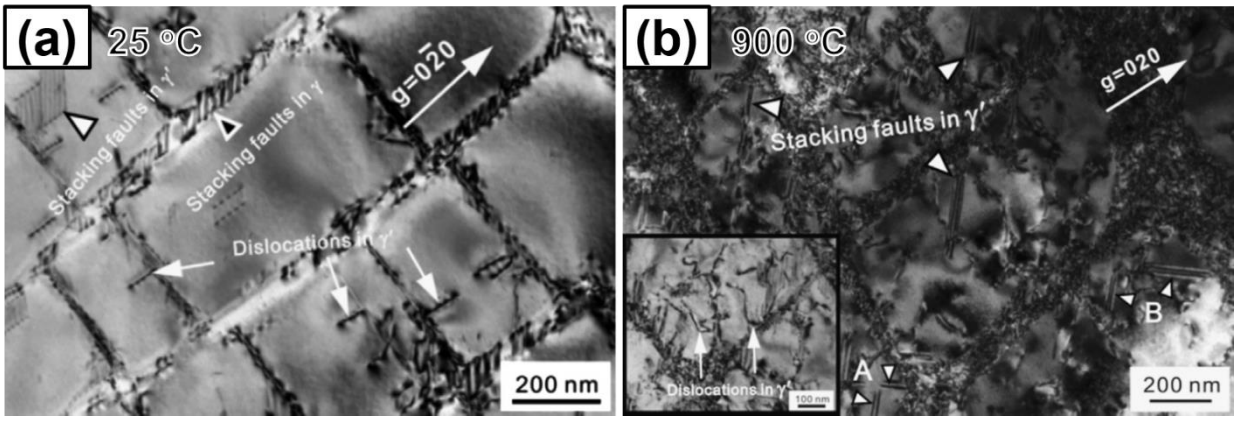

Figure 1.21 TEM micrographs showing the blockage effect of γ' precipitates to the movement of stacking faults and dislocations in the γ matrix channel of the single crystalline nickel-based alloy after tensile tests at (a) room temperatures and (b) 900 ^{o}C [218].

The creep resistance is another property of nickel-based superalloys that is essential to the performance of them at high temperatures. The corresponding creep mechanisms at elevated temperatures and different stress levels have been extensively investigated by researchers [219–224]. In general, the extraordinary creep resistance of superalloys is largely attributed to the resistance of precipitates to shearing. During creep, the dislocations must overcome the precipitate in different manners, depending on creep conditions and microstructural parameters such as the precipitates size, density and morphology. Several shearing mechanisms have been proposed, including dislocation climb, looping, stacking fault related shearing and micro-twinning [220,222,223]. The creep resistance depends largely on the size and spacing of γ' phases. Prior studies reveal that highest creep life was achieved usually when the volume fraction of γ' phase higher than 50% [224]. Fig.1.22a shows the relationship of volume fraction of γ' phases and creep rupture life of single crystalline TMS-75 and polycrystalline IN713C nickel-based alloys [224]. It shows that the strength peaks located at the position of 60% volume fraction of γ' phases. Once dislocation glide through the narrow channel of matrix, the dislocation was forced to bow through the channel due to the resistance of γ' phases to shearing (in Fig.1.22b). Similar γ' precipitates/dislocation microstructure has also been found in GTD-111 alloy when creep at 982 ^{o}C and 152 MPa, as shown in Fig.1.22c [220]. The creep behavior also dependents with temperatures. At intermediate temperatures, stress usually insufficient for the shearing of γ' precipitates. While at high temperatures, shearing of γ' phase occurs, leading to the rapid accumulation of microstructural damage and acceleration of tertiary creep rates. Detailed information about the creep can be found in many other works [158,220].

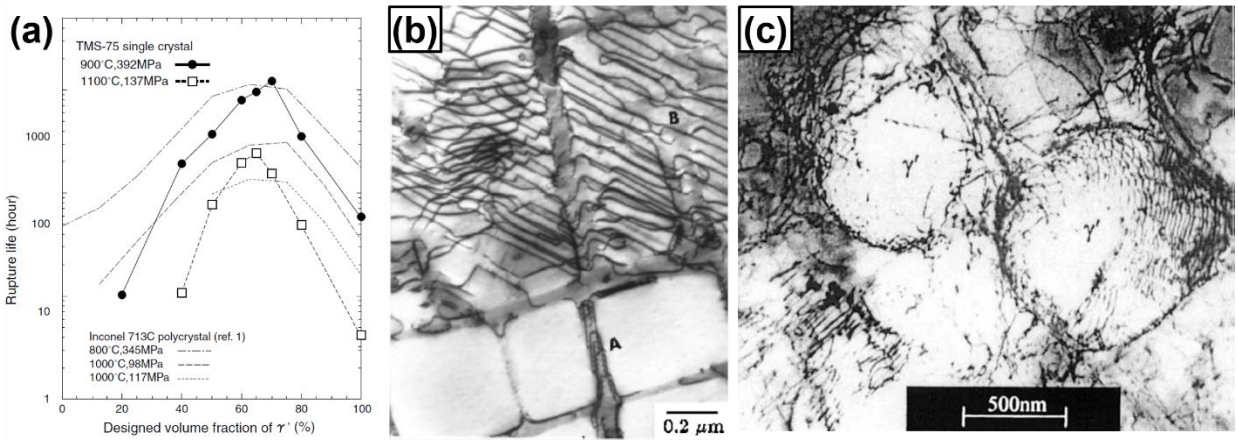

Figure 1.22 (a) Relationship of designed volume fraction of γ' phases and creep rupture life of single crystalline TMS-75 and polycrystalline IN713C alloys [224]. (b) TEM micrograph shows that dislocations were forced to bow through the channel in CMSX-3 alloys [221]. (c) TEM micrograph showing dislocation networks in γ' phase during creep of GTD-111 alloy [220].

The effect of other precipitates that grow incoherently with the matrix to the strength of superalloys are complex. The precipitation of δ and η phases is generally detrimental to the mechanical properties (both in strength and ductility), which is partially owing to the absence of coherency strain hardening [204,205]. The other reason lies in that the precipitation of these phases would be at the expense of alloying elements like Nb and Al etc. resulting in a reduced fraction of γ' and γ" density and therefore the strength. The stress concentration generated in the region that close to the strip-like μ phase promotes the nucleation and propagation of cracks during creep, resulting in a drastic creep reduction of creep life time for a 6%W nickel-based alloy [225]. However, the precipitation of other phases is not necessarily detrimental to the mechanical properties of superalloys. The serrated grain boundaries formed due to the precipitation of δ and η phases are likely to improve the intergranular fatigue crack resistance. The pinning effect of precipitates that decorated along grain boundaries has benefit to the grain stabilization [205]. For carbide, fine blocky dispersed precipitates along grain boundaries can inhibit the grain boundaries sliding and consequently, improving the creep and rupture strength. While if they present at the grain boundaries as continuous films, the ductility of the alloys will be significantly sacrificed [211].

In summary, the mechanical properties of nickel-based alloys are highly sensitive to the precipitates formed within the γ matrix. The precipitation behavior controlled both by the thermomechanical history and chemical compositions of these alloys. Optimization of the

metallurgy process and chemical components of nickel-based alloys that can meet the demands of different service conditions is therefore achievable.

1.7. Motivation and objective

Two kinds of commonly used nickel-based alloys: Hastelloy C-22HS and IN718 were studied in this project. The motivation of this project can be divided into two main parts. First is to investigate the microstructure evolution and mechanical behaviors of GS C-22HS and IN718, especially that of each individual layer of gradient structures. Second is to study the effect of thermomechanical history to the precipitation behavior of GS nickel-based alloys, and the corresponding properties (including mechanical and thermal stability) responses using microstructural characterization techniques like SEM and TEM and in-situ micropillar compression tests.

Gradient structures have been successfully introduced into several kinds metallic materials by means of severely surface modification methods like SMAT, SMGT, SMRT etc. The strengthening and work hardening mechanisms of gradient structures have also been studied. However, the mechanical properties of different regions of GS materials are rarely studied. In this thesis work, in-situ compression tests have been performed to study the mechanical properties of specific regions of the gradient microstructures formed in nickel-based alloys, and the underlying deformation mechanisms are discussed.

As aforementioned, the precipitation behaviors are critical to the properties of nickel-based alloys. Prior studies also suggest that the precipitation behavior can be influenced by the initial microstructure, such as grain size and dislocation density. For instance, cold rolling is found to accelerates the of γ’ and γ” phases precipitate, and also the γ” → δ phase transformation. This is attributed to the fact that high density of defects can serve as nucleation site of precipitates and accelerate the diffusion rate of alloying elements through dislocation pipe diffusion rather than lattice diffusion. In this study, SMGT was used for the processing of GS metals. SMGT has been proven to be a more effective approach than other heavy plastic deformation techniques like ECAP and HPT in metal deformation. Therefore, the precipitation behavior of gradient structure layer formed in nickel-based alloys is different with the undeformed matrix. Consequently, microstructures with precipitates size/type/density gradient are expected to be form in nickel-based

alloys after heat treatment. The mechanical behavior and thermal stability of gradient C-22HS and IN718 samples are studied using in situ micropillar compression tests and TEM. Detailed precipitates evolutions in GS C-22HS and IN718 samples are captured and discussed.

CHAPTER 2. EXPERIMENTAL

2.1 Fabrication: surface mechanical grinding treatment

SMGT was firstly invented by Lu et al. and co-workers for the severe surface modification of metallic materials [85]. Similar design was adopted for introduction of gradient structures into the surface of nickel-based alloys in this thesis ork. Fig.2.1a shows the setup of SMGT. A MicroLux bench lathe with maximum rotation speed of 2500 rpm was modified to meet the requirement of SMGT. The magnified processing stage of the machine is presented in Fig.2.1b.

As schematically illustrated in Fig.1.4, a hard and half-spherical tool penetrated into the rotated rod surface and slided along the longitudinal direction during SMGT for the generation of gradient structured surface layer. There are four parameters for the control of gradient structures formed on the surface of metallic rod: (i) rotation speed of processed metal rod (v_1), (ii) gliding speed of half-spherical tool (v_2), (iii) penetration depth of the tool into the rod surface (d) and (iv) the total processing passes (n). The rotation speed v_1 was adjusted accordingly to keep the shearing rate of different samples are comparable. Significant surface scraping occurs at high shearing speed and a proper rotation speed v_1 is required to retain the gradient layer after SMGT. For instance, for nickel-based alloys with poor machinability, a relative slow rotation speed of 400 rpm was adopted for the rod with diameter of 10 mm. The sliding speed was kept at ~ 10 mm/min for all processed samples in this thesis work. The other parameter that is critical for the surface quality of processed specimens is the penetration depth d. Scraping takes place when process metals that exhibit poor work hardening ability or machinability with large penetration depth. Penetration depth d ranges from 20 – 30 μm was adopted in this thesis study. The specimens of this thesis work were treated 6 – 10 passes according to the objectives of studies. Detailed information about the processing parameters of each specimens will be presented in each chapter.

During SMGT process, one end of the processed bar was clamped by the chuck and the other end was fixed by the dead center, as illustrated in Fig.2.1b, preventing the rod from bending since significant axial force will be applied during surface grinding. Surface turning was performed to the rod prior to surface grinding. The hard and half spherical tool with diameter of 6 mm was made of tungsten carbide (WC). Other hard materials like silicon carbide (SiC) or diamond also

suitable for grinding. Both commercial coolant and liquid nitrogen were used for temperature control during SMGT for different cooling rate requirements.

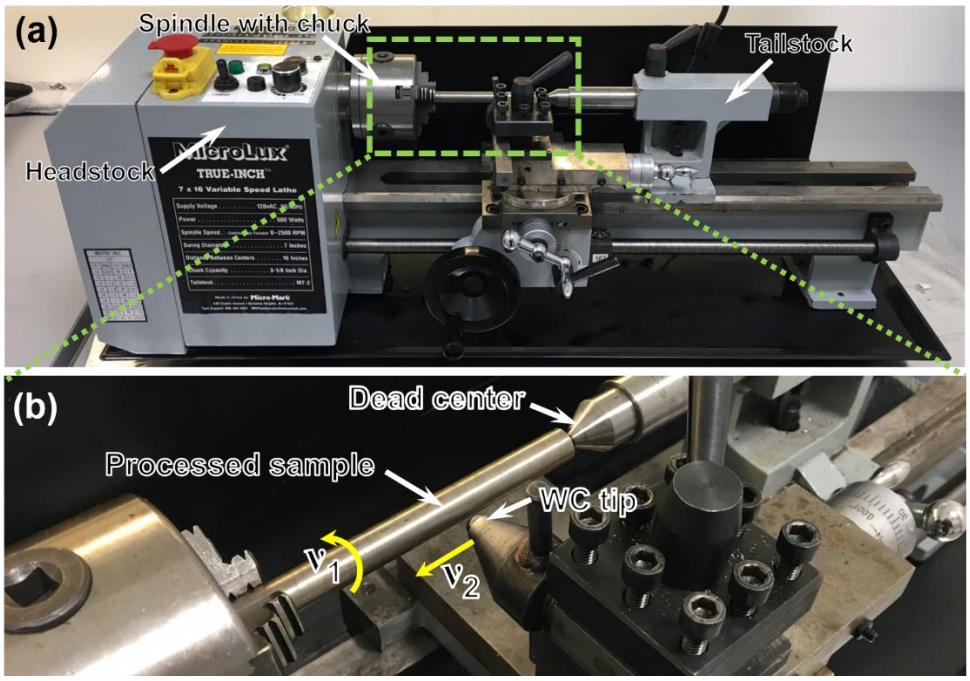

Figure 2.1 Set-up of surface mechanical grinding treatment (SMGT).

2.2. Microstructural characterization: TEM

TEM is indispensable for microstructure characterization of nanostructured materials, including morphologies, textures and imaging of atoms etc. [226]. A classic TEM microscope is composed of four main components: the electron gun (illumination), electrostatic lenses, sample stage and imaging system, as illustrated schematically in Fig.2.2a [226]. Electrons are accelerated through 80 – 300 kV accelerating voltage in the electron gun consisting a cathode and an anode. The high energy electron beams that be ejected from the electron gun pass through a thin-film specimen (normally less than 100 nm), yielding comprehensive information about the sample [227]. For instance, the electrons direct transmit through the specimen can generate micrographs which are generally known as bright filed (BF) images. Whereas those electrons be diffracted by the lattice of specimen can be collected to take dark filed (DF) images, which are found to be favorable for the characterization of defect. The coherent electron beam that is focused through series condenser lenses (as shown in Fig.2.2a) strikes the specimens, parts of the beams are

transmitted, and the rest are diffracted. By adjust the position of objective aperture, either the transmitted or diffracted electron beams are selected, leading to the imaging of either BF or DF micrographs.

Selected area diffraction (SAD) pattern of specimen is determined by the intermediate lens aperture size when parallel electron beam transmits through the selected small area of the thin foil. Similar to the working principle of X-ray diffraction (XRD), the formation mechanism of SAD is governed by Bragg's law:

$\lambda = 2d\sin\theta$ Equation 2.1

where λ represent the wavelength for the incident beam, d is the spacing between crystallographic plane, and θ represents the angle between incident beam and the crystallographic plane. The SAD pattern enables the crystallographic identification of different features like twin boundaries and amorphous structures etc.

The other assistant function of TEM is the scanning electron microscopy (STEM). The electron beam of STEM is focused to a spot and scanned sequentially over the sample when transmit through the thin foil. Secondary electrons, X-rays and other signals are aroused during the scanning process, leading to the contrast that reflect the atomic mass differences between different scanned areas in STEM image. Hence, STEM mode is especially favorable to identify of structures with atomic mass contrast and perform element composition mapping. It is typically accompanied by chemical analysis techniques like mapping by energy dispersive X-ray (EDX) spectroscopy and electron energy loss spectroscopy (EELS) etc.

TEM and STEM analyses in this thesis were performed using an FEI Talos 200X analytical microscope, coupled with EDX detector, as shown in Fig.2.2b. Some high-resolution STEM (HRSTEM) imaging for atomic scale characterization were performed in Birck Nanotechnology Center at Purdue University using a ThermoFisher Themis Z TEM operated at 200 kV.

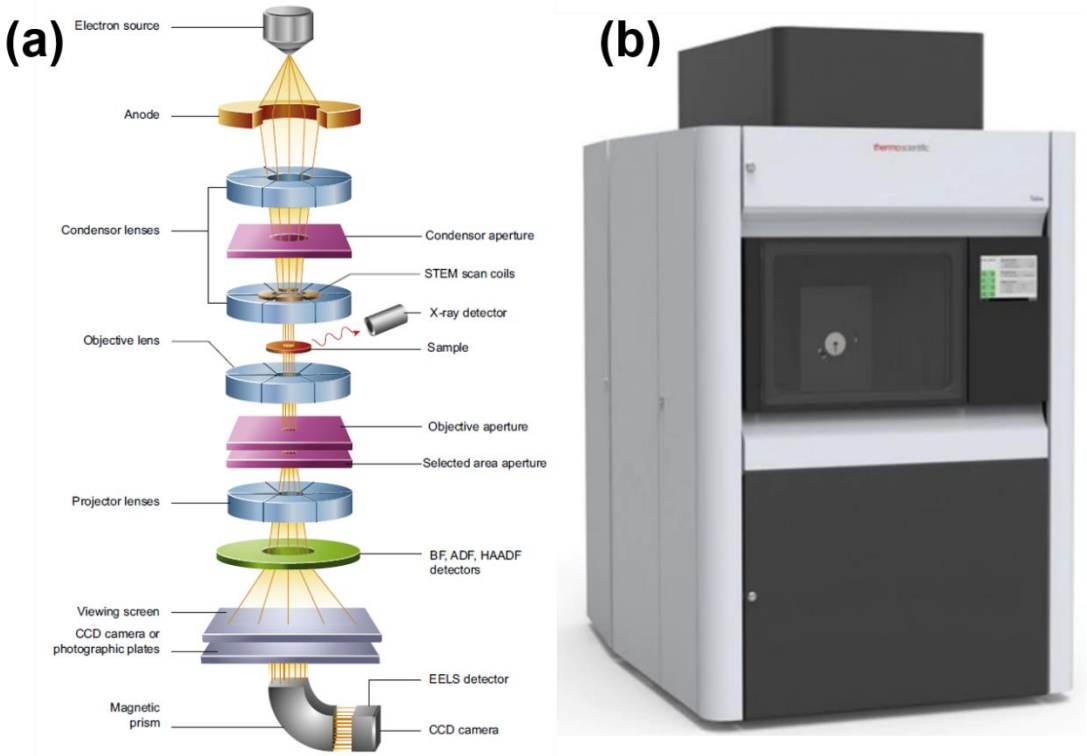

Figure 2.2 (a) Schematic of main components of TEM microscope [226]. (b) Picture of an FEI Talos 200X TEM microscope.

The fabrication of TEM specimens were performed using focus ion beam (FIB) technique by following typical protocols. The SEM for TEM sample preparation using FIB consists of an Omniprobe lift-out system, a highly focused Ga ion beam, and a gas injection system (GIS) for Pt gas injection. The Ga ion beam is for precise machining and the angle between ion beam and electron beam is 52^{o}. During TEM sample preparation, a Pt protection layer was deposited on the surface of specimen, preventing the sample from ion damaging during subsequent process. Then a lamella beneath the Pt protection layer was lifted out using the Omniprobe system and mounted onto a TEM Cu grip before final thinning. The thinning process consists of three steps: (i) thinning the lamella to ~250 nm using 30 kV accelerating voltage with 0.3 nA current density, (ii) lowering the accelerating voltage to 5 kV and further thin the lamella to ~ 120 nm and (iii) polishing the lamella with even lower accelerating voltage of 2 kV and thin the TEM foil to < 100 nm. The specific parameters of preparation process vary slightly from different samples.

2.3. Mechanical behavior testing

Generally, the influence depth of SMGT process, or the thickness of gradient layer formed on the surface of processed samples is limited to be several hundreds of micrometers. Hence, conventional tensile or compression tests in macroscale are not applicable for the characterization of mechanical properties of each individual layers of gradient structures. In situ micropillar compression tests were therefore carried out. A Brukers- Hysitron PI 88 × R PicoIndenter equipped with diamond flat-punch indenter with different diameters were used. The in situ micropillar compression testing system was assembled in a 15^{o} tilted sample stage of an FEI Quanta 3D FEG SEM, as illustrated schematically in Fig.2.3a. The morphological evolution of the micropillar was captured during compression. The thermal drift rate was controlled to lower than 0.05 nm/s before the compression tests were performed.

Micropillars for in situ compression tests were fabricated by FIB technique as well. The diameter of micropillar was designed as ~ 2.0 μm and the height-to-diameter aspect ratio of each micropillars was kept at ~ 2.0 to avoid buckling during compression. A big trench with outer and inner diameters of ~ 35 μm and ~ 6 μm, respectively, was fabricated first, as shown in Fig.2.3b. The big trench was fabricated to guarantee that the whole morphology of the pillar that is fixed in the 15^{o} tilted sample stage can be captured by SEM, as shown in Fig.2.3c. The current density applied for the milling of big trench was as high as 15 nA for efficiency. The current density was then decreased gradually to 1 nA and 0.3 nA when further milling the pillar with 6.0 μm in diameter to ~ 2.0 μm (with height of ~ 4.0 μm). Current density of 0.1 nA or 50 pA was adopted for final surface polishing to minimize the ion milling damage. The sizes of pillars were measured before the test based on the SEM image of pillar from 52^{o} tilted view, as shown in Fig.2.3d. Both the diameter of the pillar top (D_t) and bottom (D_b) were measured.

Vickers hardness of specimens were measured by using a LECO LM247 microhardness tester with a Vickers indenter. Due to the limited measurement area of the thin gradient structured layer formed after SMGT, a low applied load of 25 g was used to minimize the overlapping effect of adjacent indents, with the holding time of 13 s. Generally, samples were mechanically ground and polished before hardness measurements.

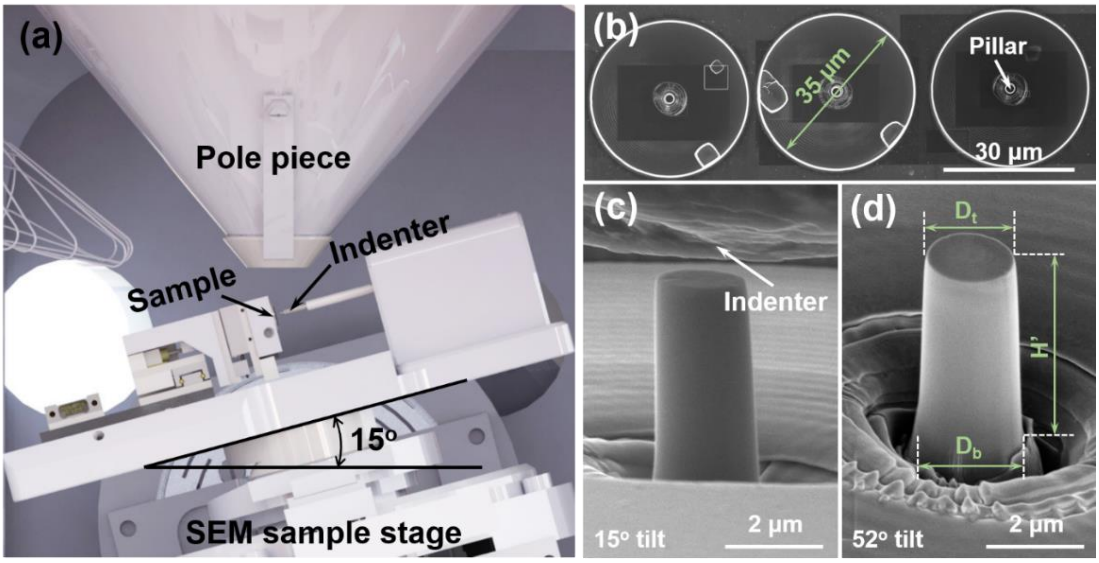

Figure 2.3 (a) Schematic illustrating the configuration of in situ micropillar compression testing system in SEM chamber. (b) Top-down overview of micropillars prepared by FIB showing the diameter of trench. (c) SEM image of pillar from 15° tiled view showing the configuration of micropillar compression tests in SEM. (d) SEM image of pillar from 52° tilted view illustrating how the sizes of pillar were measured.

2.4. Thermal treatment

Series heat treatments were carried out for either solid solution treatment or thermal stability studies. The solid solution treatment was performed using a conventional tube furnace in atmospheric environment. For the thermal stability studies, samples were heat treated in a vacuum furnace system. Samples were loaded into the furnace before the vacuum system starts to work. The vacuum system consists of a mechanical and a turbo vacuum pump. The mechanical vacuum pump vented the tube furnace to the vacuum level $< 1 \times 10^{-1}$ torr before the turbo vacuum pump was turned on. Heat treatment was carried out when the vacuum level reaches 2×10^{-6} torr. The heating speed of the vacuum furnace is adjustable and ~ 50 °C/min was used in this thesis work. Specimens was furnace cooled to room temperature after annealing.

CHAPTER 3. MECHANICAL BEHAVIOR OF GRADIENT STRUCTURED NICKEL ALLOY

The gradient structured nickel-based alloy was fabricated by Jie Ding and Dr. Sichuang Xue. In situ micropillar compression tests and microstructure characterization were performed by Dr. Jie Ding at Purdue University, with great help from Dr. Qiang Li, Dr. Jin Li and Dr. Zhe Fan. The data analysis and writing were completed by Jie Ding with guidance and editing by Dr. Xinghang Zhang.

3.1 Overview

Certain structurally gradient materials have shown a combination of high strength and work hardening capability. The fundamental mechanisms behind such a unique mechanical behavior remain less well understood. Here we processed NiCrMo based C22 HS alloys by surface mechanical grinding treatment to achieve a gradient microstructure consisting of surface nanolaminated layer, deformation twinned layer and severely deformed layers. *In situ* micropillar compression tests performed inside a scanning electron microscope reveal different mechanical behaviors of each layer. This study suggests that the increase of intergranular back stress may have contributed to the high strain hardening behavior of the gradient material.

3.2 Introduction

Grain refinement via severe plastic deformation (SPD) has been investigated extensively over the last two decades as fine-grained materials typically have high mechanical strength [5,29,47]. Several primary SPD techniques, including equal channel angular pressing (ECAP) [25,228], accumulative roll bonding (ARB) [46,229] and high-pressure torsion (HPT) [45], have been used for grain refinement. However, these ultrafine grained (UFG) and nanocrystalline (NC) materials fabricated by SPD techniques usually have limited tensile ductility, which has been a

roadblock to hinder their practical applications [2,75]. The lack of plasticity can be ascribed to the absence of strain hardening capability in nanograins. According to the Considère's criterion, to maintain a reasonable ductility, a higher strain hardening rate is necessary to surpass the flow stress [47,80,230]. To improve the ductility of NC materials, several strategies have been proposed, including bimodal microstructure [83], transformation-induced plasticity (TRIP) [231,232], twinning-induced plasticity (TWIP) [233], nanoparticle hardening [69] etc.

Recently gradient microstructures have been introduced into metallic materials to improve both strength and ductility [67,73,85]. Gradient structured (GS) materials refer to the materials with gradient distribution of nanoscale to microscale grain sizes [73]. GS metallic materials generally contain several layers according to the grain size and defect distributions: an outermost NC/nanolaminated (NL) layer with an average grain size smaller than 100 nm; a UFG or ultrafine laminated (UFL) layer with an average grain size ranging from 100 to 500 nm; a deformed CG layer characterized by dislocation tangles or dislocation cell walls with grain size varying from submicrons to microns; and the unaffected CG core. To synthesize GS materials with NC surface layer, several surface plastic deformation techniques have been proposed, including surface mechanical attrition treatment (SMAT) [86,87,95], surface mechanical grinding treatment (SMGT) [94,136] and surface mechanical rolling treatment (SMRT) [92,103]. An important parameter that controls the grain refinement mechanism is the stacking fault energy (SFE) of metallic materials. Deformation twinning dominates the grain refinement process for metallic materials with low SFE, whereas dislocation activities control the grain size evolution for materials with high SFE [94,97].

GS materials with hard NG surface layer and soft inner core have shown unique mechanical behaviors [73,86]. For instance, interstitial free (IF) steel with gradient structures synthesized by Wu et al. [86] through SMAT exhibited a yield strength that is several times higher than that of untreated ones with a slightly decreased ductility. GS Cu [85] has a maximum tensile strength of ~660MPa, 10 times higher than CG Cu without sacrificing tensile ductility. In addition, Huang et al. [103] reported that the GS 316L stainless steel treated by SMRT technique showed significantly enhanced fatigue performance. Zhu's research group reported that the plastic strain incompatibility in GS materials promoted the accumulation of geometrically necessary dislocations (GNDs) during deformation, which resulted in significant back stress and strain hardening [93,95]. The extraordinary tensile ductility of GS Cu prepared by SMGT, reported by Lu's group [85], was attributed to the deformation induced grain coarsening.

In spite of the success in fabricating gradient microstructures, the deformation behaviors of each individual layer of GS materials at microscale are less well understood; consequently, the contribution of each layer to the overall mechanical properties of GS materials remains unclear. In this study, GS has been introduced into a C-22HS alloy by SMGT. The microstructural evolution has been examined by transmission electron microscopy (TEM), and the corresponding grain refinement mechanism is clarified. In situ micropillar compression tests have been carried out to investigate the mechanical behavior of each layer of the gradient microstructure, and the underlying deformation mechanisms are discussed.

3.3 Experimental

3.3.1 Materials and processing

The materials used in this work are Hastelloy C-22HS Nickel-based alloy, which has a chemical composition (in Wt.%) of Cr 21.0, Mo 17.0, Fe 2.0, C 0.01, Si 0.08, balanced by Ni. Prior to processing, the C-22HS alloy was annealed at 1100 ^{o}C for 1 hour, followed by air cooling. During the SMGT processing, the annealed C-22HS bar with a diameter of 12 mm and a length of 100 mm rotated at a velocity of 400 rpm, while a WC/Co tool penetrated into sample surface by 20 μm and slide along axial direction at a velocity of 10 mm/min. The sample is considered as being treated by one pass as the tool tip slides from one end of the rod surface to the other end. To increase the plastic strain, the samples used in this work were treated by 6 passes. Cooling oil was used for temperature control during processing.

3.3.2 Microstructure characterization

Cross-sectional microstructures of C-22HS alloy were analyzed by electron back scatter diffraction (EBSD) and focused ion beam (FIB) imaging technique. A Philips XL-40 microscope with EBSD attachment and a Quanta 3D FEG microscope with Ga ion beam source were used to obtain EBSD and FIB images, respectively. All observations were made at 30 kV acceleration voltage and a working distance of 10 mm. Transmission electron microscopy (TEM) experiments were performed on an FEI Talos 200 X operated at 200 kV. The cross-section TEM specimens of

the SMGTed C-22HS alloys were prepared by FIB technique using an FEI Quanta 3D FEG Dual beam FIB/SEM following typical protocols [63,64].

3.3.3 Mechanical testing

Microhardness measurement along the depth direction from cross-section specimens was conducted by using a LECO LM247 microhardness tester with a Vickers indenter tip. The maximum applied load for this study was 25g, with a holding time of 13 s. Micropillars were prepared by using FIB technique from each representative region of the GS C-22HS Ni alloy. The height-to-diameter aspect ratio of pillars was kept at 1.8-2.1 to avoid buckling during compression and the average pillar diameter is ~ 2 μm. The taper of the pillars was approximately 3° on average. The *in situ* microcompression tests were performed in an FEI Quanta 3D FEG SEM by using a Brukers-Hysitron PI 87×R PicoIndenter equipped with a 5 μm diamond flat-punch indenter tip. The collection of force-displacement data was enabled by the piezoelectric actuator in the capacitive transducer. A real-time video recorded the morphological evolution of the micropillar during compression. All micropillars were compressed under displacement controlled mode until up to 18% of strain, followed by 0.5 s holding before unloading. A constant strain rate of ($\dot{\varepsilon}$) of 1 × 10^{-3}/s was used for most studies. The loading-fully unloading tests were also performed at the same strain rate with a total of 7 unloading cycles.

Pillar diameter, measured at the half-height of the pillar, was used for the calculation of engineering stress. Given the taper of pillars by ~ 3°, the engineering stress calculated in this study represents an approximate average value. In order to obtain an accurate measurement of strain, the equation derived by Sneddon was applied to calculate displacement, x, [234,235]

$$x = x_{meas} - \frac{1-\nu_i{}^2}{E_i}\left(\frac{F_{meas}}{D_t}\right) - \frac{1-\nu_b{}^2}{E_b}\left(\frac{F_{meas}}{D_b}\right) \qquad \text{Equation 3.1}$$

where x_{meas} and F_{meas} represent the measured displacement and force, respectively. ν_i and Ei are the Poisson's ratio and Young's modulus of diamond punch taken to be 0.07 and 1220 GPa, respectively, while ν_b and E_b represent the Poisson's ratio and Young's modulus of nickel taken to be 0.31 and 205 GPa, respectively. After correcting the displacement, the engineering stress-strain curves were obtained, and subsequently converted to true stress-strain curves by using the homogeneous deformation model (assume no volume change during the deformation).

The strain hardening behavior of the pillar at a strain level ranging from yielding point, ε_y, to ~10% can be described by the power-law strain hardening equation, i.e. Ludwik's equation as follow: [236,237]

$$\sigma = K_1 + K_2 \cdot {\varepsilon_p}^n \qquad \text{Equation 3.2}$$

where K_1 represents the initial stress of the strain hardening stage, K_2 is the strengthening coefficient (i.e. the stress increment due to strain hardening when plastic strain $\varepsilon_p = 1$), and n represents the strain hardening exponent. The strain hardening parameters of the pillars were derived by fitting the true stress-strain curves using equation (2).

The calculation of back stress σ_b was carried out by using the equation proposed by Yang et al. [93] as follows:

$$\sigma_b = \frac{\sigma_r + \sigma_u}{2} \qquad \text{Equation 3.3}$$

where σ_r and σ_u represent the reload and unload yield stress derived from the unloading-reloading hysteresis loops. In this study, the yield points were determined by a plastic offset strain by 10^{-4}, which has been used by several others previously [238]. Detailed information about the derivation of σ_b can be found in Ref. [93].

3.4 Results

3.4.1 Overview of microstructure and hardness

The EBSD images of annealed C-22HS alloys (Fig.3.1a) show equiaxed grains with an average grain size of ~90 μm. High-angle grain boundaries (GBs) and twin boundaries (TBs) are represented by black and yellow lines, respectively. The gradient microstructure along depth direction introduced by the SMGT process was revealed by FIB image (Fig.3.1b). Prominent microstructure changes were observed in the top ~ 50 μm thick layer of treated specimens (although only the top 20 μm thick surface layer is shown). The plastically deformed regions can be divided into 3 layers according to their distinct microstructures. The outermost surface layer, ~7 μm in thickness, has microstructures that are too fine to be resolved under SEM. As shown by TEM observation in following section, the fine structures in this layer contain nanolaminated (NL) grains and hence is referred to as NL region hereafter. The adjacent 7 μm thick subsurface layer has high-density deformation twins (DTs) as identified by TEM observations, and is denoted as

DT layer. The region of 15-50 μm from surface has severely deformed (SD) structure characterized by parallel shear band (SB) and DTs and is named as SD layer.

The corresponding hardness profile (Fig.3.1c) reveals that the hardness decreases drastically from 6.0 GPa in NL layer to ~ 5.3 GPa in the DT layer, and then gradually decreases from 5.0 GPa to 3.0 GPa into the SD layer over a depth of 15-95 μm. The hardness of unaffected matrix (2.16 GPa) is labeled with a dash line as a reference.

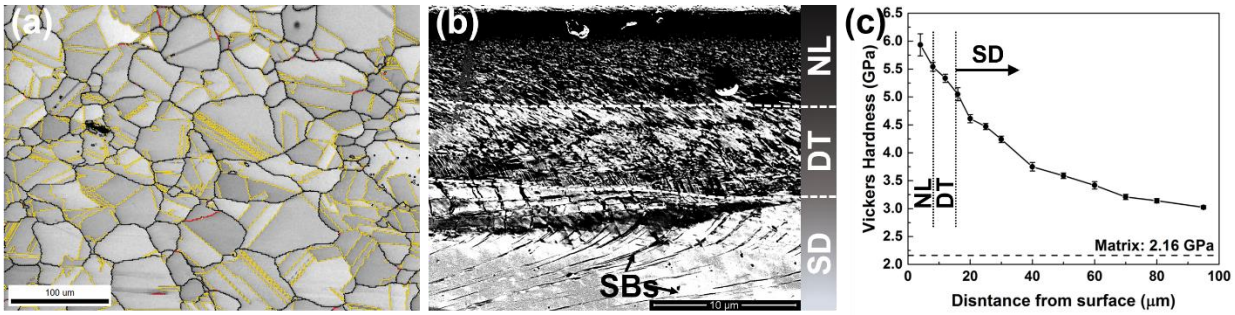

Figure 3.1 (a) EBSD image of an annealed C-22HS alloy. (b) FIB ion microscopy image of gradient structure of C-22HS alloy processed by SMGT showing a NL layer, DT layer, and SD layer. SBs formed in SD layer. (c) Variation of average Vickers microhardness along the depth direction of the processed C-22HS samples.

3.4.2 Microstructure of the SD and DT layer

Cross-section TEM experiments were performed to examine the microstructure of NL layer, the DT layer at a depth of ~10 μm, and SD layer at a depth of ~20 μm

Microstructures at positions deeper than 15 μm (in Fig.3.2a) show large grains with SBs and scattered DTs. High-density dislocations and laminar boundaries were observed in the SBs. The inserted selected area diffraction (SAD) pattern indicates the formation of low angle GBs and TBs. The structure consisting of both DTs and SBs is in agreement with prior studies on the deformation of alloys with low SFEs [239]. The thickness of lamellae in the SBs is much thinner than that in adjacent area with DTs. The formation of such microstructure in SB zone will be discussed later. Fig.3.2b shows a typical laminar boundary in the SB zone with 12° misorientation angle as confirmed by the inserted fast Fourier Transformation (FFT), indicating that the laminar boundaries are indeed mostly low angle grain boundaries.

At a depth of 7-15 μm from surface, abundant nanolaminated structures form with lamellar thicknesses varying from several to ~100 nm as shown in bright field (BF) and dark field (DF) TEM micrographs in Fig.3.2c-d. The inserted SAD pattern (from representative laminate interfaces) shows characteristic twin diffraction spots. Most diffraction spots are curved, implying small misorientation among TBs. The DF TEM image in Fig.3.2d shows the formation of high-density dislocations trapped within the lamellae. The laminate interfaces and TBs in the DT layer has formed a greater average inclination angle to the shear direction (as indicated by arrow) than that in the SD layers, an indication of higher shear strain level in the DT layer. High resolution TEM (HRTEM) image in Fig.3.2e shows high-density TBs with an average twin thickness of several nm. Higher magnification HRTEM micrograph in Fig.3.2f shows that a typical TB (in box f in Fig.3.2e) is decorated by several layers of stacking faults (SFs), implying that a strong twin-dislocation interaction could have taken place during deformation.

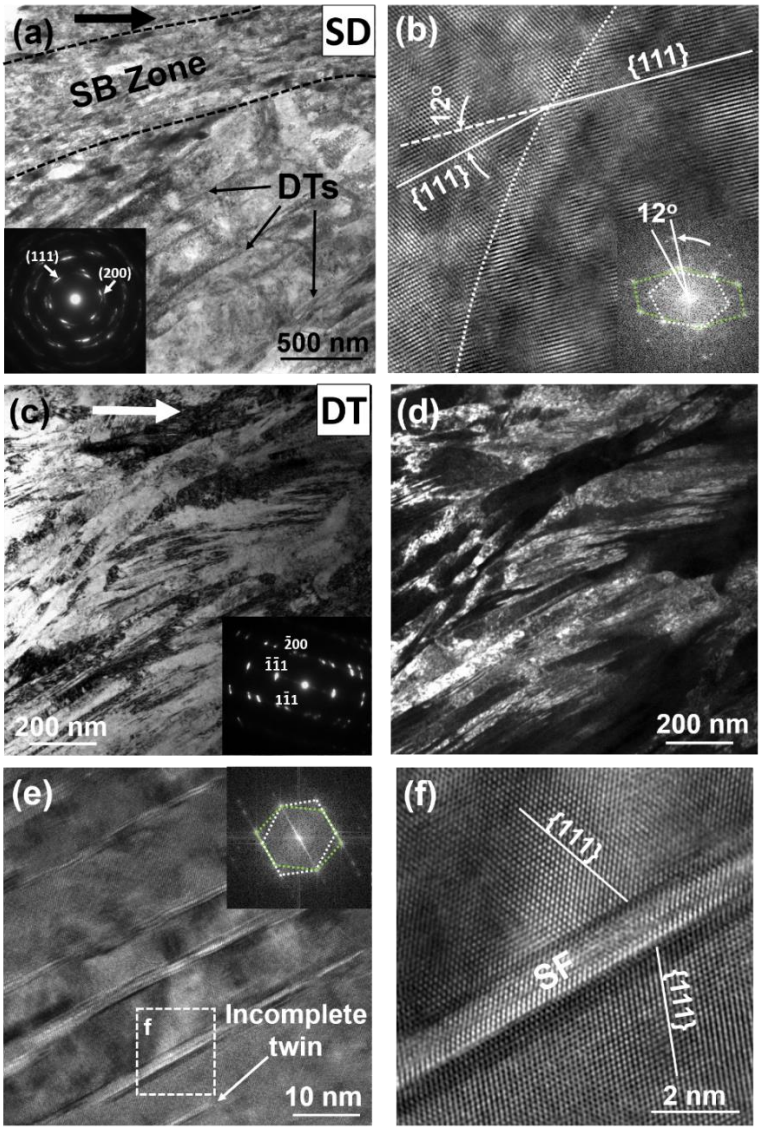

Figure 3.2 Comparison of microstructure of the (a-b) SD layer and (c-f) DT layer. (a) Cross-sectional BF TEM image of the SD layer, at a depth of ~20 μm from surface, shows the lamellar structure of SBs and scattered DTs. Arrow indicates shear direction. (b) HRTEM image of the SB zone and corresponding FFT pattern showing the formation of a low angle grain boundary. (c-d) Cross-sectional BF and DF TEM images of DT layer at a depth of ~10 μm. Arrow indicates shear direction. (e) HRTEM image showing high-density twin boundaries in DT layer and corresponding FFT pattern. (f) HRTEM image of the dashed square box f in Fig.e showing a twin boundary decorated with SFs.

3.4.3 The microstructure of the NL layer

In the topmost NL layer (Fig.3.3a-b), lamellar structures have thickness ranging from several to ~60 nm. The inserted SAD pattern shows rings with (111) texture orthogonal to the layer

interfaces. HRTEM image (Fig.3.3c-e) shows DTs, several nm in thickness, and SFs. Some wavy patterns decorated along the layer interfaces are also observed (as shown in the box e). The FFT (Fig.3.3d2) reveals that the {111} atomic planes of the adjacent lamella with 23° inclination angle. This evidence indicates that high-angle GBs formed in the NL layer. Fig.3.3e1 shows an array of SFs and the corresponding FFT (Fig.3.3e2) confirms the formation of twisted 9R phase.

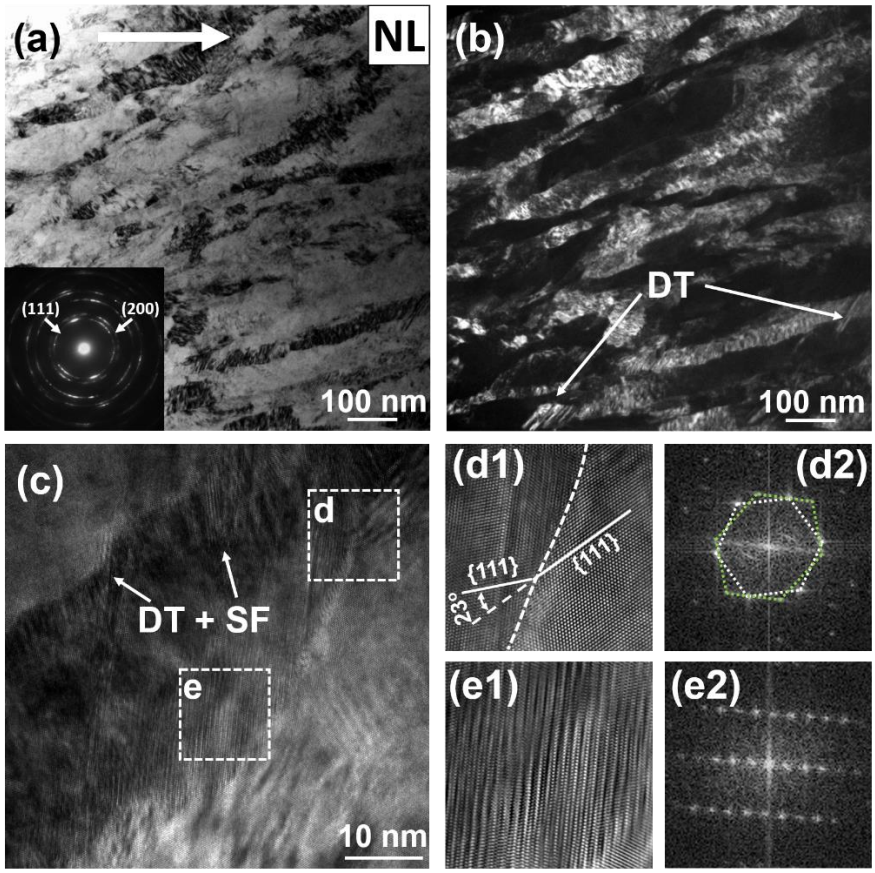

Figure 3.3 Cross-sectional BF and DF TEM images of surface NL layer at a depth of 5 μm showing fine lamellae. Shear direction is indicated by the arrow. (c) HRTEM image showing the microstructure of the lamellae consisting of deformation twins and SFs. (d1) HRTEM image and (d2) corresponding FFT pattern of the dashed square box d in Fig.c showing a high angle grain boundary. (e1) HRTEM image and (e2) corresponding FFT pattern of the dashed box e in Fig.c shows twisted 9R phase.

3.4.4 The mechanical behavior of unaffected matrix

The positions selected to fabricate micropillars from unaffected matrix are at a depth of 500 μm away from the treated surface. Given that the average grain size of the annealed grain is

90 μm, and the designed diameter of micropillar is 2 μm, the pillars in this region are more likely made of single crystals. The true stress-strain curve for the *in situ* compression tests in Fig.3.4a shows a yield strength of ~ 450 MPa, followed by numerous shear serrations as indicated by stress drops, which may result from the initiation and penetration of slip bands during compression. The fitting of the strain hardening stage by using Equation (2) derives that n = 0.43. Fig.3.4b is the SEM image of the pillar before compression taken at a 75° tilt angle. During compression, 3 major slip bands were generated from the free surface and penetrated through the pillar. The 3 slip bands took place at the strain of 2.2, 6.0 and 11.5%, respectively as shown in the snapshot in Fig.3.4c-4e, and each slip band corresponds to a major load drop. Similar phenomenon has also been observed in other *in situ* compression study [240]. The SEM image of the pillar after compression test (Fig.3.4f) reveals 3 major and several tiny slip bands, with no sign of barreling.

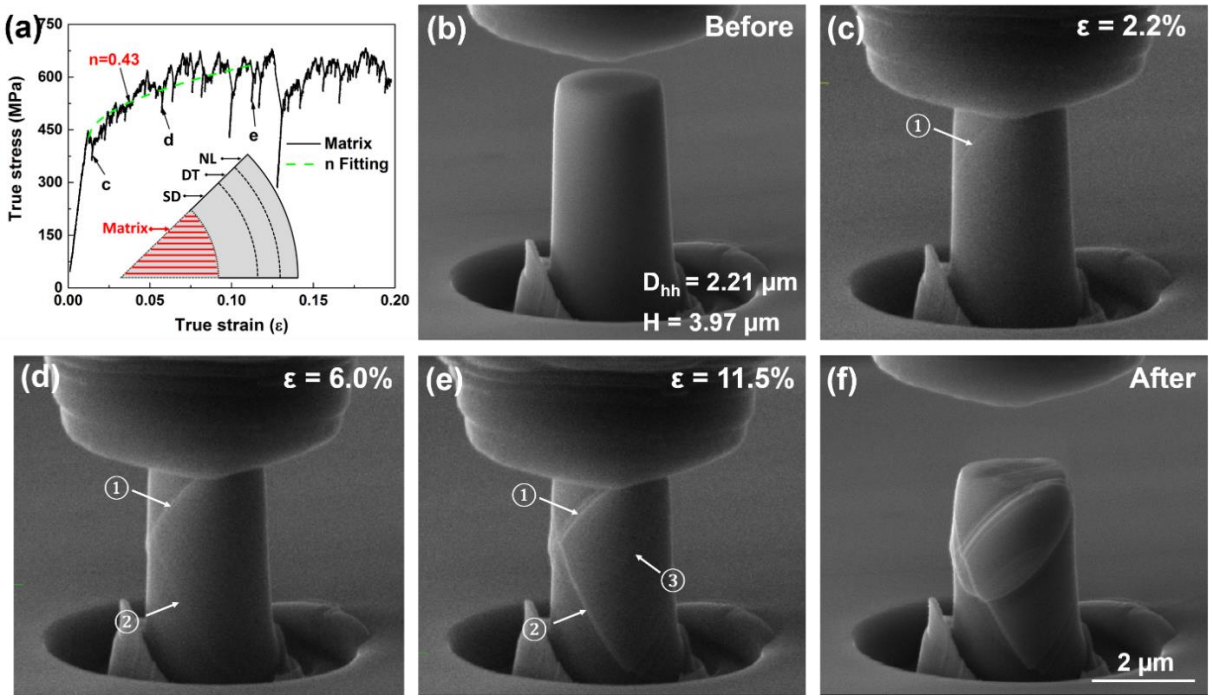

Figure 3.4 In situ micropillar compression test of unaffected matrix area. (a) True stress-strain curve at a strain rate of 1×10^{-3}/s showing strain hardening exponent of 0.43 with prominent shear serrations. The inserted schematics indicates the position of micropillars selected for *in situ* compression tests in the red shaded zone. (b) SEM image of the pillar before compression. The image was taken at an angle of 75° relative to the normal direction to the bulk surface. (c-e) SEM images of the pillar at a true strain (ε) level of 2.2, 6.0 and 11.5% respectively, corresponding to the initiation of 3 major slip bands, labeled by ①, ② and ③ respectively. The formation of slip bands corresponds to the load drops shown in Fig. a. (f) The pillar after compression test contains several major slip bands.

3.4.5 The mechanical behavior of the SD and DT layers

The pillars for the *in situ* compression tests of the SD and DT layers were located at a depth of ~18 μm and ~10 μm from the treated surface, respectively. The true stress-strain curves of the SD layer (Fig.3.5a) and DT layer (Fig.3.6a) behave similarly, where elastic region followed by a strain hardening stage and subsequent stress plateau before unloading. The n values of these two layers are 0.51 (SD) and 0.48 (DT), respectively. Comparing with the true stress-strain curve of unaffected matrix area (Fig.3.4a), the stress-strain curves of SD and DT layers are comparably smooth and no stress drops appeared during compression. SEM snap shots of the deformed SD layer in Fig.3.5b-d show two major slip bands at the strain of 10.0 and 14.3%, respectively. Similarly, for the DT layer, there are several major slip bands (Fig.3.6c-e) shown by snap shots

taken at the strain of 10.0 and 15.6%, respectively. The 2nd and 3rd major slip band appear almost simultaneously. The SEM images of the deformed pillars of SD and DT layers (Fig.3.5f and 3.6f) show that both shearing and slight barreling took place during compression.

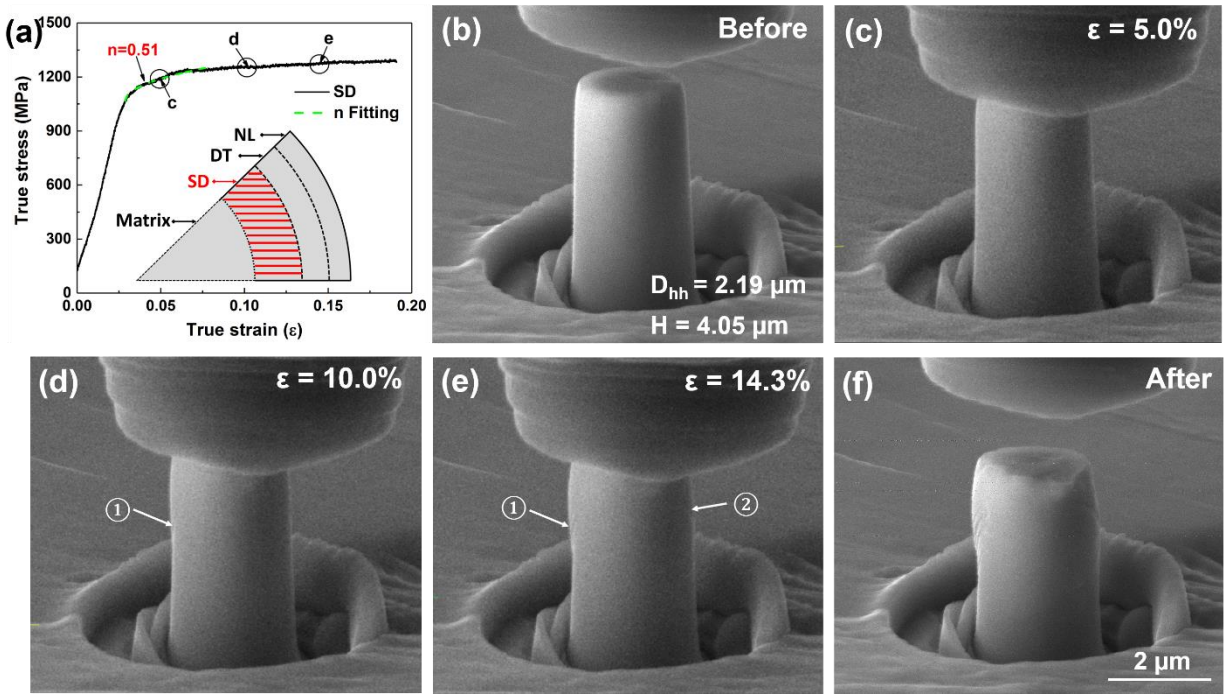

Figure 3.5 In situ micropillar compression test results of the SD layer. (a) True stress-strain curve at a strain rate of 1×10^{-3}/s showing a strain hardening exponent of 0.51. (b) SEM image of the pillar before compression. (c-e) SEM images of pillar at a true strain (ε) level of 5.0, 10.0, and 14.3% respectively, slip bands appears during compression labeled by ① and ②. (f) SEM image of the pillar after compression showing shearing and barreling of the pillar.

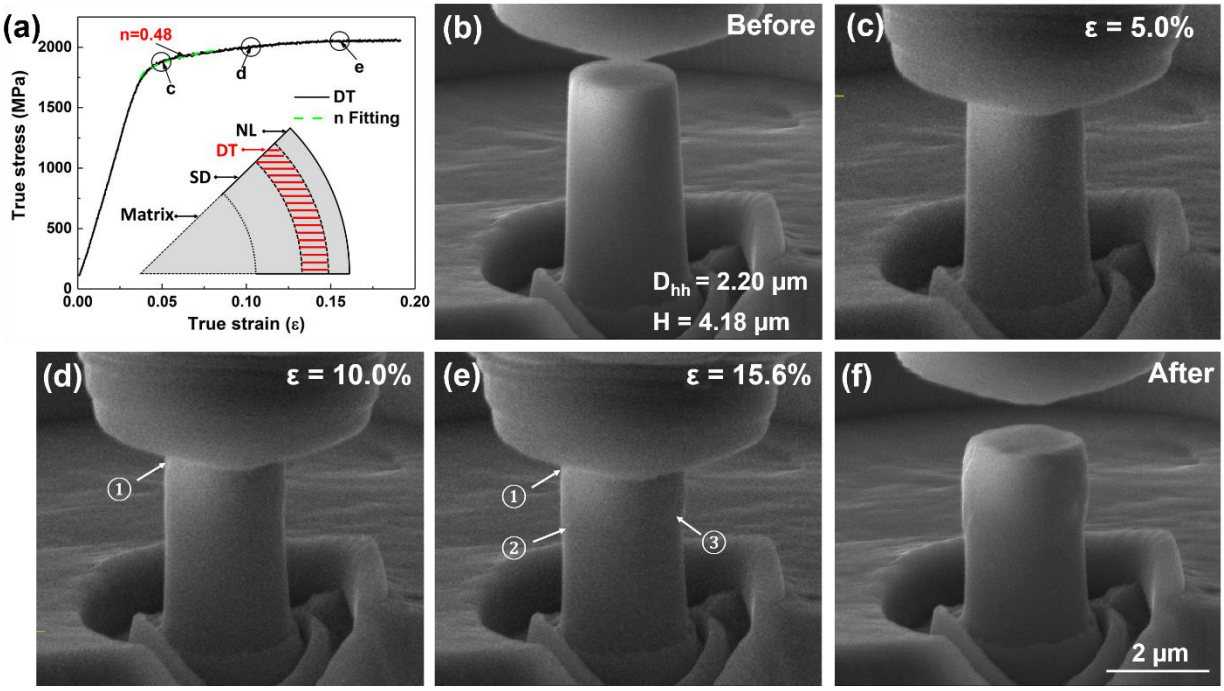

Figure 3.6 In situ micropillar compression test results of the DT layer. (a) True stress-strain curve at a strain rate of 1×10^{-3}/s showing a strain hardening exponent of 0.48. (b) SEM image of the pillar before compression. (c-e) SEM images of pillar at a true strain (ε) level of 5.0, 10.0, and 15.6% respectively, slip bands appearing during compression are labeled by ①, ② and ③. (f) SEM image of the pillar after compression showing shearing and barreling.

3.4.6 Mechanical behavior of the NL layer

The true stress-strain curve of the top surface NL layer (Fig.3.7a) is different from the other layers as there are apparently two strain hardening stages. The first stage between yielding and a strain of ~ 6.3% has n_1 of 0.79, and the 2nd stage has n_2 of 0.48. The high n value observed in the first strain hardening stage will be discussed later. The SEM snap shots taken at the strain of 6.3, 10.0 and 14.0% (Fig.3.7c-e) show that there were no major slip bands during compression. After 18.0% of compression strain, a slight barreling appeared at the top portion of the deformed pillar (Fig.3.7f).

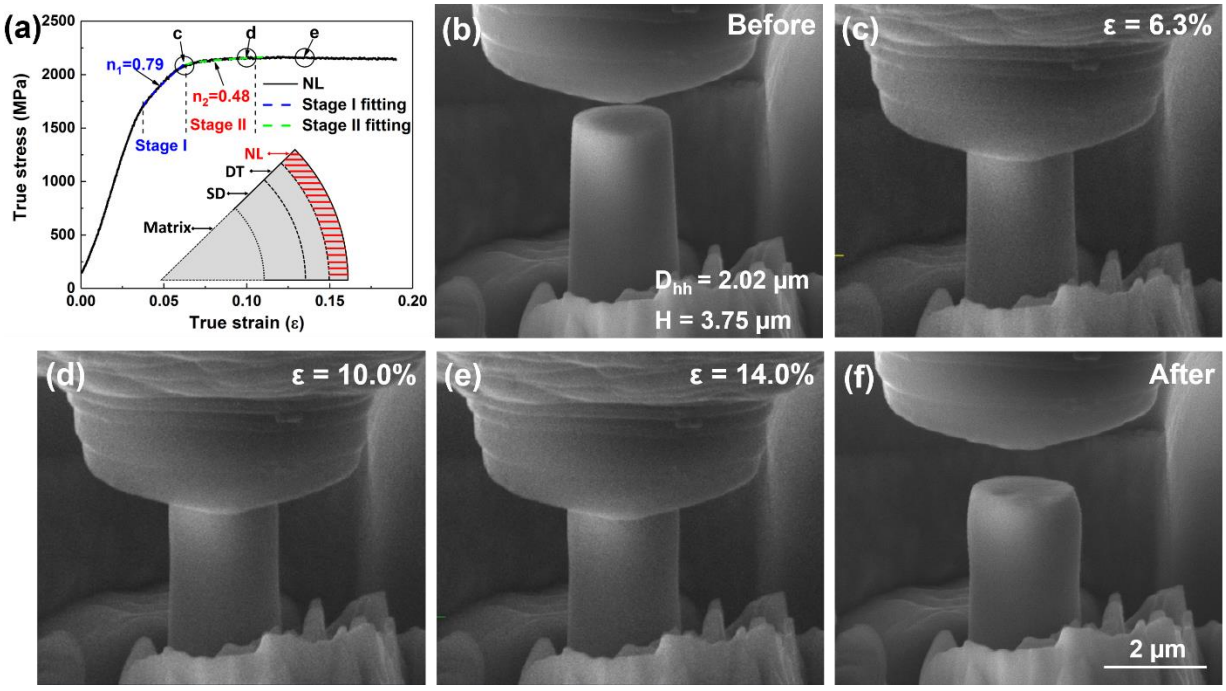

Figure 3.7 In situ micropillar compression test results of surface NL layer. (a) True stress-strain curve at a strain rate of 1×10^{-3}/s. Two strain hardening regimes are identified with exponent of 0.79 and 0.48, respectively. (b) SEM image of the pillar before compression. (c-e) SEM images of pillar at a true strain (ε) level of 6.3, 10.0 and 14.3% respectively. (f) SEM image of the pillar after compression showing barreling of the pillar.

Fig.3.8a shows the compiled true stress-strain curves of each layer. Compared to unaffected matrix, the flow stresses increase in the sequence of SD, DT and NL layers. It's interesting to note that the yield strength of the pillars in DT and NL layers is almost identical (~ 1650 MPa), while the flow stress of NL layer (~ 2150 MPa) is higher than that of DT layer (~ 2030 MPa). The high n value at the first strain hardening stage of NL layer may contribute to the higher flow stress and details will be discussed later. Fig.3.8b shows the evolution of n value with the depth from the treated surface. It is clear that, except the extraordinary high n value during the first work hardening stage of the NL layer, the n values remain similar in different layers of the deformed region before seeing a slight decrease in the unaffected matrix area.

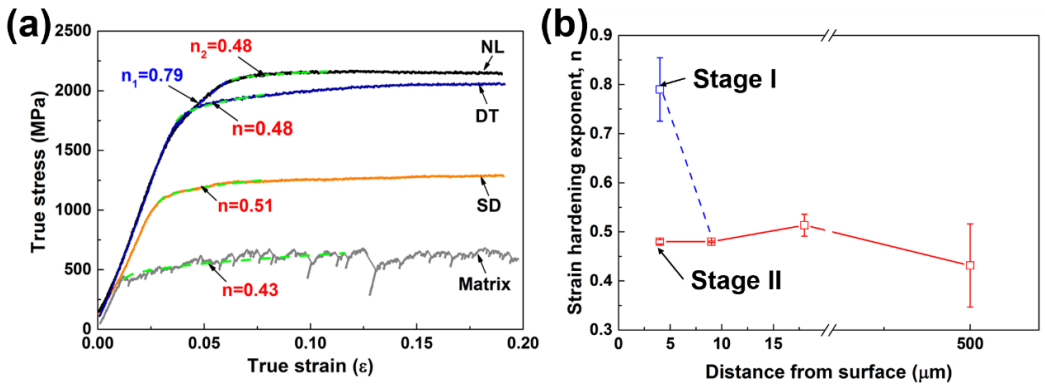

Figure 3.8 (a) Comparison of true stress-strain curves of each layer of GS C-22HS alloy. (b) The strain hardening exponent, n as a function of depth from the treated surface. The NL layer has two strain hardening exponents.

3.5 Discussion

The microstructural evolution, such as grain refinement, in bulk metallic materials processed by severe plastic deformation has been extensively studied in the past [22,61,62]. Generally, dislocation slip and twinning are the two main mechanisms to accommodate the plastic deformation, especially at ambient temperature. For metals with medium-to-high SFEs, dislocation slip plays a dominant role, while for metals with low SFEs, twinning is the favorable deformation mechanism [106,241]. The C-22HS alloys employed in this work have chemical composition similar to the C-2000 alloy (C 0.01, Si 0.08, Cu 1.6, Mo 16.0, Cr 23.0 and Ni balance). The C-2000 alloy has an extremely low SFE, thus we speculate that the SFE of C-22HS is more likely in the low-to-medium range.

3.5.1 The microstructure of the SD layer

During SMGT, the accumulated shear strain in the SD layer is comparable to that introduced by conventional SPD techniques, and consequently the microstructures formed are similar to those in heavily deformed bulk metallic materials. In the SD layer close to the unaffected matrix region, dislocation arrays and grids attributed to the inhibition of cross-slip of dislocations are usually observed [21,97]. It is generally believed that the critical shear stress necessary for the initiation of deformation twinning deceases with the decrease of the SFE. Higher strain rate will further facilitate the twinning process by suppressing the thermally activated dislocation process

[97]. As C-22HS alloy has low SFE, DTs with several nanometers in thickness were frequently observed and the TBs subdivided the original coarse grains into lamellae (Fig.3.2a).

Most DTs are distributed in a parallel fashion and no twin-twin intersections are observed, similar to the DTs formed in Inconel 600 alloys, prepared by SMAT, with low-medium SFE. For metals with even lower SFEs, like C-2000 nickel-based alloy and AISI 304 stainless steel, twin-twin intersection is a prominent feature in the region where strain and strain rate are comparable to those of the SD layer in this study [21,97]. One possible reason for the absence of twin-twin intersections in the SD layer of our C-22HS is that the driving force needed for secondary deformation twinning to overcome the barrier of the primary DTs is too high compared with that in metals with lower SFEs. Also, the uniform shearing condition during SMGT process may inhibit twin-twin intersection, as a favorably stressed orientation other than that for primary deformation twinning is needed for the activation of secondary twins [106].

Localized deformation occurs in the form of SBs when further work hardening becomes difficult [106]. The much higher strain and strain rate that SB regime experienced than the adjacent DT populated regime result in finer lamella thickness (Fig.3.2a). Within the SBs, shear strain twists the TBs and leads to the formation of randomly oriented nanolaminate. Similar elongated grains formed by the breakdown of twin/matrix lamella and rotation of fine crystallite have also been observed in dynamic plastically deformed copper [242]. With the increase of strain and strain rate, preexisting SBs thicken at the expense of adjacent twin/matrix lamellae, forming alternating SBs and DTs.

3.5.2 The microstructure of the DT layer

With the increasing strain, the DT layer has a significant increase in twin density, and the nanotwins subdivide the lamellae into even finer ones. The average twin thickness in DT layer is ~30 nm, much smaller than the lamellae in the SD layer, ~ several hundred nanometers. To accommodate the large shear strain, TBs become curved and decorated with high-density dislocations (Fig.3.2f). Similar curved TBs have been observed in severely deformed C-2000 nickel based alloy as well [21]. Also, sessile unit dislocations with a Burgers vector of $\frac{1}{2}[\bar{1}\bar{1}0]$ were observed in C-2000 nickel based alloys. A sessile unit dislocation can be introduced by the

reaction between an immobile Frank partial dislocation in a TB and a Shockley partial dislocation traveling along the TB via an equation shown below [21]:

$$\frac{1}{6}[\bar{1}\bar{1}2] + \frac{1}{3}[\bar{1}\bar{1}\bar{1}] = \frac{1}{2}[\bar{1}\bar{1}0] \qquad \text{Equation 3.4}$$

This dislocation creates a step in the TB, and the array of these steps eventually results in the curvy TB.

3.5.3 The microstructure of the NL layer

The NL layer experiences the highest strain and strain rate during SMGT comparing to the other layers. In general, a high strain rate facilitates the generation and suppresses the annihilation of dislocations [94]. More importantly, the presence of strain gradient introduces geometrically necessary dislocations (GNDs) in addition to the statistically stored dislocations to maintain the crystal continuity [94]. Hence, the higher strain rate and strain gradient introduced more dislocations in the NL layer than the other layers of the GS specimens. These high-density dislocations were trapped between TBs. As fine twins inhibit the formation of dislocation clusters or cells, these dislocations piling up against TBs may gradually increase the misorientation between the matrix and twinned lamella, which eventually results in the formation of high-angle GBs among nanolaminates in the NL layer [97].

High strain rate also facilitates deformation twinning. Nanotwins with thickness of several nanometer have been observed in the surface layer of SMGT processed pure nickel with the high SFE (~ 120 mJ/m^2) [243], in which a high strain rate in the range of 10^3-10^4/s was imposed [94]. In this study, DTs with thickness of a few nanometers (Fig.3.3) were introduced in nanolaminates to accommodate plastic strain. The fine nanolaminates may promote the formation of these DTs due to size effect. Prior studies show that twin-twin and twin-dislocation interactions can gradually subdivide the nanolaminate into equiaxed nanocrystalline grains [97]. But this phenomenon was not observed in the current C-22HS alloys.

3.5.4 The mechanical behavior of gradient structures

In situ micropillar compression tests provide opportunity to evaluate the mechanical behaviors of each layer in GS C-22HS alloys. The yield strength of NL and DT layers is ~ 1650

MPa, much greater than that of matrix, ~ 450 MPa. The fine nanolaminates and nanotwins may account for the significant strengthening in the NL and DT layers. It is also worth mentioning that most slip bands in deformed SD and DT layers didn't penetrate through the pillars even after a 18% compressive strain, different from the prominent slip bands in the deformed pillars in unaffected matrix area. This difference may arise because the propagation of ship bands was blocked by laminar boundaries and twin boundaries within the SD and DT layers. The blockage of slip band also contributes to the absence of stress drops (serrations) during compression for the SD and DT layers.

The large, two-stage strain hardening of NL layer is surprising as NC metals with similar dimensions typically suffer from poor work hardening ability and low deformability. The limited dislocation activities in nanograins and accelerated dynamic recovery process result in the absence of apparent strain hardening in a majority of NC metals [2,64].

Several mechanisms have been identified in few cases where NC/UFG metals and alloys possess considerable ductility. Fang et al. [85] reported that deformation induced grain coarsening took place in NC copper. The dislocation-free coarse grains enable the accommodation of more dislocations and improve the plasticity of the nanograined structures. BF and DF TEM micrograph in Fig.3.9a-b show the deformed micropillar of the NL layer (4 μm from the treated surface) after 72% of compression strain, examined from the longitudinal direction. No dislocation-free grains appear after compression, and the average lamellar thickness is ~ 28 nm. Fig.3.9c shows the lamellar thickness in as-treated NL layers increases gradually from ~ 20 nm (at 2 μm depth) to ~ 50 nm at a depth of 7 μm. The thickness of lamellae barely changes after compression. The absence of grain coarsening after compression is not unexpected as NL structure has been shown to be more stable than equiaxed nanograin with a similar dimension [99]. Deformation induces grain coarsening for equiaxed grains in NC metals by grain rotation and/or GB sliding under shear stress [85,244]. However, both grain rotation and GB sliding are difficult in the nanolamellae in this study.

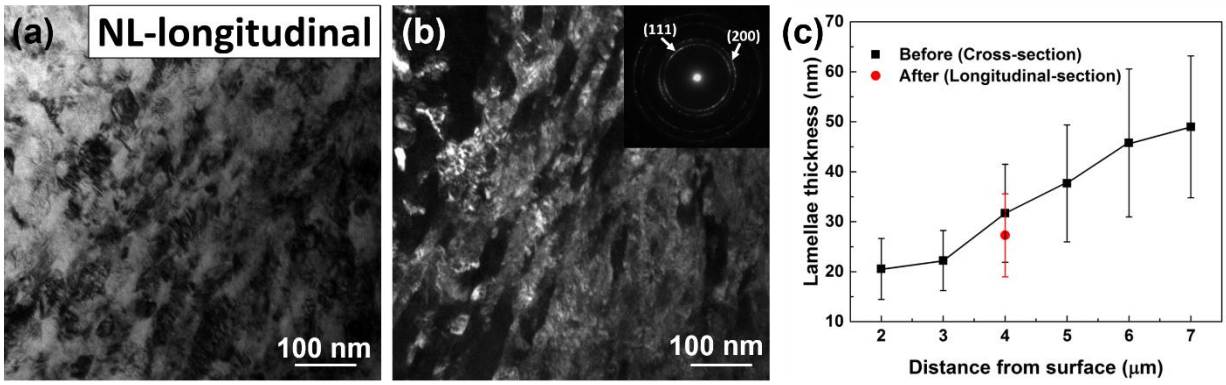

Figure 3.9 (a,b) BF and DF TEM images of the pillar in NL layer after 72% of compression strain examined along longitudinal direction. Inserted SAD pattern implies the polycrystalline nanostructure of NL layer. (c) The evolution of lamellae thickness of NL layer with depth from treated surface before and after compression tests. The laminate thickness after compression is ~ 28 nm, slightly thinner than that before compression, ~ 31 nm, from cross sectional view at a depth of 4 μm.

Recent studies show that the hardness gradient of GS materials generally results in mechanical incompatibility and strain gradient during deformation process [86,95]. To accommodate the deformation incompatibility between adjacent layer of GS materials, GNDs are generated, and consequently, the back stress induced by GNDs may introduce work hardening in GS materials [238,245]. In this study, the significant hardness gradient in the SPDed NL and DT layer may also lead to mechanical incompatibility during pillar compression as the prior study claimed [86,95], and further results in the generation of GNDs. In the gradient structure of this work, the NL layers may have a larger strain gradient than the other two and consequently high-density GNDs. To investigate if back stress indeed exists in the GS Ni alloys, a series of *in situ* loading-unloading-reloading tests were performed for the NL layer and DT layers (Fig.3.10a). Hysteresis loops were observed in both NL and DT layers (but not in the SD layers and matrix). Fig.3.10b represents the details for determination of σ_u and σ_r in the loops of NL and DT layers at a strain of ~ 6.8 and 6.5%, respectively. The back stresses calculated according to Eq.3.3 with increasing strain are shown in Fig.3.10c. The back stress in the NL layer rises to a maximum value at the strain of ~ 6.8% before gradual decline at increasing strain level, whereas the back stress in the DT layer decreases monotonically from the beginning. Interestingly, the strain (6.8%) at the highest back stress in the NL layer coincides with the strain that demarcates the two strain hardening stages (~ 6.3%) (Fig.3.7). This study suggests that the much greater strain hardening exponent in stage I (~ 0.79) than that in stage II (~ 0.48) in the NL layer may arise from the large

back stress. From the microstructure point of view, the back stress induced hardening in the NL layer may be attributed to the accumulation of GNDs after yielding.

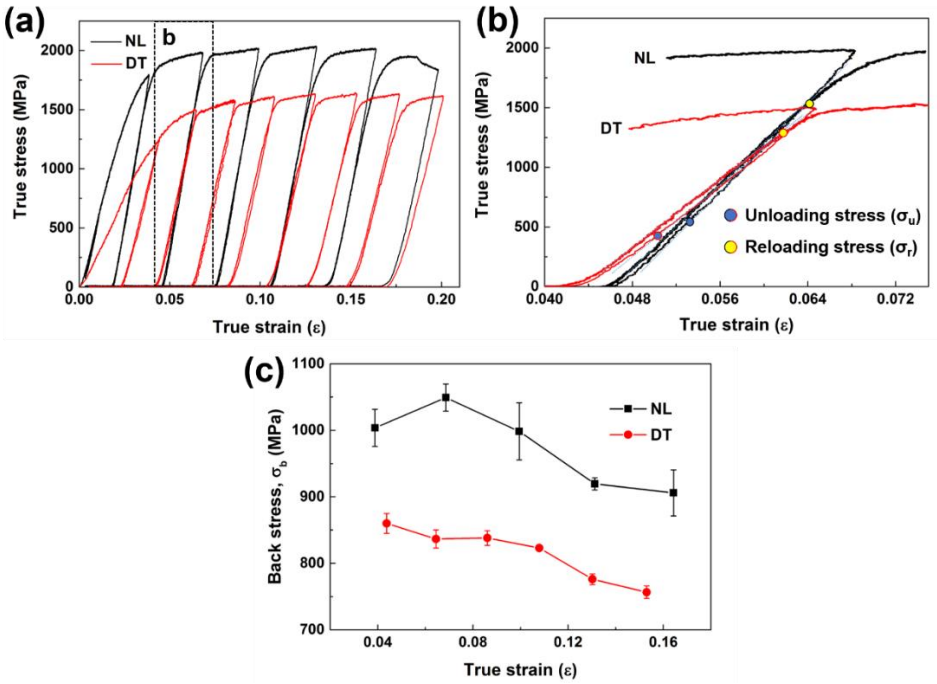

Figure 3.10 Successive unloading and reloading test hysteresis loops measured for the NL and DT layers at a depth of ~ 5 and 12 μm, respectively. (b) Measured hysteresis loops from NL and DT layers at a strain of ~ 6.8 and 6.5%, respectively, with σ_u and σ_r defined. The unloading and reloading yield points are determined by a plastic strain offset of 5×10^{-4}. (c) Evolution of back stress σ_b with increasing strain for the NL and DT layers.

The evolution of back stress with strain warrants further discussion. In general, the long-range back stress is composed of two ingredients, intergranular back stress and intragranular back stress. The intergranular back stress is derived from the plastic strain incompatibility among grains, while the intragranular back stress arises from the heterogeneous distribution of dislocations inside grains [238,245,246]. The new generated GNDs during compression tests of this study may pile up against both the grain boundaries and the pre-existing dislocation clusters inside grains, and consequently lead to both intragranular and intragranular back stress. The changes of the two components with increasing plastic strain can lead to the evolution of back stress into 3 stages [238]. In the first stage where plastic strain is low, GBs act as a strong barrier to the movement of dislocations. With the increase of strain, dislocations pile up against the GBs and, consequently, impose a back stress, which is intergranular back stress. The intragranular back stress is not

activated at this stage since no dislocation distribution change takes place. With the further increase of plastic strain, in stage II, cross-slip and multiple slip systems are activated to maintain the plastic strain compatibility among grains, consequently intergranular back stress decreases. Meanwhile, the slip also promotes the heterogeneity of dislocation structures inside grains, the result of which is to increase the intragranular back stress [238]. The overall trend of back stress in stage II is declining with strain. In stage III, the effect of intergranular back stress disappears and the intragranular back stress become the only component.

In this study, the nanolamellae in the NL layer contains DTs and laminar boundaries that act as effective barriers to the slip of dislocations. Hence, a significant increase of back stress with increasing strain is observed in stage I. After the strain exceeds 6.8%, cross-slip and slip transmission across GBs take places in NL layer, leading to the decrease of back stress in stage II. In the DT layer, although TBs can block dislocations, at increasing strain the interaction of dislocations with TBs may lead to the TB migration due to the existence of abundant Shockley partials. Consequently, back stress decreases rapidly with increasing strain. However, the decrease of back stress in stage II did not results in the strain softening in both NL and DT layers, which may be attributed to the increasing effective stress originated from multiple slip of dislocations [238]. In summary, the localized gradient structures in NL layers support back stress due to GNDs that derived from the hardness gradient of GS C-22HS alloy, and thus enable significant strain hardening capability.

3.6 Conclusion

Gradient structures have been introduced into C-22HS nickel-based alloy by SMGT technique. The microstructure of gradient structured C-22HS samples evolves from NL to DT layers and subsequent SD layers adjacent to the unaffected matrix. *In situ* micropillar compression tests coupled with microscopy studies show the followings.

(1) The strengths of NL and DT layers are significantly greater than that of the unaffected matrix.
(2) The NL layer has a two-stage work hardening behavior, and the first stage has a large work hardening exponent.
(3) Back stresses develop in NL and DT layers during deformation due to the existence of GNDs.
(4) The lamella structure of the NL layer is stable during compression, with little grain coarsening.

CHAPTER 4. THICK GRAIN BOUNDARY INDUCED STRENGTHENING IN NANOCRYSTALLINE NICKEL ALLOY

The gradient structured nickel-based alloy was fabricated by Jie Ding and Zhongxia Shang. In situ micropillar compression tests and microstructure characterization were performed by Dr. Jie Ding at Purdue University, with great help from Dr. Qiang Li and Ruizhe Su. The molecular dynamic simulation was performed by Dajla Neffati with guidance by Dr. Yashashree Kulkani at University of Huston. The data analysis and writing were completed by Jie Ding with guidance and editing by Dr. Xinghang Zhang.

4.1 Overview

Grain refinement has been extensively used to strengthen metallic materials for decades. Grain boundaries act as effective barriers to the transmission of dislocations and consequently lead to strengthening. Conventional grain boundaries have a thickness of 1-2 atomic layers, typically ~0.5 nm for most metallic materials. Here we report, however, the formation of ~3 nm thick grain boundaries in nanocrystalline Ni alloy. *In-situ* micropillar compression studies coupled with molecular dynamics simulations suggest that the thick grain boundaries are stronger barriers than conventional grain boundaries to the transmission of dislocations. This study provides a fresh perspective for the design of high strength, deformable nanostructured metallic materials.

4.2 Introduction

The contribution of grain boundaries (GBs) to the strength of polycrystalline metals has been intensively investigated since the beginning of 1950s, when Hall and Petch reported the dependence of strength on grain size of metallic materials by using the Hall-Petch equation [7,8]:

$$\sigma_y = \sigma_0 + kd^{-1/2} \qquad \text{Equation 4.1}$$

where σ_y is yield strength, σ_0 is friction stress, k is a coefficient describing the barrier resistance of GBs to slip transmission of dislocations, and d is the average grain size [7,9,247]. The grain size dependent strengthening mechanisms have been studied extensively for various types of boundaries or interfaces in nanostructured metallic materials fabricated by plastic deformation [9,47,74,248], electrodeposition [75,249,250] and magnetron sputtering [251–258].

As predicted by the Hall-Petch equation, the strengthening effect becomes more prominent with a higher k value. The coefficient k characterizes the intrinsic resistance of GBs to the slip transmission of dislocations. It has been proven that the character and structure of GBs play an important role in impeding dislocation slip in metallic materials [259]. Sangid *et al.* [259] studied the effect of energy barrier to dislocation transmission through GBs and dislocation nucleation from GBs, and showed that the coherent (Σ3) twin boundary is a stronger barrier to the transmission of dislocations than other types of GBs, such as the Σ13 and Σ19 GBs. Koning *et al.* [260] also found that the slip transmission resistance of GB is determined by three variables: the ratio of resolved stress on the incoming slip system to that on the outgoing slip system, the magnitude of any residual Burgers vector content left in the GB, and the angle between the traces of the incoming and outgoing slip planes. Several other mechanisms on interfaces induced strengthening, including modulus and lattice parameter mismatch [253,255,261,262], interfacial shear strength [261–264], have also been discussed. Prior study also showed that nitrogen increases the k value of austenitic steel (Cr18Ni16Mn10) significantly by blocking dislocation source in grains [265]. Hu *et al.* [250] reported that annealing of the electrodeposited nanocrystalline (NC) NiMo alloy led to high hardness, 11.0 GPa, due to the segregation of Mo nanoclusters to GBs.

GB segregation and the formation of GB complexions, have been investigated previously [152,266–274]. GB complexion was first reported in ceramic systems [275], and has since also been observed in metallic materials. For instance, the segregation of Ga in Al GBs is believed to play an important role in embrittlement due to the formation of GB complexion [266]. Similar phenomena have also been observed in Cu-Bi [270], Ni-Mo [268] and W-Ni [267] systems. While for the Zr doped nanograind Cu powders, the mechanical tests showed a yield strength exceeding 1 GPa and a strain to failure of more than 50%, which is rare in traditional Cu alloys [274]. The combination of high strength and good ductility of the Cu-Zr powder is attributed to the formation of amorphous intergranular films in the Cu GBs, as the amorphous intergranular films can increase

the GB tolerance to the transmission of dislocations by absorbing dislocations and acting as an effective defect sinks [152,274].

Most previous studies focus on the strengthening effect of GBs with thickness of 1-2 atomic layers, ~0.5 nm. The influences of thick GBs or GB complexions on the mechanical properties of metallic materials, especially for bulk metallic materials, are largely unclear. In this study, we reported the formation of thick GBs, with an average thickness of ~3 nm, in nanocrystalline (NC) Ni alloy fabricated by severe plastic deformation. The thick GBs formed by Mo segregation to the GBs during heat treatment. *In-situ* micropillar compression tests show that thick GBs induced much more pronounced strengthening effect than conventional GBs. Molecular dynamics (MD) simulations provide atomistic insights into the underlying strengthening mechanism of thick GBs.

4.3 Experimental

4.3.1 Materials and processing

A Hastelloy C-22HS Ni alloy rod (12 mm in diameter), with a chemical composition (in Wt.%) of Cr 21.0, Mo 17.0, Fe 2.0, C 0.01, Si 0.08, balanced by Ni, was subjected to SMGT at room temperature. Prior to processing, the C-22HS alloy was annealed at 1100 ^{o}C for 1 hr, followed by air cooling. Details on the SMGT technique can be found elsewhere [276]. During processing, the rod rotated at a speed of 400 rpm, while a hemispherical WC/Co tool tip penetrated into sample surface by 30 μm and slid along axial direction at a velocity of 10 mm/min. The process was repeated 8 times to generate subsequent deformation zones underneath the surface. Heat treatment of the processed alloys was carried out at 650 ^{o}C for 5 hr in a tube furnace.

4.3.2 Microstructure characterization

The microstructure and composition analysis of the specimens were carried out on an FEI Talos 200X analytical transmission electron microscope operated at 200 kV, equipped with a supper X energy-dispersive X-ray spectroscopy (EDS) detector. TEM specimens were prepared by focused ion beam (FIB) technique using an FEI Quanta 3D FEG Dual beam FIB scanning electron microscope following typical protocols.

4.3.3 *In-situ* micropillar compression tests

Micropillars were prepared using FIB technique along the longitudinal direction of both as-processed and heat-treated C-22HS alloy in the NC layer. The micropillars have a diameter of ~2 μm and height of ~ 5 μm with a height-to-diameter aspect ratio of ~2.5 to avoid buckling during compression tests. *In-situ* microcompression tests at a constant strain rate of $1 \times 10^{-3}s^{-1}$ were performed in an FEI Quanta 3D FEG SEM microscope using a Brukers-Hysitron PI 88×R PicoIndenter equipped with a 5 μm diameter diamond flat-punch indenter tip. The force-displacement data were collected by the piezoelectric actuator in the capacitive transducer. The morphological evolution of the micropillar during compression was recorded by SEM video. All micropillars were compressed under displacement control mode until ~18% of strain, followed by 0.5 s holding before unloading. The drift rate was measured to be 0.1 nm/s.

Pillar diameters, measured at the half-height of the pillar, were used for the calculation of engineering stress. The engineering stress calculated in this study represents an approximation considering the small taper angle of pillars, < 3°. To obtain an accurate measurement of strain, the equation derived by Sneddon [234] was applied to calculate displacement, x:

$$x = x_{meas} - \frac{1-\nu_i^2}{E_i}\left(\frac{F_{meas}}{D_t}\right) - \frac{1-\nu_b^2}{E_b}\left(\frac{F_{meas}}{D_b}\right) \qquad \text{Equation 4.2}$$

where x_{meas} and F_{meas} represent the measured displacement and force, respectively. ν_i and E_i are the Poisson's ratio and Young's modulus of diamond punch, taken to be 0.07 and 1220 GPa, respectively. ν_b and E_b for Ni are 0.31 and 205 GPa, respectively. D_t and D_b are the diameter of the pillar near the top and bottom portion, respectively. The engineering stress-strain curves were obtained after the correction of displacement, and subsequently converted to true stress-strain curves by using the homogeneous deformation model (assume no volume change during the deformation).

4.3.4 MD simulation details

MD simulations were performed on two different sets of NiMo bilayers with pre-existing GBs using the Large-scale Atomic/Molecular Massively Parallel Simulator (LAMMPS) [277] and the results were visualized using Ovito [278] and DXA [279]. The bilayers are 11 nm × 11 nm × 10.5 nm and are periodic in the z-direction. The GBs separate two grains of equal thicknesses in

the y-direction. The first simulation is intended to study the effect of a regular Σ5 GB on dislocation nucleation and motion. To investigate the effect of a thick GB, we take a sample with a similar setup as the one previously described and create an amorphous boundary separating the two grains following the steps in Ref.[280]. First, the atoms are held rigid except for a 1.5 nm slab around the GB that is melted to 1600K and held for 200 ps. Then, the melted atoms are quenched from 1600K to 800K over 200 ps. Later, to relax the system, the fixed atom constraint is removed and the entire sample is quenched from 800 to 300K over 40 ps. Finally, the sample is relaxed at 300K under the NVT ensemble with a Nose-Hoover thermostat for an additional 20 ps, resulting in a bilayer with a thick amorphous boundary of ~2.5 nm. In both samples, a thin layer of 10 nm in thickness and 5.5 nm in width is removed to create a step that acts as a dislocation nucleation site. Eventually, both structures undergo equilibration at 300K for 50 ps under the same ensemble previously used. Tension is applied for 600 ps in the x-direction at a strain rate of 10^8 s^{-1}. The Ni-Mo, Ni-Ni and Mo-Mo atomic interactions are described by the embedded-atom method (EAM) potential developed by Zhou et al. [281].

4.4 Results

4.4.1 Microstructure characterization

The microstructure of the as-processed sample in Fig.4.1 reveals that NC grains, as verified by the inserted selected area diffraction (SAD) pattern, have formed after SMGT (Fig.4.1a1). The average grain size is ~ 37 nm at ~ 8 μm from treated surface. The scanning transmission electron microscopy (STEM) image and corresponding EDS maps in Fig.4.1a2 show that the major chemical elements (Ni, Mo, Cr) are distributed uniformly in the as-processed specimen. High resolution TEM (HRTEM) image in Fig.4.1a3 shows deformation twins (DTs), several nanometers in thickness, and stacking faults (SFs) inside grains. The GBs (as labeled by white dotted lines) are sharp and narrow. However, after heat treatment at 650 ^oC for 5 hr, the average grain size of NC grains at the same depth coarsened to ~ 53 nm (Fig.4.1b1). The EDS maps in Fig.4.1b2 show the enrichment of Mo along GBs, accompanied by the depletion of Ni in the heat-treated Ni alloy. An EDS map at lower magnification including multiple grains in Fig.4.2 shows that most GBs in the heat-treated specimen are enriched in Mo. The corresponding compositional line profile across a typical GB in Fig.4.2c (as marked by the dash line in STEM image in Fig.4.2b) also verifies the

Mo-enrichment of GBs, and the thickness of Mo-rich zone is several nanometers. The HRTEM image in Fig.4.1b3 reveals that the thickness of Mo rich GBs is ~ 3 nm, which is much thicker than those in the as-processed alloy, ~ 0.5 nm. The atomic arrangement within the thick GB region is disordered, as indicated by the yellow dashed circles. The corresponding fast Fourier Transform (FFT) of the image exhibits a combination of diffraction spots and amorphous ring, indicating the coexistence of crystalline and disordered structure within the thick GB region.

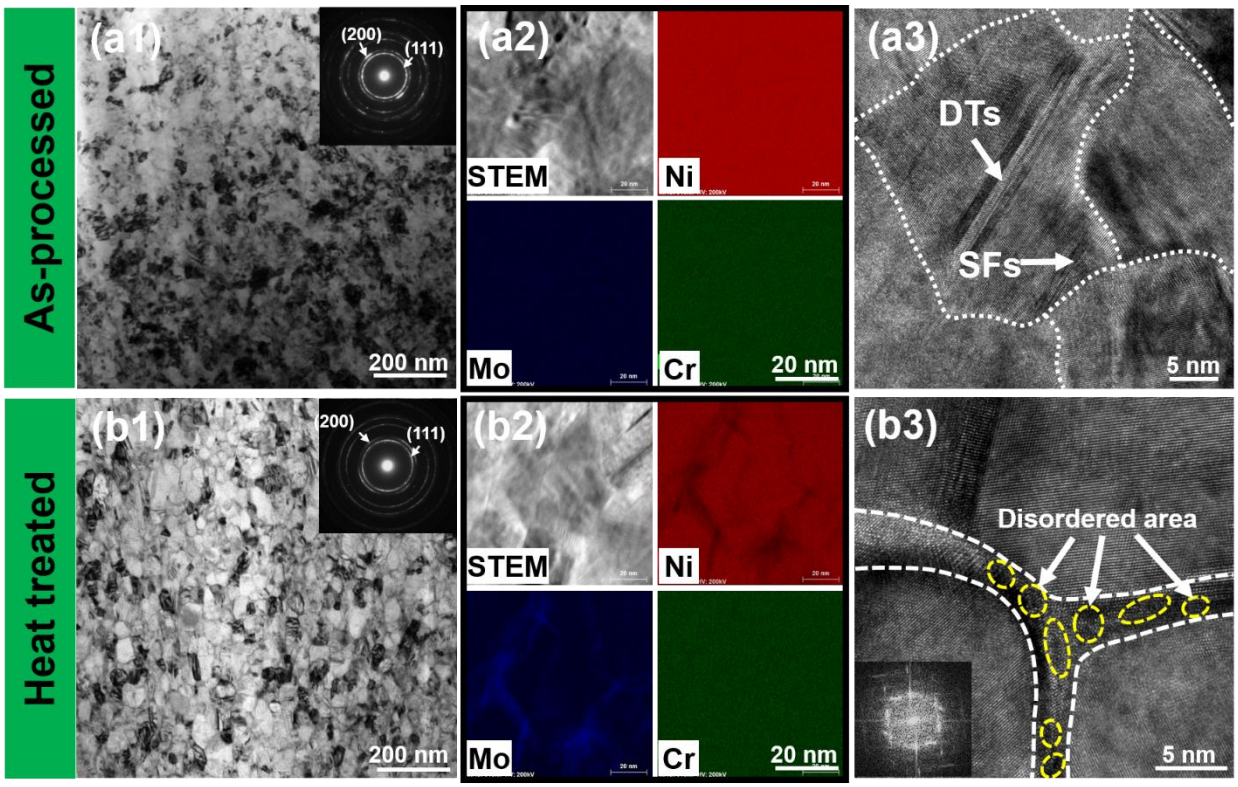

Figure 4.1 Comparison of the microstructures of the nanocrystalline surface layers of (a) as-processed and (b) 650 °C/5h heat-treated C-22HS specimens. (a1, b1) TEM images showing nanocrystalline grains of specimens before and after heat treatment. (a2, b2) The STEM images and corresponding EDS maps showing the uniform distribution of major chemical elements (Ni, Mo, Cr) in as-processed specimen vs Mo enrichment in the GBs of the heat-treated specimen. (a3, b3) HRTEM images showing DTs and SFs inside grains of the as-processed specimen, and the thick Mo enriched GBs in the heat-treated specimen.

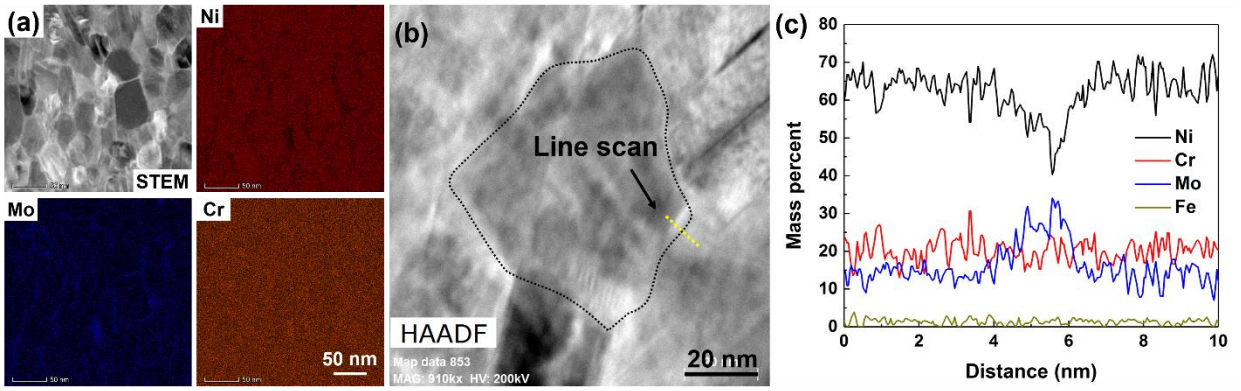

Figure 4.2 (a) The STEM image and corresponding EDS maps showing the distribution of major chemical elements (Ni, Mo, Cr) of heat-treated Ni alloy sample. (b and c) The STEM image and corresponding EDS line scanning results along the line that crossing thick GBs in the STEM image in Fig.b showing the enrichment of Mo and depletion of Ni in the boundary area.

4.4.2 Mechanical properties

In-situ micropillar compression tests were performed in the NC layer of both as-processed and heat-treated specimens. The true stress-strain curves in Fig.4.3a1 and 4.3b1 show that the flow stress of as-processed specimen with thin GBs (refers to thin GB sample hereafter) is ~ 1.8 GPa, whereas the flow stress of heat-treated specimen with thick GB (refers to thick GB sample hereafter) increases to ~ 2.4 GPa. Multiple micropillar compression tests were performed and the results are reproducible. The SEM snapshots of the video captured during compression of the thin GB specimens in Fig.4.3(a2-a6) show the uniform deformation of pillar as evidenced by classical barreling near the top of the deformed pillar. The corresponding pillar morphology evolution of the thick GB specimen in Fig.4.3(b2-b6) reveals similar uniform deformation behavior up to the compression strain of ~ 20%.

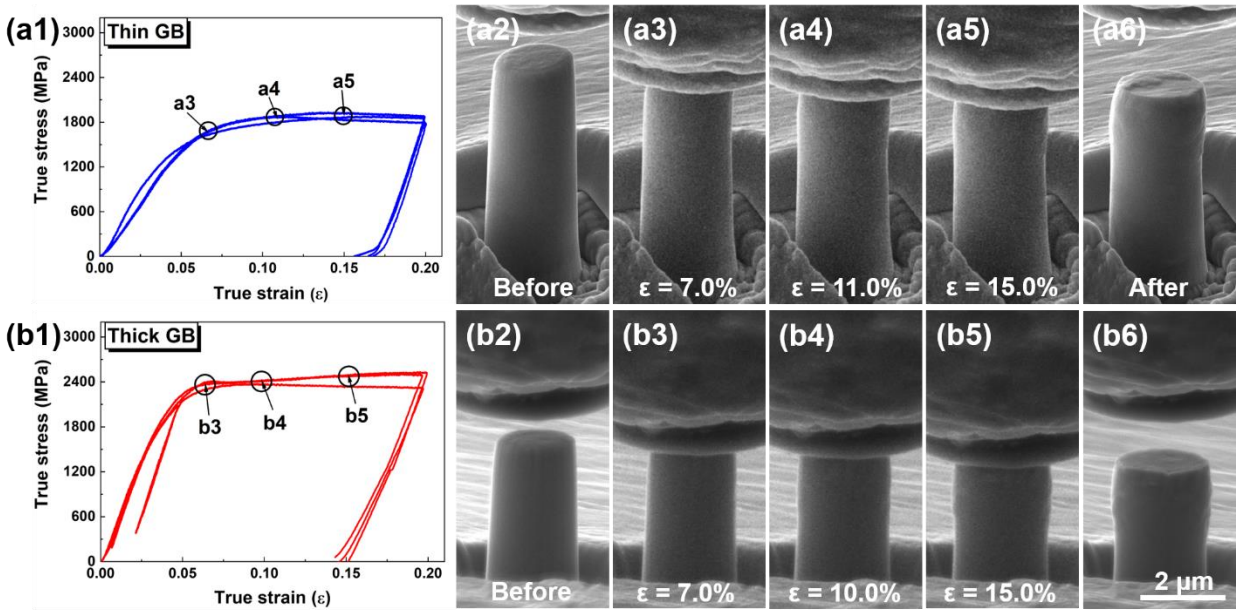

Figure 4.3 *In-situ* compression test results of pillars obtained from thin GB and thick GB specimens. (a1 and b1) The true stress-strain curves of thin GB and thick GB specimens. (a2-a6 and b2-b6) Corresponding SEM images of the specimens showing the pillar morphology evolution during compression tests.

4.4.3 Hall-Petch relationship

Gradient structure with increasing grain size along the depth direction is produced after SMGT. To reveal the relationship of grain size and mechanical properties of both thin GB and thick GB specimens, the statistical studies of grain size along the depth direction were performed, and the corresponding Vickers hardness evolution was investigated. Fig.4.4a shows the evolution of grain size and Vickers hardness of the thin GB and thick GB specimens. The grain size of thin GB sample was ~ 33 nm at the depth of ~ 4 μm under the treated surface, then increased to ~ 104 nm at the depth of ~ 30 μm. Meanwhile, the hardness of the corresponding region decreased from ~ 5.8 GPa from the surface layer to ~ 4.3 GPa at the depth of ~ 40 μm from surface. After heat treatment at 650 ^{o}C for 5 hr, the average grain size coarsened slightly, from ~ 42 nm near the surface to ~ 120 nm at a depth of ~ 30 μm from surface. However, the Vickers hardness of thick GB sample is much higher than that of the thin GB one. The Vickers hardness on the topmost layer is ~ 7.7 GPa, then decreased to ~ 5.6 GPa at the depth of ~ 40 μm. Fig.4.4b shows the comparison of the Hall-Petch plot of the thin GB and thick GB specimens in this work with those data on NC Ni [13,17,18,282–287]. It reveals that the thin GB sample has similar Hall-Petch slope (as shown

by the red dash line) compared to the published data. While the hardness of the thick GB specimens is much higher than the thin GB specimen with similar grain size, and thus resulting in a greater Hall-Petch slope (red solid line) than other Ni alloys in Fig.4.4b.

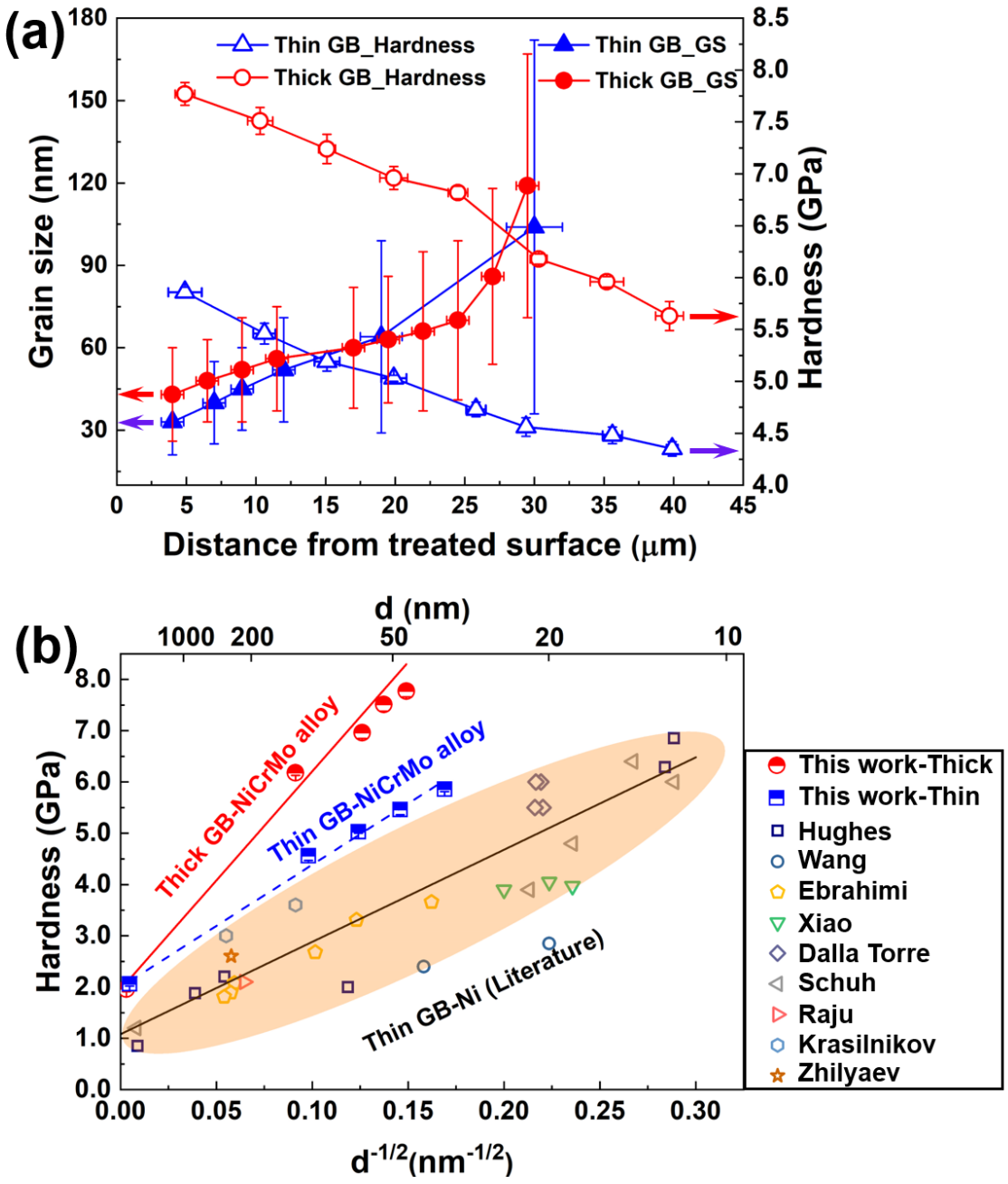

Figure 4.4 (a) The evolution of average grain size and Vickers hardness of thin GB and thick GB samples along the depth direction. (b) Comparison of the Hall-Petch plot from this study to published work on NC Ni [43–51].

4.5 Discussion

4.5.1 The formation of Mo-rich thick GB

The GB segregation and the formation of GB complexion have been studied extensively. The GB segregation phenomena in several binary systems, such as Cu-Zr [274,288], Cu-Nb [288–290], Cu-Bi [270], Cu-Fe [289,290], Cu-Ag [290], Ni-Zr [288], Ni-Mo [268], W-Ni [267] and alloys such as Fe-Mn-C steels [291] reveal that GB segregation by heat treatment is an effective approach for tailoring the mechanical properties of metallic materials. Six types of complexions have been classified by Dillion *et al.* [292] according to their thickness, ordering and composition, while the disordered versions can be further classified as amorphous intergranular films (AIFs). The Mo-rich thick GB with disordered atomic structures observed in this study can be treated as AIFs. In literature, the formation of complexion at the GB are controlled by the enthalpy of segregation (ΔH_{seg}), enthalpy of mixing (ΔH_{mix}) and atomic radius mismatch. ΔH_{seg} and ΔH_{mix} are the primary factors determining the type of complexions, and the atomic radius mismatch determines the stability of AIFs [288]. A positive ΔH_{seg} coupled with a negative ΔH_{mix} may promote the formation of AIF in alloys [288]. In this study, the Ni-Mo binary system possesses positive ΔH_{seg} and negative ΔH_{mix} [293], a nanoscale AIF with disordered atomic structures along the GBs is therefore expected to form after heat treatment, consistent with the experimental observations.

4.5.2 Experimental evidence of thick GB induced strengthening

The microstructure characterizations show that the heat treatment induced grain coarsening by over 30% within 10-15 micron near surface (Fig.4.4a). However, the *in-situ* micropillar compression tests reveal that the flow stress of pillars increased from 1.8 GPa for the thin GB sample to 2.4 GPa for the thick GB one, consistent with the Vickers hardness measurement at similar depth. The strengthening effect accompanied with the grain coarsening is surprising as conventional wisdom suggests that smaller grains often lead more pronounced strengthening [18]. Meanwhile other widely discussed conventional strengthening mechanisms arising from higher density defect or precipitates [22,294–297], solute atoms [298,299] are also absent in this case.

These observations imply that the thick Mo enriched GB may play a critical role in annealing induced strengthening in NiCrMo alloy.

Hall-Petch mechanism typically dominates the grain size dependent strengthening of metallic materials when grain size is larger than 30 nm [260–262]. The Hall-Petch slope k is a measure of the GB resistance to slip transmission of dislocation and can be described by [300]:

$$k = \sqrt{\frac{\tau^* \mu b}{\pi(1-\nu)}} \qquad \text{Equation 4.3}$$

where τ* is the critical shear stress required for slip transmission of dislocation across boundaries and is an indication of boundary barrier strength, μ is the shear modulus, b is the magnitude of Burgers vector and ν is the Poisson's ratio. The measured Hall-Petch slope for Vickers hardness plot $k_{Hardness}$ can be converted to k by considering a Taylor factor of 3.1 and a hardness-to-flow stress conversion factor of 2.7 ($k = k_{Hardness}/3.1/2.7$) [268,269]. The measured Hall-Petch slope for the thin GB and thick GB samples is 23.87 GPa$\sqrt{\text{nm}}$ and 42.54 GPa$\sqrt{\text{nm}}$, respectively. Thus, we obtain k_{thin} = 2.85 GPa$\sqrt{\text{nm}}$ and k_{thick} = 5.08 GPa$\sqrt{\text{nm}}$ for the thin GB and thick GB specimens. By using μ = 80 GPa, b = 0.248 nm and ν = 0.30 for Ni alloy, the boundary barrier strengths of thin GB and thick GB samples are calculated to be τ^*_{thin} = 0.90 GPa and τ^*_{thick} = 2.86 GPa, respectively. These analyses suggest that the thick GB is a much stronger barrier to the transmission of dislocations than the conventional GB of the thin GB Ni alloys.

To investigate the response of thick GBs to deformation, post compression TEM analyses were performed on the deformed pillars of thick GB specimen (36% of compression strain). The bright field and dark field TEM images in Fig.4.5a and b show that there is an insignificant grain size variation in the deformed pillar. HRTEM image showing the interior of grains in the deformed region (Fig.4.5c) reveals high-density SFs generated during compression (indicated by orange arrows), as verified by the corresponding FFT pattern in Fig.4.5d. The FFT patterns of the grains on the left and right side of thick GB in Fig.4.5c reveal that there was only a ~ 5º tilting between the (111) planes of these two grains. Interestingly, these SFs in the left grain were mostly blocked by the ~ 3 nm thick GB (labeled by double white dash lines). HRTEM image in Fig.4.5e (the magnified box e from Fig.4.5c) shows the SFs (indicated by white arrows) were not able to transmit across the thick GB.

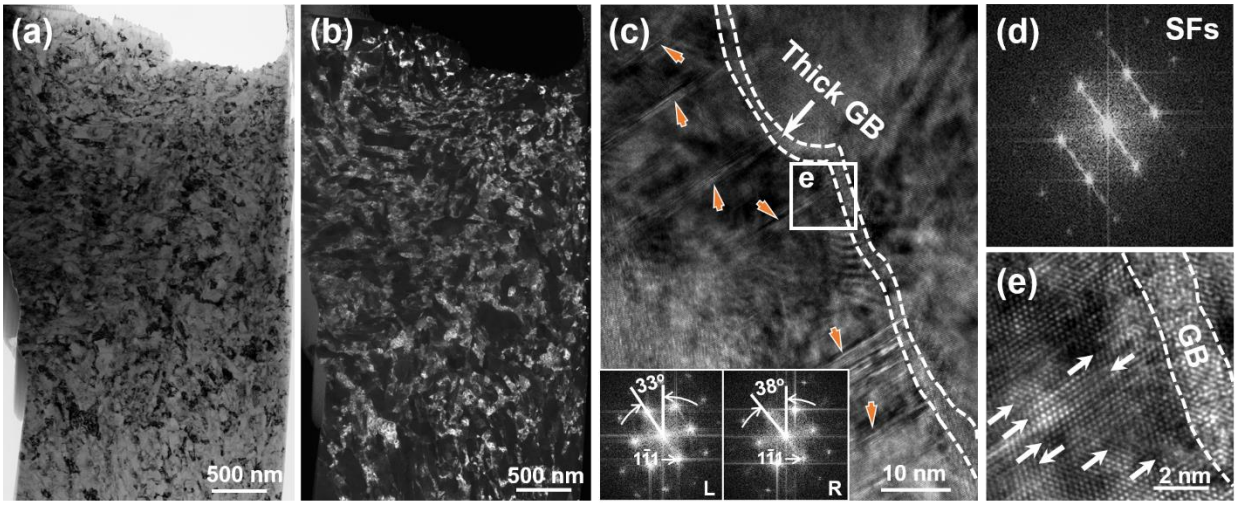

Figure 4.5 (a) BF and (b) DF TEM image of the deformed pillar from the heat-treated specimen after 36% of compression strain. (c) HRTEM image of grains after compression showing high density SFs (as indicated by orange arrows). These SFs were blocked by a thick GB. (d) The SFs are verified by the corresponding FFT pattern. (e) The HRTEM image of the white box e in Fig.4c showing the blocking of SFs (indicated by white arrows) by the thick GB.

Most prior studies focused on the formation mechanism of GB complexion after heat treatment [288,301]. However, the influence of GB complexion on the mechanical properties of metallic materials has rarely been reported. Khalajhedayati *et al.* [152,274] systematically investigated the formation of GB complexions in nanocrystalline Cu-Zr alloys and the corresponding response of mechanical properties. Their study reveals that AIFs form after heat treatment above 850 ^{o}C and the Cu-Zr alloy with amorphous interfaces exhibits a yield strength exceeding 1 GPa and a strain to failure of more than 50%. The extraordinary mechanical properties are attributed to two factors: the crystalline/amorphous interface that impacts the nucleation and transmission of dislocations, and the reduced boundary energy resulting from GB [152,274]. Vo *et al.* [289,290] also attributed the strengthening of nanocrystalline Cu-Nb, Cu-Fe and Cu-Ag alloys with GB segregations to the reduced GB energy comparing with the pure Cu. Both MD simulations and experimental results reveal that the strength increases monotonically with reduction of GB energy [152,274,289]. Khalajhedayati *et al.* [274] argued that reducing GB energy may make the nucleation and propagation of dislocation harder during deformation. Rupert *et al.* [302] also attributed the strengthening to the reduction in the number of available sources for dislocation emission. Both experiments and MD simulations have suggested that the solute

segregation to GBs can reduce GB energy. By ignoring the entropy change of the system on adding solutes to GBs, the GB energy (γ) can be calculated by [290,303,304]:

$$\gamma = \gamma_0 - \Gamma \Delta H_{seg} \qquad \text{Equation 4.4}$$

where γ_0 is GB energy of undoped state, Γ represents average coverage of solute in the GB (proportional to solute concentration) and ΔH_{seg} is the enthalpy of segregation. As stated in the previous section, the ΔH_{seg} is positive for Ni-Mo system. It implies that the segregation of Mo in GB beneficial to the reduction of GB energy, leading to the formation of thick GB. The underlying strengthening mechanism due to thick GBs will be discussed in detail via MD simulation results in the following section.

4.5.3 Strengthening mechanisms revealed by MD simulations

The following MD simulations were performed by Dr. Dajla Neffati and Dr. Yashashree Kulkani at University of Huston.

Foregoing discussions confirm that thick GBs are indeed strong barriers to the transmission of dislocations. The fundamental mechanisms behind thick GB induced strengthening, however, remain largely unclear. In what follows, we discuss the strengthening mechanisms revealed by MD simulations.

MD simulations were performed on model NiMo alloys containing a thin (conventional) Σ5 GB (2-3 atomic layers) and a 2.5 nm thick amorphous boundary (mimicking the experimental observation of amorphous like disordered thick GBs). The stress strain response in Fig.4.6a reveals that the sample with thin GBs yields at ~ 2.9 GPa, whereas the yielding of the thick GB specimen occurs at higher stress, ~ 3.5 GPa, consistent with the experimental studies. The magnified stress-strain curves in Fig.4.6b show a couple of labels at various strain levels, and the microstructure evolution at positions will be shown next.

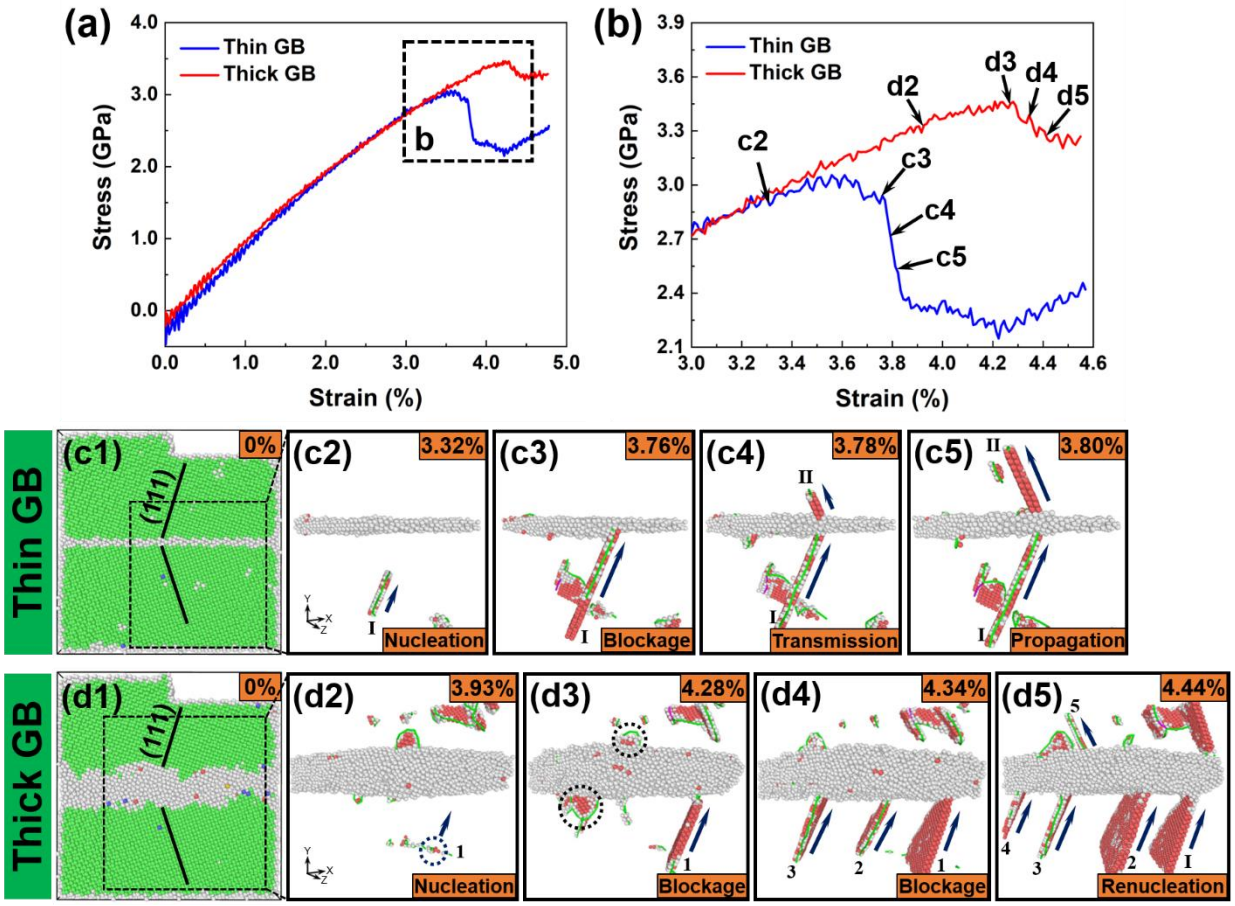

Figure 4.6 MD simulations of NiMo alloy with thin and thick GB. (a) The comparison of stress-strain curves for NiMo alloy with thin and thick GB under tension. The yield stress of the thin GB sample is ~ 2.9 GPa, whereas that of thick GB sample reaches ~ 3.5 GPa. (b) The magnified stress-strain curves showing the yielding behaviors of thin and thick GB samples. Evolution of atomistic configurations of (c) thin GB and (d) thick GB samples at different strains illustrated in Ovito using common neighbor analysis. FCC atoms are colored in green, HCP atoms are colored in red and amorphous atoms are colored in gray. Using dislocation analysis, the green and purple lines represent Shockley partials and stair-rod dislocations, respectively.

The evolution of atomistic configurations for both samples under tension with increasing of strain are illustrated in Ovito using common neighbor analysis and represented in Fig.4.6c and 4.6d, respectively. FCC, HCP and amorphous atoms are colored in green, red and gray, respectively. The (111) planes of lower and upper grain forming Σ5 grain relationship in simulation cell are labeled in Fig.4.6c1and 4.6d1. The detailed microstructure evolutions in the dashed boxes in Fig.4.6c1 and 6d1 are shown in Fig.4.6c2-6c5 and Fig.4.6d2-6d5. Using dislocation analysis, the green and purple lines represent Shockley partials and stair-rod dislocations, respectively. FCC atoms were removed for clarification. For thin GB sample, Shockley partials nucleated and

thereafter disappeared frequently under tension to accommodate the strain. The first set of stable Shockley partials (#I) was captured until the strain increased to ~ 3.32%, as shown in Fig.4.6c2. The stable Shockley partials propagated towards and then blocked by the thin GB when strain increased to ~3.76%, as illustrated in Fig.4.6c3. A further increase of the strain resulted in the transmission (in Fig.4.6c4) and further propagation (in Fig.4.6c5) of Shockley partials (#II) through the thin GB, contributing to the drastic stress drop as shown in Fig.4.6b. The snapshot reveals that the Shockley partials transmitted through the thin GB follow the Σ5 twinning orientation relationship. Similar transmission phenomena have been reported in other MD simulation studies as well [305,306].

For the thick GB sample, the dislocation activity before yielding is similar with the thin GB sample. The difference is that the first set of stable Shockley partials doesn't captured until the strain increased to ~ 3.93%, as shown in Fig.4.6d2, higher than that (3.32%) of thin GB sample. The Shockley partial then propagated towards the thick GB and was blocked. When the tensile strain increases to ~ 4.28%, plastic yielding took place, as shown in Fig.4.6d3. Comparing to the Shockley partial transmission induced yielding for thin GB sample, the yielding of thick GB sample was attributed to the nucleation and propagation of more Shockley partials in the lower grain, as shown in Fig.4.6d4 (#1-3). At this stage, several pre-existing Shockley partials nucleated before yielding (as labeled by black dotted circles in Fig.4.6d3) disappeared, presumably due to their absorption by the thick GB. With the further increase of the strain, a new Shockley partial (#5) nucleated and propagated above the thick GB at the strain of ~ 4.44% (as illustrated in Fig.4.6d5), leading to the further stress decease. It is worth mentioning that the new Shockley partial (#5) in the upper grain did not occur at the coincident site where the Shockley partials (#1-4) intercept with the thick GB. The comparison of the evolution of new activated Shockley partials in the upper grain for both samples are presented in Fig.6.7. It shows two Shockley partials have transmitted cross the thin GB (at the same incident sites) after yielding and propagated upwards, as illustrated by the black arrows in Fig.6.7a. In contrast, Shockley partials (#1-4) once blocked by the thick GBs, often propagated along directions parallel to the GB, as denoted by arrows in Fig.6.7b. These evidences suggest that the deformation mechanisms of thin GB and thick GB samples are different. Transmission of Shockley partials across the thin GB attributes to the yielding of the thin GB sample. For thick GB sample with amorphous boundary, however, no

apparent transmission phenomenon has been observed during deformation. And the plastic yielding is derived from the renucleation of new Shockley partials on either side of thick GBs.

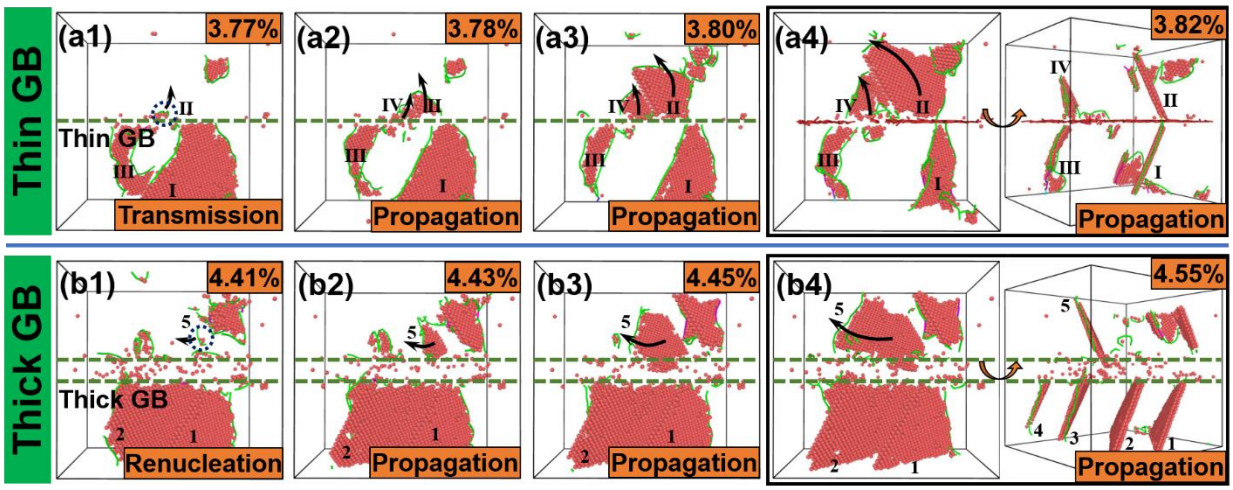

Figure 4.7 Evolution of atomistic configurations showing (a) the transmission of Shockley partials across the thin GB and thereafter propagate upwards, (b) the renucleation of a new Shockley partial on the other side of thick GB and thereafter propagate parallelly with the thick GB. Fig.a4 reveals that the two Shockley partials transmitted through the thin GB follow the Σ5 twinning orientation relationship with those in the lower grain. Whereas the new Shockley partials nucleated randomly on the upper grain for thick GB sample after yielding in Fig.b4.

Previous studies on Cu/amorphous CuZr multilayers show that during deformation, the glide dislocations nucleated in Cu layer were absorbed by the crystalline/amorphous interface, and alleviate the atomic shear strain concentration on amorphous layer [307,308]. These observations imply that the interface between crystalline and disordered structure could be an effective dislocation sink during deformation. Upon absorption by the interface, the dislocation core will dissociate or spread, and thus the stress/strain concentration at the interface will be smeared. Consequently, the singularity that enables the dislocation to slip through lattice is lost, and a higher stress is necessary to promote the transmission of dislocations across the interface, resulting in higher yield stress. MD simulations on Cu/Nb multilayers with FCC/BCC structure also reveal that a single dislocation cannot slip through the Cu/Nb layer interface even at a resolved shear stress of 1.0 GPa [261]. In this study, the strengthening from the thick disordered GBs may also arise from the absorption of dislocations by the GBs. To verify our hypothesis, the evolution of total length of Shockley partials of both samples with increasing strain has been statistically

calculated and plotted in Fig.4.8a. It shows that the length of Shockley partials (dislocation density) for thin GB sample increased drastically after straining beyond ~ 3.0%. The total length increased from ~ 400 nm to over 1100 nm after yielding, resulting from the transmission and propagation of Shockley partials through the thin GB. In comparison, for the thick GB specimen, the total length of Shockley partials didn't increase until being strained to ~ 3.3%, and the corresponding increase of dislocation length is much less than the thin GB sample. Fig.4.8b reveals that the partials have indeed been absorbed by the thick GB during deformation. The absorption of partials smeared the stress/strain concentration at the boundary and prevented the transmission of Shockley partials from happening. Consequently, the yielding of thick GB sample takes place at higher strain and stress level compared with the thin GB sample.

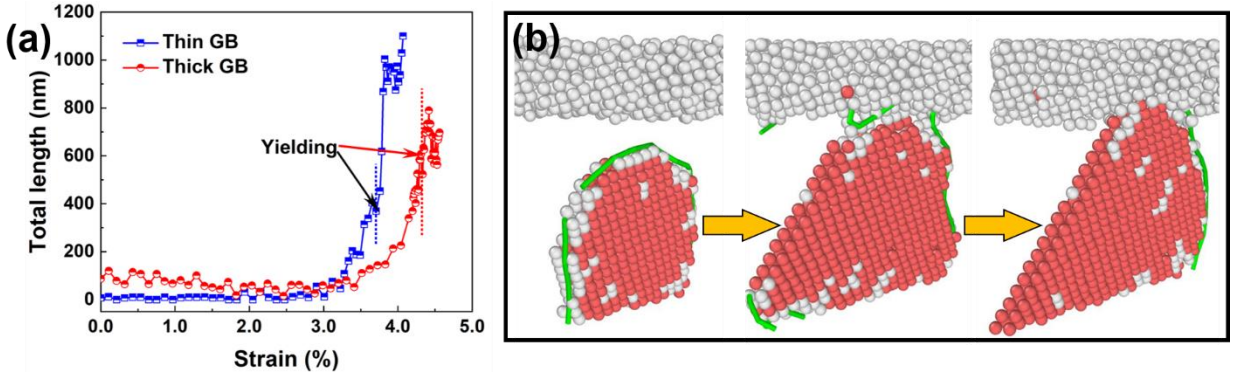

Figure 4.8 (a) The evolution of total length of Shockley partials for thin and thick GB samples with increasing of strain. The total length of Shockley partials is much greater for the thin GB specimen and increases sharply after yielding. (b) Evolution of atomistic configurations showing the absorption of Shockley partials by the amorphous thick GB

4.6 Conclusion

In summary, we reported the formation of ~3 nm thick GBs in nanocrystalline NiCrMo alloy after heat treatment. The Ni alloy with thick GBs is much stronger than the nanocrystalline Ni alloys with conventional (thin) GBs. The thick GBs effectively block the transmission of dislocations by acting as dislocation sinks, as confirmed by explicit MD simulations. This study provides new perspective for the design of high-strength, deformable nanocrystalline metals**.**

CHAPTER 5. TAILORING THE THERMAL STABILITY OF NANOCRYSTALLINE NICKEL ALLOY BY THICK GRAIN BOUNDARIES

The gradient structured nickel-based alloy was fabricated by Jie Ding and Zhongxia Shang. The data analysis and writing were completed by Jie Ding with guidance and editing by Dr. Xinghang Zhang.

5.1 Overview

Nanocrystalline (NC) metals have high strength, but are highly susceptible to grain growth at elevated temperatures due to the driving force to reduce the energy stored at grain boundaries (GBs). In this study, we compared the thermal stability of NC Ni alloy with conventional thin GBs and thick GBs. Thermomechanical treatment was applied to induce thick GBs in the Ni alloy. After annealing at 800 ^{o}C, significant grain growth occurs in the Ni alloy with thin GBs; whereas the nanograins with Mo-rich thick GBs remain stable. This study provides a fresh perspective on improving the thermal stability of NC alloys.

5.2 Introduction

Nanocrystalline (NC) metals that are characterized by high volume fraction of grain boundaries (GBs) have demonstrated remarkable mechanical properties including increased strength [52,309,310] and wear resistance [132,311,312] than the CG counterparts. However, while GBs contribute to the high mechanical strength, they often deteriorate the thermal stability of NC materials [313–319]. The high interfacial energy of nanograins provides a large driving force for grain coarsening through the removal of excess GBs. For instance, grain growth occurs at temperature as low as 200 ^{o}C for pure NC Ni, accompanied by substantial softening [318]. This tendency of grain growth prevents the widespread application of high strength NC metals.

One of the important parameters that describe the grain growth behavior of NC metals is GB velocity (ν), which can be expressed as [148,149]:

$$\nu = M_{gb} \cdot \gamma_{gb} \cdot \kappa \qquad \text{Equation 5.1}$$

where M_{gb} represents the GB mobility, γ_{gb} is the GB energy and κ is the local boundary curvature. Eq.1 implies that the grain growth process of NC materials is controlled by both kinetic and thermodynamic components. In general, two approaches have been proposed to hinder grain coarsening and improve the thermal stability of NC materials [149,152,173,320]. One is kinetics-driven stabilization approach in which GBs are pinned by solute drag [150,321] or second phase Zener drag [16,151,153,321–323] to decease the GB mobility. The other one is the thermodynamics-driven stabilization approach in which solute segregation to GBs reduces the driving force for grain growth as it is energetically favorable for solutes to reside at GBs [152,153,322,324–326]. Both kinetic and thermodynamic approaches are associated with alloying elements [149,153]. Using the kinetic stabilization approach by introducing thermally-stable γ' precipitates, Sun et al. [173] reported that the NC Inconel 718 Ni-based alloy exhibits remarkably improved thermal stability close to 700 ^{o}C (0.62 T_m, T_m represents melting temperature in K). Zheng et al. [327] also found that finely dispersed β' phase plays a critical role in inhibiting coarsening of ultra-fine-grained Mg alloy. Similar stabilization strategy has been successfully applied in Al alloys [328], Ti alloys [329,330] and steels [153,326,331–333]. Using thermodynamic stabilization strategy by lowering the GB free energy, several thermally stable binary alloys, such as W-Ti [324], Fe-Mg [326] and Cu-Zr [152], have been fabricated. Recent studies reveal that amorphous intergranular films (AIFs) observed in some alloys provide an alternative route other than conventional solute segregation to lower GB energy, and therefore hinder grain growth [149,152,292,334]. Rupert et al. [152,325] reported no apparent grain coarsening in the NC Ni-W alloy with AIF even after annealing at 1100 ^{o}C. The grain size of NC Cu-Zr alloy with AIF only coarsened from 20 nm to 54 nm after a week of annealing at 950 ^{o}C (98% of solidus temperature) [152]. However, the formation of AIF is limited to certain alloying systems. Schuler and Rupert [288] found that a negative enthalpy of mixing (ΔH^{mix}) coupled with a positive enthalpy of segregation (ΔH^{seg}) promotes the formation of nanoscale AIFs in binary metallic alloys. Koch et al. [320] compared the effectiveness of both thermodynamic and kinetic approaches in stabilizing several NC metallic systems and concluded that Zener pinning by nanoparticles is perhaps more effective than the thermodynamic stabilization strategy.

Inspired by previous discussions, this letter reports simultaneous introduction of AIFs and nanocrystalline phase to the GBs of NC metallic materials to limit grain growth at high temperatures. A NC Ni-based alloy with thick GBs consisting of disordered amorphous structure and intermetallic nanoparticles was obtained by employing thermomechanical treatment. The thermal stability of these alloys with thin and thick GBs was investigated at various annealing temperatures ranging from 600 to 900 ^{o}C. The underlying stabilization mechanism was discussed by investigating the microstructure evolutions of both alloys.

5.3 Experimental

The Hastelloy C-22HS Ni-based alloy used in this study has a chemical composition (in wt.%) of Cr 21.0, Mo 17.0, Fe 2.0, C 0.01, Si 0.02, balanced by Ni. The NC sample was prepared via surface mechanical grinding treatment (SMGT) technique. The thick GBs was formed by annealing the NC sample at 650 ^{o}C for 5 hours followed by air cooling [335]. To compare the thermal stability of the alloys with thin and thick GBs, samples were annealed in a vacuum furnace over 600 - 900 ^{o}C for 1 hour, followed by furnace cooling. Annealing was conducted when the vacuum level reaches 2×10^{-6} torr. The microstructure evolutions of the alloys were examined on an FEI Talos 200 X transmission electron microscope operated at 200 kV, equipped with a supper X energy-dispersive X-ray spectroscopy (EDS) detector. Transmission electron microscopy (TEM) samples were prepared using focus-ion beam (FIB) lift-out technique in a Quanta 3D FEG scanning electron microscope by following typical protocols [276]. Mechanical properties were characterized by Vickers hardness using a LECO LM247 microhardness tester. The maximum applied load was 25 g, with a holding time of 13 s.

5.4 Results

Nanograins were observed in the as-processed Ni alloy as shown in bright-field TEM image in Fig.5.1a. The inserted selected area diffraction (SAD) pattern shows continuous diffraction rings, an indication of the nanocrystalline character of the sample. The high resolution TEM (HRTEM) micrograph in Fig.5.1b shows conventional thin GBs (labeled by white dotted lines in Fig.5.1b). The STEM micrograph and corresponding EDS mapping results in Fig.5.1c reveal that the major chemical elements (Ni, Cr and Mo) were distributed uniformly. The statistic

of grain size in Fig.5.1d shows that the average grain size is ~ 37 nm. TEM image in Fig.5.1e shows that the nanograined structure of NC Ni alloy retained after annealing at 650 ^{o}C for 5 hours, as verified by the inserted SAD pattern. The corresponding HRTEM image in Fig.5.1f reveals the formation of thick GB networks after annealing, and the average thickness of GB is ~ 3 nm. The inserted fast Fourier transform (FFT) pattern of the dotted box shows that the thick GBs exhibit a disordered structure, somewhat similar to the AIF that was reported in literature [149]. The formation of AIF in Mo-Ni binary alloy may be related to the fact that the alloy has a positive ΔH^{seg} coupled with a negative ΔH^{mix} [288]. The positive ΔH^{seg} suggests that the alloy favors GB segregation of Mo, and the negative ΔHmix promotes formation of thick GBs [147]. Schuler et al. reported that the formation of either amorphous-like structures or intermetallic phases may be correlated to the magnitude of ΔHmix, since a very negative value may lead to the formation of intermetallic phases. Other factors may include the alloying of other elements like Cr and Fe, and the grain boundaries characteristics.

Another factor that may influence the formation of either amorphous or intermetallic phase at the thick GBs may be the thickness of the GBs. The distribution of the GB thickness in Suppl. Fig.S1 reveals that the average thickness of amorphous-like structures is ~ 3.2 nm, much thinner than that of intermetallic phases, ~ 13 nm. Although the fundamental mechanisms behind such a thickness dependent formation of amorphous and intermetallic thick GB remain unclear, the strain energy between the GB phase and matrix may play some role. For instance, the thin intermetallic phase (2-3 nm in thickness) could form a coherent or semicoherent interface with the matrix, and thus increase the strain energy of the system. Consequently, the formation of thin amorphous phase may reduce the strain energy of the system. On the other hand, when the GB phase has a much greater thickness (~ 10 nm), the coherency stress has been released, and thus a thick intermetallic phase may prevail along the GBs. Such a hypothesis requires more systematic experimental investigations and MD simulations.

In addition to the amorphous structure, intermetallic patches with crystalline structure were frequently identified along the thick GBs, as indicated by arrows in Fig.5. 1f. The formation of intermetallic phase may be related to the existence of other alloying elements, such as Cr and Fe. Another noteworthy phenomenon is that thin GBs still exist (as indicated by yellow dashed lines in Fig.5.1f). The statistic study reveals that ~ 65% (length fraction) of GBs have been transformed to the thick GBs. The STEM image and the associated EDS maps in Fig.5.1g reveal the enrichment

of Mo along thick GBs, accompanied by the depletion of Ni. The distribution of Cr is uniform across the thick GBs. The EDS line scan results in Chapter IV have confirmed the enrichment of Mo and depletion of Ni of thick GBs. The statistic distribution in Fig.5.1h reveals that the average grain size coarsened to ~ 53 nm after 5 hours of annealing.

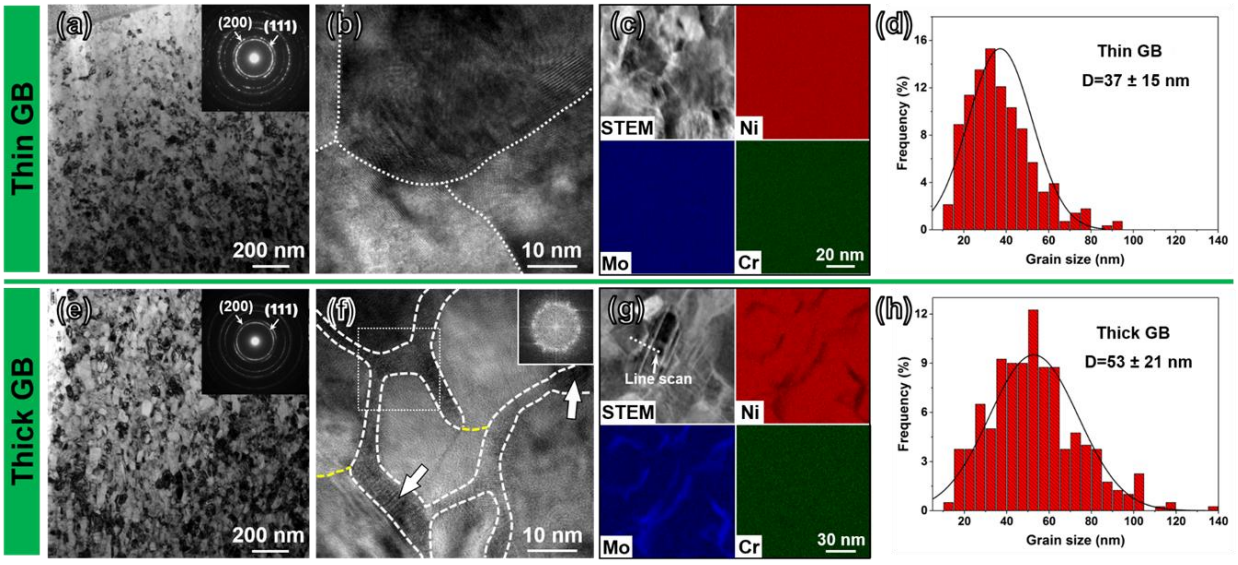

Figure 5.1 Comparison of microstructure of NC Ni alloy with (a-d) thin and (e-h) thick GBs. (a-b) TEM and HRTEM micrograph of NC Ni alloy with conventional thin GBs. (c) The STEM micrograph and corresponding EDS maps show that the major elements (Ni, Mo, Cr) are distributed uniformly. (d) The corresponding statistic distribution of grain size reveals that the average grain size is ~ 37 nm. (e-f) TEM and HRTEM micrograph showing NC Ni alloy with thick GB networks. (g) STEM image and corresponding EDS maps showing the enrichment of Mo along thick GBs. (h) The corresponding statistic distribution reveals an average grain size of ~ 53 nm.

Separate samples with conventional thin GBs and thick GBs were then subjected to annealing treatment at different temperatures ranging from 600 to 900 ^{o}C and the microstructure evolution was examined by TEM. As shown in Fig.5.2a, the average grain size (~ 37 nm) of NC Ni alloy with thin GBs coarsened to ~ 67 nm after annealing at 700 ^{o}C. Scattered large grains, ~ 200 nm or greater in size, were observed, as labeled by arrows in the both TEM image and statistical results in Fig.2a. Annealing at 800 ^{o}C coarsened the grain size further to ~ 113 nm, accompanied by abnormal grain growth, as shown in Fig.5.2b. The size and area fraction of coarse grains is ~ 418 nm and 60%, respectively. The inhomogeneous accumulation of dislocations during SMGT resulted in a large difference in the stored energy within grains and at different types of

GBs [35]. It is anticipated that the recrystallization during annealing preferentially occurs in the region with greater stored energy, leading to the abnormal grain growth [35]. Similar abnormal grain growth phenomena have been reported in other severely deformed metals [35,336]. In contrast, the average grain size of NC Ni alloy with Mo-rich thick GBs just slightly coarsened from 53 to ~ 56 nm after annealing at 700 ^{o}C (in Fig.5.2c). Merely 5% of grains experienced abnormal grain growth with an average grain size of ~ 140 nm. After annealing at 800 ^{o}C, the fine grains remained small, ~ 61 nm in grain size, whereas the area fraction of large grains experiencing abnormal grain growth increased to ~ 40% with an average grain size of ~ 411 nm, as shown in Fig.5.2d.

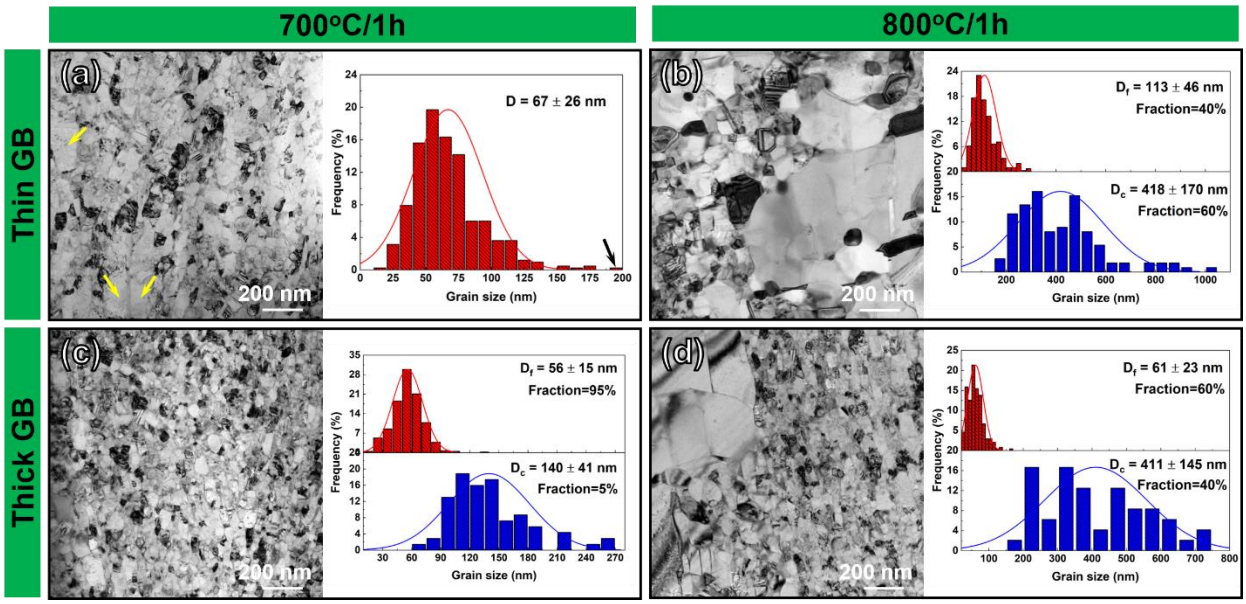

Figure 5.2 Microstructure evolution after annealing of NC Ni alloy with (a-b) thin and (c-d) thick GBs. (a) TEM micrograph and corresponding statistics showing an average grain size of 67 nm after annealing at 700 ^{o}C for 1h. (b) Annealing at 800 ^{o}C/1h led to abnormal grain growth, as indicated by the formation of coarse grains (with an average grain size, D_c, of 418 nm, and area fraction of 60%), and fine grains (with grain size D_f of 113 nm). (c) After annealing (700 ^{o}C/1h) of the specimen with thick GB, nanograins slightly coarsen to 56 nm, ~ 5% of grains grew abnormally to 140 nm in size. (d) After 800 ^{o}C annealing for 1h, the fine grains remain ~ 61 nm in grain size, whereas 40% of the grains coarsened to ~ 411 nm.

The corresponding EDS maps of the annealed samples are presented in Fig.5.3. For the specimens with thin GBs, annealing at 700 ^{o}C led to the Mo segregation to GBs, as shown in supplementary Fig.5.3a. This microstructure is somewhat similar to the microstructure of

specimen with thick GBs (Fig.5.1e). However, after annealing of NC Ni alloy (with thin GBs) at 800 ^{o}C (supplementary Fig.5.3b), Mo and Cr-rich precipitates with an average grain size of ~ 54 nm formed. No Mo-rich thick GBs were detected. In comparison, for the specimens with thick GBs, Mo-rich GBs sustained after annealing at 700 ^{o}C, and gradual dissolution of Mo from GBs was observed after annealing at 800 ^{o}C (as shown in Fig.5.3c-d), suggesting that the thick GBs are more stable than the thin ones.

It is worth mentioning that the formation of thick GBs is sensitive to the annealing conditions. For instance, the specimen with thick GBs derived from annealing of NC Ni alloys at 650 ^{o}C (for 5 h). Although annealing at 700^{o}C for 1 h can form similar microstructure, the Mo segregation to GBs is not as pronounced as the specimen annealed at 650 ^{o}C for 5 hours. Furthermore, STEM-EDS mapping results show that, after annealing at 600 ^{o}C, the major chemical elements were distributed uniformly without apparent Mo segregation.

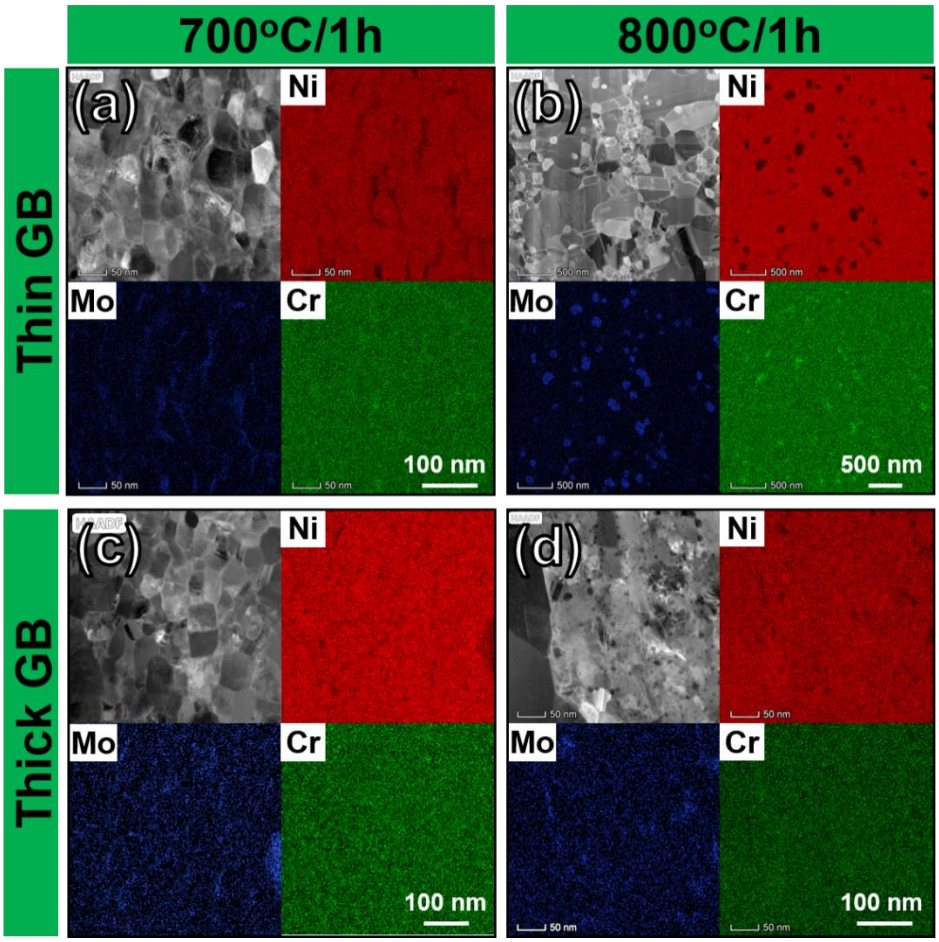

Figure 5.3 STEM micrographs and corresponding EDS maps of NC Ni alloys with (a, b) thin GBs and (c, d) Mo-rich thick GBs after annealing at 700 °C and 800 °C for 1h. (a) For the sample with thin GBs, Mo-enriched thick GBs were observed after 700 °C annealing. (b) After annealing at 800 °C, Mo and Cr-rich precipitates with an average diameter of ~ 54 nm formed. (c, d) For the sample with thick GBs, the Mo-enrich GBs sustained up to 800 °C.

Evolutions of average grain size and Vickers hardnesses of the annealed NC Ni alloys with thin and thick GBs at different annealing temperatures (for 1 h) are plotted in Fig.5.4. For the samples with abnormal grain growth, only the size of fine grains is plotted. The average grain size of the NC Ni alloy with thin GBs coarsened from 37 to 67 nm at 700 °C, and then rapidly increased to 113 nm at 800 °C. The corresponding hardness of annealed thin GB specimen increased first and reach a maximum value of 7.0 GPa at 700 °C, followed by drastic softening to 4.8 GPa at 800 °C. The strengthening of annealed sample at 700 °C is attributed to the formation of Mo-rich thick GBs (as shown in Fig.5.3a). Whereas the abnormal grain growth and rapid coarsening of fine grains (from 67 to 113 nm) at 800 °C lead to significant hardness drop. In contrast, the average

grain size of thick GB specimens coarsened slightly from 53 to 61 nm at 800 °C. Their corresponding hardness sustained at 7.0 GPa up to 800 °C. This comparison study suggests that the Mo-rich thick GBs play a crucial role on the thermal stability and retention of high strength in the annealed NC Ni alloys.

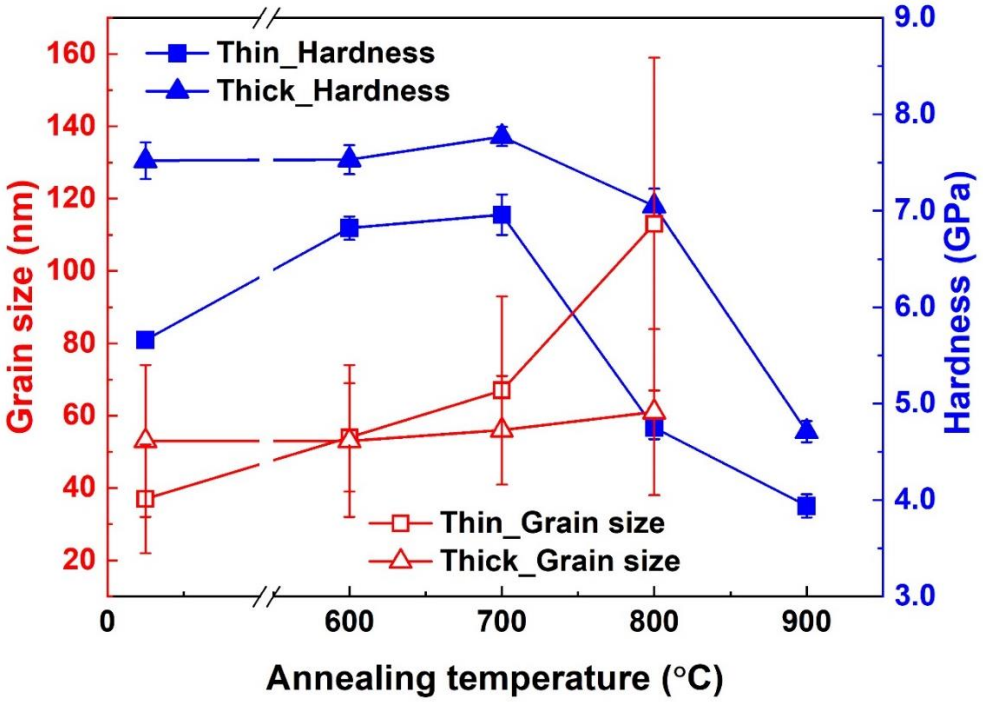

Figure 5.4 Variations of the average grain size and hardness of the NC Ni alloy with thin and thick GBs at various annealing temperatures. The hardness of sample with thin GBs decreased drastically from 7.0 to 4.8 GPa after annealing at 800 °C, whereas the hardness of the specimens with thick GBs sustained at 7 GPa up to 800 °C. After annealing at 800 °C for 1h, the grain size of the thin GB sample coarsened substantially from 37 to 113 nm, in contrast to the slight grain coarsening from 53 to 61 nm for the thick GB sample.

5.5 Discussion

To understand how Mo-rich thick GBs stabilized the nanograins at high temperature, detailed TEM and STEM studies were performed on the specimen annealed at 800 °C. Fig.5.5a shows the bright field TEM image of the specimen consisting of large and small grains. The corresponding STEM micrograph and EDS maps in Fig.5.5b-e reveal little Mo enrichment along the GB of the large grain. Whereas the GBs of nanograins appear to be enriched with Mo. EDS line scan results across the thin and thick GB (line ① and ② in the STEM image in Fig.5.5b) are

presented in Fig.5.6a and 6b, respectively. The major chemical elements distributed uniformly across the thin GB, while the enrichment of Mo and depletion of Ni across the thick GBs of nanograins sustained after annealing at 800 ^{o}C. Several Mo-rich thick GB debris were detected inside the abnormal large grains, as indicated by arrows in Fig.5.5b-d. As ~ 65% of the GBs have transformed to Mo-rich thick GBs after annealing at 650 ^{o}C /5 h (as shown in Fig.5.1f), we may conclude that the remaining thin GBs have migrated significantly during the abnormal grain growth and wrapped the stable Mo-rich thick GBs inside the coarse grains after annealing at 800 ^{o}C. HRTEM micrographs were taken at several locations (f, g and h) in Fig.5.5a along the GBs surrounding the large and fine grains. Fig.5.5f shows the formation of conventional straight and thin GBs between two large grains experiencing abnormal grain growth. However, in region g, the thick GB contains amorphous structure as shown by HRTEM micrograph in Fig.5.5g. In region h, crystalline intermetallics sustained within the thick GB as shown in Fig.5.5h. These thick GBs have blocked the coarsening of large grains during annealing, leading to the enhanced thermal stability at 800 ^{o}C compared with the sample with thin GBs.

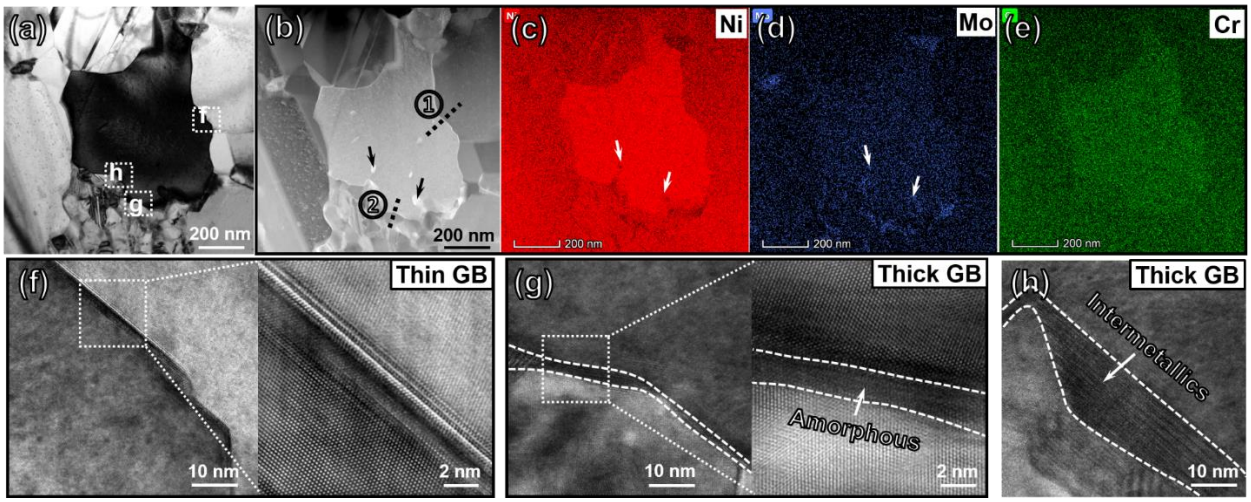

Figure 5.5 (a) TEM micrograph showing the coexistence of large and small grains in NC Ni alloy with thick GBs after annealing (800 ^{o}C/1h). (b-e) STEM image and the corresponding EDS maps reveal that there is no Mo enrichment along the GBs between large grains, whereas the GBs among nanograins appear to be enriched with Mo. Several Mo-enriched thick GB debris (as denoted by arrows) were observed in the interior of large grains. (f) HRTEM micrographs show a straight and thin GB formed during abnormal grain growth. (g and h) Thick GBs between large and small grains containing amorphous or crystalline intermetallic layers.

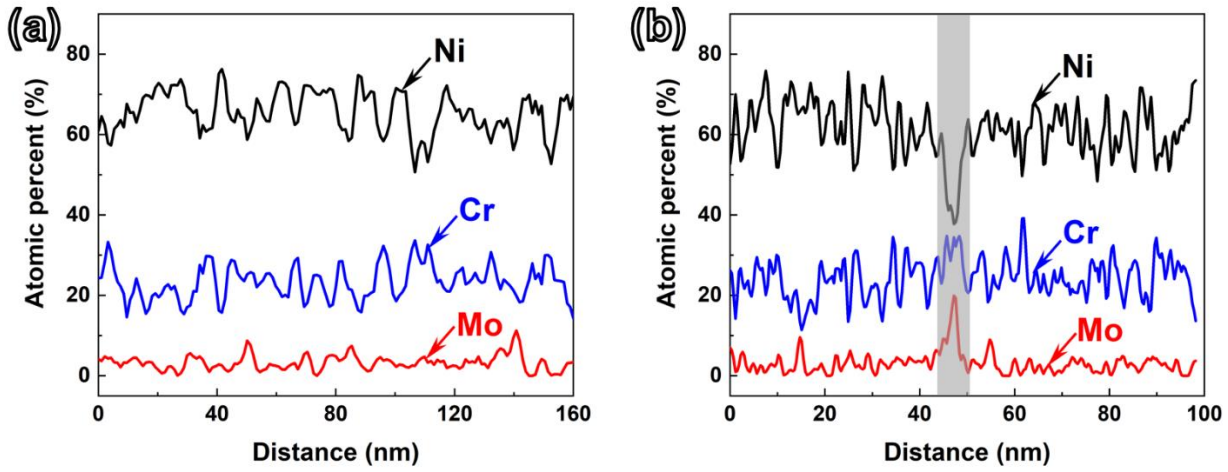

Figure 5.6 EDS line scanning results along the lines across (a) thin GB and (b) thick GBs in the STEM image in Fig.5.5b. The chemical elements distributed uniformly across the thin GB (line ①), while the enrichment of Mo and depletion of Ni of thick GB (line ②) sustained even after 800 °C annealing for 1h.

Foregoing discussions suggest that there are at least two basic strategies through which grain coarsening can be inhibited. The first one is the kinetic approach in which GBs are pinned by second phase drag, solute drag or chemical ordering, leading to a reduced GB mobility [147,150,173,337]. The other one is the thermodynamic way in which GB energy is reduced by solute segregation, decreasing the driving force for grain growth [147,149]. In this study, the outstanding thermal stability of NC Ni alloy with Mo-rich thick GBs derives from the prominent drag effects from the Mo solutes and the formation of crystalline intermetallic phase, as shown in Fig.1f and 1g.

From the thermodynamics point of view, the solute segregation to GBs affects the GB energy depending on the overall solute concentration (c_s) according to the Gibbs equation [147]:

$$\frac{\partial \gamma_b}{\partial ln c_s} = -RT\Gamma_s \qquad \text{Equation 5.2}$$

where γ_b is the specific interfacial energy, T is the temperature and Γ_s represents the interfacial excess of solute atoms. According to the Eq.2, the solute segregation ($\Gamma_s > 0$) results in the decrease of γ_b with increasing c_s. The Mo enrichment along GBs in this study decreases the GB energy and the subsequent driving force for grain coarsening. The combination of kinetic and thermodynamic stabilization effects of solute segregation have also been found in other alloys such as NC Pd with Zr addition [338,339]. In addition to the stabilization effect mentioned earlier, the disordered

amorphous structure in the thick GBs may serve as another stabilization route, similar to AlF stabilized NC Ni-W and Cu-Zr binary metals [149,152]. Hence, the combination of solute drag effect of Mo segregation, the second phase drag effect of intermetallic phase and thermally stable amorphous structure of the Mo-rich thick GBs may contribute to the improved thermal stability of NC Ni alloy.

5.6 Conclusion

In summary, a NC Ni alloy was fabricated by SMGT. The subsequent heat treatment at 650 ^{o}C introduced several nm thick Mo-rich GBs, consisting of disordered amorphous structures and crystalline intermetallic phase. Annealing studies of the NC Ni alloys show that the nanograins in the samples with thin GBs coarsened substantially from 37 to 113 nm and the hardness decreased prominently at 800 ^{o}C, whereas nanograins in the thick GB specimens grew slightly from 53 to 61 nm and the high hardness retained. TEM and chemical analyses show that the Mo-rich thick GBs are stable up to 800 ^{o}C. The solute segregation, second phase drag effect, and the thermally stable amorphous layer at the thick GBs lead to the improved thermal stability of the NC Ni alloy compared with the sample with conventional thin GBs.

CHAPTER 6. CHARACTERIZATION OF PRECIPITATION IN GRADIENT INCONEL 718 SUPERALLOY

The gradient structured nickel-based alloy was fabricated by Jie Ding and Zhongxia Shang. Microstructure characterization of precipitates was performed by Jie Ding, with grateful help from Dr. Sichuang Xue. The data analysis and writing were completed by Jie Ding with guidance and editing by Dr. Xinghang Zhang.

6.1 Overview

Inconel 718 (IN718) superalloy is a well-established material for the application of aircraft engine and power generator due to its excellent performance at high temperatures. The outstanding high temperature properties of IN718 is largely determined by the precipitates. Here, we studied the precipitation behaviors and the corresponding mechanical properties of the heat-treated gradient IN718 alloy. The microscopy studies reveal that high-density hexagonal η phase with chemistry of Ni3(Al,Ti,Nb) formed in the nanograins. The compressive stress introduced during severe plastic deformation may have prohibited the formation of γ" phase while accelerated the precipitation of γ' phase, consequently favoring the precipitation of η phase. The corresponding evolution of mechanical behavior of gradient Ni alloys is investigated.

6.2 Introduction

Nickel-based superalloys are widely used in aerospace industry due to their extraordinary high temperature yield strength, creep and corrosion resistance [164–176]. Inconel 718 (IN718) is a common precipitation strengthened Ni-based superalloy for application in high-pressure turbine discs in jet engines [167,177,178,185–190]. The high temperature performance of IN718 are primarily determined by the quantity and characteristics of intermetallic phases [161,179–184,191,192]. It has been found that the major intermetallic precipitates in face-centered-cubic (fcc) IN718 matrix are mostly: (i) the body-centered tetragonal (bct) structured ($D0_{22}$) γ"- Ni_3Nb phase, (ii) the fcc structured ($L1_2$) γ'-Ni_3(Al,Ti) phase and (iii) the orthorhombic structured ($D0_a$) δ-Ni_3Nb phase [162,191,197–203]. Prior studies on the precipitation of γ' and γ" phase reveal that

the volume fraction and sequence of precipitation of these two phases are controlled by the relatively concentration of Al, Ti and Nb of the alloy [161,162]. The precipitation of γ' precedes γ" when the ratio of Al+Ti/Nb greater than 0.8 and when the ratio is between 0.9 and 1.0, a compact morphology develops where a γ" shell formed on all six faces of cuboidal shape of γ' phase [195]. The precipitation of γ" and γ' phase usually takes place at relatively low temperatures (600 – 900 ^{o}C) [179,340]. The equilibrium δ phase, however, precipitates directly from γ matrix at temperature above 900 ^{o}C. At temperatures below 900 ^{o}C, the metastable γ" phase transforms to stable δ phase over long-term exposure [161,179,204,341]. The coherent γ" is the primary phase for precipitation strengthening, and the coherent γ' is less effective in strengthening [161,216,342]. Hence, the transformation of γ" → δ is detrimental to the strength of IN718 at high temperature [179,204]. However, moderate fraction of δ phase has been demonstrated to benefit the impact toughness [343]. The precipitation of δ phase at grain boundaries can inhibit the grain boundaries sliding and thereby improve creep resistance at high temperature [210]. It has also been proven that the presence of δ phase during hot working can avoid undesirable grain coarsening [189].

The precipitation behavior of IN718 can be influenced by its initial microstructure, such as grain size and dislocation density [161,181,187,344,345]. Singh et al. [346] found that the slip bands formed during cold rolling might serve as the nucleation sites for δ phase, consequently accelerating the precipitation of δ phase below 900 ^{o}C. The amount of γ" precipitates (having identical composition to δ phase) was therefore reduced. Li et al. [344] and Liu et al. [204] studied the effect of cold rolling on the precipitation behavior of IN718 and concluded that cold rolling not only accelerates the γ" → δ transformation, but also the precipitation of γ" phase. Liu et al. [204] also found that the nose of precipitation-time-temperature (PTT) curves of δ precipitation are located at ~910 ^{o}C. Mei et al. [181] reported that the onset, peak and finishing temperature of γ" precipitation decrease with the increasing of cold rolling strain. In contrary, the corresponding temperatures of δ precipitation increase first and then decrease with cold rolling. However, both the strain and strain rate of cold rolling of IN718 in previous studies were relatively low. The precipitation behavior and corresponding mechanical properties of IN718 subjected to severe plastic deformation remain less well understood.

Surface mechanical grinding treatment (SMGT) has been proven to be an effective severe plastic deformation technique to refine the microstructure of metallic materials in addition to equal channel angular pressing (ECAP) [25,39,228] and high pressure torsion (HPT) [22]. Furthermore,

SMGT can induce gradient microstructure where the grain size of processed metallic materials varying from microns to tens of nanometers. In the present work, we investigated the precipitation behaviors and the corresponding mechanical properties of a gradient IN718 that was fabricated by SMGT. Transmission electron microscopy (TEM) studies coupled with ASTAR crystal orientation mapping and EDS chemical analyses reveal the formation of unusual η phase. The hardness of the gradient alloy after heat treatment was investigated and the correlation between precipitation and mechanical behavior is discussed.

6.3 Experimental methods

6.3.1 Materials and processing

The chemical composition (both in weight and atomic percent) of the IN718 superalloy is given in Table 6.1. Cylinder bars with diameter of 10 mm were fabricated using electrical discharge machining (EDM) technique. Prior to processing, the bar was solution treated at 1,100 ^{o}C for 1 hour followed by quenching in water (denoted as as-received sample hereafter). During SMGT processing, the IN718 bar rotated at a velocity of 400 rpm, while a WC/Co tool tip penetrated into sample surface by 30 μm and slid along axial direction at a speed of 10 mm/min. The process was repeated 8 times to generate subsequent deformation zone underneath the surface. Coolling oil was used for temperature control during processing. Subsequently, the processed samples were annealed in vacuum furnace at 700 ^{o}C for 5 h followed by furnace cooling. Annealing was conducted when the vacuum level reaches 2×10^{-6} torr.

Table 6.1 Chemical composition of IN718 superalloy

	Cr	Fe	Co	Nb	Mo	Al	Ti	Ta	Ni
Wt.%	18.57	18.00	0.11	5.02	2.86	0.58	0.97	<0.01	58.7
At.%	20.70	18.70	0.11	3.13	1.73	1.24	1.17	<0.01	53.22

6.3.2 Characterization

The samples used for metallographic studies were ground and polished using conventional metallographic preparation technique. The metallographic studies were then carried out using optical microscope and FEI Quanta 650 FEG scanning electron microscope operated at 20 kV. The microstructure and chemical composition analyses of the as-processed and annealed samples were performed on an FEI Talos 200X analytical transmission electron microscope operated at 200 kV, equipped with a supper X energy-dispersive X-ray spectroscopy (EDS) detector. High resolution scanning transmission electron microscopy (STEM) images for detailed precipitates characterization were obtained from the ThermoFisher Themis Z TEM operated at 300 kV. The grain orientation analysis of TEM samples were performed using the NanoMegas ASTAR (to generate EBSD like automatic crystal orientation map with 4-5 nm spacial resolution) setup installed in the FEI Talos 200X transmission electron microscope. The post data analyses were conducted by OIM Analysis software. The transmission electron microscopy (TEM) specimens were prepared by focused ion beam (FIB) technique using an FEI Quanta 3D FEG scanning electron microscope following typical protocols. The hardness tests were conducted using a LECO LM247 microhardness tester with a Vickers indenter tip. The maximum applied load was 25g, with a holding time of 13 s.

6.4 Results

6.4.1 Overview of microstructure and hardness

The optical microscopy (OM) image in Fig.6.1a shows the equiaxed grain structure of the as-received IN718 with an average grain size of ~ 150 μm after annealing at 1100 ^{o}C for 1 hour. After SMGT, a severely deformed gradient structures were introduced, as revealed by the scanning electron microscopy (SEM) image in Fig.6.1b. The gradient structure can be divided into 2 layers based on their distinct microstructures. The outermost surface layer, ~ 30 μm in thickness, has nanograined (NG) structures, as verified by the TEM observation in following section and is referred to as NG layer hereafter. The microstructure of the adjacent subsurface layer is dominated by deformation twins (DT) as identified by TEM observation, and hence is denoted as DT layer hereafter. After annealing at 700 ^{o}C for 5 hours, high-density of precipitates formed at the top ~

70 μm of the processed specimen, as verified by the SEM image in Fig.6.1c. The microstructures of the deeper region of gradient structure and undeformed matrix area doesn't change after annealing from metallographic observations.

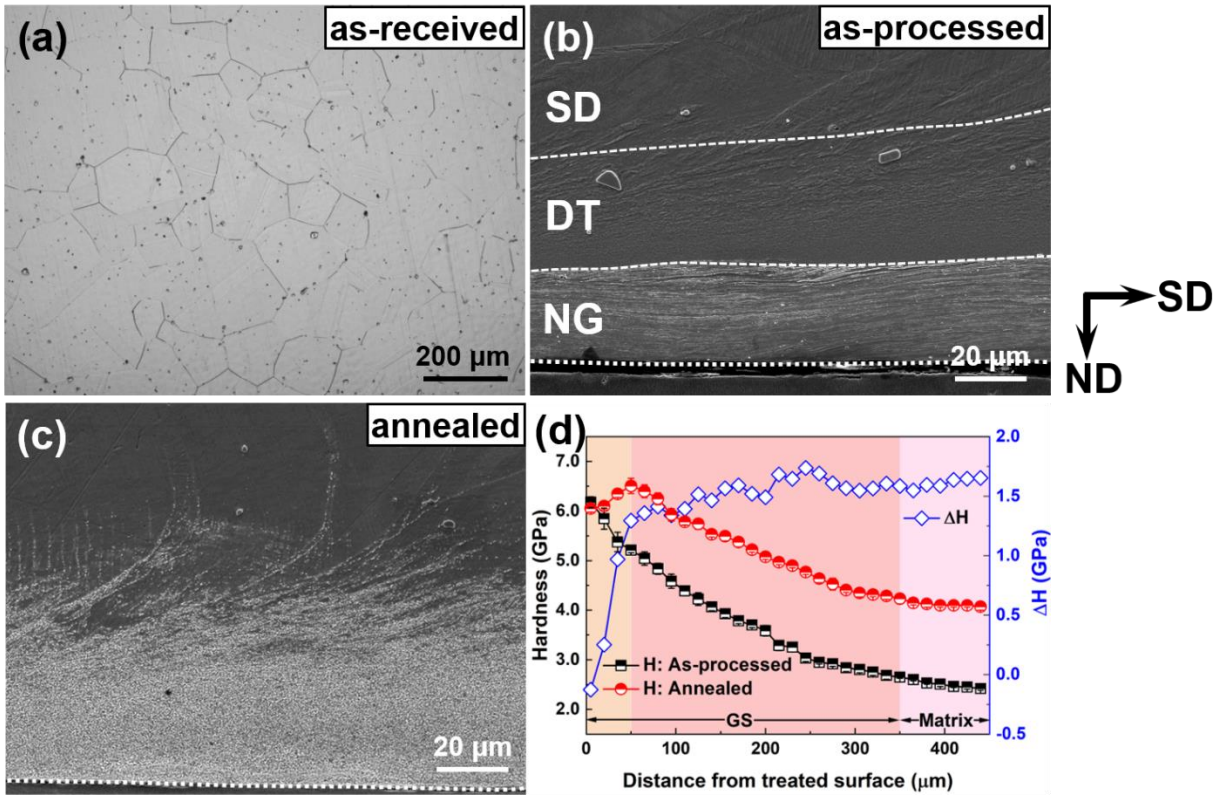

Figure 6.1 (a) OM image showing the equiaxed grains of the as-received IN718 superalloy with an average grain size of ~ 150 μm. (b) SEM image of the processed sample showing the gradient structure consisting of surface nanograined (NG) layer, deformation twined (DT) layer and severely deformed (SD) layer (c) SEM image showing the formation of high-density precipitates in both NG and top part of DT layer after annealing at 700 ^{o}C for 5 h. (d) Variation of average Vickers hardnesses of both as-processed and annealed samples, and the corresponding hardness differences along the depth direction. (SD: shear direction, ND: normal direction)

The corresponding hardness profile along the depth direction in Fig.6.1d reveals that the hardness of the as-processed specimen decreased gradually from ~ 6.2 GPa in the top NG layer to ~ 2.4 GPa in the undeformed matrix region. The penetration depth of the deformed region with gradient structure is ~ 350 μm. After annealing, the hardness of the annealed sample increased through nearly the entire region except the outermost region. The maximum hardness appears at the depth of ~ 50 μm from treated surface. The corresponding hardness differences between the

as-processed and annealed samples (open blue diamond) in Fig.6.1d show that the magnitude of strengthening reaches ~ 1.5 GPa in the matrix, and decreases gradually to ~ 1.25 GPa with decreasing distance to 50 μm from the treated surface. Strengthening decreases sharply thereafter to slightly negative values adjacent to the treated surface.

6.4.2 TEM study of the as-processed sample

The microstructures of the as-processed specimen were examined in detail by TEM. We begin by examining the region containing boundary between SD and DT layer at a depth of ~ 50 μm from the surface. The cross-section TEM image in Fig.2a shows the twin boundaries (TBs) dominated microstructures in the DT layer. The average twin spacing is measured to be ~ 90 nm. Shear band (SB) structures characterized by fine grains are also observed. The formation of SB structures is derived from the inhomogeneous deformation during SMGT. The high resolution TEM (HRTEM) image and the inserted fast Fourier Transform (FFT) pattern in Fig.2b also verify the formation of DTs. The microstructures of SD layer are dominated by large grains characterized by dislocation cells (as labeled by arrows in Fig.2a). The ASTAR reverse pole figure image of the SB/DT interface region (box c in Fig.2a) in Fig.2c reveals the formation of finer grains in the SB region. The corresponding grain boundary map shows that the majority of grain boundaries in SB region are HAGBs (denoted by black lines). Whereas TBs (denoted by yellow lines) dominated in the DT region. The proportion of LAGBs (denoted by blue lines) is low in both regions. Similar ASTAR orientation analyses were performed in the DT/SD interface region (box d in Fig.2a), as shown in Fig. 2d. The reverse pole figure image on the left shows severely distorted large grains in the SD region. The corresponding grain boundary map on the right confirms that the dislocation cell structures in the SD region doesn't transform to LAGBs after SMGT.

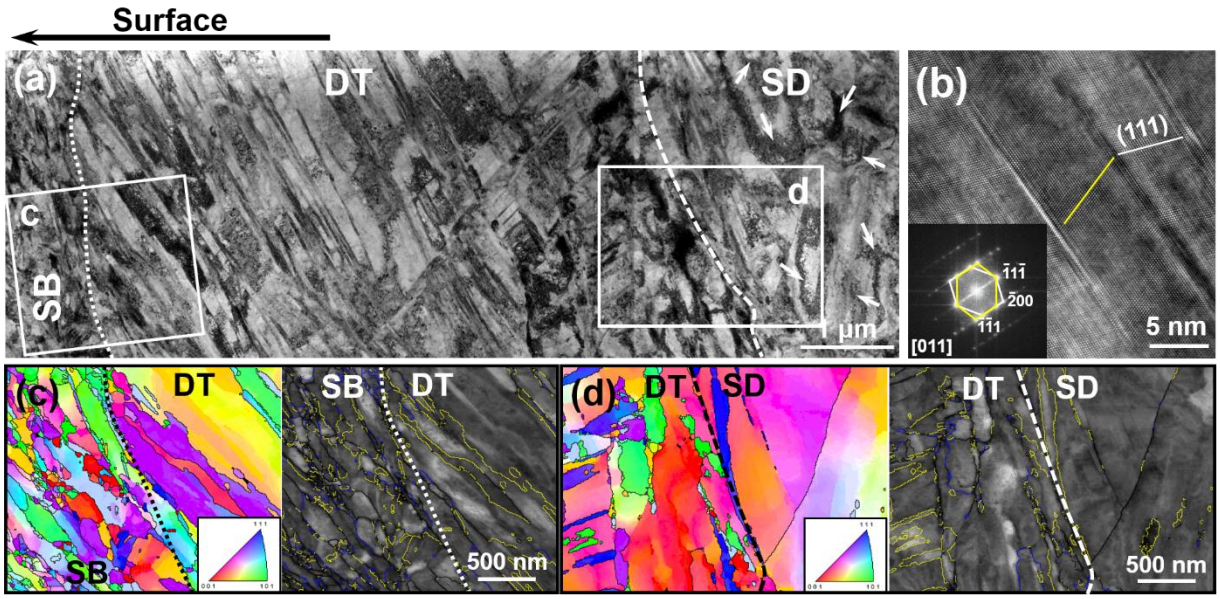

Figure 6.2 (a) TEM image of the microstructure of DT/SD interface region. (b) HRTEM image and corresponding FFT pattern showing the typical TBs in the DT region. (c) ASTAR crystal orientation analysis of the box c in (a) showing the nanograins formed in the SB region and the twin structures in the DT region. (d) ASTAR crystal orientation analysis of the box d in (a) showing the severely deformed coarse grains in the SD region. (Black, yellow and blue lines represent high angle, twin and low angle grain boundaries, respectively)

TEM image in Fig.3a shows that NG layer in the region of ~ 5 μm from the treated surface is consisted of nanograins, with an average grain size of ~ 45 nm (as shown in Fig.3b). The inserted selected-area diffraction (SAD) pattern also indicates the formation of nanograins. The corresponding ASTAR orientation maps in Fig.3c show that majority of grain boundaries are HAGBs, the proportion of LAGBs and TBs is low.

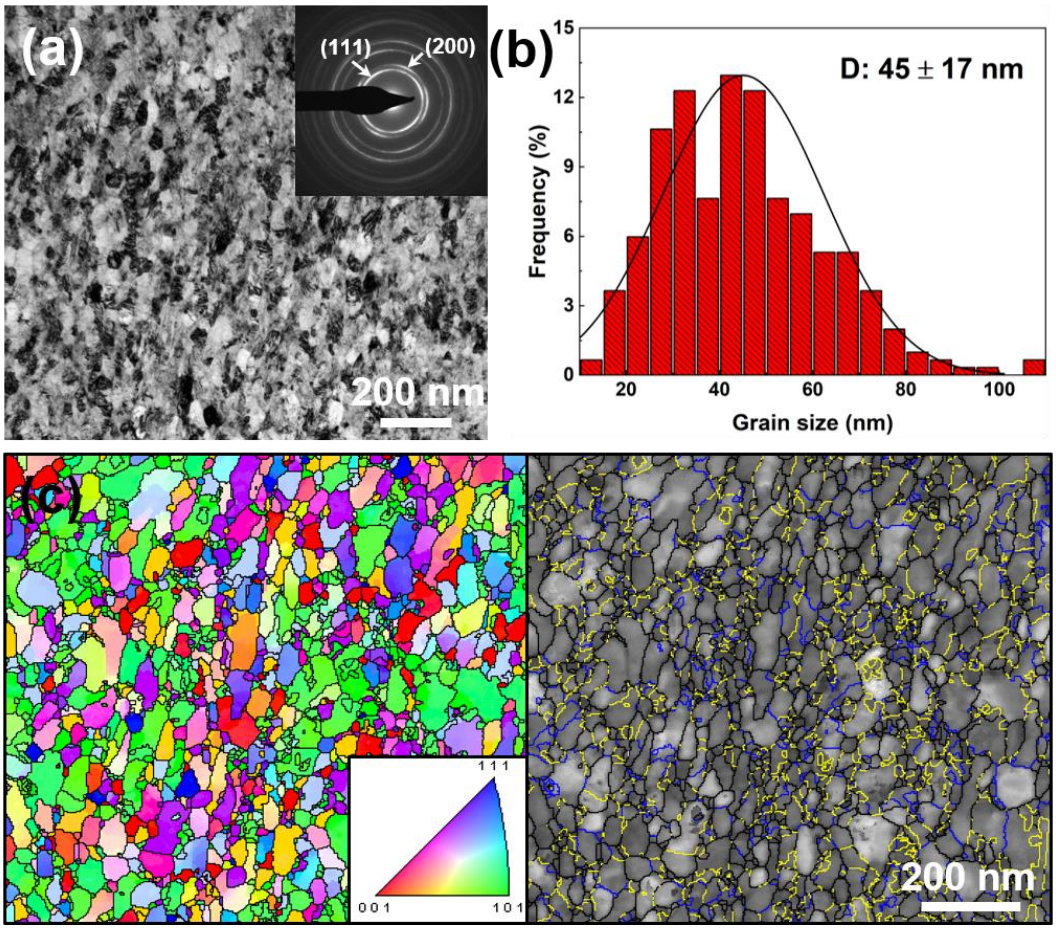

Figure 6.3 (a) Bright-field TEM image and SAD pattern of the NG layer of processed sample showing nanograined structure. (b) The statistic of the grain size distribution showing an average grain size of ~ 45 nm. (c) ASTAR crystal orientation analysis of the NG region.

6.4.3 TEM study of the annealed sample

After annealing at 700 ^{o}C for 5 h, precipitation phenomenon occurred in both matrix region and severely deformed gradient layer. However, the types of precipitates formed vary in different regions, as verified by the TEM studies shown in the following section.

In the undeformed matrix region, high-density precipitates with size of several nanometers are observed, as shown in the Fig. 6.4a. The SAD pattern taken from the [100] zone axis of matrix in Fig.6.4b exhibits superlattice reflections for both γ’ and γ” phases, conforming the presence of these two types of strengthening precipitates in IN718.

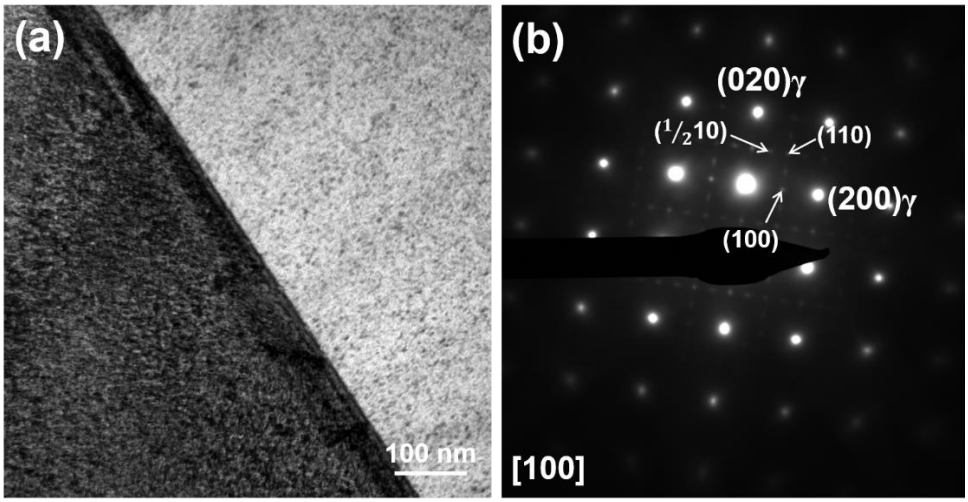

Figure 6.4 (a) TEM image of the matrix area after annealing showing the formation of high-density precipitates. (b) Diffraction pattern taken from [100] zone axis of γ matrix. The extra reflections conform the presence of both γ' and γ" precipitates.

Microstructures at depth of ~ 50 μm (Fig.6.5a) shows that recrystallization took place in the DT region after 700 ^{o}C annealing for 5 h. The DT and SB structures transformed to equiaxed nanograins with average grain size of ~ 135 nm (Fig.6.5b). It's interesting to note that the dislocation cell structures of the adjacent SD region sustained after annealing. Needle-like and spherical precipitates are observed in this region. The STEM image and corresponding EDS maps of the box c in the recrystallized area in Fig.6.5a are presented in Fig.6.5c. It reveals that the needle-like precipitates are enriched with Ni, Nb, Al, Ti and depleted with Cr, whereas the spherical precipitates are enriched with Cr. The precipitation only took place at the recrystallized region. No large precipitates were observed in the SD region with dislocation cells, as verified by the STEM and corresponding EDS maps in Fig.6.5d.

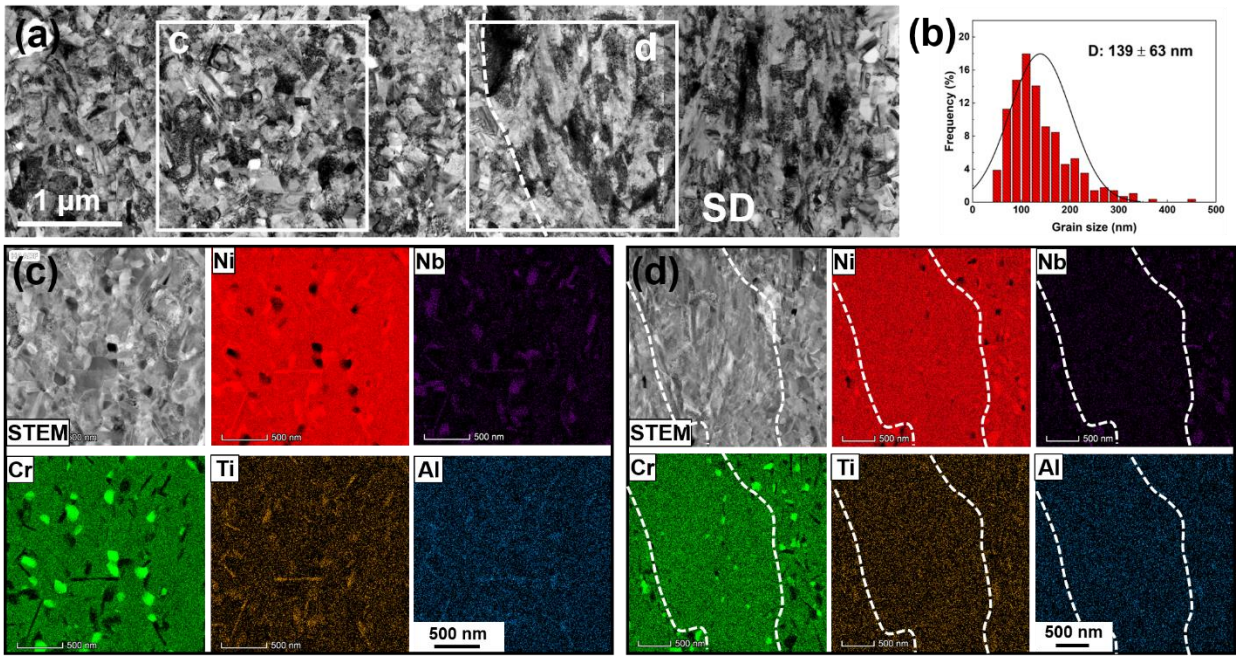

Figure 6.5 (a) TEM image of the microstructure of the DT/SD interface region after annealing at 700 ^{o}C for 5h. Recrystallization and precipitation have taken place in the DT and SB region, whereas the dislocation cell structures of SD region (as denoted by dash lines) sustained after annealing. (b) The statistic of grain size distribution shows that the average grain size of grains after recrystallization is ~ 139 nm. (c) The STEM image and corresponding EDS maps of the area c in (a) showing the enrichment of Ni, Nb, Ti, Al and depletion of Cr of the needle-like precipitates, and the Cr-enriched spherical precipitates in the DT region. (d) The STEM image and corresponding EDS maps of the area d in (a) showing the absence of needle-like precipitates in the SD large grain region.

Recrystallization and precipitation also took place in the top NG layer. The TEM image in Fig.6.6a reveals the grain coarsening of the NG region (~ 5 μm away from treated surface). The average grain size of the large grains is ~ 148 nm, as shown in Fig.6.6b. Around 40% of nanograins with average size of ~ 47 nm sustained after annealing. A detailed TEM observation in Fig.6.6c reveals the formation of high-density of needle-like precipitates, as denoted by arrows. The corresponding STEM and EDS maps in Fig.6.6d show that the chemical composition of the needle-like precipitates is similar to that was observed in the DT layer. The difference between these two regions is that the proportion of Cr-rich spherical precipitates in the NG layer is much lower than that in the DT layer.

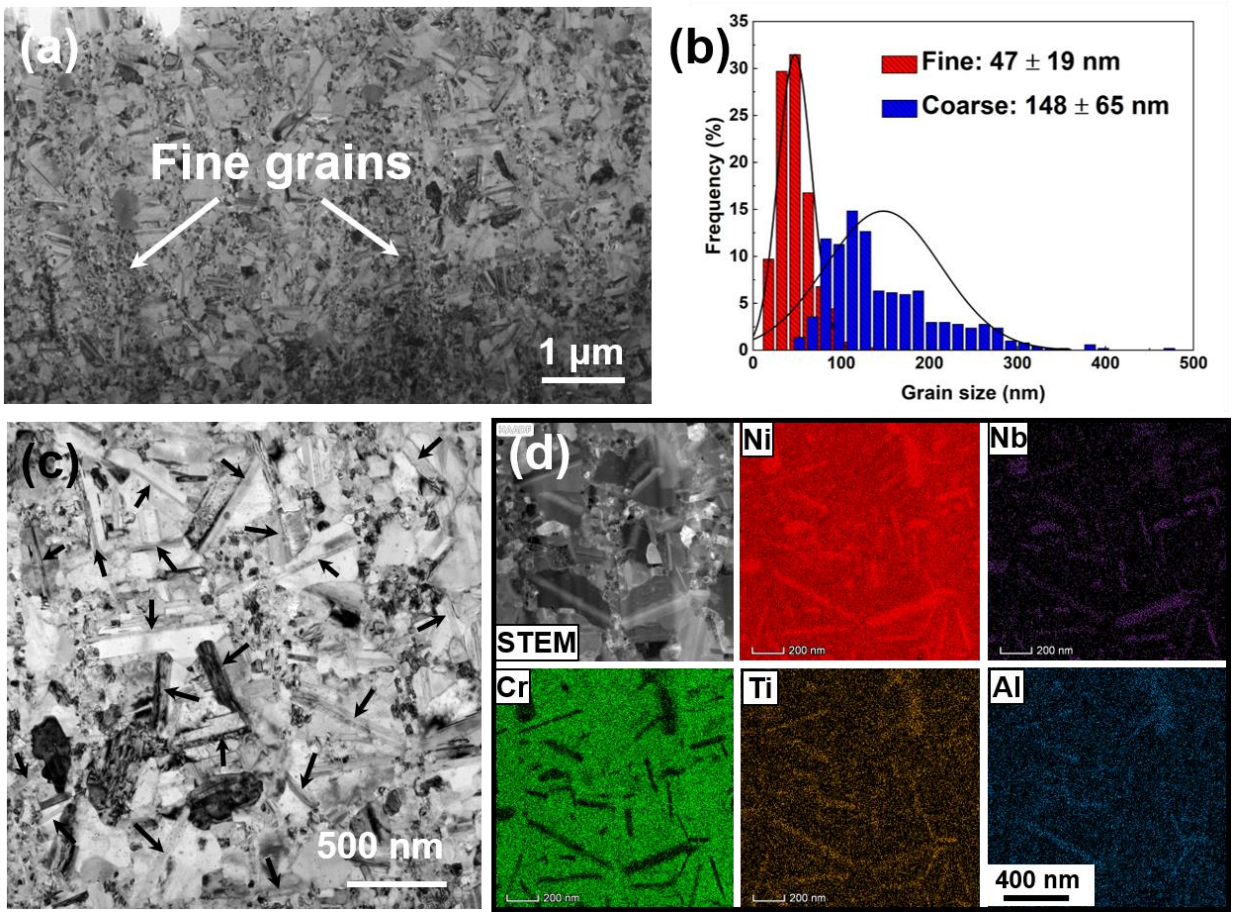

Figure 6.6 (a) TEM image of the microstructure of NG layer after annealing at 700 ^{o}C for 5 hours. (b) The statistic of grain size distribution shows that the average grain size of nanograins is ~ 47 nm, similar to that before annealing (45 nm), whereas that of the recrystallized grains increases to ~ 148 nm after annealing. (c) Detailed TEM image showing the precipitation of needle-like precipitates (as indicated by arrows) and the sustained nanograins. (d) The STEM image and corresponding EDS maps showing the enrichment of Ni, Nb, Ti, Al and depletion of Cr of the needle-like precipitates.

6.5 Discussion

6.5.1 Characterization of precipitates

The precipitation behavior of IN718 has been intensively studied [161,183,204]. Three different kinds of ordered intermetallic precipitates can be distinguished [198,199]: γ' [Ni3(Al,Ti)], γ" (Ni3Nb), and δ [Ni3Nb] phases. After annealing at 700 ^{o}C for 5 h, high-density γ' and γ" precipitates formed in the undeformed matrix region, as verified by the SAD pattern of Fig.6.4b. In Fig.6.4b, the <100> type superlattice reflections are arise from γ' precipitates, and the <110>

type reflections could arise both from γ' and γ" precipitates. The fractional indexes, <1/2 10> type reflections belong only to γ" precipitates [202]. While in other works, both <100> and <110> type reflections are believed to arise from both γ' and γ" precipitates, and the <1/2 10> type reflections can only be associated with γ" precipitates [347]. Both indexing results confirm the simultaneous precipitation of γ' and γ" phases in this alloy. Prior studies have concluded that γ" phase constitutes the major strengthening precipitates with a volume fraction of about three times of that of γ' phase for IN718 [162,342,348].

Upon annealing, the metastable γ" precipitates will transform to the equilibrium δ precipitates with temperature increasing or annealing time prolonging [199,201]. According to previous studies, this transformation process can be promoted by cold rolling [181,187]. The metallographic observation in Fig.6.1c and TEM observations in Fig.6.5 and Fig.6.6 also reveal the formation of different types of precipitates in the severely deformed top surface layer and the undeformed matrix region. The detailed identification of these δ-like precipitates was performed using TEM.

TEM image in Fig.6.7a shows that high-density δ-like precipitates with different aspect ratios formed in the NG layer after annealing. Previous studies concluded that the δ phase precipitation occurs at grain boundaries first, then in the interior of grains over long-term exposure [187,205]. In this study, the δ-like precipitates in Fig.6.7a stretch far into, even across, some grains due to the fine grain size. The SAD pattern obtained from the δ-like precipitate #1 with zone axis parallel to the $[011]_\gamma$ is presented in Fig.6.7b. It verifies the precipitation of δ phases with a $D0_a$ orthorhombic crystal structure [202]. However, the SAD pattern taken from the δ-like precipitate #2 with zone axis parallel to the $[011]_\gamma$ (Fig.6.7c) reveals the precipitation of different phase. These patterns are inconsistent with that of δ phases, but closely match the η phases with a $D0_{24}$ hexagonal crystal structure [205,207].

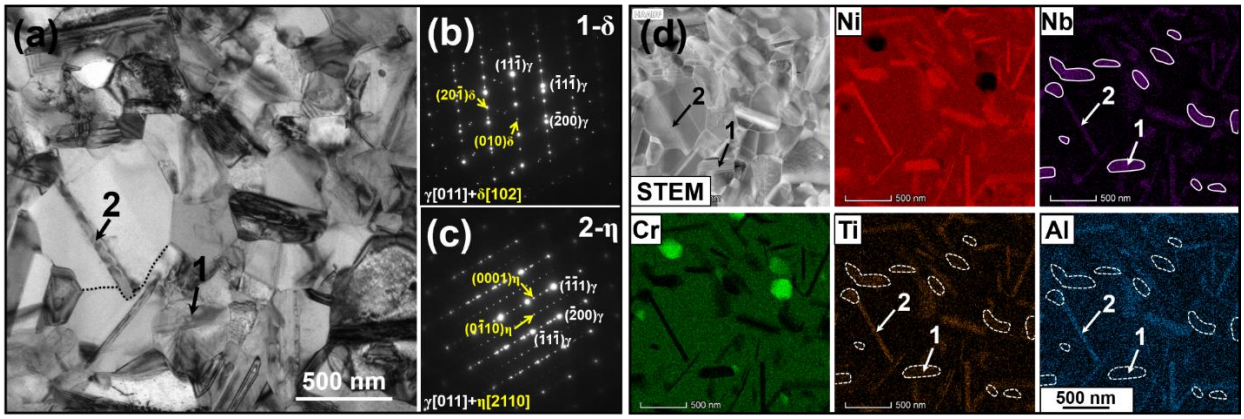

Figure 6.7 (a) TEM image and (b-c) corresponding SAD patterns of the precipitates 1 and 2 revealing the simultaneous precipitation of δ and η phases. (d) STEM and corresponding EDS maps showing the chemical differences between δ and η phases. It shows that the δ phase with smaller aspect ratio (as labeled by white circles) exhibits more Nb enrichment than the η phase with larger aspect ratio, while the Al and Ti concentration of η phase is higher than that of δ phase.

The STEM image and corresponding EDS maps of the precipitates in Fig.6.7d. It reveal that the Ni, Nb, Al, Ti are partitioned in the precipitates, supporting the common knowledge that the δ-like precipitates grow at the expense of strengthening phases (γ' and γ") [204]. The chemical composition differences between these two kinds of precipitates reveal that the δ phase with smaller aspect ratio (as labeled by white circles) exhibits more Nb enrichment than the η phase with larger aspect ratio, whereas the Al and Ti concentration of η phase is higher than that of δ phase. Similar Nb- and Al-rich η-Ni_6NbAl hexagonal phases have been previously reported in Allvac 718Plus superalloy [205,207]. The Cr-rich spherical particles are believed to be α-Cr phase that is always precipitates in the vicinity of δ phase as δ phase was reported to rejects Cr into the γ matrix during growth [349]. Cr was reported to have limited solubility (average about 3-4 at.%) in δ phase [208]. Quantitative chemical composition of these two precipitates are measured using TEM EDX, and presented in Table 6.2. It confirms the higher concentration of Al, Ti and Cr of η phase than δ phase, whereas the concentration of Nb of δ phase is almost twice of that of η phase. The chemistry of the η phase of this study is therefore close to Ni_3(Al,Ti,Nb) considering the almost equivalent amount of Al, Ti and Nb elements. It is worth mentioning that the transmission electron beam of TEM EDX appears to underestimate the composition enrichment of the precipitates embedded in the γ matrix, leading to an inaccurate quantitative measurement. For

instance, the measured high content of Cr and Fe of these precipitates in Table 6.2 are attributed to the high Cr and Fe content of γ matrix.

Table 6.2 Chemical composition (At.%) of the η and δ phases.

Phase	Al	Co	Cr	Fe	Mo	Nb	Ni	Ti
η	5.1±1.6	2.0±1.5	6.4±3.6	3.5±3.4	0.8±0.6	5.8±2.6	69.8±4.5	6.6±2.5
δ	2.5±0.7	2.1±0.5	3.3±1.0	3.0±1.0	1.4±0.6	9.2±1.4	73.3±3.5	3.1±1.0

Detailed crystal structure analyses of both types of precipitates were performed using high resolution TEM (HRTEM) images. Fig.6.8a is the HRTEM image of δ precipitate. The FFT patterns of δ precipitate and γ matrix are presented as well. The HRTEM micrograph of the box b in Fig.6.8a is shown in Fig.6.8b, where the lattice orientation of both δ and γ phases are labeled. It reveals that the orientation relationship between the δ phase and γ matrix is:

$\{111\}_\gamma||\{010\}_\delta$, and $\langle 110\rangle_\gamma||\langle 100\rangle_\delta$,

consistent with the previous characterization results of IN718 reported by Sundararaman et al. [162], and of Fe-Ni-Cr-Nb system by Kirman [350]. The orthorhombic structure of δ phase comprises of near-hexagonal stacking layers along the b-direction with an ABAB-type stacking sequence perpendicular to the habit $(111)_\gamma$ plane, as labeled in Fig.6.8b.

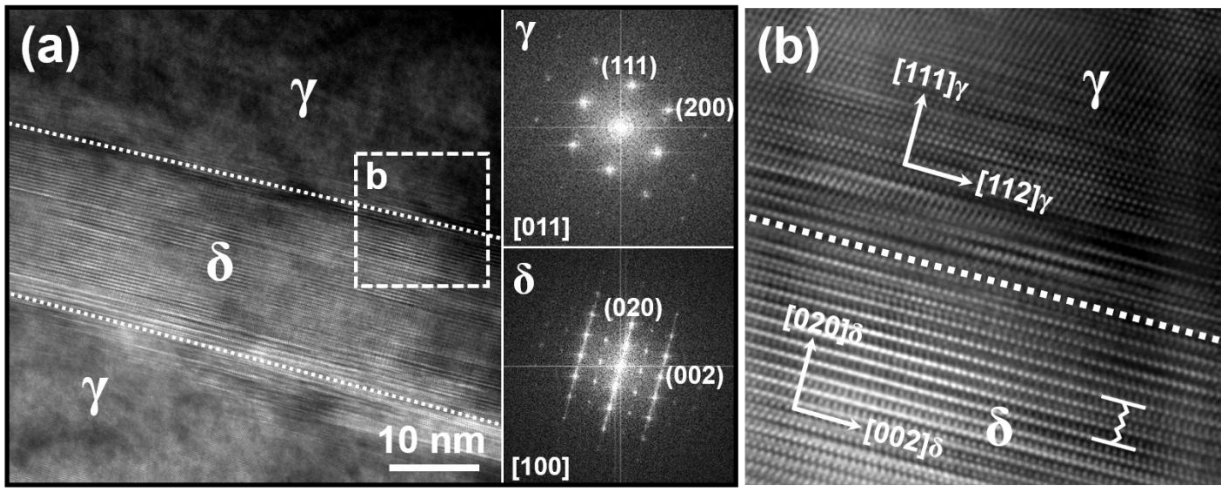

Figure 6.8 (a) HRTEM image and corresponding FFT patterns showing the crystal orientation relationship between γ matrix and δ phase. (b) The atomic-scale HRTEM image of the box b in (a) showing interface between γ and δ follows the orientation relationship as follow: $\{111\}_\gamma$ $||\{010\}_\delta$; $\langle 110\rangle_\gamma$ $||\langle 100\rangle_\delta$; The ABAB-type stacking sequence of δ phase is labeled.

Similar analyses were performed for η phase, as shown in Fig.6.9. It shows that the η phase precipitates from a random grain boundary, rather than from the adjacent twin boundary. The corresponding FFT patterns also confirm the twin structure and the formation of η phase. Pickering et al. [205] found that twin boundaries are resistant to precipitates formation in Allvac 718Plus superalloy. The corresponding HRTEM micrograph of the box b in Fig.6.9a is shown in Fig.6.9b. It reveals that the η phase and γ matrix is related through the Blackburn orientation relationship as follows [207]:

$\{\bar{1}\bar{1}1\}_\gamma||\{0001\}_\eta$, and $\langle 011\rangle_\gamma||\langle 2110\rangle_\eta$, $\langle 112\rangle_\gamma||\langle 0\bar{1}10\rangle_\eta$.

Same orientation relationship between γ and η phase has been reported before [205,207]. The ABAC-type stacking sequence of the η phase with hexagonal structure normal to the $(111)_\gamma$ habit plane is labeled in Fig.6.9b. Despite the difference in chemical composition, the structure of η and δ phases is similar to one another, and the only difference is the presence of a C-layer in η phase instead of B. Hence, a fully coherent interface between the close packed planes of these two phases are expected to form [207].

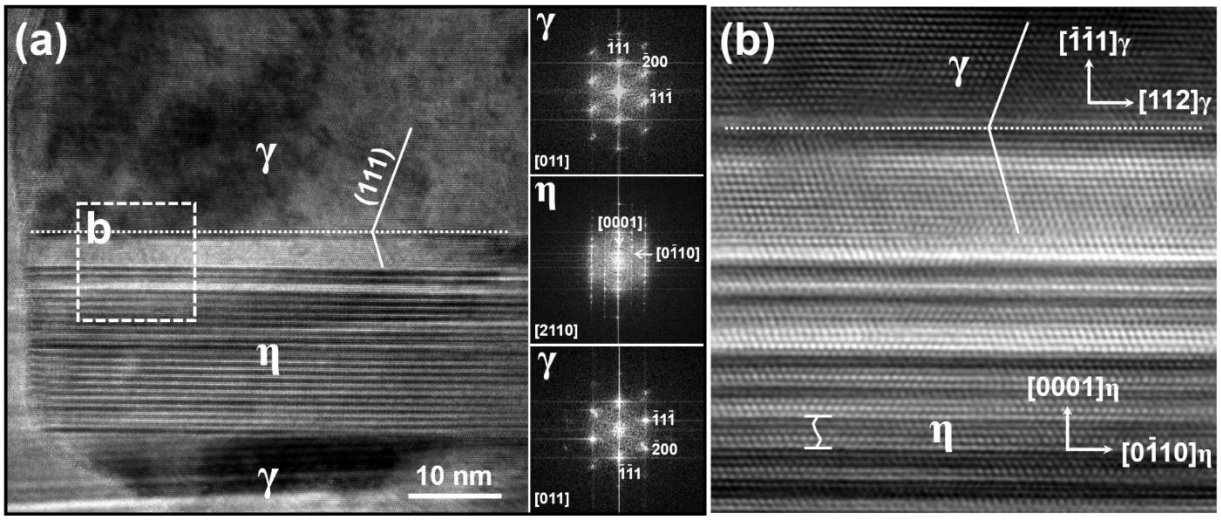

Figure 6.9 (a) HRTEM image and corresponding FFT patterns showing the crystal orientation relationship between γ matrix and η phase. (b) The atomic-scale HRTEM image of the box b in (a) showing interface between γ and η follows the orientation relationship as follow: $\{\bar{1}\bar{1}1\}_\gamma||\{0001\}_\eta$; $\langle 110\rangle_\gamma||\langle 2110\rangle_\eta$; $\langle 112\rangle_\gamma||\langle 0\bar{1}10\rangle_\eta$. The ABAC-type stacking sequence of η phase is labeled.

The quantitative statistic studies of precipitates (δ, η and α-Cr phase) in both DT and NG layer were conducted by distinguishing their chemical composition difference, and listed in Table

6.3. It shows that the size of precipitates in NG region is larger than that in the DT region, same as for the area fraction of η and δ phases. Whereas the area fraction of α-Cr phase in the NG region is slightly lower than that in the DT region. The overall area fraction of precipitates in the NG region (12.12%) is also higher than that in the DT region (10.84%), which is believed to be attributed to the higher density of grain boundaries in the surface NG region since precipitation preferably takes place in the grain boundary first [167,200,201]. The precipitation of different phases and their evolution in various regions of gradient layer will be discussed in the following two sections.

Table 6.3 Size evolution of precipitates in the NG (5 μm depth) and DT (50 μm depth) region after annealing at 700 °C for 5 hours.

	η Phase				δ Phase				α-Cr	
Region	Length (nm)	Width (nm)	Aspect ratio	Area fraction	Length (nm)	Width (nm)	Aspect ratio	Area fraction	Diameter (nm)	Area fraction
NG	317±129	32±11	10.0	4.44%	255±111	40±21	6.4	5.75%	130±76	1.93%
DT	247±104	28±11	8.8	2.33%	161±60	50±21	3.2	5.45%	95±29	3.06%

6.5.2 Precipitation of δ phase

In solution-treated IN718 alloy, the precipitation of δ phase often takes place from 750 °C to 1020 °C [181,204]. Below 900 °C, the precipitation of γ" phase precedes the δ precipitation. With increasing of aging time, the nucleation of δ phases takes place at the stacking faults within pre-existing metastable γ" phases and subsequently grows into the matrix. Fully transformation from γ" → δ phase occurs after longer exposure [204]. Above 900 °C (the end temperature of the precipitation of γ" phase), the δ phase precipitates directly from the grain interior [181,204]. However, high-density δ precipitates formed at the top ~70 μm of the processed specimen after annealing at 700 °C for just 5 h in this study. The precipitation of δ phase may be attributed to the high strain level of the gradient layer that being imposed during SMGT since the kinetics of precipitation of γ" and δ phase are influenced by plastic deformation [181,187,345].

Singh et al. [346] investigated the influence of cold rolling on the precipitation kinetics of both γ" and δ phase of IN718 at the temperature below 900 °C. Their results suggest that the precipitation of γ" phase was more frequent than the δ phase for the 30% cold rolled sample, whereas the precipitation of δ phase was more favorable for the 50% cold rolled sample. They argued that the slip band formed during cold rolling might serves as the nucleation site of δ phase,

consequently leading to the decrease of the content of γ" phase since γ" and δ phase has same chemical composition. Liu et al. [204] also reported the similar results and found that the relationship between the apparent activation energy of δ phase (E_A) and cold rolling reduction (ε, in percent) below 900 °C can be described by the equation [204]:

$$E_A = (1450 \pm 90) - (14.0 \pm 1.9) \cdot \varepsilon \qquad \text{Equation 6.1}$$

Gradient shear strain was imposed in various depth of the processed layer during SMGT. The plastic shear strain and strain rate in the severely deformed surface layer after SMGT in this study was estimated using an annealing twin boundary that was almost perpendicular to the tangent of cylinder surface, as shown in the Fig.6.10a. The depth (x) dependence of displacement field (y) follows the rule of $y(x) = y_s exp(-kx)$ [94]. The agreement between real data and the linear fitting result of ln(y) vs. x in Fig.6.10b implies a reasonable description of the depth-displacement dependence. In this work, the depth dependence of displacement field can be described as $y(x) = 1110 \cdot exp(-0.036 \cdot x)$ in the unit of μm. The shear strain γ(x) can therefore be obtained by differentiating the displacement y(x) with displacement: $\gamma(x) = -\frac{\partial y(x)}{\partial x} = 40 \cdot exp(-0.036 \cdot x)$. The further differentiation of shear strain with displacement refers to the shear strain gradient, as plotted in Fig.6.10c. The estimated shear strain at the depth of ~ 50 μm and 5 μm is calculated to be 6.6 and 34, corresponding to a 77% and 94% compression reduction, respectively, given a constant volume during deformation. According to Eq.6.1, the corresponding apparent activation energy of δ phase is calculated to be ~ 372 kJ/mol at the 50 μm depth of DT layer and ~ 134 kJ/mol at the 5 μm depth of surface NG layer, respectively, much lower than that in solution-treated IN718 alloy (1450 kJ/mol). It implies that prestraining may facilitates and decreases the onset temperature of the precipitation of δ phase. Extensive studies on the effect of cold rolling to the precipitation behaviors of γ" and δ phase have concluded that cold rolling promote not only the precipitation of γ" phase but also the γ" → δ phase transformation [187,204,351]. The competing between accelerated precipitation of γ" phase, leading to the increase in γ" content, and accelerated γ" → δ phase transformation, leading to the decrease in γ" content, resulted in different precipitation behaviors in samples with various strain level and different aging time. In this story, the majority of γ" phases, especially for those formed in the top NG layer with highest prestrainning level, have transformed to δ phase. There are two factors that may have contributed to the accelerated precipitation of δ phase after prestraining: the increased nucleation site (grain boundaries) of δ

phase, and the accelerated diffusion rate of alloying elements (Nb) of δ phase through dislocation pipe diffusion than that through lattice diffusion [204,352].

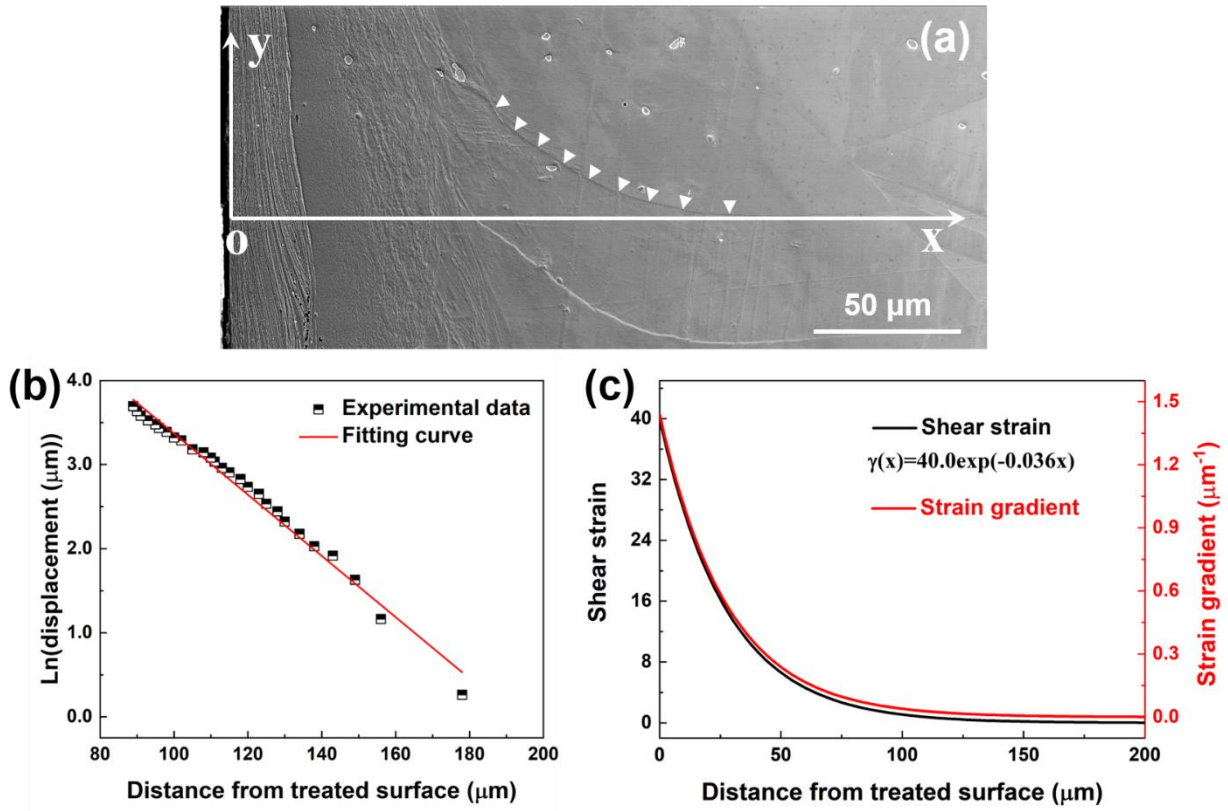

Figure 6.10 (a) SEM image showing the shear deformation induced deflection of a twin boundary in the processed sample. (b) Experimental data and the least square fitting of the depth dependence of the displacement of the twin boundary in Fig.a. (c) Estimated shear strain and strain gradient as a function of depth.

6.5.3 Precipitation of η phase

The other type of $D0_{24}$ structured needle-like precipitate (η phase) has never been found in IN718 alloy before. Pickering et al. [205] identified the η-Ni_6AlNb phase in Allvac 718Plus alloy after ageing. However, the chemical composition of Allvac 718Plus superalloy was significantly modified with respect to IN718 by the addition of Al, Co and W to stabilize γ' over γ" phase. The precipitation of η phase in Allvac 718Plus alloy is most likely due to the increased Al content [205]. Antonov et al. [208] systematically investigated the thermal stability and compositional dependence on alloying elements in several Ni-base superalloys and found that the prevalent phase (δ or η) of the alloy could be determined by the chemical ratio of (Nb+Ta)/(Al+Ti) in at.%. Alloys

with a ratio greater than 1 are largely comprised of δ phase, whereas those with a ratio less than 1 are mainly precipitate η phase. This rule fit well with all superalloys be studied in their work, including Inconel 625, Inconel 706, Allvac 718Plus, Inconel 740 and IN718 etc. According to previous study, the IN718 alloy with ratio of (Nb+Ta)/(Al+Ti) = 1.30 (refers to Table 6.1) in this study should have precipitated δ rather than η phase after heat treatment. However, high-density of η precipitates were observed in the top NG layer (4.44% of area fraction), almost comparable with that of the δ precipitates (5.75%), as shown in Table 6.3.

Prior studies show that the precipitation of η phase occurs mainly at grain boundaries and at the expense of γ' phase, leading to a γ' depleted zone around precipitates [205,207]. As aforementioned, the volume fraction of γ' phase is only one third of that of γ" phase in solution-treated IN718 [162,348]. However, the plastic deformation in the gradient layer might have altered the precipitation behavior of both γ' and γ" phases. It has been recognized that recovery was the dominant mechanism for microstructural changes for cold-rolled IN718 alloy that was annealed at temperature below 850 ^{o}C for a short period of time [187]. The recrystallization takes place slowly at this stage. It implies that the significant compressive stress that was imposed by SMGT may sustained and have influenced the precipitation of γ' and γ" phases [103]. Zhou et al. [348] calculated the misfit stress caused by coherent precipitation of γ' and γ" phases and found out that, the misfit stress inside γ" phase is compressive and could reach GPa level due to its relatively large transformation strain. Whereas the misfit stress inside γ' phase is tensile as the stress-free-transformation strain for $\gamma \rightarrow \gamma'$ transformation (cubic to cubic transformation) is negative. During ageing, the extremely high level of compressive stress of gradient layer could have prohibited the precipitation of γ" phase with compressive misfit stress, whilst accelerated the precipitation of γ' phase with tensile misfit stress. Higher content of γ' precipitates, serve as the embryos of η phases, are therefore expected to be formed in the surface NG layer than in the DT layer that with relatively lower compressive stress. The experimental data also verifies the assumption as shown in Table 6.3, the area fraction of η phase in NG region (4.44%) almost doubled than that in the DT region (2.33%).

Two growth mechanisms of η phase have been proposed: (i) discontinuous precipitation, and (ii) growth by diffusing alloying elements and by the transformation of γ' phase [205,207]. The classic microstructure after discontinuous precipitation is characterized by serrated grain boundaries, as denoted by dashed line in Fig.6.7a. In both cases the chemical ordering by diffusion

are required for η precipitation [205]. Further investigation about the precipitation of η phase were performed using Themis Z microscopy and image analyses. The HRSTEM image in Fig.6.11a shows a brighter η phase than γ matrix, indicating a higher mean atomic number within the precipitate. A ledge with width of several atomic layers are observed between η and γ phase, as labeled by the dotted box b. Studies about η precipitation reveals that η phase was grow by producing ledges and the growth was limited by the ordering required at the ledges [207]. It implies that ledge in Fig.6.11a moves upward and leads to the growth of η phase. The other interesting phenomenon that worthwhile mentioned is that the area of the γ matrix that ahead the moving direction of the ledge (adjacent to η/γ interface) is brighter than the region that far away from the η phase, indicating a different chemical composition. The EDS line scan results along the line across the η/γ interface (as labeled by dashed line in Fig.6.11a) in Fig.6.12 reveal that there is a chemical composition transition zone between η and γ phase. The transition zone has the same stacking with γ matrix and only being observed ahead of the ledge. These evidences imply that the chemical ordering may occurs first, followed by γ → η transformation.

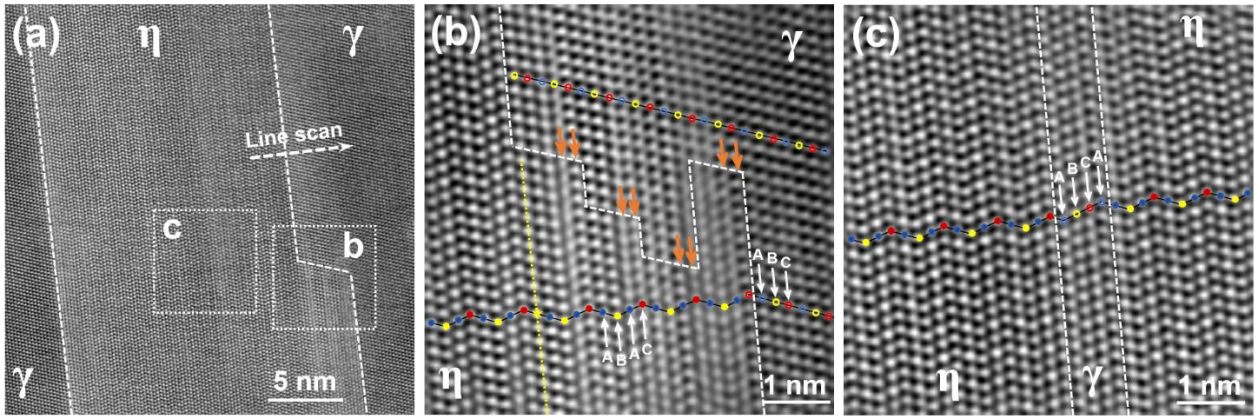

Figure 6.11 (a) High resolution STEM image of η precipitate in NG layer after annealing. (b) the atomic scale STEM image of the area b in Fig. a showing the ledged region between matrix (γ) and precipitates (η). The ABAC-type stacking is evident in the η phase. The Shockley partials on two adjacent planes in each four layers are labeled by arrows. (c) the atomic scale STEM image of the area c in Fig. a showing a thin sandwiched region demonstrating ABCA-type of stacking, equivalent to matrix γ, between η precipitates.

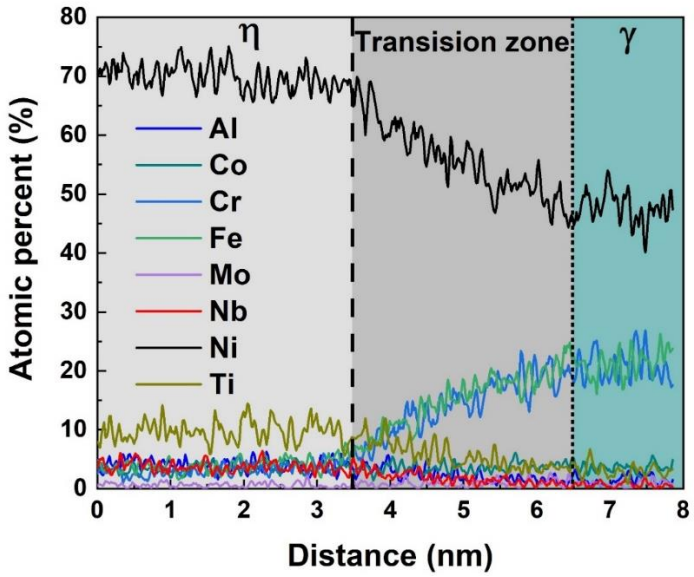

Figure 6.12 EDS line scanning results along the line that crossing the η/γ interface in the STEM image in Fig.11a showing the chemical composition transition zone between η and γ phase.

Transformation of fcc-γ matrix "ABCA" stacking to hcp-η phase "ABAC" stacking has been schematically illustrated in previous study [207]. This phase transformation can be achieved by inserting Shockey partials on two adjacent planes in each four stacking layers. However, no experimental results have been reported for verification. A detailed observation of the ledge in Fig.6.11a is presented in Fig.6.11b. The A, B and C-layer of η phase are labeled using spots in blue, yellow and red color, respectively. Those of γ phase are labeled using open circles for clarification. It further confirms the formation of ABAC stacked η phase. Investigation about the stacking of the ledge region reveals that two Shockley partials exist adjacently in every four layers, as denoted by green arrows. The inserting of Shockley partials transformed the fcc stacking of γ matrix to the hcp stacking of η phase, consistent with the illustration in ref. [207]. Mis-stacking occurs occasionally during transformation, as labeled by the yellow dotted line. In other area, multiple mis-stacking resulted in an ABCA-type of stacking, equivalent to matrix γ, as shown in the atomic scale HRTEM image of Fig.6.11c that was taken from the dotted box c in Fig.6.11a. Similar mis-stacking has also been reported in Allvac 718Plus superalloy, where the presence of δ lath in η precipitates was formed for the accommodation of local chemical composition [205,207]. The difference between their work with this study is that the δ-Ni_3Nb phase in Allvac 718Plus sample was precipitated to accommodate the excess Nb that was repelled by the substitution of Al

in η-Ni_6AlNb lattice during precipitation. While the γ matrix lath in this study was formed to accommodate the lack of Al and Ti in the lattice of η-Ni_3(Al,Ti,Nb) during precipitation.

6.5.4 Mechanical properties

Precipitation hardening is the dominant strengthening mechanism for IN718 [165,169,351]. γ' and γ" precipitates that are coherent with the γ matrix are the main particles responsible for the precipitation hardening and γ" is the major strengthening phase [178,351]. According to studies by Oblak and Fisk [180,216], the dislocation-particle shearing process contributed to the strengthening effect of γ' and γ" precipitates. However, with the temperature increasing or annealing time prolonging, the γ" → δ and γ' → η transformation take place. Such change in microstructure was found to detrimental to the strength of IN718 alloy [204]. As shown in Fig.6.1d and Fig.6.3, high-density γ" and γ' precipitates formed after annealing at 700 °C for 5 h, contributing to ~ 1.5 GPa strengthening in the undeformed matrix region and the inner layer of gradient structure. Precipitation of γ" and γ' precipitates induced strengthening has been studied extensively and, hence, no more discussion will be presented in this study [168,180,216]. However, in the top NG layer, where majority of γ' and γ" phase have transformed to η and δ phase, respectively, slight strength softening (ΔH = 200 MPa) is observed. The absence of strengthening in NG layer may attributed to three factors: (i) grain coarsening induced softening, (ii) weaker solid-solution strengthening effect induced softening, and (iii) load-bearing effect of reinforcements (δ and η phase) induced strengthening.

The grain coarsening induced softening can be calculated by the classic Hall-Petch equation as follows [7]:

$$\sigma = \sigma_0 + k \cdot d^{-1/2} \qquad \text{Equation 6.2}$$

where σ represents yielding strength, σ_0 is friction stress (~ 325 MPa for IN718), k is the Hall-Petch coefficient and d is the grain size. A value of k = 750 MPa $\mu m^{1/2}$ was generally used [353]. However, most of previous works were focused on γ' and γ" strengthened IN718 alloys. Wallow et al. [354] found out that the value of k varies with volume fraction and size of γ' phase, indicating synergetic effects between grain boundary- and γ'-strengthening. Since all γ' phase have transformed to η phase in the top NG layer, the strengthening effect derived from γ' phase is negligible and, hence, a lower value of k = 600 MPa $\mu m^{1/2}$ was adopted in this work. Around 60%

of nanograins with average size of ~ 45 nm in NG layer coarsened to ~ 148 nm after annealing at 700 ^{o}C for 5 hours, as shown in Fig.5b. The equivalent grain size is calculated to be ~ 107 nm. The yield strength decreases due to grain coarsening according to Eq.6.2 is therefore calculated to be $\Delta\sigma_{H\text{-}P}$ = 993 MPa. As for the weaker solid-solution strengthening effect that was resulted from the precipitation of σ and η phase, the corresponding strength softening should be insignificant considering the relatively low content of precipitates. Besides, the solution strengthening of γ matrix was mostly attributed to the addition of Mo and W in most instances [174]. Since no apparent Mo and W segregation occurs during the precipitation of δ and η phase (refers to Table 6.1 and 6.2), the influence of δ and η to the solution strengthening should be negligible.

The δ and η phase don't contribute to precipitation strengthening due to the nature, morphology and formation kinetic of these two types of precipitates [178,181]. Instead, the strengthening mechanism of these needle-like precipitates is mainly attributed to the load-bearing effect of whiskers, which is proportional to the volume fraction (V) and aspect ratio (AR) of precipitates [355]. According to shear lag model that was developed by Cox [356] and modified by Nardone [357], the strengthening derived from the load-bearing effect of δ and η precipitates can be expressed as:

$$\Delta\sigma_{PPT} = 0.5 \cdot V \cdot AR \cdot \sigma_{matrix} \qquad \text{Equation 6.3}$$

where σ_{matrix} represents the strength of matrix, calculated to be ~ 2160 MPa according to Eq.6.2 given d = 107 nm. Using the statistic results listed in Table 6.3, the corresponding strength increment due to δ and η precipitation according to Eq.6.3 is $\Delta\sigma_{PPT}$ = 883 MPa. Consequently, the softening derived from grain coarsening coupled with the strengthening derived from precipitation of δ and η phase leading to a net strength softening with value of $\Delta\sigma = \Delta\sigma_{H\text{-}P} - \Delta\sigma_{PPT}$ = 110 MPa. The corresponding hardness drop is 297 MPa, following Tabor relation (H = 2.7σ) [251,252,358], slightly higher than the experimental results (~ 200 MPa).

6.6 Conclusion

The precipitation behavior and the influence of precipitates on the strength of gradient IN718 superalloy was studied. The TEM studies reveal that high-density γ" and γ' phase precipitated in the undeformed matrix and inner layer of gradient structure after annealing at 700 ^{o}C for 5 h. Whereas γ" and γ' phase in the severely deformed DT and NG layer transformed to δ

and η phases, respectively. The D024 hexagonal crystal structured η phase has a chemistry of Ni3(Al,Ti,Nb). The extremely high compressive stress level in the top NG layer may prohibited the precipitation of γ" phase whilst accelerated the precipitation of γ' phase, consequently, leading to higher concentration of η phase. The HRSTEM analyses reveal that chemical composition ordering preceded the $\gamma \rightarrow \eta$ phase transformation. Hardness measurement results reveal that the grain coarsening induced softening overweight the strengthening derived from the load-bearing effect of δ and η phases, leading to softening in the top NG layer.

CHAPTER 7. THERMAL STABILITY AND DEFORMATION BEHAVIORS OF GRADIENT INCONEL 718 SUPERALLOY

The gradient structured nickel-based alloy was fabricated by Jie Ding and Zhongxia Shang. Microstructure characterization and in situ micropillar compression tests were performed by Jie Ding, with grateful help from Dr. Sichuang Xue and Ruizhe Su. The data analysis and writing were completed by Jie Ding with guidance and editing by Dr. Xinghang Zhang.

7.1 Overview

Gradient structures containing nanograined (NG) surface layer have been introduced into Inconel 718 (IN718) nickel-based alloy using surface mechanical grinding treatment (SMGT) technique. The thermal stability of NG IN718 alloy, and the deformation behavior of the undeformed matrix region and severely plastic deformed NG region of both as processed and annealed samples were investigated. The annealing studies of NG IN718 alloy at 700 ^{o}C for various times reveal that nanograins with size smaller than the critical value of ~ 40 nm exhibited significantly enhanced thermal stability than those with size larger than 40 nm. The enhanced thermal stability was attributed to the formation of grain boundaries that are in lower energy configuration during SMGT, and the grain boundaries relaxation. The *in situ* micropillar compression tests results reveal that the precipitation of high-density of γ" phases after annealing strengthened the matrix from 500 MPa to 900 MPa. The flow stress of NG region after annealing at 700 ^{o}C for 24 h was comparable to that of the as processed samples, owing to the strengthening effect of high-density of δ and η phases with large sizes. Post compression TEM analyses reveal that the activation and propagation of stacking faults (SFs) enabled the formation of primary slip bands (SBs) in the pillar obtained from γ" phase strengthened IN718 matrix. The shearing of γ" phase transformed the body-centered tetragonal (BCT) structured γ" phase to face-centered cubic (FCC) structures. The microstructure of the significantly coarsened γ" phase that was survived in the annealed topmost NG layer shows that coherency between the γ" phase with size of several hundred nanometers and γ matrix vanished due to the mismatch strain between them. Two kinds of SFs that were activated and propagated along the (002) and (111) planes of γ" phases were detected after deformation. Detailed analyses about the shearing of γ" phases with nano-scaled

sizes and microstructure of deformed γ" phases with larger sizes, accompanied with that of deformed δ and η phases are required in future studies.

7.2 Introduction

Nanograined (NG) metals that are characterized by high volume fraction of grain boundaries have demonstrated extraordinary mechanical properties than their CG counterparts [52,309,310]. Severe plastic deformation (SPD) techniques like equal channel angular press (ECAP) [20,32] and high-pressure torsion (HPT) [18,41,45] etc. have been proven effective in grain refinement of metallic materials. However, the same grain boundaries that contribute to the desirable characteristics in turn serve to deteriorate the thermal stability of NG metals [313–316]. The high level of grain boundaries energy of nanograins provides a large driving force for grain coarsening through the removal of excess grain boundaries. For instance, grain boundaries migration takes place at low temperature as 300 ^{o}C for NG Nb obtained by HPT in liquid nitrogen with average grain size of ~ 75 nm, owing to the high density of defects inside nanograins and to the pronounced non-equilibrium state of grain boundaries [359]. Grain growth occurs at temperature as low as 200 ^{o}C for pure NC Ni, accompanied by the substantial hardness drop [318]. For the nanocrystalline Ni fabricated by electrodeposition with average grain size of 10-20 nm, the temperature at which the nanograins tend to become unstable was found to be as low as 80 ^{o}C [155]. Similarly, grain growth takes place even at ambient temperature for NG Cu. The inherent thermal instability hinders the application of NG metallic materials at elevated temperatures [360].

Recently, severe surface modification techniques like surface mechanical grinding treatment (SMGT) [85], surface mechanical attrition treatment (SMAT) [86,95,103] and surface mechanical rolling treatment (SMRT) [103] have been proposed for the introduction of gradient microstructures into the surface of metallic materials to improve both strength and ductility. Gradient structures containing extremely fine-grained top surface layer have been introduced into several kinds of metals. It has been reported that these surface modification techniques are more effective than conventional SPD approaches in grain refinement [94]. Grain coarsening is therefore expected to be taken place at the topmost NG layer of gradient structured metals. However, the annealing studies of gradient structured pure Cu and Ni that were fabricated using SMGT in liquid nitrogen reveal that the nanograins with sizes smaller than the critical values (~ 70 nm for Cu and

~ 43 nm for Ni) were reported to be more stable than those with larger grain sizes [154]. This enhanced thermal stability of NG samples with smaller grain sizes than their counterparts with larger grain sizes was attributed to the unique grain boundaries be generated that are in lower energy configurations during SMGT [154,361]. These evidences imply that the thermal stability of NG alloys not necessarily be deteriorated after grain refinement via SPD.

Inconel 718 (IN718) nickel-based alloy is one of the most commonly used precipitation strengthened superalloy for application in gas turbine and jet engine. The high temperature performance of IN718 are primarily determined by the quantity and characteristics of precipitates formed [179,180,191,192]. The major intermetallic phases that precipitate in face centered cubic (FCC) IN718 matrix are: (i) the body-centered tetragonal (BCT) structured ($D0_{22}$) γ" phase, (ii) the FCC structured ($L1_2$) γ' phase and (iii) the orthorhombic structured ($D0_a$) δ phase [197–199]. The strengthening of IN718 at elevated temperatures is mainly attributed to the coherency strain hardening effect of ellipsoidal γ" phase that precipitates coherently with the γ matrix. Contribution of coherent γ' phase to the strengthening of the alloy is less effective as the volume fraction of γ' phase is only one third or quarter of that of γ" phase in solution-treated IN718 [161,193,216,342]. The transformation of metastable γ" phase to equilibrium δ phase over long-term exposure at high temperatures has been concluded to be detrimental to the high temperature strength of the alloy [179,204]. The deformation behavior of precipitates, especially γ" phase strengthened IN718 alloy is critical for the understanding of the underlying strengthening mechanisms. Extensive research works have been reported [362–365]. Generally, the deformation of IN718 alloy characterized by the formation of planar slip bands [363,364]. However, the deformation mechanisms differ within different works and conflicting observations have been reported. Clavel et al. [366] found that the formation of planar deformation bands was attributed to micro-twins, consistent with what was reported by Merrick [367]. Oblak et al. [216] reported that the deformation was achieved by the shearing of γ" phase through the motion of a/2<110> dislocation pairs. Sundararaman et al. [362] found that the deformation mechanism was dependent with the size of γ" phases. For γ" phases with size that is smaller than the critical value (~ 20 nm in diameter), shearing of γ" phases occurred by the motion of group of dislocations. Whereas when the size of γ" phases exceeds the critical value, γ" precipitates were sheared by twinning. These studies were focused on the deformation behaviors of γ" phases that are coherent with the γ matrix. Prior studies have reported that the pre-straining accelerates the precipitate and growth rate of γ" phases [161,181,204]. The coherency

between γ” phases and γ matrix couldn’t be sustained when the size of γ” phases exceeds critical value [368]. The deformation behavior of these incoherent γ” phases has rarely been reported. It implies that the precipitation and the corresponding deformation behavior of severely deformed IN718 alloys may different with that of solution-treated alloys. Hence, a systematic study about the comparison of precipitation and deformation behavior of solution-treated and severe plastic deformed IN718 alloy is required.

In this study, gradient structures containing severely deformed NG surface layer were fabricated in IN718 nickel-based alloy via SMGT technique. Thermal stability of NG surface layer was investigated by annealing the samples at 700 ^{o}C for different hours and the underlying stabilization strategies were discussed. Precipitation behavior of undeformed matrix and severe plastic deformed NG layer after annealing were checked using transmission electron microscopy (TEM). Comparison of the deformation behavior of annealed matrix and NG region with different precipitates characters were studied using in situ micropillar compression tests. The corresponding deformation mechanisms of precipitates in different regions were investigated by checking the post compression TEM image of deformed pillars.

7.3 Experimental

7.3.1 Materials and processing

The IN718 Ni-based alloy with a chemical composition as listed in Table 7.1 was subjected to SMGT. Prior processing, a cylindric bar was fully solution treated at 1100 ^{o}C for 1 hour followed by quenching (denoted as as-received sample hereafter). During processing, the bar rotated at a velocity of 400 rpm, while a WC/Co tool tip penetrated into the surface by 30 μm and slid along axial direction at a speed of 10 mm/min. The process was repeated 8 times to generate subsequent deformation zone. Liquid nitrogen was used as coolant during processing. Subsequently, the processed samples were annealed in a vacuum furnace at the temperature of 700 ^{o}C for 5, 24 and 100 h, followed by furnace cooling. Annealing was conducted when the vacuum level reaches 2×10^{-6} torr.

Table 7.1 Chemical composition of IN718 alloy (in wt.%)

Cr	Fe	Co	Nb	Mo	Al	Ti	Ta	Ni
18.57	18.00	0.11	5.02	2.86	0.58	0.97	<0.01	58.7

7.3.2 Microstructure characterization

The samples used for metallographic observations were ground and polished using conventional metallographic preparation technique, and then carried out by optical microscope. TEM samples were prepared by the focused ion beam (FIB) technique using an FEI Quanta 3D FEG Dual Beam FIB scanning electron microscope following typical protocols. The microstructure and chemical composition analyses of the both as-processed and annealed samples were performed on an FEI Talos 200X analytical transmission electron microscope operated at 200 kV, equipped with a supper X energy-dispersive X-ray spectroscopy (EDS) detector.

7.3.3 Mechanical testing

Vickers hardness measurements along the depth direction of both as processed and annealed specimens were conducted using a LECO LM247 microhardness tester with a Vickers indenter tip. The applied load was 25 g, with a holding time of 13 s. Micropillars were prepared using the FIB technique along the longitudinal direction of both as processed and annealed IN718 alloys in the severely deformed topmost layer and undeformed matrix region. The micropillars have a diameter of ~ 2 μm and the height-to-diameter aspect ratio of pillars was kept at ~ 2.0 to avoid buckling during compression. In situ micropillar compression tests at a constant strain rate of $1 \times 10^{-3}\ s^{-1}$ were performed on an FEI Quanta 3D FEG SEM using a Bruker's Hysitron PI 88×R PicoIndenter equipped with a 10 μm diameter diamond flat-punch indenter tip. The force-displacement data were collected using the piezoelectric actuator in the capacitive transducer. Detailed information about testing process and data analyses can be found in our previous works.

7.4 Results

7.4.1 Overview of microstructure and hardness

The optical microscopy (OM) image in Fig.7.1a shows the equiaxed grains of the as-received IN718 with mean grain size of ~ 150 μm after annealing at 1100 ^{o}C for 1 hour. Upon SMGT, a severely deformed gradient structure formed on the surface, as shown in the OM image in Fig.7.1b. NG structures were observed on the topmost region of the gradient structured layer according to the TEM characterization results in the following section. The penetration depth of the gradient structured layer varies in different regions, as labeled by the dotted line, an indication of the inhomogeneous microstructure in different regions of the processed samples. After annealing at 700 ^{o}C, sharp interface formed between the topmost NG layer and the deeper region of the sample, as revealed by the OM images in Fig.7.1c. The microstructure characterization results of these annealed samples in the following sections reveal that the topmost NG layer was more thermally stable than the deeper layer of the gradient structure. What worthwhile mentioning is that the thickness of the thermally stable NG layer varies with positions due to the inhomogeneous penetration depth of the gradient structure after SMGT (as shown in Fig.7.1b). The thickness of the thermally stable area of NG layer ranges from a few to ~ 30 μm. The corresponding hardness profile along the depth direction in Fig.7.1d reveals that the hardness decreased gradually from ~ 6.9 GPa in the top NG layer of as processed sample to ~ 2.4 GPa in the undeformed matrix region. The penetration depth of the deformed region with gradient structure is ~ 300 μm. After annealing, the hardness of the annealed sample increased in the whole depth range. It is worth emphasizing that no softening was observed in the NG layer even after 100 h annealing at 700 ^{o}C.

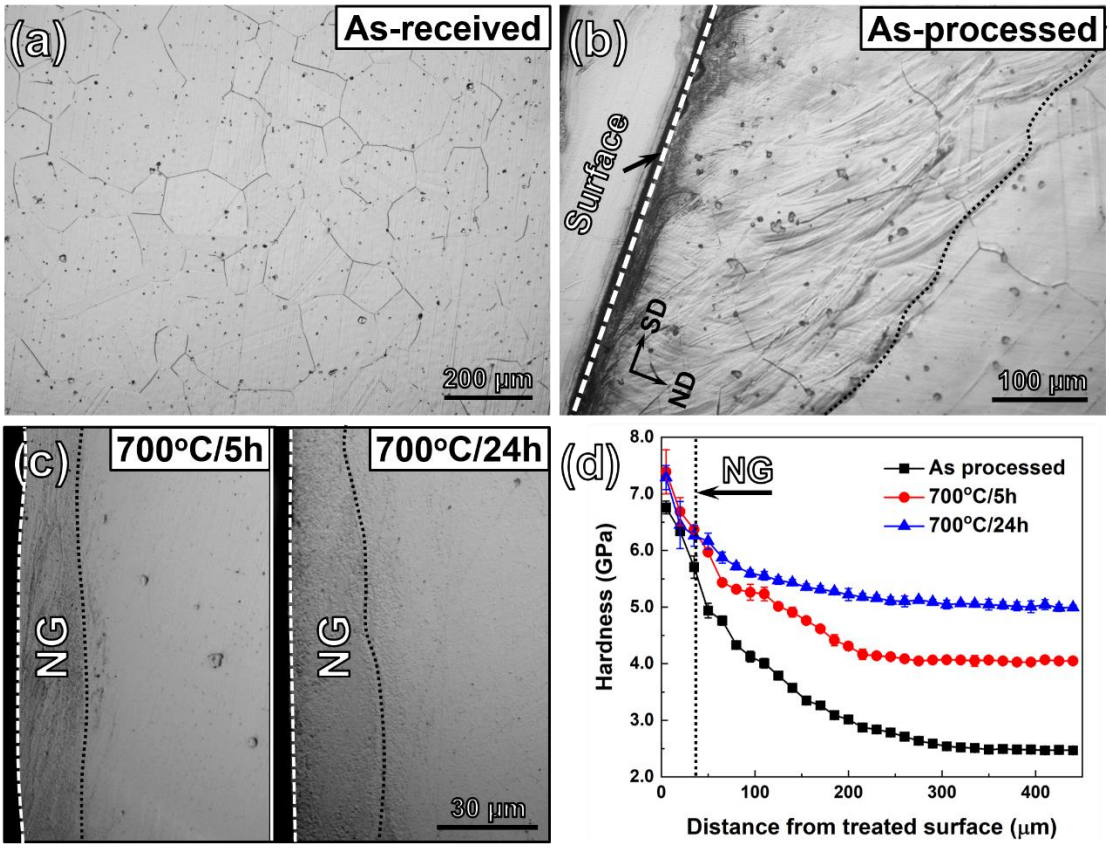

Figure 7.1 OM images of (a) as received IN718 and (b) gradient structures of IN718 specimens processed by SMGT. (c) OM images of the gradient structure of processed IN718 specimens after annealing at 700 ^{o}C for 5 and 24 h, respectively. (d) Vickers hardnesses evolution of both as processed and annealed IN718 specimens. (SD: shear direction, ND: normal direction)

7.4.2 TEM characterization

The microstructure of as processed sample in Fig.7.2a reveals that NG structures formed in the surface of IN718 alloy after SMGT, as verified by the inserted selected area diffraction (SAD) pattern. However, areas with extremely fine grains were observed in the NG layer, as labeled by the dotted lines in Fig.7.2a. TEM image in Fig.7.2b shows the alternately distributed relative fine (F)/coarse (C) NG structures of the topmost NG layer (at a depth range of 2-5 μm). The corresponding grain size evolution profile reveals that the average size of extremely fine-grained area is ~ 14 nm, whereas that of NG region with relative larger grains is ~ 28 nm. The corresponding STEM image and EDS maps of NG layer reveal that the chemical composition distributed uniformly, and no chemical segregation occurs in the fine-grained area. The formation

of these finer grain area in the NG layer may be attributed to the discontinuous cooling of liquid nitrogen during SMGT.

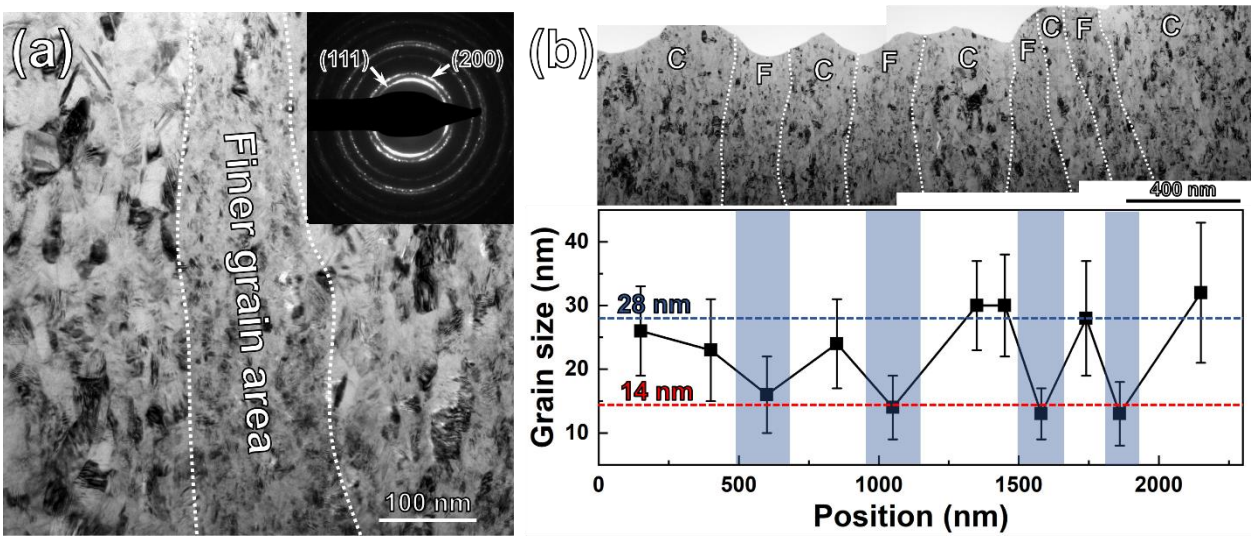

Figure 7.2 (a) TEM image of the surface NG layer of gradient structure showing nanograins of the as processed IN718 alloy. Extremely fine grains are observed and labeled by dashed lines. (b) TEM image and the corresponding grain size evolution of the topmost NG layer (at a depth range of 2-5 μm) showing the alternately distributed relative fine (F)/coarse (C) grained NG structures.

High density of nanoprecipitates formed in the undeformed matrix region after annealing at 700 ^{o}C. Fig.7.3a shows the STEM image and the corresponding SAD pattern of the matrix region after 24 h annealing. The indexing of the SAD pattern reveals that these disc-like nanoprecipitates are mostly γ" phases. The coherent interface between γ" and γ matrix follows the orientation relationship as: $\{100\}_{\gamma"}//\{100\}_{\gamma}$, $<001>_{\gamma"}//<001>_{\gamma}$. The strong spots are from γ matrix and those weak superlattice spots are from γ" phase [199]. The EDS maps in Fig.7.3b shows the enrichment of Al, Ti, Ni and Nb elements of γ" phases. The high resolution TEM (HRTEM) image in Fig.7.3c reveals the superlattice of γ" phases, as noted by the green dotted circles. The facets of $\{100\}_{\gamma"}$ are parallel to the $\{100\}_{\gamma}$, consistent with the index results of SAD. The corresponding fast Fourier transformation (FFT) patterns of the area d with γ" phases (Fig.7.3d) and area e with γ matrix (Fig.7.3e) also verify that superlattice spots (as labeled by arrows) only appears in the γ" phase region.

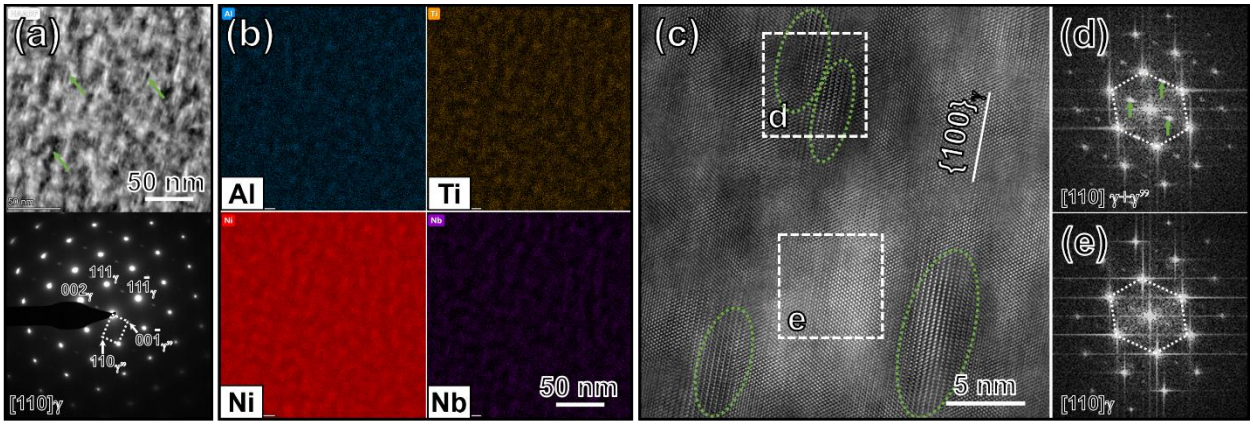

Figure 7.3 (a) TEM image and corresponding SAD pattern of the undeformed matrix region of IN718 alloy after annealing at 700 ºC for 24 h showing the precipitation of high-density of γ" phases. (b) The corresponding EDS maps showing the enrichment of Al, Ti, Ni and Nb elements of γ" phases. (c) HRTEM image of γ" phase and γ matrix clearly shows the superlattice of γ" phase (as labeled by green dotted circles). Corresponding FFT patterns of (d) γ" phase and (e) γ matrix area in Fig.c show the superlattice spots of γ" phases.

Upon annealing, the nanograins of the topmost region of NG layer retained, whereas recrystallization and grain coarsening happened at the rest part of gradient structured layer. Fig.7.4a shows the microstructure of the sharp interface (as denoted by dashed line) formed between the thermally stable topmost NG area and the grain coarsened area after annealing for 24 h. The other phenomenon that worthwhile mentioning is that the alternatively distributed F/C NG structures in the thermally stable area sustained after annealing (as labeled by dotted lines in Fig.7.4a). The statistic results of grain size in Fig.7.4b show that the average grain size of fine grains and coarse grains in the thermally stable area is 18 nm and 37 nm, respectively. Whereas that of the grain coarsened area is measured to be 90 nm. The STEM images and corresponding EDS maps of both thermally stable and grain coarsened area in Fig.7.4c and 7.4d show that large Ni and Nb-rich δ phases and Al, Ni and Nb-rich η phases formed after annealing. The difference between these two areas is that high-density of nanosized α-Cr phases were observed in the thermally stable area, whereas the density of α-Cr phases in the grain coarsened area was much lower and larger in size.

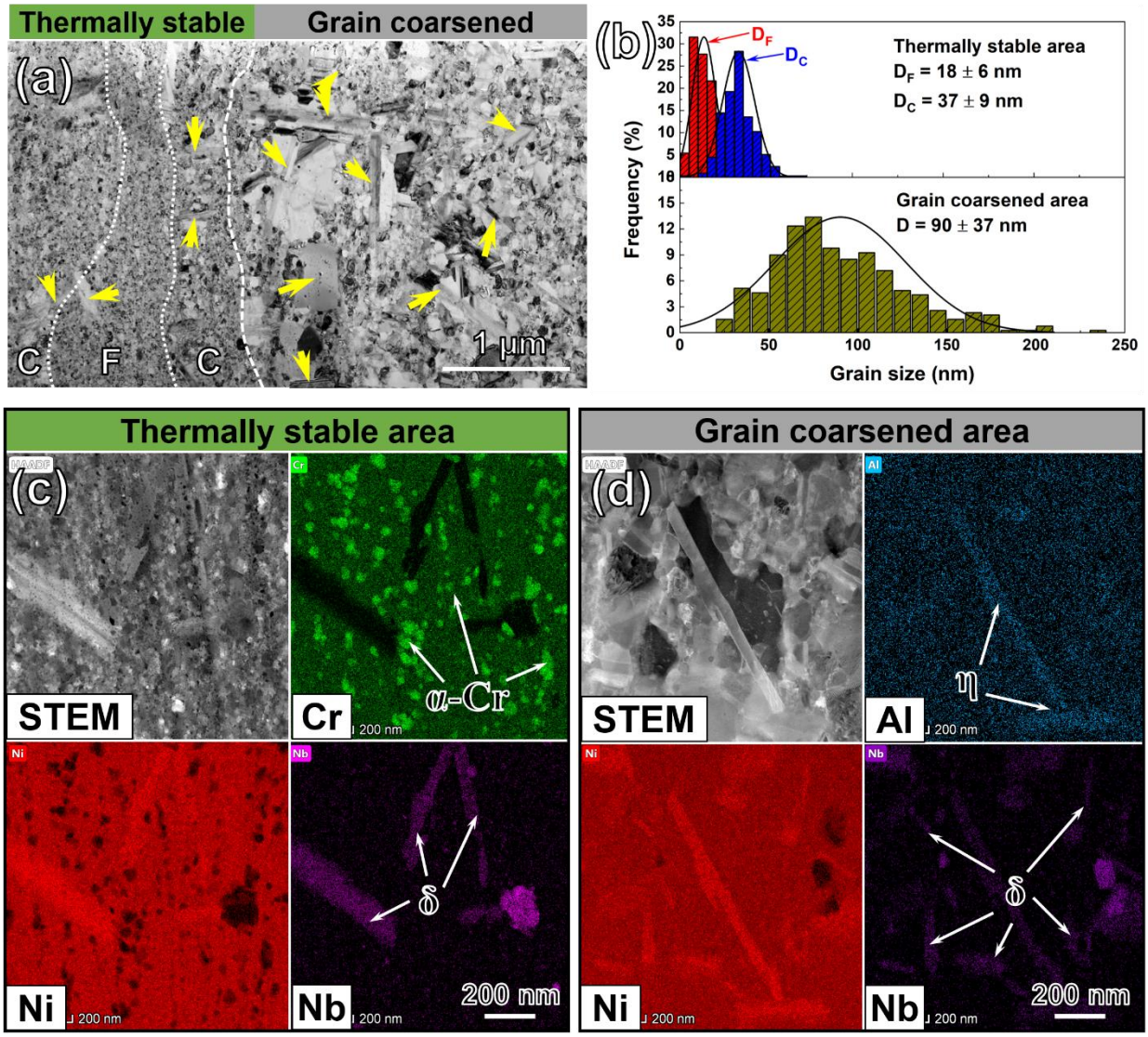

Figure 7.4 (a) TEM image of surface NG layer after annealing at 700 ^{o}C for 24 h showing the sharp interface formed between the thermally stable and grain coarsened NG area. (b) The statistics of the average grain size of the thermally stable and grain coarsened NG area. (c) STEM image and corresponding EDS maps of the thermally stable area showing the precipitation of high-density of nanograined α-Cr particles and Ni/Nb-rich δ phases. (d) STEM image and corresponding EDS maps of grain coarsened area showing the precipitation of Al/Ni/Nb-rich η phases and Ni/Nb-rich δ phases.

Prolonging the annealing time to 100 h further coarsened the grains in both thermally stable and grain coarsened areas of the gradient structured layer. However, the sharp interface between those two areas still sustained, as labeled by dashed line in Fig.7.5a. The alternatively distributed F/C grained structures were also observed, whereas the grain size difference between the relative

fine-grained and coarse-grained structures is much larger than that was annealed for 24 h (in Fig.7.4a). The statistic results of grain size reveal that the grain size of the fine-grained structure in the thermally stable area is 62 nm (in Fig.7.5b), still in the NG range. Whilst that of the coarse-grained structure coarsened to 219 nm (in Fig.7.5c), located in the ultra-fine grained (UFG) range. As for the grain coarsened area, the statistic result of grain size in Fig.7.5d shows that the grains further coarsened to 295 nm after 100 h annealing.

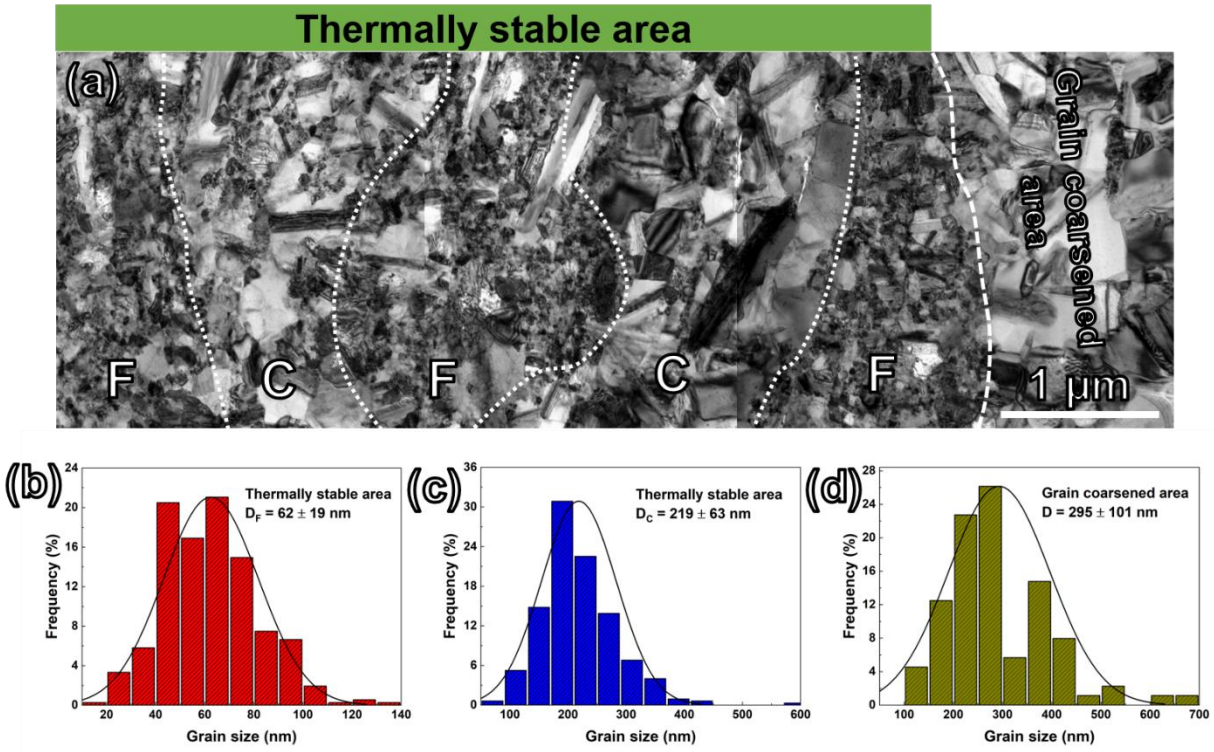

Figure 7.5 (a) TEM image of surface NG layer after annealing at 700 ^{o}C for 100 h showing the sustained interface between the thermally stable and grain coarsened NG area. The statistics of the average grain size of relative (b) fine-grained and (c) coarse-grained structures of thermally stable NG area, and (d) grain coarsened NG area.

7.4.3 In situ micropillar compression tests

In situ micropillar compression tests results of the undeformed γ matrix region before and after annealing at 700 ^{o}C for 24 h are presented in Fig.7.6. The true stress-strain curves in Fig.7.6a and 7.6d show that the average flow stress of the as received specimens without precipitates is ~ 500 MPa, whereas the flow stress of annealed specimens with high-density of γ" phases increased to ~ 900 MPa. The inserted SEM images showing the morphologies of the compressed pillars

reveal the formation of multiple slip bands (SBs) during compression. The captured videos recorded the morphological evolution of the micropillars show that the activation and propagation of each SB corresponds to a stress drop of the stress-strain curves. The magnified SEM snapshots of the video captured during compression of both as received (Fig.7.6b and 7.6c) and annealed (Fig.7.6e-7.6g) samples reveal that multiple SB systems were activated for the as received specimens, whilst only one primary SB was observed for the annealed specimens. It may be attributed to the grain orientation difference between the pillars obtained from these two samples.

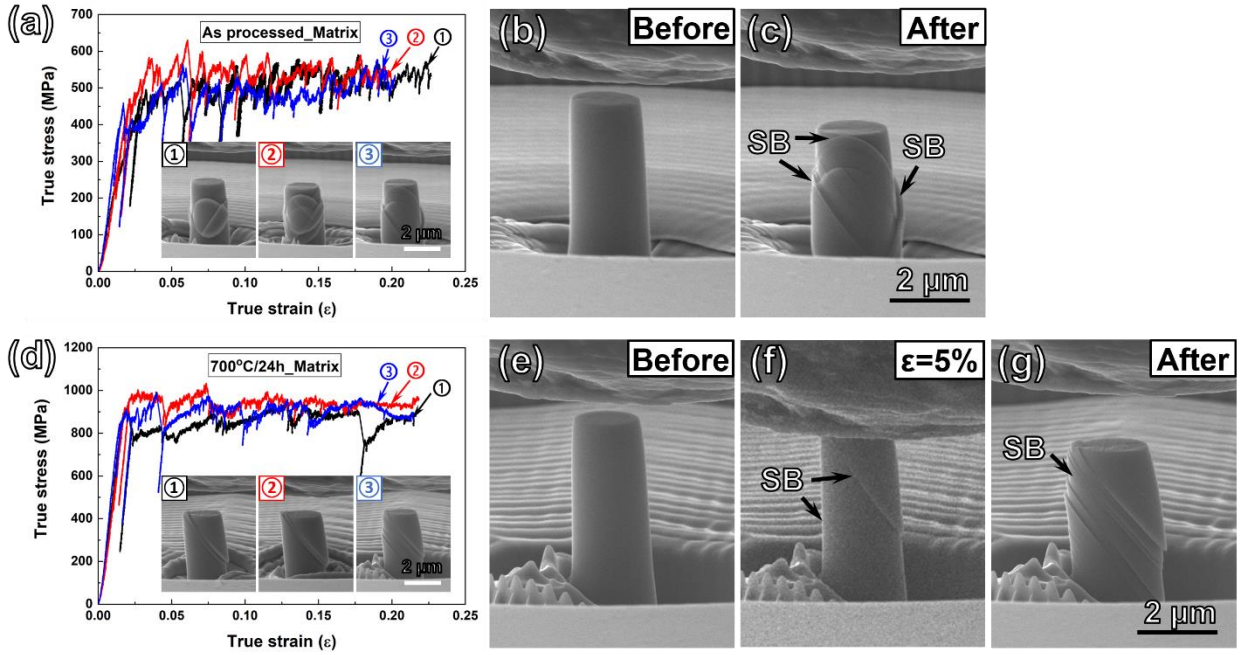

Figure 7.6 In situ micropillar compression test results of pillars obtained from the undeformed matrix regions of both as processed and annealed IN718 sample. True stress-strain curves and SEM images showing the morphologies of deformed pillars of (a) as processed and (d) annealed specimens. (b and c) Detailed SEM images showing the pillar morphology of as processed specimens before and after compression tests. Multiple SBs systems were observed. (e-f) Detailed SEM images showing the pillar morphology evolution of annealed specimens during compression tests. Only one primary SB system was observed.

In situ micropillar compression tests were also performed in the NG layer that is ~ 10 μm from the treated surface in both the as processed samples and the samples after annealing at 700 ^{o}C for 24 h. The true stress-strain curves of pillars obtained from the NG layer of as processed sample in Fig.7.7a show that the pillars yielded at ~ 2.6 GPa and then strain hardened to ~ 3.0 GPa. The inserted SEM images showing the morphologies of the compressed pillars reveal the uniform

deformation of the pillars, as evidenced by the magnified SEM snapshots of the video captured during compression in Fig.7.7b-7.7d showing the classical barreling near the top of the deformed pillar. As for the pillars obtained from the NG layer of annealed sample, the deformation behaviors differ in different pillars due to the inhomogeneous microstructure of NG layer after annealing (as revealed by Fig.7.4). For the pillars obtained mainly from the grain coarsened area (pillar ① and ② in Fig.7.7e), the yielding and flow stress of them are ~ 2.6 GPa and ~ 3.0 GPa, respectively, similar to that of the as processed samples. Whereas the yielding stress of the pillar obtained mainly from the thermally stable area (pillar ③ in Fig.7.7e) increased to ~ 3.1 GPa. The inserted SEM images showing the morphologies of the compressed pillars reveal the surface roughening after compression. The magnified SEM snapshots of the video captured during compression in Fig.7.7f-7.7h show that the roughening took place at high strain level (>10%), and no major cracks were observed during compression.

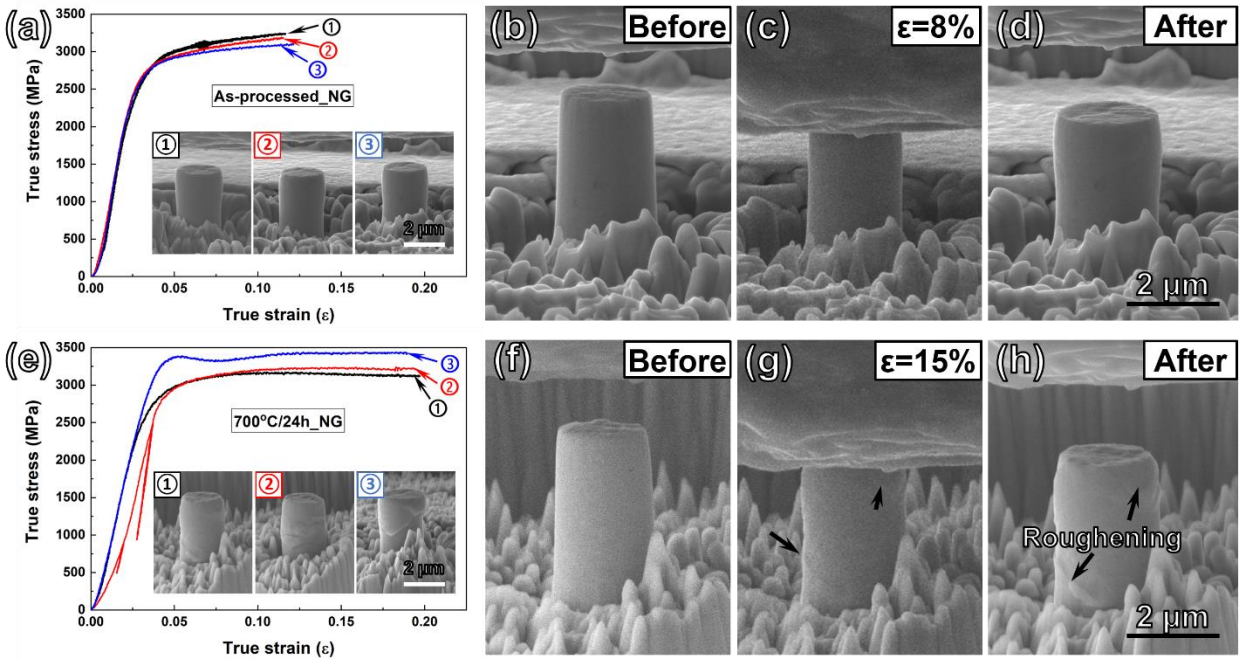

Figure 7.7 In situ micropillar compression test results of pillars obtained from the NG regions of both as processed and annealed IN718 sample. True stress-strain curves and SEM images showing the morphologies of deformed pillars of (a) as processed and (e) annealed specimens. (b-d and f-h) Detailed SEM images showing the pillar morphology evolution of the specimens during compression tests.

7.5 Discussion

7.5.1 Thermal stability of NG IN718 alloy

As aforementioned, the high density of grain boundaries of nanocrystalline metals that contribute to the desirable mechanical properties in turn provide a strong driving force for grain coarsening and corresponding properties degradation [313]. The grain coarsening of NG metals can be pictured by looking at the GB velocity (v), which can be expressed as [148,149]:

$$v = M_{gb} \cdot \gamma_{gb} \cdot \kappa \qquad \text{Equation 7.1}$$

where M_{gb} represents the GB mobility, γ_{gb} is the GB energy and κ is the local boundary curvature. It implies that except for the kinetics-driven stabilization approach in which grain coarsening is suppressed by pinning grain boundaries with second phase Zener drag or by solute drag, lowering grain boundaries energy can also effectively reduce the thermal dynamic driving force for grain coarsening and therefore stabilize NG metals [153,321,322]. Specifically, the driving force for grain coarsening of NG metals is the stored energy in the form of dislocations and grain boundaries. Zhou et al. [154] measured the grain boundaries excess energy of NG Cu fabricated by SMGT with various grain size. They found out that the grain boundaries energy decreased from ~ 0.52 J/m^2 for the average grain size of 125 nm to ~ 0.25 J/m^2 for the average grain size of 50 nm, indicating a more thermally stable NG layer when the average grain size smaller than a critical value of ~ 70 nm for Cu. The grain boundaries energy drop in their case was partially attributed to the unique grain refinement mechanism in which plenty of grain boundaries that are in low energy configuration were generated through the fragmentation and shearing of nanometer-scaled twins and stacking faults (SFs). The other factor contributed to the grain boundaries energy drop was the grain boundaries relaxation [154].

In this study, a gradient NG surface layer was introduced into an IN1718 alloy by SMGT. The topmost region of NG layer with smaller grain size exhibited better thermal stability than the deeper region with larger grain size at high temperatures (in Fig.7.4 and 7.5), similar to the reported thermally stable NG Cu [154]. The HRTEM image of the nanograins in the topmost NG layer is presented in Fig.7.8a. It reveals that plenty of SFs formed inside nanograins, as labeled by arrows. The magnified HRTEM of dashed box b in Fig.7.8a is shown in Fig.7.8b. Nano-twinned structures with average twin thickness of ~ 2 nm was observed. The {111} planes that forming twinning

relationship and the twin boundaries (TBs) are labeled by solid and dashed lines, respectively. These evidences imply that the partial dislocation activities dominated the grain refinement process when the grain size refined to this nanometer scale, leading to the formation of grain boundaries that are in lower energy configuration than other conventional high angle grain boundaries. Our previous work about the microstructure evolution of gradient structured C-22HS Ni-based alloy that was processed by SMGT also reveals that the nanolaminated structure in the topmost layer was transformed from deformation twinned structures in the sublayer [276]. Zhang et al. [369] also reported that the grain boundaries of Cu that were transformed from low-energy TBs possess lower grain boundaries energy than conventional high angle grain boundaries.

Besides, plastic straining may trigger grain boundaries relaxations in NG metals with low stacking faults energy (SFE), and metals with high SFE when high shear stress was applied [154,370]. The grain boundaries relaxation involves the process that grain boundaries structure transforms to a lower energy state through the dissociation of grain boundaries. The dissociation generally occurs by the emission of SFs from one boundary that are terminated by Shockley partials at a second boundary [370]. Whereas Zhou et al. [154] reported that the formation of both SFs and nanotwins from grain boundaries involves emission of partial dislocations, leading to grain boundaries relaxation and subsequent stabilized structures. In this work, partial dislocation activities dominated the accommodation of plastic deformation during SMGT at the topmost NG layer. The magnified HRTEM image of the dashed box c and d in Fig.7.8a are presented in Fig.7.8c and 7.8d, respectively, where the FFT patterns of each grains are inserted and the {111} atomic planes are labeled by solid lines. As denoted by dotted lines, broad grain boundaries that are decorated with plenty of SF-like structures formed between each grain. Several SFs are labeled by green dotted boxes in Fig.7.8c. The formation of these SFs decorated broad grain boundaries indicates that grain boundaries dissociation may have taken place in the topmost NG layer during SMGT, inducing grain boundaries relaxation to lower energy states and stabilization. The microstructure of deeper layer of NG region that was dramatically grain coarsened after annealing (grain coarsened region) will be checked in the future study. The comparison of the grain boundaries characters of these two regions is required for evidencing the argument that grain boundaries with lower energy configuration has attributed to the improved thermal stability of NG structures with finer grain sizes.

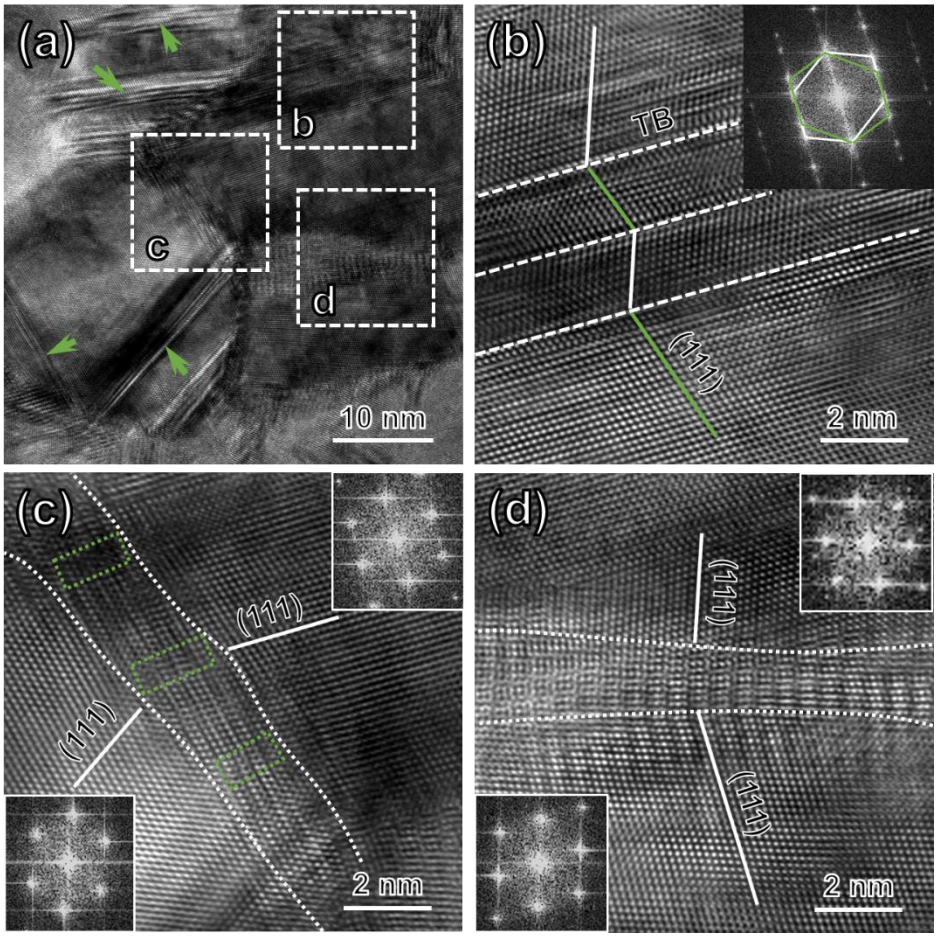

Figure 7.8 (a) HRTEM image of NG layer showing SFs formed inside nanograins, as labeled by arrows. (b) HRTEM image of the box area b in Fig.a shows the formation of nano twinned structures. (c and d) HRTEM images of the box area c and d in Fig.a show the grain boundaries dissociation by the emission of SFs from grain boundaries. Some SFs are labeled by green dotted boxes in Fig.c.

The partial dislocation activity rather than full dislocation activity dominated grain refinement process has led to the formation of thermally stable topmost NG layer. Based on Orowan relation [154], the resolved shear stress (τ_{RSS}) required for the expansion of a dislocation loop derived from a Frank-Reed source with a diameter of D can be expressed as $\tau_{RSS} = \mu b/D$, where μ represents the shear modulus and b is the Burgers vector. Hence, the minimum grain size (D*) required for the multiplication of full dislocations at the yield strength (σ_y) can be calculated by:

$$D^* = \frac{\mu b M}{\sigma_y(D^*)} \qquad \text{Equation 7.2}$$

where M is the Schmid factor (3.0 for polycrystalline metals). The shear modulus and Burgers vector for Ni is ~ 76 GPa and ~ 0.25 nm, respectively. The yield strength $\sigma_y(D^*)$ can be calculated by the classic Hall-Petch equation as [7,8]: $\sigma_y(D^*) = \sigma_0 + K \cdot (D^*)^{-1/2}$, where σ_0 is the friction stress and K represents Hall-Petch slop. Zhou et al. [154] calculated the critical size for pure Ni using Eq.7.2 and yielded D* = 43 nm, similar to that was calculated by Legros et al. (38 nm) [371]. Considering that the value of K for Ni alloys is higher than that for pure Ni, the calculated critical size D* for IN718 alloys is expected to be smaller than that of pure Ni. Hence, the average value of that was reported by Zhao et al. and Legros et al: D* = 40 nm is adopted in this story. It implies that as the grain size of IN718 smaller than 40 nm, full dislocation activities are suppressed and partial dislocation activities become favorable, leading to grain boundaries relaxation. The experimental observation is consistent with the calculated results. As shown in Fig.7.4, the average grain size of the relative coarse-grained structures in the thermally stable area is ~ 37 nm after 24 h annealing, whereas drastic grain coarsening occurs in the grain coarsened area wherein the initial grain size is expected to be larger than 40 nm.

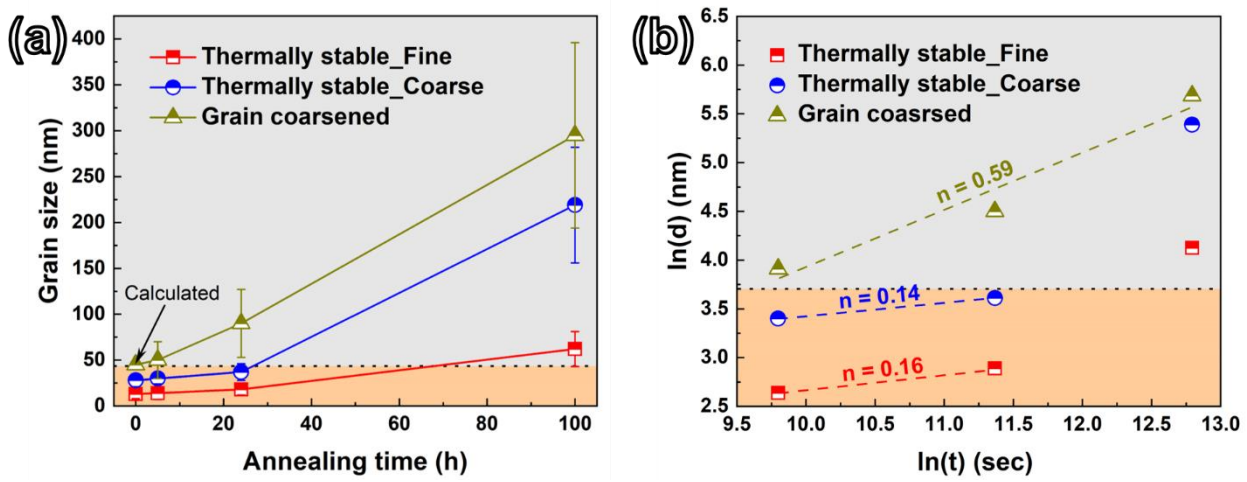

Figure 7.9 (a) The evolution of grain size of relative fine-grained and coarse-grained structures of the thermally stable area, and the grain-coarsened area of NG layer after annealing at 700 ^{o}C for different hours. (b) Plot of ln (d) vs. ln (t) for different area, where d and t represent grain size and annealing time, respectively.

The grain size evolution of the relative fine-grained and coarse-grained structures of the thermally stable area, and the grain coarsened area with increasing of annealing time is presented in Fig.7.9a. The calculated critical grain size (40 nm) is labeled by dotted line. It clearly reveals

that the grain coarsening rate of grains with size smaller than 40 nm is lower than that with size larger than 40 nm. The grain growth kinetic, correlating the grain size (d) to the annealing time (t) can be expressed as [35]:

$$d^n - d_0^n = kt \qquad \text{Equation 7.3}$$

where d_0 is the initial grain size, n represents grain growth exponent and k is a rate constant. The evolution of grain size (ln(d)) and annealing time (ln(t)) in different area is shown in Fig.7.9b. The values of n can be determined by the slops of linear fit lines. It reveals that the average grain growth exponent (n) of thermally stable area with initial grain size smaller than 40 nm is ~ 0.15, whereas that of the grain coarsened area increased to ~ 0.59, quantitatively indicating a more thermally stable NG structure that with size smaller than the critical value.

7.5.2 Deformation behavior of annealed samples

In situ compression tests for both matrix and NG region of IN718 alloy before and after annealing at 700 ^{o}C for 24 h were performed. Upon annealing, high density of nanosized γ" precipitates formed in the undeformed matrix area, leading to a significant flow stresses increment (from 500 MPa to 900 MPa), as shown in Fig.7.6. The strengthening effect of γ" phases has been investigated extensively by researchers [193,204,362]. It's generally believed that the coherency strain hardening overwhelms the ordering hardening and dominates the strengthening of γ" phases [193]. The deformation of IN718 alloy characterized by the formation of planar SBs, owing to the ordered characters of γ" phases [363]. Generally, precipitation hardened alloys exhibit wavy slips during deformation, similar to that shown by single-phase alloys with high SFE. However, planar slip occurs when the precipitates have an ordered crystal structure [363]. To investigate the effect of γ" phase to the deformation behavior of IN178 alloy, the microstructure of deformed pillars obtained at the matrix region of annealed IN718 alloy after 24 h annealing was checked using TEM, as shown in Fig.7.10. The overview of deformed pillar in Fig.7.10a reveals that plenty of primary planar SBs were observed after compression tests. The corresponding STEM images in Fig.7.10b shows that secondary SBs along another (111) planes was activated as well. However, conflicting observation about the deformation mechanisms of IN718 alloy have been reported, as stated in the introduction section. For this study, the average diameter of ellipsoidal γ" particles is ~ 9 nm, and the aspect ratio is ~ 2. The HRTEM image of SBs that penetrated through several γ"

precipitates (as labeled by dotted circles) is presented in Fig.7.10c. The comparison of FFT patterns of SBs area and matrix region verifies that stacking faults (SFs) generated along the SBs during deformation as the elongated diffraction spots that indicating the existence of SFs only occur in the FFT pattern of SBs area. A magnified HRTEM image of SB area is presented in Fig.7.10d and a Burgers circuit (starting at s and ending at f) were drawn. It reveals the Shockley partial with a Burgers vector of $1/6< 1\bar{1}\bar{2} >$. No twinning phenomenon was observed, which is consistent with that was reported by Sundararaman et al. [362] as twinning wouldn't be activated until the average size of γ" phases exceeds the critical value (20 nm). The HRTEM images of sheared γ" phase in Fig.7.10e reveals that the movement of Shockley partials during deformation transformed the BCT structured γ" phase into FCC structures, as denoted by yellow dotted circle. The stacking of (002) planes of γ" phase and (111) planes of FCC structures were labeled using spots with different colors for clarification. Xiao et al. [364] also reported that the shearing of γ" phase significantly reduced their size during cyclic loading, an indication of phase transformation from γ" phase to γ matrix. A detailed analysis of the shearing of γ" phases will be performed in the future.

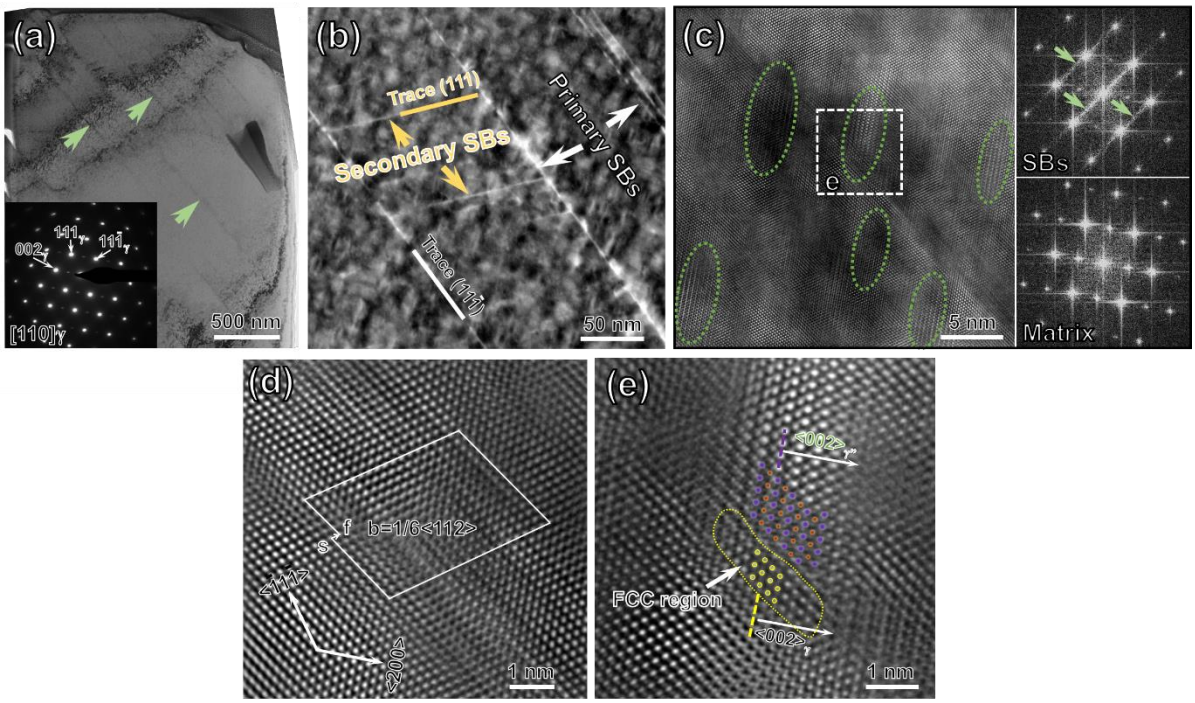

Figure 7.10 (a) TEM image of deformed pillar in the matrix area of the annealed IN718 sample shows the formation of primary SBs during compression. (b) STEM image shows the primary and secondary planar SBs formed in the $(11\bar{1})$ and (111) planes, respectively. (c) HRTEM image of deformed pillar shows SBs penetrated through several γ" phases. (d) HRTEM image of a partial dislocation showing the Burgers circuit (starting at s and ending at f). (e) The magnified HRTEM image of the dashed box e in Fig.c reveals that the shearing of γ" phase transformed it from $D0_{22}$ structure to FCC structure.

In the topmost NG layer, grain growth takes place after annealing at 700 ^{o}C for 24 h, especially in the grain coarsened area. However, the flow stresses of pillars are comparable with that of pillars obtained from the as processed sample, which is attributed to the precipitation of high density of precipitates, as shown in the TEM image of compressed pillar obtained from NG layer after annealing in Fig.7.11a. Plenty of plate-like precipitates with size of several hundred nanometers were observed. Prior studies reveal that pre-straining accelerates the precipitation and coarsening of γ" phases, and the γ" → δ phase transformation [204,344]. Results of Chapter 6 also show that most of γ" and γ' phases transformed to δ and η phases, respectively, in the topmost NG layer of IN718 alloy that was processed by SMGT after annealing at 700 ^{o}C for just 5 h. Similar phenomenon was observed in this study, as shown in Fig.7.4. Most of plate-like precipitates were identified as Ni/Nb-rich δ phases and Al/Ni/Nb-rich η phases. The contribution of these precipitates to the strengthening of the alloy has been quantitatively discussed in Chapter 6. The

precipitation of these hard precipitates with large size may contributes to the surface roughening of pillars during compression. However, a few γ" phases survived and coarsened to several hundred nanometers in size in this study after annealing for 24 h, as shown in Fig.7.11b. Previous studies concluded that pre-straining accelerate the growth of γ" phases, inducing the formation of γ" phase with much larger diameter in the severely deformed topmost NG layer after annealing [204,344]. The coherency of γ" phase with γ matrix diminishes with the increasing of size and vanishes when the size of γ" phase exceeds the critical value, owing to the mismatch strain between γ" phase and γ matrix [368]. The SAD pattern in Fig.7.11b reveals that a misorientation angle $\theta = 6.5^{o}$ between the (002) planes of γ" phase and γ' matrix was detected, an indication of the loss of coherency between γ" phase and γ matrix. The other factor that contributes to the misorientation angle is the distortion of lattice after deformation, as verified by the curved diffraction spots of γ matrix.

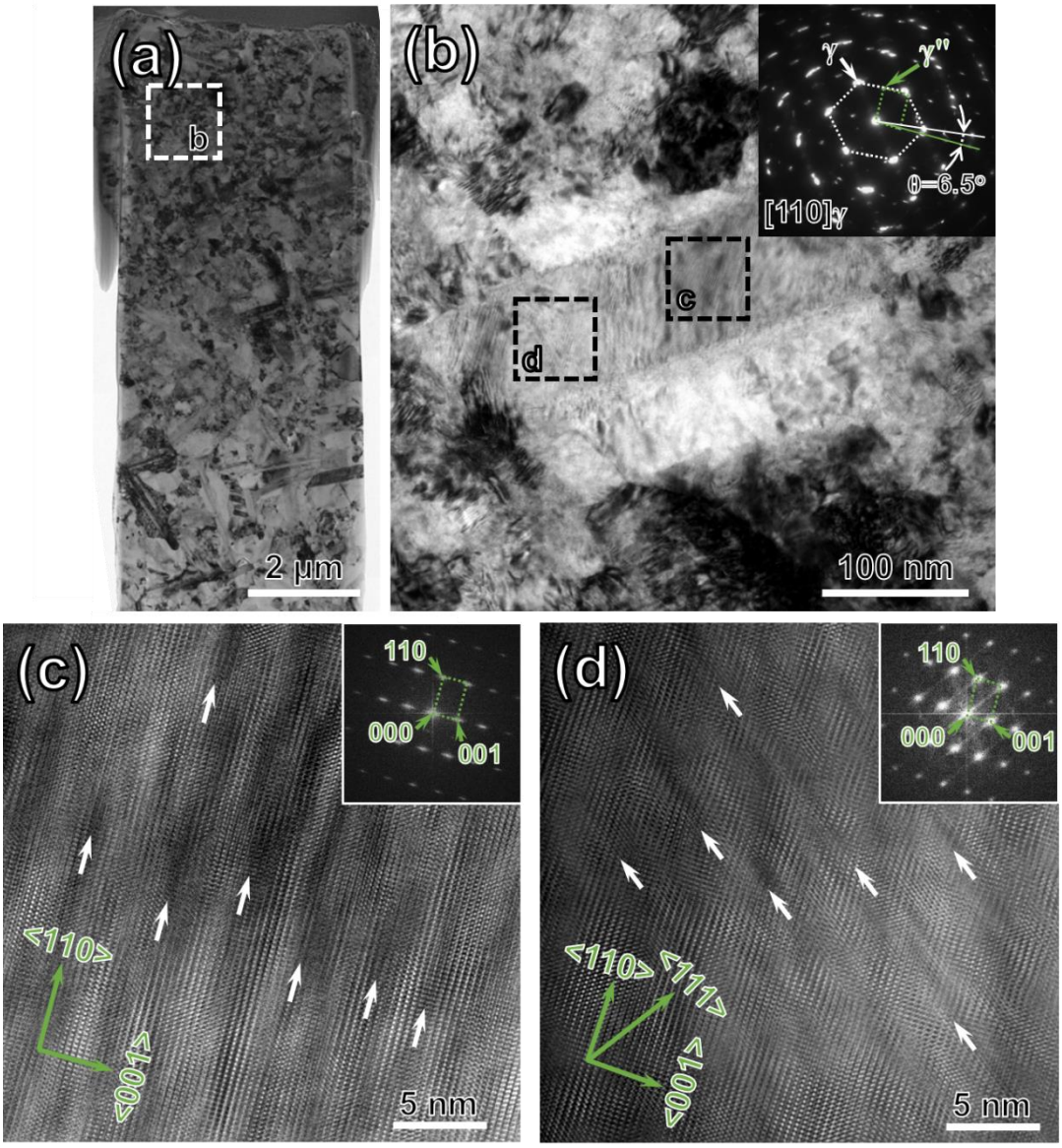

Figure 7.11 (a) TEM image of deformed pillar in the topmost NG area of the annealed IN718 sample. (b) Magnified TEM image of the dashed box b in Fig.a and the corresponding SAD pattern reveal that lattice misorientation between γ matrix and large γ" phase is ~ 6.5°. (c and d) HRTEM images of the dashed box c and d in Fig.b show that two kinds of SFs formed in γ" phases during deformation, as labeled by arrows.

The deformation behavior of γ" phase with size larger than the critical value is deferent with that with smaller size due to the absent of coherency strain hardening and ordering strengthening effect. The HRTEM images and the corresponding FFT patterns of the dashed box c and d in Fig.7.11b are presented in Fig.7.11c and 7.11d, respectively. High-density of SFs (as labeled by arrows) were observed. The indexing of FFT patterns indicating that two kinds of SFs

were generated during compression: first one was activated along the (002) planes of γ" phase (in Fig.7.11c) and the other one was along the (111) planes of γ" phase (in Fig.7.11d). Sundararaman et al. [362] have reported that twinning dominated the shearing of γ" phase when the size exceeds the critical value of 20 nm. However, no twinning system was activated in this γ" phase with size over 100 nm. It may be attributed to the loss of coherency of γ" with γ matrix that leading to the absent of shearing of γ" phases. The deformation behavior of γ" phases that is incoherent with the γ matrix has never been reported before. Detailed analyses about the microstructure of deformed γ" phases, accompanied with that of deformed δ and η phases will be performed in the future.

7.6 Conclusion

Gradient structures containing NG surface layer have been fabricated in IN718 nickel-based alloy by SMGT technique. The alternatively distributed relative fine/coarse grained structures were observed in the surface NG layer. Annealing studies of the NG IN718 alloy show that nanograins with size smaller than the critical value of ~ 40 nm exhibited significantly enhanced thermal stability than that with larger size. The corresponding average grain growth exponent of thermally stable NG structures was measured to be ~ 0.15, in contrast to ~ 0.59 for the NG structure with size exceeds the critical value. The enhanced thermal stability of NG IN718 alloy might be partially attributed to the generation of grain boundaries that are in low energy states during SMGT. The other factor lies in the fact that partial dislocation activities become dominant in the deformation of nanograins with size smaller than the critical value. The emission of SFs or nanotwins from grain boundaries results in the dissociation of grain boundaries, inducing grain boundaries relaxation to lower energy states and stabilization.

The in situ micropillar compression tests of the undeformed matrix region and severely plastic deformed NG surface layer of both as processed and annealed samples reveal that the flow stresses of matrix increased from 500 MPa to 900 MPa due to the precipitation of high-density of nanosized γ" phases. The flow stresses of NG layer after annealing at 700 ^{o}C for 24 h were still comparable with that of the as processed samples. Post compression TEM analyses show that the activation and propagation of SFs enabled the formation of primary SBs in the pillars obtained from the γ" phase strengthened matrix area during compression. The shearing of γ" phase led to the phase transformation from BCT structured γ" phases to FCC structures. In the topmost NG

layer, the coherency between the γ” phase and γ matrix vanished when the size of γ” phase coarsened to hundreds of nanometers. The microstructures of deformed γ” phase reveal that two kinds of SFs, activated and propagated along the (002) and (111) planes of γ” phase, respectively, formed during deformation. It may be attributed to the loss of coherency of γ” with γ matrix that leading to the absent of shearing of γ” phases. Detailed analyses about the shearing of γ” phases with nano-scaled sizes and microstructure of deformed γ” phases with larger sizes, accompanied with that of deformed δ and η phases are required in future studies.

CHAPTER 8. CONCLUSIONS AND FUTURE WORKS

8.1 Conclusions

The major findings and conclusions of this thesis are summarized as follows:

1. Gradient microstructures that were introduced in Hastelloy C-22HS Ni-based superalloy through surface mechanical grinding treatment (SMGT) technique evolve from nanolaminated (NL) to deformation twinned (DT) layers and subsequent severely deformed (SD) layers adjacent to the adjacent undeformed matrix. *In situ* micropillar compression tests coupled with microscopy studies reveal that NL layer has a two-stage work hardening behavior, and the first stage has a large work hardening exponent. The increase of intergranular back stress may have contributed to the high strain hardening behavior (see Chapter 3).
2. Mo-rich thick grain boundaries (GBs) formed in the topmost nanocrystalline (NC) layers of gradient structured (GS) C-22HS alloy after annealing at 650 ^{o}C for 5 h. *In situ* micropillar compression studies coupled with molecular dynamics (MD) simulations suggest that the thick grain boundaries are stronger barriers than conventional grain boundaries to the transmission of dislocations, leading to significant strengthening (see Chapter 4). The formation of thick GBs also attributes to the improved thermal stability of NC C-22HS alloy comparing with its counterpart with conventional thin GBs (see Chapter 5).
3. High density of η phases that have never been reported in Inconel 718 (IN718) Ni-based superalloy generated in the severe plastic deformed surface layer of GS IN718 alloy after annealing at 700 ^{o}C (see Chapter 6). Thermal stability studies show that NC IN718 alloy with grain sizes smaller than the critical value of ~ 40 nm is more thermally stable than that with larger grain sizes at elevated temperatures (see Chapter 7).
4. The underlying mechanisms of strengthening and improved thermal stabilities, as well as the precipitation behaviors of studied C-22HS and IN718 Ni-based alloys were discussed based on TEM microstructural characterization and MD simulations.

8.2 Future works

One of the highlights of the findings of this thesis work is the formation and the corresponding mechanical (Chapter 4) and thermal stability (Chapter 5) studies of thick GBs in nanocrystalline Ni-based alloys. It reveals that the introduction of thick GBs improves the strength and thermal stability of nanocrystalline Ni-based alloys significantly. Similar strategy may also be applied to other alloys. As shown in Fig.8.1a-g, segregation of Ni, Nb, Ti and depletion of Cr, Fe in twin boundaries were also observed in IN718 Ni-based alloy with high density DT microstructures after annealing at 700 ^{o}C for 24 h. The corresponding HRTEM in Fig.8.1h reveals that the Ni/Nb/Ti-rich thick boundary (as denoted by dotted lines) is decorated with high density SFs (as verified by the inserted FFT pattern), similar to the thick GBs with intermetallic phases in annealed C-22HS alloy (in Chapter 4 & 5). These evidences suggest that strengthen and improving thermal stability of metallic materials by introducing thick GBs may applicable to other metals. Hence, the future work will be focused on the formation of thick GBs in other severely deformed metallic materials, and their effects to the mechanical properties and thermal stability of the alloys.

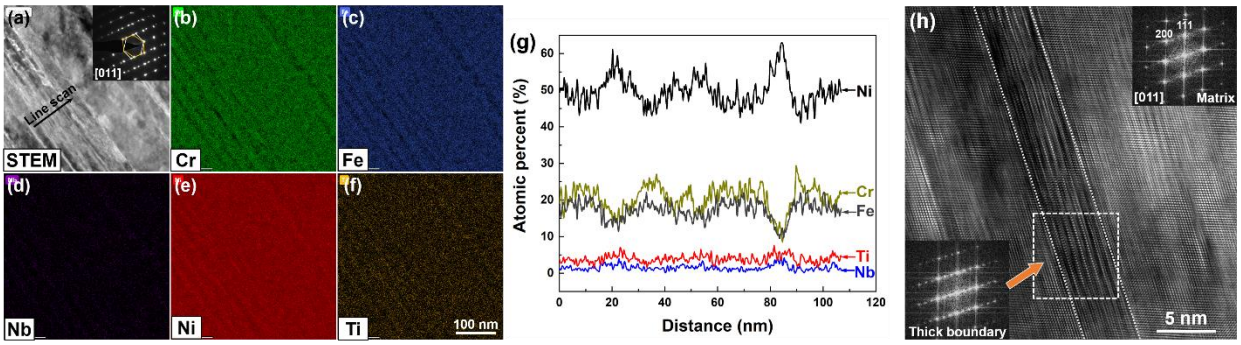

Figure 8.1(a) STEM image and (b-f) the corresponding EDS maps of IN718 Ni-based alloy with high density DT microstructures showing the enrichment of Nb, Ni, Mo and depletion of Cr, Fe along the twin boundaries after annealing at 700 ^{o}C for 24 h. (g) The correspond EDS line scan results verify the depletion of Nb, Ni, Ti and depletion of Cr, Fe in twin boundaries. (h) HRTEM image of the thick boundaries decorated with high density SFs, as verified by the inserted FFT pattern.

Besides, the service properties of GS Ni-based superalloy are mostly determined by the microstructural characteristics including grain size, GBs type, precipitates characters (density, volume fraction and morphology) and residual stresses etc. This thesis has systematically

investigated the microstructure evolution and precipitation behaviors, as well as the corresponding properties responses (including strength and thermal stabilities) of individual layers of the gradient structures that were fabricated in GS C-22HS and IN718 Ni-based superalloys through SMGT technique. However, the macro mechanical properties of GS samples haven't been studied. As aforementioned in Chapter 1, GS metals possess unique properties including the synergy of high strength and good ductility, and improved fatigue and wear/friction resistance. Therefore, the other focus of the future work will be investigating the macroscopic mechanical properties responses of GS Ni-based alloys, which is critical for exploring the practical applications of GS metallic materials in industry.

REFERENCES

[1]. H. Gleiter, Nanocrystalline materials, Prog. Mater. Sci. 33 (1989) 223–315.

[2]. R.Z. Valiev, R.K. Islamgaliev, I. V. Alexandrov, Bulk nanostructured materials from severe plastic deformation, Prog. Mater. Sci. 45 (2000) 103-189.

[3]. A.P. Zhilyaev, B.K. Kim, G. V. Nurislamova, M.D. Baró, J.A. Szpunar, T.G. Langdon, Orientation imaging microscopy of ultrafine-grained nickel, Scr. Mater. 46 (2002) 575–580.

[4]. M.W. Chen, E. Ma, K.J. Hemker, H.W. Sheng, Y. Wang, X. Cheng, Deformation twinning in nanocrystalline aluminum, Science 300 (2003) 1275–1277.

[5]. Y.T. Zhu, T.C. Lowe, T.G. Langdon, Performance and applications of nanostructured materials produced by severe plastic deformation, Scr. Mater. 51 (2004) 825–830.

[6]. Y.T. Zhu, X. Liao, Nanostructured metals: retaining ductility, Nat. Mater. 3 (2004) 351–352.

[7]. E.O. Hall, The Deformation and Ageing of Mild Steel .3. Discussion of Results, Proc. Phys. Soc. London Sect. B. 64 (1951) 747–753.

[8]. J.N. Petch, The Cleavage Strength of Polycrystals, J. Iron Steel Inst. 174 (1953) 25–28.

[9]. J. Gil Sevillano, P. van Houtte, E. Aernoudt, Large strain work hardening and textures, Prog. Mater. Sci. 25 (1980) 69–134.

[10]. R.Z. Valiev, I. V. Alexandrov, Y.T. Zhu, T.C. Lowe, Paradox of strength and ductility in metals processed by severe plastic deformation, J. Mater. Res. 17 (2002) 5–8.

[11]. N.A. Krasilnikov, Z. Pakiela, W. Lojkowski, R.Z. Valiev, Grain refinement and mechanical properties of nickel subjected to severe plastic deformation, Solid State Phenom. 94 (2003) 51–54.

[12]. Y.S. Sato, Y. Kurihara, S.H.C. Park, H. Kokawa, N. Tsuji, Friction stir welding of ultrafine grained Al alloy 1100 produced by accumulative roll-bonding, Scr. Mater. 50 (2004) 57–60.

[13]. N. Krasilnikov, W. Lojkowski, Z. Pakiela, R. Valiev, Tensile strength and ductility of ultra-fine-grained nickel processed by severe plastic deformation, Mater. Sci. Eng. A. 397 (2005) 330–337.

[14]. C.X. Huang, Y.L. Gao, G. Yang, S.D. Wu, G.Y. Li, S.X. Li, Bulk nanocrystalline stainless steel fabricated by equal channel angular pressing, J. Mater. Res. 21 (2006) 1687–1692.

[15]. R.B. Figueiredo, I.P. Pinheiro, M.T.P. Aguilar, P.J. Modenesi, P.R. Cetlin, The finite element analysis of equal channel angular pressing (ECAP) considering the strain path dependence of the work hardening of metals, J. Mater. Process. Technol. 180 (2006) 30–36.

[16]. M. Ravi Shankar, B.C. Rao, S. Chandrasekar, W. Dale Compton, A.H. King, Thermally stable nanostructured materials from severe plastic deformation of precipitation-treatable Ni-based alloys, Scr. Mater. 58 (2008) 675–678.

[17]. K.S. Raju, M.G. Krishna, K.A. Padmanabhan, K. Muraleedharan, N.P. Gurao, G. Wilde, Grain size and grain boundary character distribution in ultra-fine grained (ECAP) nickel, Mater. Sci. Eng. A. 491 (2008) 1–7.

[18]. A.P. Zhilyaev, A.A. Gimazov, E.P. Soshnikova, Á. Révész, T.G. Langdon, Microstructural characteristics of nickel processed to ultrahigh strains by high-pressure torsion, Mater. Sci. Eng. A. 489 (2008) 207–212.

[19]. J. Ribbe, D. Baither, G. Schmitz, S. V. Divinski, Ultrafast diffusion and internal porosity in ultrafine-grained copper-lead alloy prepared by equal channel angular pressing, Scr. Mater. 61 (2009) 129–132.

[20]. Y. Iwahashi, Z. Horita, M. Nemoto, T.G. Langdon, The process of grain refinement in equal-channel angular pressing, Acta Mater. 46 (1998) 3317–3331.

[21]. J.C. Villegas, L.L. Shaw, Nanocrystallization process and mechanism in a nickel alloy subjected to surface severe plastic deformation, Acta Mater. 57 (2009) 5782–5795.

[22]. R. Pippan, S. Scheriau, A. Taylor, M. Hafok, A. Hohenwarter, A. Bachmaier, Saturation of fragmentation during severe plastic deformation, Annu. Rev. Mater. Res. 40 (2010) 319–343.

[23]. B.X. Sauvage, A. Ganeev, Y. Ivanisenko, N. Enikeev, M. Murashkin, Grain Boundary Segregation in UFG Alloys Processed by Severe Plastic Deformation, Adv. Eng. Mater. 14 (2012) 968–974.

[24]. M. Song, R. Zhu, D.C. Foley, C. Sun, Y. Chen, K.T. Hartwig, X. Zhang, Enhancement of strength and ductility in ultrafine-grained T91 steel through thermomechanical treatments, J. Mater. Sci. 48 (2013) 7360–7373.

[25]. M. Song, C. Sun, J. Jang, C.H. Han, T.K. Kim, K.T. Hartwig, X. Zhang, Microstructure refinement and strengthening mechanisms of a 12Cr ODS steel processed by equal channel angular extrusion, J. Alloys Compd. 577 (2013) 247–256.

[26]. Z. Li, B. Zheng, Y. Wang, T. Topping, Y. Zhou, R.Z. Valiev, A. Shan, E.J. Lavernia, Ultrafine-grained Ti – Nb – Ta – Zr alloy produced by ECAP at room temperature, J. Mater. Sci. 49 (2014) 6656–6666.

[27]. X.H. An, Q.Y. Lin, G. Sha, M.X. Huang, S.P. Ringer, Y.T. Zhu, X.Z. Liao, Microstructural evolution and phase transformation in twinning- induced plasticity steel induced by high-pressure torsion, Acta Mater. 109 (2016) 300–313.

[28]. R.Z. Valiev, R.K. Islamgaliev, Enhanced superplasticity of ultrafine-grained alloys processed by severe plastic deformation, Mater. Sci. Forum. 304–306 (1999) 39–46.

[29]. T.C. Lowe, R.Z. Valiev, Producing Nanoscale Microstructures through Severe Plastic Deformation, JOM. (2000) 27–28.

[30]. V. V. Stolyarov, Y.T. Zhu, T.C. Lowe, R.Z. Valiev, Microstructure and properties of pure Ti processed by ECAP and cold extrusion, Mater. Sci. Eng. A. 303 (2001) 82–89.

[31]. V. V. Stolyarov, Y. Theodore Zhu, I. V. Alexandrov, T.C. Lowe, R.Z. Valiev, Influence of ECAP routes on the microstructure and properties of pure Ti, Mater. Sci. Eng. A. 299 (2001) 59–67.

[32]. M. Furukawa, Z. Horita, M. Nemoto, T.G. Langdon, Review: Processing of metals by equal-channel angular pressing, J. Mater. Sci. 36 (2001) 2835–2843.

[33]. K. Park, D.H. Shin, Annealing behavior of submicrometer grained ferrite in a low carbon steel fabricated by severe plastic deformation, Mater. Sci. Eng. A. 334 (2002) 79–86.

[34]. K. Neishi, Z. Horita, T.G. Langdon, Grain refinement of pure nickel using equal-channel angular pressing, Mater. Sci. Eng. A. 325 (2002) 54–58.

[35]. C. Sun, Y. Yang, Y. Liu, K.T. Hartwig, H. Wang, S.A. Maloy, T.R. Allen, X. Zhang, Thermal stability of ultrafine grained Fe-Cr-Ni alloy, Mater. Sci. Eng. A. 542 (2012) 64–70.

[36]. C. Xu, M. Furukawa, Z. Horita, T.G. Langdon, The evolution of homogeneity and grain refinement during equal-channel angular pressing: A model for grain refinement in ECAP, Mater. Sci. Eng. A. 398 (2005) 66–76.

[37]. M. Kulczyk, W. Pachla, A. Mazur, M. Sus-Ryszkowska, N. Krasilnikov, K.J. Kurzydlowski, Producing bulk nanocrystalline materials by combined hydrostatic extrusion and equal-channel angular pressing, Mater. Sci. Pol. 25 (2007) 991–999.

[38]. Y. Amouyal, S. V. Divinski, L. Klinger, E. Rabkin, Grain boundary diffusion and recrystallization in ultrafine grain copper produced by equal channel angular pressing, Acta Mater. 56 (2008) 5500–5513.

[39]. C. Sun, K.Y. Yu, J.H. Lee, Y. Liu, H. Wang, L. Shao, S.A. Maloy, K.T. Hartwig, X. Zhang, Enhanced radiation tolerance of ultrafine grained Fe-Cr-Ni alloy, J. Nucl. Mater. 420 (2012) 235–240.

[40]. B.H. Park, H.Y. Um, J.G. Kim, H.Y. Jeong, S. Lee, H.S. Kim, Large Deformation Behavior of Twin-Induced Plasticity Steels Under High-Pressure Torsion, Met. Mater. Int. 22 (2016) 1003–1008.

[41]. A.P. Zhilyaev, T.G. Langdon, Using high-pressure torsion for metal processing: Fundamentals and applications, Prog. Mater. Sci. 53 (2008) 893–979.

[42]. Y. Cao, Y. Wang, X.H. An, X. Liao, Concurrent microstructural evolution of ferrite and austenite in a duplex stainless steel processed by high-pressure torsion, Acta Mater. 63 (2014) 16–29.

[43]. W. Wu, M. Song, S. Ni, J. Wang, Y. Liu, B. Liu, X. Liao, Dual mechanisms of grain refinement in a FeCoCrNi high entropy alloy processed by high pressure torsion, Sci. Rep. 7 (2017) 1–13.

[44]. Q. Wei, H.T. Zhang, B.E. Schuster, K.T. Ramesh, R.Z. Valiev, L.J. Kecskes, R.J. Dowding, L. Magness, K. Cho, Microstructure and mechanical properties of super-strong nanocrystalline tungsten processed by high-pressure torsion, Acta Mater. 54 (2006) 4079–4089.

[45]. M. Kawasaki, T.G. Langdon, Review: Achieving superplasticity in metals processed by high-pressure torsion, J. Mater. Sci. 49 (2014) 6487–6496.

[46]. N. Tsuji, Y. Saito, S.H. Lee, Y. Minamino, ARB (accumulative roll-bonding) and other new techniques to produce bulk ultrafine grained materials, Adv. Eng. Mater. 5 (2003) 338–344.

[47]. R. Valiev, Nanostructuring of metals by severe plastic deformation for advanced properties, Nat. Mater. 3 (2004) 511–516.

[48]. A.P. Zhilyaev, G. V. Nurislamova, B.K. Kim, M.D. Baró, J.A. Szpunar, T.G. Langdon, Experimental parameters influencing grain refinement and microstructural evolution during high-pressure torsion, Acta Mater. 51 (2003) 753–765.

[49]. D. V. Gunderov, A. V. Polyakov, I.P. Semenova, G.I. Raab, A.A. Churakova, E.I. Gimaltdinova, I. Sabirov, J. Segurado, V.D. Sitdikov, I. V. Alexandrov, N.A. Enikeev, R.Z. Valiev, Evolution of microstructure, macrotexture and mechanical properties of commercially pure Ti during ECAP-conform processing and drawing, Mater. Sci. Eng. A. 562 (2013) 128–136.

[50]. A.A. Karimpoor, U. Erb, K.T. Aust, G. Palumbo, High strength nanocrystalline cobalt with high tensile ductility, Scr. Mater. 49 (2003) 651–656.

[51]. T.T. Sasaki, T. Mukai, K. Hono, A high-strength bulk nanocrystalline Al-Fe alloy processed by mechanical alloying and spark plasma sintering, Scr. Mater. 57 (2007) 189–192.

[52]. K.M. Youssef, R.O. Scattergood, K.L. Murty, J.A. Horton, C.C. Koch, Ultrahigh strength and high ductility of bulk nanocrystalline copper, Appl. Phys. Lett. 87 (2005) 85–88.

[53]. R. Valiev, Nanomaterial advantage, Nature. 419 (2002) 887, 889.

[54]. I. Ovid'ko, Deformation of Nanostructures, Science 295 (2002) 2386.

[55]. L. Lu, Y. Shen, X. Chen, L. Qian, K. Lu, Ultrahigh strength and high electrical conductivity in copper, Science 304 (2004) 422–426.

[56]. E. Ma, Instabilities and ductility of nanocrystalline and ultrafine-grained metals, Scr. Mater. 49 (2003) 663–668.

[57]. X.H. Chen, J. Lu, L. Lu, K. Lu, Tensile properties of a nanocrystalline 316L austenitic stainless steel, Scr. Mater. 52 (2005) 1039–1044.

[58]. D. Jia, K.T. Ramesh, E. Ma, Effects of nanocrystalline and ultrafine grain sizes on constitutive behavior and shear bands in iron, Acta Mater. 51 (2003) 3495–3509.

[59]. A. V Sergueeva, V. V Stolyarov, R.Z. Valiev, A.K. Mukherjee, Advanced mechanical properties of pure titanium with ultrafine grained structure, Scr. Mater. 45 (2001) 747–752.

[60]. H. Wen, T.D. Topping, D. Isheim, D.N. Seidman, E.J. Lavernia, Strengthening mechanisms in a high-strength bulk nanostructured Cu-Zn-Al alloy processed via cryo-milling and spark plasma sintering, Acta Mater. 61 (2013) 2769–2782.

[61]. T.G. Langdon, Twenty-five years of ultrafine-grained materials: Achieving exceptional properties through grain refinement, Acta Mater. 61 (2013) 7035–7059.

[62]. T.C. Lowe, R.Z. Valiev, The use of severe plastic deformation techniques in grain refinement, Jom. 56 (10) (2004) 64–68.

[63]. H. Ueno, K. Kakihata, Y. Kaneko, S. Hashimoto, A. Vinogradov, Nanostructurization assisted by twinning during equal channel angular pressing of metastable 316L stainless steel, J. Mater. Sci. 46 (2011) 4276–4283.

[64]. M.A. Meyers, A. Mishra, D.J. Benson, Mechanical properties of nanocrystalline materials, Prog. Mater. Sci. 51 (2006) 427–556.

[65]. Y. Wang, M. Chen, F. Zhou, E. Ma, High tensile ductility in a nanostructured metal, Nature. 419 (2002) 912–915.

[66]. X. Huang, N. Hansen, N. Tsuji, Hardening by Annealing and Softening by Deformation in Nanostructured Metals, Science 312 (2006) 249–251.

[67]. Y. Wei, Y. Li, L. Zhu, Y. Liu, X. Lei, G. Wang, Y. Wu, Z. Mi, J. Liu, H. Wang, H. Gao, Evading the strength–ductility trade-off dilemma in steel through gradient hierarchical nanotwins, Nat. Commun. 5 (2014) 1–8.

[68]. Y. Zhao, T. Topping, J.F. Bingert, J.J. Thornton, A.M. Dangelewicz, Y. Li, W. Liu, Y. Zhu, Y. Zhou, E.J. Lavernia, High tensile ductility and strength in bulk nanostructured nickel, Adv. Mater. 20 (2008) 3028–3033.

[69]. G. Liu, G.J. Zhang, F. Jiang, X.D. Ding, Y.J. Sun, J. Sun, E. Ma, Nanostructured high-strength molybdenum alloys with unprecedented tensile ductility, Nat. Mater. 12 (2013) 344–350.

[70]. W.S. Zhao, N.R. Tao, J.Y. Guo, Q.H. Lu, K. Lu, High density nano-scale twins in Cu induced by dynamic plastic deformation, Scr. Mater. 53 (2005) 745–749.

[71]. X. Wu, M. Yang, F. Yuan, G. Wu, Y. Wei, X. Huang, Y. Zhu, Heterogeneous lamella structure unites ultrafine-grain strength with coarse-grain ductility, Proc. Natl. Acad. Sci. U. S. A. 112 (2015) 14501–14505.

[72]. R. Liu, Y.Z. Tian, Z.J. Zhang, P. Zhang, X.H. An, Z.F. Zhang, Exploring the fatigue strength improvement of Cu-Al alloys, Acta Mater. 144 (2018) 613–626.

[73]. K. Lu, Making strong nanomaterials ductile with gradients, Science 345 (2014) 1455–1456.

[74]. Y.M. Wang, E. Ma, M.W. Chen, Enhanced tensile ductility and toughness in nanostructured Cu, Appl. Phys. Lett. 80 (2002) 2395–2397.

[75]. K.S. Kumar, S. Suresh, M.F. Chisholm, J.A. Horton, P. Wang, Deformation of electrodeposited nanocrystalline nickel, Acta Mater. 51 (2003) 387–405.

[76]. K.S. Kumar, H. Van Swygenhoven, S. Suresh, Mechanical behavior of nanocrystalline metals and alloys, Acta Mater. 51 (2003) 5743–5774.

[77]. A. Hasnaoui, H. Van Swygenhoven, P.M. Derlet, Dimples on Nanocrystalline fracture surface as evidence for shear plane formation, Science 300 (2003) 1550–1552.

[78]. Y. Xiang, T. Li, Z. Suo, J.J. Vlassak, High ductility of a metal film adherent on a polymer substrate, Appl. Phys. Lett. 87 (2005) 1–3.

[79]. S. Cheng, E. Ma, Y.M. Wang, L.J. Kecskes, K.M. Youssef, C.C. Koch, U.P. Trociewitz, K. Han, Tensile properties of in situ consolidated nanocrystalline Cu, Acta Mater. 53 (2005) 1521–1533.

[80]. C.C. Koch, Optimization of strength and ductility in nanocrystalline and ultrafine grained metals, Scr. Mater. 49 (2003) 657–662.

[81]. D.S. Gianola, S. Van Petegem, M. Legros, S. Brandstetter, H. Van Swygenhoven, K.J. Hemker, Stress-assisted discontinuous grain growth and its effect on the deformation behavior of nanocrystalline aluminum thin films, Acta Mater. 54 (2006) 2253–2263.

[82]. X. Wu, N. Tao, Y. Hong, J. Lu, K. Lu, $\gamma \rightarrow \varepsilon$ Martensite transformation and twinning deformation in fcc cobalt during surface mechanical attrition treatment, Scr. Mater. 52 (2005) 547–551.

[83]. E. Ma, Eight routes to improve the tensile ductility of bulk nanostructured metals and alloys, Jom. 58 (2006) 49–53.

[84]. N. Lu, X. Wang, Z. Suo, J. Vlassak, Failure by simultaneous grain growth, strain localization, and interface debonding in metal films on polymer substrates, J. Mater. Res. 24 (2009) 379–385.

[85]. T.H. Fang, W.L. Li, N.R. Tao, K. Lu, Revealing extraordinary intrinsic tensile plasticity in gradient nano-grained copper, Science 331 (2011) 1587–1590.

[86]. X.L. Wu, P. Jiang, L. Chen, J.F. Zhang, F.P. Yuan, Y.T. Zhu, Synergetic strengthening by gradient structure, Mater. Res. Lett. 2 (2014) 1–7.

[87]. K.Y. Zhu, A. Vassel, F. Brisset, K. Lu, J. Lu, Nanostructure formation mechanism of α-titanium using SMAT, Acta Mater. 52 (2004) 4101–4110.

[88]. K. Lu, J. Lu, Nanostructured surface layer on metallic materials induced by surface mechanical attrition treatment, Mater. Sci. Eng. A. 375–377 (2004) 38–45.

[89]. Y. Lin, J. Lu, L. Wang, T. Xu, Q. Xue, Surface nanocrystallization by surface mechanical attrition treatment and its effect on structure and properties of plasma nitrided AISI 321 stainless steel, Acta Mater. 54 (2006) 5599–5605.

[90]. W.L. Li, N.R. Tao, K. Lu, Fabrication of a gradient nano-micro-structured surface layer on bulk copper by means of a surface mechanical grinding treatment, Scr. Mater. 59 (2008) 546–549.

[91]. H.T. Wang, N.R. Tao, K. Lu, Architectured surface layer with a gradient nanotwinned structure in a Fe-Mn austenitic steel, Scr. Mater. 68 (2013) 22–27.

[92]. Q. Wang, Y. Yin, Q. Sun, L. Xiao, J. Sun, Gradient nano microstructure and its formation mechanism in pure titanium produced by surface rolling treatment, J. Mater. Res. 29 (2014) 569–577.

[93]. M. Yang, Y. Pan, F. Yuan, Y. Zhu, X. Wu, Back stress strengthening and strain hardening in gradient structure, Mater. Res. Lett. 4 (2016) 145–151.

[94]. X.C. Liu, H.W. Zhang, K. Lu, Formation of nano-laminated structure in nickel by means of surface mechanical grinding treatment, Acta Mater. 96 (2015) 24–36.

[95]. X. Wu, P. Jiang, L. Chen, F. Yuan, Y.T. Zhu, Extraordinary strain hardening by gradient structure, Proc. Natl. Acad. Sci. 111 (2014) 7197–7201.

[96]. X. Yang, X. Ma, J. Moering, H. Zhou, W. Wang, Y. Gong, J. Tao, Y. Zhu, X. Zhu, Influence of gradient structure volume fraction on the mechanical properties of pure copper, Mater. Sci. Eng. A. 645 (2015) 280–285.

[97]. N.R. Tao, H. Zhang, J. Lu, K. Lu, Development of nanostructures in metallic materials with low stacking fault energies during surface mechanical attrition treatment (SMAT), Mater. Trans. 44 (2003) 1919–1925.

[98]. J. Li, A.K. Soh, Enhanced ductility of surface nano-crystallized materials by modulating grain size gradient, Model. Simul. Mater. Sci. Eng. 20 (2012) 085002.

[99]. X.C. Liu, H.W. Zhang, K. Lu, Starin-induced ultrahard and ultrastable nanolaminated structure in Nickel, Science 342 (2013) 337–341.

[100]. X.C. Liu, H.W. Zhang, K. Lu, Formation of nanolaminated structure in an interstitial-free steel, Scr. Mater. 95 (2015) 54–57.

[101]. W. Chen, Z.S. You, N.R. Tao, Z.H. Jin, L. Lu, Mechanically-induced grain coarsening in gradient nano-grained copper, Acta Mater. 125 (2017) 255–264.

[102]. J.C. Villegas, K. Dai, L.L. Shaw, P.K. Liaw, Nanocrystallization of a nickel alloy subjected to surface severe plastic deformation, Mater. Sci. Eng. A. 410–411 (2005) 257–260.

[103]. H.W. Huang, Z.B. Wang, J. Lu, K. Lu, Fatigue behaviors of AISI 316L stainless steel with a gradient nanostructured surface layer, Acta Mater. 87 (2015) 150–160.

[104]. P. Xu, H. Luo, S. Li, Y. Lv, J. Tang, Y. Ma, Enhancing the ductility in the age-hardened aluminum alloy using a gradient nanostructured structure, Mater. Sci. Eng. A. 682 (2017) 704–713.

[105]. K. Wang, N.R. Tao, G. Liu, J. Lu, K. Lu, Plastic strain-induced grain refinement at the nanometer scale in copper, Acta Mater. 54 (2006) 5281–5291.

[106]. N.R. Tao, K. Lu, Nanoscale structural refinement via deformation twinning in face-centered cubic metals, Scr. Mater. 60 (2009) 1039–1043.

[107]. T. Roland, D. Retraint, K. Lu, J. Lu, Fatigue life improvement through surface nanostructuring of stainless steel by means of surface mechanical attrition treatment, Scr. Mater. 54 (2006) 1949–1954.

[108]. H.W. Zhang, Z.K. Hei, G. Liu, J. Lu, K. Lu, Formation of nanostructured surface layer on AISI 304 stainless steel by means of surface mechanical attrition treatment, Acta Mater. 51 (2003) 1871–1881.

[109]. N.R. Tao, Z.B. Wang, W.P. Tong, M.L. Sui, J. Lu, K. Lu, An investigation of surface nanocrystallization mechanism in Fe induced by surface mechanical attrition treatment, Acta Mater. 50 (2002) 4603–4616.

[110]. M.F. Ashby, The deformation of plastically non-homogeneous materials, Philos. Mag. 21 (1970) 399–424.

[111]. X. Wu, N. Tao, Y. Hong, B. Xu, J. Lu, K. Lu, Microstructure and evolution of mechanically-induced ultrafine grain in surface layer of AL-alloy subjected to USSP, Acta Mater. 50 (2002) 2075–2084.

[112]. Z. Zeng, X. Li, D. Xu, L. Lu, H. Gao, T. Zhu, Gradient plasticity in gradient nano-grained metals, Extrem. Mech. Lett. 8 (2016) 213–219.

[113]. H. GAO, Y. Hang, W.D. Nix, J.W. Hutchinson, Mechanism-based strain gradient plasticity - I. Theory, J. Mech. Phys. Solids. 47 (1999) 1239–1263.

[114]. K. Zhang, J.R. Weertman, J.A. Eastman, The influence of time, temperature, and grain size on indentation creep in high-purity nanocrystalline and ultrafine grain copper, Appl. Phys. Lett. 85 (2004) 5197–5199.

[115]. D. Pan, S. Kuwano, T. Fujita, M.W. Chen, Ultra-large room-temperature compressive plasticity of a nanocrystalline metal, Nano Lett. 7 (2007) 2108–2111.

[116]. T.J. Rupert, D.S. Gianola, Y. Gan, K.J. Hemker, Experimental observations of stress-driven grain boundary migration, Science 326 (2009) 1686–1690.

[117]. J.W. Cahn, Y. Mishin, A. Suzuki, Coupling grain boundary motion to shear deformation, Acta Mater. 54 (2006) 4953–4975.

[118]. H. Conard, Grain size dependence of the flow stress of Cu from millimeters to nanometers, Metall. Mater. Trans. A. 35A (2004) 2681–2695.

[119]. D. Berman, S.A. Deshmukh, S.K.R.S. Sankaranarayanan, A. Erdemir, A. V. Sumant, Macroscale superlubricity enabled by graphene nanoscroll formation, Science 348 (2015) 1118–1122.

[120]. K. Holmberg, P. Andersson, A. Erdemir, Global energy consumption due to friction in passenger cars, Tribol. Int. 47 (2012) 221–234.

[121]. C. Greiner, Z. Liu, L. Strassberger, P. Gumbsch, Sequence of stages in the microstructure evolution in copper under mild reciprocating tribological loading, ACS Appl. Mater. Interfaces. 8 (2016) 15809–15819.

[122]. D.A. Rigney, Transfer, mixing and associated chemical and mechanical processes during the sliding of ductile materials, Wear. 245 (2000) 1–9.

[123]. H.J. Kim, S. Karthikeyan, D. Rigney, A simulation study of the mixing, atomic flow and velocity profiles of crystalline materials during sliding, Wear. 267 (2009) 1130–1136.

[124]. D.A. Rigney, S. Karthikeyan, The evolution of tribomaterial during sliding: A brief introduction, Tribol. Lett. 39 (2010) 3–7.

[125]. J.B. Singh, J.G. Wen, P. Bellon, Nanoscale characterization of the transfer layer formed during dry sliding of Cu-15 wt.% Ni-8 wt.% Sn bronze alloy, Acta Mater. 56 (2008) 3053–3064.

[126]. X. Chen, Z. Han, K. Lu, Wear mechanism transition dominated by subsurface recrystallization structure in Cu-Al alloys, Wear. 320 (2014) 41–50.

[127]. X. Chen, Z. Han, X. Li, K. Lu, Lowering coefficient of friction in Cu alloys with stable gradient nanostructures, Sci. Adv. 2 (2016) e1601942.

[128]. H.A. Padilla, B.L. Boyce, C.C. Battaile, S. V. Prasad, Frictional performance and near-surface evolution of nanocrystalline Ni-Fe as governed by contact stress and sliding velocity, Wear. 297 (2013) 860–871.

[129]. S. V. Prasad, C.C. Battaile, P.G. Kotula, Friction transitions in nanocrystalline nickel, Scr. Mater. 64 (2011) 729–732.

[130]. D. Linsler, T. Schlarb, T. Weingärtner, M. Scherge, Influence of subsurface microstructure on the running-in of an AlSi alloy, Wear. 332–333 (2015) 926–931.

[131]. D. Shakhvorostov, K. Pöhlmann, M. Scherge, Structure and mechanical properties of tribologically induced nanolayers, Wear. 260 (2006) 433–437.

[132]. Y.S. Zhang, Z. Han, K. Wang, K. Lu, Friction and wear behaviors of nanocrystalline surface layer of pure copper, Wear. 260 (2006) 942–948.

[133]. X. Chen, Z. Han, K. Lu, Friction and Wear Reduction in Copper with a Gradient Nano-grained Surface Layer, Appl. Mater. Interfaces. 10 (2018) 13829–13838.

[134]. L. Li, M. Kim, S. Lee, M. Bae, D. Lee, Influence of multiple ultrasonic impact treatments on surface roughness and wear performance of SUS301 steel, Surf. Coat. Technol. 307 (2016) 517–524.

[135]. X. Zhao, G. Xue, Y. Liu, Results in Physics Gradient crystalline structure induced by ultrasonic impacting and rolling and its effect on fatigue behavior of TC11 titanium alloy, Results Phys. 7 (2017) 1845–1851.

[136]. H.W. Huang, Z.B. Wang, X.P. Yong, K. Lu, Z.B. Wang, X.P. Yong, K.Lu, Enhancing torsion fatigue behaviour of a martensitic stainless steel by generating gradient nanograined layer via surface mechanical grinding treatment, Mater. Sci. Technol. 29 (2013) 1200–1205.

[137]. V. Pandey, K. Chattopadhyay, N.C.S. Srinivas, V. Singh, Role of ultrasonic shot peening on low cycle fatigue behavior of 7075 aluminium alloy, Int. J. Fatigue. 103 (2017) 426–435.

[138]. C.W. Shao, P. Zhang, Y.K. Zhu, Z.J. Zhang, J.C. Pang, Z.F. Zhang, Improvement of low-cycle fatigue resistance in TWIP steel by regulating the grain size and distribution, Acta Mater. 134 (2017) 128–142.

[139]. H. Ueno, K. Kakihata, Y. Kaneko, S. Hashimoto, A. Vinogradov, Enhanced fatigue properties of nanostructured austenitic SUS 316L stainless steel, Acta Mater. 59 (2011) 7060–7069.

[140]. V. Pandey, K. Chattopadhyay, N.C.S. Srinivas, V. Singh, Low cycle fatigue behavior of AA7075 with surface gradient structure produced by ultrasonic shot peening, Procedia Struct. Integr. 2 (2016) 3288–3295.

[141]. Z. Ma, J. Liu, G. Wang, H. Wang, Y. Wei, H. Gao, Strength gradient enhances fatigue resistance of steels, Sci. Rep. (2016) 1–11.

[142]. I. Altenberger, B. Scholtes, U. Martin, H. Oettel, Cyclic deformation and near surface microstructures of shot peened or deep rolled austenitic stainless steel AISI 304, Mater. Sci. Eng. A. 264 (1999) 1–16.

[143]. K. Shiozawa, L. Lu, Very high-cycle fatigue behaviour of shot-peened high-carbon–chromium bearing steel.pdf, Fatigue Fract Engng Mater Struct. 25 (2002) 813–822.

[144]. L. Yang, N.R. Tao, K. Lu, L. Lu, Enhanced fatigue resistance of Cu with a gradient nanograined surface layer, Scr. Mater. 68 (2013) 801–804.

[145]. T. Hanlon, E.D. Tabachnikova, S. Suresh, Fatigue behavior of nanocrystalline metals and alloys, Int. J. Fatigue. 27 (2005) 1147–1158.

[146]. C.C. Koch, Structural nanocrystalline materials: An overview, J. Mater. Sci. 42 (2007) 1403–1414.

[147]. C.C. Koch, R.O. Scattergood, K.A. Darling, J.E. Semones, Stabilization of nanocrystalline grain sizes by solute additions, J. Mater. Sci. 43 (2008) 7264–7272.

[148]. J.E. Burke, D. Turnbull, Recrystallization and grain growth, Prog. Met. Phys. 3 (1952) 220–244.

[149]. J.D. Schuler, O.K. Donaldson, T.J. Rupert, Amorphous complexions enable a new region of high temperature stability in nanocrystalline Ni-W, Scr. Mater. 154 (2018) 49–53.

[150]. A. Michels, C.E. Krill, H. Ehrhardt, R. Birringer, D.T. Wu, Modelling the influence of grain-size-dependent solute drag on the kinetics of grain growth in nanocrystalline materials, Acta Mater. 47 (1999) 2143–2152.

[151]. T. Xia, Y. Xie, C. Yang, W. Zeng, Z. Bi, J. Liang, G. Zhu, J. Wang, D. Zhang, E.J. Lavernia, Strengthening effects and thermal stability of the ultrafine grained microstructure of a nickel base superalloy at room and elevated temperatures, Mater. Charact. 145 (2018) 362–370.

[152]. A. Khalajhedayati, T.J. Rupert, High-Temperature Stability and Grain Boundary Complexion Formation in a Nanocrystalline Cu-Zr Alloy, JOM. 67 (2015) 2788–2801.

[153]. K.A. Darling, L.J. Kecskes, M. Atwater, J. Semones, R.O. Scattergood, C.C. Koch, Thermal stability of nanocrystalline nickel with yttrium additions, J. Mater. Res. 28 (2013) 1813–1819.

[154]. X. Zhou, X.Y. Li, K. Lu, Enhanced thermal stability of nanograined metals below a critical grain size, Science 360 (2018) 526–530.

[155]. U. Klement, U. Erb, A.M. El-Sherik, K.T. Aust, Thermal stability of nanocrystalline Ni, Mater. Sci. Eng. A. 203 (1995) 177–186.

[156]. E. Akca, A. Gürsel, A Review on Superalloys and IN718 Nickel-Based INCONEL Superalloy, Period. Eng. Nat. Sci. 3 (2015).

[157]. G.R. Thellaputta, P.S. Chandra, C.S.P. Rao, Machinability of Nickel Based Superalloys: A Review, Mater. Today Proc. 4 (2017) 3712–3721.

[158]. T.M. Pollock, S. Tin, Nickel-based superalloys for advanced turbine engines: Chemistry, microstructure, and properties, J. Propuls. Power. 22 (2006) 361–374.

[159]. A. Pineau, S.D. Antolovich, High temperature fatigue of nickel-base superalloys: A review with special emphasis on deformation modes and oxidation, Eng. Fail. Anal. 16 (2009) 2668–2697.

[160]. A. Thakur, S. Gangopadhyay, State-of-the-art in surface integrity in machining of nickel-based super alloys, Int. J. Mach. Tools Manuf. 100 (2016) 25–54.

[161]. S.A. Nalawade, M. Sundararaman, J.B. Singh, A. Verma, R. Kishore, Precipitation of γ′ phase in δ-precipitated Alloy 718 during deformation at elevated temperatures, Mater. Sci. Eng. A. 527 (2010) 2906–2909.

[162]. M. Sundararaman, P. Mukhopadhyay, S. Banerjee, Some aspects of the precipitation of metastable intermetallic phases in INCONEL 718, Metall. Trans. A. 23 (1992) 2015–2028.

[163]. M.J. Donachie, S.J. Donachie, Superalloys: a technical guide, ASM International, 2002.

[164]. F. Theska, A. Stanojevic, B. Oberwinkler, S.P. Ringer, S. Primig, On conventional versus direct ageing of Alloy 718, Acta Mater. 156 (2018) 116–124.

[165]. Y.T. Chen, A.C. Yeh, M.Y. Li, S.M. Kuo, Effects of processing routes on room temperature tensile strength and elongation for Inconel 718, Mater. Des. 119 (2017) 235–243.

[166]. A.C. Yeh, K.W. Lu, C.M. Kuo, H.Y. Bor, C.N. Wei, Effect of serrated grain boundaries on the creep property of Inconel 718 superalloy, Mater. Sci. Eng. A. 530 (2011) 525–529.

[167]. Z. Wang, K. Guan, M. Gao, X. Li, X. Chen, X. Zeng, The microstructure and mechanical properties of deposited-IN718 by selective laser melting, J. Alloys Compd. 513 (2012) 518–523.

[168]. M. Ni, C. Chen, X. Wang, P. Wang, R. Li, X. Zhang, K. Zhou, Anisotropic tensile behavior of in situ precipitation strengthened Inconel 718 fabricated by additive manufacturing, Mater. Sci. Eng. A. 701 (2017) 344–351.

[169]. K. Prasad, R. Sarkar, P. Ghosal, V. Kumar, Tensile deformation behavior of forged disc of IN 718 superalloy at 650°C, Mater. Des. 31 (2010) 4502–4507.

[170]. M. Azarbarmas, M. Aghaie-Khafri, J.M. Cabrera, J. Calvo, Microstructural evolution and constitutive equations of Inconel 718 alloy under quasi-static and quasi-dynamic conditions, Mater. Des. 94 (2016) 28–38.

[171]. M.S. Rahman, J. Ding, A. Beheshti, X. Zhang, A.A. Polycarpou, Tribology of Incoloy 800HT for nuclear reactors under helium environment at elevated temperatures, Wear. 436–437 (2019) 203022.

[172]. M.S. Rahman, J. Ding, A. Beheshti, X. Zhang, A.A. Polycarpou, Helium Tribology of Inconel 617 at Elevated Temperatures up to 950°C: Parametric Study, Nucl. Sci. Eng. 193 (2019) 998–1012.

[173]. Y. Sun, L. Fu, Z. Fu, A. Shan, E.J. Lavernia, Enhanced thermal stability and ductility in a nanostructured Ni-based alloy, Scr. Mater. 141 (2017) 1–5.

[174]. M. Detrios, R.C. Helmink, S. Tin, Microstructural Stability and Hot Deformation of γ–γ′–δ Ni-Base Superalloys, Metall. Mater. Trans. A. 45A (2014) 5332–5343.

[175]. M.S. Rahman, J. Ding, A. Beheshti, X. Zhang, A.A. Polycarpou, Elevated temperature tribology of Ni alloys under helium environment for nuclear reactor applications, Tribol. Int. 123 (2018) 372–384.

[176]. D. McAllister, D. Lv, B. Peterson, H. Deutchman, Y. Wang, M.J. Mills, Lower temperature deformation mechanisms in a γ″-strengthened Ni-base superalloy, Scr. Mater. 115 (2016) 108–112.

[177]. H.J. Zhang, C. Li, Y.C. Liu, Q.Y. Guo, Y. Huang, H.J. Li, J.X. Yu, Effect of hot deformation on γ″ and δ phase precipitation of Inconel 718 alloy during deformation & isothermal treatment, J. Alloys Compd. 716 (2017) 65–72.

[178]. A. Drexler, B. Oberwinkler, S. Primig, C. Turk, E. Povoden-Karadeniz, A. Heinemann, W. Ecker, M. Stockinger, Experimental and numerical investigations of the γ″ and γ′ precipitation kinetics in Alloy 718, Mater. Sci. Eng. A. 723 (2018) 314–323.

[179]. A. Chamanfar, L. Sarrat, M. Jahazi, M. Asadi, A. Weck, A.K. Koul, Microstructural characteristics of forged and heat-treated Inconel-718 disks, Mater. Des. 52 (2013) 791–800.

[180]. M. Fisk, J. Andersson, R. du Rietz, S. Haas, S. Hall, Precipitate evolution in the early stages of ageing in Inconel 718 investigated using small-angle x-ray scattering, Mater. Sci. Eng. A. 612 (2014) 202–207.

[181]. Y. Mei, Y. Liu, C. Liu, C. Li, L. Yu, Q. Guo, H. Li, Effects of cold rolling on the precipitation kinetics and the morphology evolution of intermediate phases in Inconel 718 alloy, J. Alloys Compd. 649 (2015) 949–960.

[182]. Y.L. Kuo, S. Horikawa, K. Kakehi, The effect of interdendritic δ phase on the mechanical properties of Alloy 718 built up by additive manufacturing, Mater. Des. 116 (2017) 411–418.

[183]. H. Zhang, C. Li, Q. Guo, Z. Ma, Y. Huang, H. Li, Y. Liu, Delta precipitation in wrought Inconel 718 alloy: the role of dynamic recrystallization, Mater. Charact. 133 (2017) 138–145.

[184]. Y. Huang, T.G. Langdon, The evolution of delta-phase in a superplastic Inconel 718 alloy, J. Mater. Sci. 42 (2007) 421–427.

[185]. R. Lawitzki, S. Hassan, L. Karge, J. Wagner, D. Wang, J. von Kobylinski, C. Krempaszky, M. Hofmann, R. Gilles, G. Schmitz, Differentiation of γ′- and γ″- precipitates in Inconel 718 by a complementary study with small-angle neutron scattering and analytical microscopy, Acta Mater. 163 (2019) 28–39.

[186]. M. Anderson, A.L. Thielin, F. Bridier, P. Bocher, J. Savoie, δ Phase precipitation in Inconel 718 and mechanical properties, Mater. Sci. Eng. A. 679 (2017) 48–55.

[187]. Y.P. Mei, C.X. Liu, Y.C. Liu, X.S. Zhou, L.M. Yu, C. Li, Z.Q. Ma, Y. Huang, Effects of cold rolling on the precipitation and the morphology of δ-phase in Inconel 718 alloy, J. Mater. Res. 31 (2016) 443–454.

[188]. S. Azadian, L.Y. Wei, R. Warren, Delta phase precipitation in Inconel 718, Mater. Charact. 53 (2004) 7–16.

[189]. Y. Wang, W.Z. Shao, L. Zhen, B.Y. Zhang, Hot deformation behavior of delta-processed superalloy 718, Mater. Sci. Eng. A. 528 (2011) 3218–3227.

[190]. K.N. Amato, S.M. Gaytan, L.E. Murr, E. Martinez, P.W. Shindo, J. Hernandez, S. Collins, F. Medina, Microstructures and mechanical behavior of Inconel 718 fabricated by selective laser melting, Acta Mater. 60 (2012) 2229–2239.

[191]. C. Slama, C. Servant, G. Cizeron, Aging of the Inconel 718 alloy between 500 and 750 °C, J. Mater. Res. 12 (1997) 2298–2316.

[192]. A. Thomas, M. El-Wahabi, J.M. Cabrera, J.M. Prado, High temperature deformation of Inconel 718, J. Mater. Process. Technol. 177 (2006) 469–472.

[193]. M.C. Chaturvedi, Y.F. Han, Strengthening mechanisms in Inconel 718 superalloy, Met. Sci. 17 (1983) 1–5.

[194]. A. Baldan, Progress in Ostwald ripening theories and their applications to the γ′-precipitates in nickel-base superalloys Part II: Nickel-base superalloys, J. Mater. Sci. 37 (2002) 2379–2405.

[195]. R. Cozar, A. Pineau, Morphology of gamma prime and gamma double prime precipitates and thermal stability of Inconel 718 type alloys, Metall. Mater. Trans. B. 4 (1973) 47–59.

[196]. L.C.M. Valle, L.S. Araujo, S.B. Gabriel, J. Dille, L.H. Almeida, The effect of d phase on the mechanical properties of an Inconel 718 superalloy, JMEPEG. 22 (2013) 1512–1518.

[197]. D. Srinivasan, Effect of long-time exposure on the evolution of minor phases in Alloy 718, Mater. Sci. Eng. A. 364 (2004) 27–34.

[198]. A. Devaux, L. Nazé, R. Molins, A. Pineau, A. Organista, J.Y. Guédou, J.F. Uginet, P. Héritier, Gamma double prime precipitation kinetic in Alloy 718, Mater. Sci. Eng. A. 486 (2008) 117–122.

[199]. S.H. Chang, In situ TEM observation of γ′, γ″ and δ precipitations on Inconel 718 superalloy through HIP treatment, J. Alloys Compd. 486 (2009) 716–721.

[200]. L. Viskari, K. Stiller, Atom probe tomography of Ni-base superalloys Allvac 718Plus and Alloy 718, Ultramicroscopy. 111 (2011) 652–658.

[201]. J. Lacaze, M. Dehmas, A. Niang, B. Viguier, TEM study of high-temperature precipitation of delta phase in Inconel 718 alloy, Adv. Mater. Sci. Eng. 2011 (2011).

[202]. G.H. Cao, T.Y. Sun, C.H. Wang, X. Li, M. Liu, Z.X. Zhang, P.F. Hu, A.M. Russell, R. Schneider, D. Gerthsen, Z.J. Zhou, C.P. Li, G.F. Chen, Investigations of γ′ γ″ and δ precipitates in heat-treated Inconel 718 alloy fabricated by selective laser melting, Mater. Charact. 136 (2018) 398–406.

[203]. D.H. Ping, Y.F. Gu, C.Y. Cui, H. Harada, Grain boundary segregation in a Ni-Fe-based (Alloy 718) superalloy, Mater. Sci. Eng. A. 456 (2007) 99–102.

[204]. W. Liu, Z. Chen, F. Xiao, M. Yao, S. Wang, R. Liu, Effect of cold rolling on the kinetics of δ phase precipitation in Inconel 718, Metall. Mater. Trans. A. 30A (1999) 31–40.

[205]. E.J. Pickering, H. Mathur, A. Bhowmik, O.M.D.M. Messé, J.S. Barnard, M.C. Hardy, R. Krakow, K. Loehnert, H.J. Stone, C.M.F. Rae, Grain-boundary precipitation in Allvac 718Plus, Acta Mater. 60 (2012) 2757–2769.

[206]. S. Mahadevan, S. Nalawade, J.B. Singh, A. Verma, B. Paul, K. Ramaswamy, Evolution of δ phase microstructure in alloy 718, 7th Int. Symp. Superalloy 718 Deriv. 2010. 2 (2010) 737–750.

[207]. O.M. Messé, J.S. Barnard, E.J. Pickering, P.A. Midgley, C.M.F. Rae, On the precipitation of delta phase in ALLVAC® 718Plus, Philos. Mag. 94 (2014) 1132–1152.

[208]. S. Antonov, M. Detois, R.C. Helmink, S. Tin, Precipitate phase stability and compositional dependence on alloying additions in γ–γ′–δ–η Ni-base superalloys, J. Alloys Compd. 626 (2015) 76–86.

[209]. F. Findik, Discontinuous (cellular) precipitation, J. Mater. Sci. Lett. 7 (1998) 79–83.

[210]. C.M. Kuo, Y.T. Yang, H.Y. Bor, C.N. Wei, C.C. Tai, Aging effects on the microstructure and creep behavior of Inconel 718 superalloy, Mater. Sci. Eng. A. 510–511 (2009) 289–294.

[211]. S.S. Handa, Precipitation of carbides in a Ni-based superalloy, Master degree report. University West, Sweden (2014) 1-33.

[212]. M. Sundararaman, P. Mukhopadhyay, S. Banerjee, Carbide precipitation in nickel base superalloys 718 and 625 and their effect on mechanical properties, (2012) 367–378.

[213]. X.M. Li, J.W. Bai, P.P. Liu, Y.M. Zhu, X.S. Xie, Q. Zhan, Coherent Ni2(Cr, Mo) precipitates in Ni-21Cr-17Mo superalloy, J. Alloys Compd. 559 (2013) 81–86.

[214]. Y.L. Hu, A. Vasiliev, L. Zhang, K. Song, M. Aindow, Polymorphism in the Laves-phase precipitates of a quinternary Nb-Mo-Cr-Al-Si alloy, Scr. Mater. 60 (2009) 72–75.

[215]. D. Bhattacharyya, J. Davis, M. Drew, R.P. Harrison, L. Edwards, Characterization of complex carbide-silicide precipitates in a Ni-Cr-Mo-Fe-Si alloy modified by welding, Mater. Charact. 105 (2015) 118–128.

[216]. J.M. Oblak, D.F. Paulonis, D.S. Duvall, Coherency strengthening in Ni base alloys hardened by DO22 γ′ precipitates, Metall. Trans. 5 (1974) 143–153.

[217]. C. Yan, L. Zhengdong, A. Godfrey, L. Wei, W. Yuqing, Microstructure evolution and mechanical properties of Inconel 740H during aging at 750 °C, Mater. Sci. Eng. A. 589 (2014) 153–164.

[218]. X.G. Wang, J.L. Liu, T. Jin, X.F. Sun, Tensile behaviors and deformation mechanisms of a nickel-base single crystal superalloy at different temperatures, Mater. Sci. Eng. A. 598 (2014) 154–161.

[219]. A. Epishin, T. Link, Mechanisms of high-temperature creep of nickel-based superalloys under low applied stresses, Philos. Mag. 84 (2004) 1979–2000.

[220]. S. Nategh, S.A. Sajjadi, Dislocation network formation during creep in Ni-base superalloy GTD-111, Mater. Sci. Eng. A. 339 (2003) 103–108.

[221]. T.M. Pollock, A.S. Argon, Creep resistance of CMSX-3 nickel base superalloy single crystals, Acta Metall. Mater. 40 (1992) 1–30.

[222]. R.R. Unocic, G.B. Viswanathan, P.M. Sarosi, S. Karthikeyan, J. Li, M.J. Mills, Mechanisms of creep deformation in polycrystalline Ni-base disk superalloys, Mater. Sci. Eng. A. 483–484 (2008) 25–32.

[223]. R.R. Unocic, N. Zhou, L. Kovarik, C. Shen, Y. Wang, M.J. Mills, Dislocation decorrelation and relationship to deformation microtwins during creep of a γ′ precipitate strengthened Ni-based superalloy, Acta Mater. 59 (2011) 7325–7339.

[224]. T. Murakumo, T. Kobayashi, Y. Koizumi, H. Harada, Creep behavior of Ni-base single-crystal superalloys with various γ′ volume fraction, Acta Mater. 52 (2004) 3737–3744.

[225]. T. Sugui, W. Minggang, L. Tang, Q. Benjiang, X. Jun, Influence of TCP phase and its morphology on creep properties of single crystal nickel-based superalloys, Mater. Sci. Eng. A. 527 (2010) 5444–5451.

[226]. B.J. Inkson, Scanning Electron Microscopy (SEM) and Transmission Electron Microscopy (TEM) for Materials Characterization, Elsevier Ltd, 2016.

[227]. D.B. Williams, C.B. Carter, Transmission Electron Microscopy, 2009.

[228]. M. Song, Y.D. Wu, D. Chen, X.M. Wang, C. Sun, K.Y. Yu, Y. Chen, L. Shao, Y. Yang, K.T. Hartwig, X. Zhang, Response of equal channel angular extrusion processed ultrafine-grained T91 steel subjected to high temperature heavy ion irradiation, Acta Mater. 74 (2014) 285–295.

[229]. N. Tsuji, Y. Ito, Y. Saito, Y. Minamino, Strength and ductility of ultrafine grained aluminum and iron produced by ARB and annealing, Scr. Mater. 47 (2002) 893–899.

[230]. Y.M. Wang, E. Ma, Strain hardening, strain rate sensitivity, and ductility of nanostructured metals, Mater. Sci. Eng. A. 375–377 (2004) 46–52.

[231]. F.D. Fischer, G. Reisner, E. Werner, K. Tanaka, G. Cailletaud, T. Antretter, New view on transformation induced plasticity (TRIP), Int. J. Plast. 16 (2000) 723–748.

[232]. O. Grässel, L. Krüger, G. Frommeyer, L.W. Meyer, 1High strength Fe-Mn-(Al, Si) TRIP/TWIP steels development - properties - application, Int. J. Plast. 16 (2000) 1391–1409.

[233]. D.R. Steinmetz, T. Jäpel, B. Wietbrock, P. Eisenlohr, I. Gutierrez-Urrutia, A. Saeed-Akbari, T. Hickel, F. Roters, D. Raabe, Revealing the strain-hardening behavior of twinning-induced plasticity steels: Theory, simulations, experiments, Acta Mater. 61 (2013) 494–510.

[234]. I.N. Sneddon, The relation between load and penetration in the axisymmetric boussinesq problem for a punch of arbitrary profile, Int. J. Eng. Sci. 3 (1965) 47–57.

[235]. C.P. Frick, B.G. Clark, S. Orso, A.S. Schneider, E. Arzt, Size effect on strength and strain hardening of small-scale [1 1 1] nickel compression pillars, Mater. Sci. Eng. A. 489 (2008) 319–329.

[236]. A. Misra, X. Zhang, D. Hammon, R.G. Hoagland, Work hardening in rolled nanolayered metallic composites, Acta Mater. 53 (2005) 221–226.

[237]. J.Y. Zhang, S. Lei, J. Niu, Y. Liu, G. Liu, X. Zhang, J. Sun, Intrinsic and extrinsic size effects on deformation in nanolayered Cu/Zr micropillars: From bulk-like to small-volume materials behavior, Acta Mater. 60 (2012) 4054–4064.

[238]. X. Feaugas, On the origin of the tensile flow stress in the stainless steel AISI 316L at 300 K: Back stress and effective stress, Acta Mater. 47 (1999) 3617–3632.

[239]. B.J. Duggan, M. Hatherly, W.B. Hutchinson, P.T. Wakefield, Deformation structures and textures in cold-rolled 70:30 brass, Met. Sci. 12 (1978) 343–351.

[240]. Z. Fan, Q. Li, J. Li, S. Xue, H. Wang, X. Zhang, Tailoring plasticity of metallic glasses via interfaces in Cu / amorphous CuNb laminates, J. Mater. Res. 32 (2017) 2680–2689.

[241]. N.R. Tao, X.L. Wu, M.L. Sui, J. Lu, K. Lu, Grain refinement at the nanoscale via mechanical twinning and dislocation interaction in a nickel-based alloy, J. Mater. Res. 19 (2004) 1623–1629.

[242]. Y.S. Li, N.R. Tao, K. Lu, Microstructural evolution and nanostructure formation in copper during dynamic plastic deformation at cryogenic temperatures, Acta Mater. 56 (2008) 230–241.

[243]. C.B. Carter, S.M. Holmes, The stacking fault energy of nickel, Philos. Mag. 35 (1977) 1161–1172.

[244]. K. Zhang, J.R. Weertman, J.A. Eastman, Rapid stress-driven grain coarsening in nanocrystalline Cu at ambient and cryogenic temperatures, Appl. Phys. Lett. 87 (2005) 1–4.

[245]. C.J. Bayley, W.A.M. Brekelmans, M.G.D. Geers, A comparison of dislocation induced back stress formulations in strain gradient crystal plasticity, Int. J. Solids Struct. 43 (2006) 7268–7286.

[246]. F. Yuan, P. Chen, Y. Feng, P. Jiang, X. Wu, Strain hardening behaviors and strain rate sensitivity of gradient-grained Fe under compression over a wide range of strain rates, Mech. Mater. 95 (2016) 71–82.

[247]. N. Hansen, Hall-Petch relation and boundary strengthening, Scr. Mater. 51 (2004) 801–806.

[248]. T.G. Nieh, J. Wadsworth, Hall-Petch relation in nanocrystalline solids, Scr. Metall. Mater. 25 (1991) 955–958.

[249]. N.Y.C. Yang, T.J. Headley, J.J. Kelly, J.M. Hruby, Metallurgy of high strength Ni-Mn microsystems fabricated by electrodeposition, Scr. Mater. 51 (2004) 761–766.

[250]. J. Hu, Y.N. Shi, X. Sauvage, G. Sha, K. Lu, Grain boundary stability governs hardening and softening in extremely fine nanograined metals, Science 355 (2017) 1292–1296.

[251]. Y.F. Zhang, S. Xue, Q. Li, C. Fan, R. Su, J. Ding, H. Wang, H. Wang, X. Zhang, Microstructure and mechanical behavior of nanotwinned AlTi alloys with 9R phase, Scr. Mater. 148 (2018) 5–9.

[252]. Q. Li, S. Xue, J. Wang, S. Shao, A.H. Kwong, A. Giwa, Z. Fan, Y. Liu, Z. Qi, J. Ding, H. Wang, J.R. Greer, H. Wang, X. Zhang, High-Strength Nanotwinned Al Alloys with 9R Phase, Adv. Mater. 30 (2018) 1704629.

[253]. M. Callisti, T. Polcar, Combined size and texture-dependent deformation and strengthening mechanisms in Zr / Nb nano-multilayers, Acta Mater. 124 (2017) 247–260.

[254]. J. Li, Y. Chen, S. Xue, H. Wang, X. Zhang, Comparison of size dependent strengthening mechanisms in Ag/Fe and Ag/Ni multilayers, Acta Mater. 114 (2016) 154–163.

[255]. K.Y. Yu, Y. Liu, S. Rios, H. Wang, X. Zhang, Strengthening mechanisms of Ag/Ni immiscible multilayers with fcc/fcc interface, Surf. Coatings Technol. 237 (2013) 269–275.

[256]. Y. Chen, Y. Liu, C. Sun, K.Y. Yu, M. Song, H. Wang, X. Zhang, Microstructure and strengthening mechanisms in Cu/Fe multilayers, Acta Mater. 60 (2012) 6312–6321.

[257]. X. Zhang, A. Misra, H. Wang, T.D. Shen, M. Nastasi, T.E. Mitchell, J.P. Hirth, R.G. Hoagland, J.D. Embury, Enhanced hardening in Cu/330 stainless steel multilayers by nanoscale twinning, Acta Mater. 52 (2004) 995–1002.

[258]. Y. Liu, D. Bufford, H. Wang, C. Sun, X. Zhang, Mechanical properties of highly textured Cu/Ni multilayers, Acta Mater. 59 (2011) 1924–1933.

[259]. M.D. Sangid, T. Ezaz, H. Sehitoglu, I.M. Robertson, Energy of slip transmission and nucleation at grain boundaries, Acta Mater. 59 (2011) 283–296.

[260]. M. De Koning, R. Miller, V. V Bulatov, F.F. Abraham, Modelling grain-boundary resistance in intergranular dislocation slip transmission, Philos. Mag. A. 82 (2002) 2511–2527.

[261]. J. Wang, R.G. Hoagland, J.P. Hirth, A. Misra, Atomistic modeling of the interaction of glide dislocations with “weak” interfaces, Acta Mater. 56 (2008) 5685–5693.

[262]. R.G. Hoagland, R.J. Kurtz, C.H. Henager, Slip resistance of interfaces and the strength of metallic multilayer composites, Scr. Mater. 50 (2004) 775–779.

[263]. B. Ham, X. Zhang, High strength Mg/Nb nanolayer composites, Mater. Sci. Eng. A. 528 (2011) 2028–2033.

[264]. Z. Fan, S. Xue, J. Wang, K.Y. Yu, H. Wang, X. Zhang, Unusual size dependent strengthening mechanisms of Cu/amorphous CuNb multilayers, Acta Mater. 120 (2016) 327–336.

[265]. V. Gavriljuk, H. Berns, C. Escher, N. Glavatskaya, A. Sozinov, Y. Petrov, Grain boundary strengthening in austenitic nitrogen steels, Mater. Sci. Eng. A. 271 (1999) 14–21.

[266]. W. Sigle, G. Richter, M. Rühle, S. Schmidt, Insight into the atomic-scale mechanism of liquid metal embrittlement, Appl. Phys. Lett. 89 (2006) 1–4.

[267]. V.K. Gupta, D.H. Yoon, H.M. Meyer, J. Luo, Thin intergranular films and solid-state activated sintering in nickel-doped tungsten, Acta Mater. 55 (2007) 3131–3142.

[268]. X. Shi, J. Luo, Grain boundary wetting and prewetting in Ni-doped Mo, Appl. Phys. Lett. 94 (2009) 11–13.

[269]. J. Luo, H.K. Cheng, K.M. Asl, C.J. Kiely, M.P. Harmer, The Role of a bilayer interfacial phase on liquid metal embrittlement, Science 333 (2011) 1730–1734.

[270]. A. Kundu, K.M. Asl, J. Luo, M.P. Harmer, Identification of a bilayer grain boundary complexion in Bi-doped Cu, Scr. Mater. 68 (2013) 146–149.

[271]. P.R. Cantwell, M. Tang, S.J. Dillon, J. Luo, G.S. Rohrer, M.P. Harmer, Grain boundary complexions, Acta Mater. 62 (2013) 1–48.

[272]. T. Frolov, Effect of interfacial structural phase transitions on the coupled motion of grain boundaries: A molecular dynamics study, Appl. Phys. Lett. 104 (2014) 1–4.

[273]. S.J. Dillon, K. Tai, S. Chen, The importance of grain boundary complexions in affecting physical properties of polycrystals, Curr. Opin. Solid State Mater. Sci. 20 (2016) 324–335.

[274]. A. Khalajhedayati, Z. Pan, T.J. Rupert, Manipulating the interfacial structure of nanomaterials to achieve a unique combination of strength and ductility, Nat. Commun. 7 (2016) 1–8.

[275]. D.R. Clarke, G. Thomas, Grain boundary phases in a hot-pressed MgO fluxed silicon nitride, J. Am. Ceram. Soc. 60 (1977) 491–495.

[276]. J. Ding, Q. Li, J. Li, S. Xue, Z. Fan, H. Wang, X. Zhang, Mechanical behavior of structurally gradient nickel alloy, Acta Mater. 149 (2018) 57–67.

[277]. S. Plimpton, Fast Parallel Algorithms for Short- Range Molecular Dynamics, J. Comput. Phys. 117 (1995) 1–19.

[278]. A. Stukowski, Visualization and analysis of atomistic simulation data with OVITO: the Open Visualization Tool, Model. Simul. Mater. Sci. Eng. 18 (2010) 015012.

[279]. A. Stukowski, V. V Bulatov, A. Arsenlis, Automated identification and indexing of dislocations in crystal interfaces Automated identification and indexing of dislocations in crystal interfaces, Model. Simul. Mater. Sci. Eng. 20 (2012) 085007.

[280]. Z. Pan, T.J. Rupert, Amorphous intergranular films as toughening structural features, Acta Mater. 89 (2015) 205–214.

[281]. X.W. Zhou, R.A. Johnson, H.N.G. Wadley, Misfit-energy-increasing dislocations in vapor-deposited CoFe/NiFe multilayers, Phys. Rev. B. 69 (2004) 144113.

[282]. G.D. Hughes, S.D. Smith, C.S. Pande, H.R. Johnson, R.W. Armstrong, Hall-Petch strengthening for the microhardness of twelve nanometer grain diameter electrodeposited nickel, Scr. Metall. 20 (1986) 93–97.

[283]. N. Wang, Z. Wang, K. Aust, U. Erb, Room temperature creep behavior of nanocrystalline nickel produced by an electrodeposition technique, Mater. Sci. Eng. A. 237 (1997) 150–158.

[284]. F. Ebrahimi, G. Bourne, M. Kelly, T. Matthews, Mechanical properties of nanocrystalline nickel produced by electrodeposition, Nanostructured Mater. 11 (1999) 343–350.

[285]. C. Xiao, R.A. Mirshams, S.H. Whang, W.M. Yin, Tensile behavior and fracture in nickel and carbon doped nanocrystalline nickel, Mater. Sci. Eng. A. 301 (2001) 35–43.

[286]. F. Dalla Torre, H. Van Swygenhoven, M. Victoria, Nanocrystalline electrodeposited Ni: Microstructure and tensile properties, Acta Mater. 50 (2002) 3957–3970.

[287]. C.A. Schuh, T.G. Nieh, T. Yamasaki, Hall-Petch breakdown manifested in abrasive wear resistance of nanocrystalline nickel, Scr. Mater. 46 (2002) 735–740.

[288]. J.D. Schuler, T.J. Rupert, Materials selection rules for amorphous complexion formation in binary metallic alloys, Acta Mater. 140 (2017) 196–205.

[289]. S. Özerinç, K. Tai, N.Q. Vo, P. Bellon, R.S. Averback, W.P. King, Grain boundary doping strengthens nanocrystalline copper alloys, Scr. Mater. 67 (2012) 720–723.

[290]. N.Q. Vo, J. Schäfer, R.S. Averback, K. Albe, Y. Ashkenazy, P. Bellon, Reaching theoretical strengths in nanocrystalline Cu by grain boundary doping, Scr. Mater. 65 (2011) 660–663.

[291]. M. Herbig, M. Kuzmina, C. Haase, R.K.W. Marceau, I. Gutierrez-Urrutia, D. Haley, D.A. Molodov, P. Choi, D. Raabe, Grain boundary segregation in Fe-Mn-C twinning-induced plasticity steels studied by correlative electron backscatter diffraction and atom probe tomography, Acta Mater. 83 (2015) 37–47.

[292]. S.J. Dillon, M. Tang, W.C. Carter, M.P. Harmer, Complexion: A new concept for kinetic engineering in materials science, Acta Mater. 55 (2007) 6208–6218.

[293]. C.W. Corti, Sintering aids in powder metallurgy: the role of the platinum metals in the activated sintering of refractory metals, Platin. Met. Rev. 30 (1986) 184–195.

[294]. Y. Samih, B. Beausir, B. Bolle, T. Grosdidier, In-depth quantitative analysis of the microstructures produced by surface mechanical attrition treatment (SMAT), Mater. Charact. 83 (2013) 129–138.

[295]. R. Huang, Y. Han, Structure evolution and thermal stability of SMAT-derived nanograined layer on Ti-25Nb-3Mo-3Zr-2Sn alloy at elevated temperatures, J. Alloys Compd. 554 (2013) 1–11.

[296]. T. Zhu, J. Li, Ultra-strength materials, Prog. Mater. Sci. 55 (2010) 710–757.

[297]. L. Lu, M.L. Sui, K. Lu, Superplastic Extensibility of Nanocrystalline Copper at Room Temperature, Science 287 (2000) 1463–1466.

[298]. T.J. Rupert, Solid solution strengthening and softening due to collective nanocrystalline deformation physics, Scr. Mater. 81 (2014) 44–47.

[299]. C.A. Schuh, T.G. Nieh, H. Iwasaki, The effect of solid solution W additions on the mechanical properties of nanocrystalline Ni, Acta Mater. 51 (2003) 431–443.

[300]. A. Misra, J.P. Hirth, R.G. Hoagland, Length-scale-dependent deformation mechanisms in incoherent metallic multilayered composites, Acta Mater. 53 (2005) 4817–4824.

[301]. F. Abdeljawad, P. Lu, N. Argibay, B.G. Clark, B.L. Boyce, S.M. Foiles, Grain boundary segregation in immiscible nanocrystalline alloys, Acta Mater. 126 (2017) 528–539.

[302]. T.J. Rupert, J.R. Trelewicz, C.A. Schuh, Grain boundary relaxation strengthening of nanocrystalline Ni-W alloys, J. Mater. Res. 27 (2012) 1285–1294.

[303]. J. Weissmüller, Alloy effects in nanostructures, Nanostructured Mater. 3 (1993) 261–272.

[304]. J. Weissrmiller, Alloy thermodynamics in nanostrucutres, J. Mater. Res. 9 (1994) 4–7.

[305]. X. Zhang, A. Misra, H. Wang, M. Nastasi, J.D. Embury, T.E. Mitchell, R.G. Hoagland, J.P. Hirth, Nanoscale-twinning-induced strengthening in austenitic stainless steel thin films, Appl. Phys. Lett. 84 (2004) 1096–1098.

[306]. X. Zhang, A. Misra, H. Wang, A.L. Lima, M.F. Hundley, R.G. Hoagland, Effects of deposition parameters on residual stresses, hardness and electrical resistivity of nanoscale twinned 330 stainless steel thin films, J. Appl. Mech. 97 (2005) 094302.

[307]. Y. Cui, O.T. Abad, F. Wang, P. Huang, T.J. Lu, K.W. Xu, J. Wang, Plastic deformation modes of CuZr/Cu Multilayers, Sci. Rep. 6 (2016) 2–7.

[308]. Y. Cui, Y. Shibutani, S. Li, P. Huang, F. Wang, Plastic deformation behaviors of amorphous-Cu50Zr50/crystalline-Cu nanolaminated structures by molecular dynamics simulations, J. Alloys Compd. 693 (2017) 285–290.

[309]. Y.M. Wang, K. Wang, D. Pan, K. Lu, K.J. Hemker, E. Ma, Microsample tensile testing of nanocrystalline copper, Scr. Mater. 48 (2003) 1581–1586.

[310]. . Zhao, J.F. Bingert, X. Liao, B. Cui, K. Han, A. V Sergueeva, A.K. Mukherjee, R.Z. Valiev, T.G. Langdon, Y.T. Zhu, Simultaneously Increasing the Ductility and Strength of Ultra-Fine- Grained Pure Copper, Adv. Mater. 18 (2006) 2949–2953.

[311]. T.J. Rupert, W. Cai, C.A. Schuh, Abrasive wear response of nanocrystalline Ni – W alloys across the Hall – Petch breakdown, Wear. 298–299 (2013) 120–126.

[312]. T.J. Rupert, C.A. Schuh, Sliding wear of nanocrystalline Ni – W: Structural evolution and the apparent breakdown of archard scaling, Acta Mater. 58 (2010) 4137–4148.

[313]. M. Ames, R. Karos, A. Michels, A. Tscho, R. Birringer, Unraveling the nature of room temperature grain growth in nanocrystalline materials, Acta Mater. 56 (2008) 4255–4266.

[314]. M. Thuvander, M. Abraham, A. Cerezo, G.D.W. Smith, Thermal stability of electrodeposited nanocrystalline nickel and iron – nickel alloys, Mater. Sci. Technol. 17 (2001) 961-970.

[315]. G.D. Hibbard, V. Radmilovic, K.T. Aust, U. Erb, Grain boundary migration during abnormal grain growth in nanocrystalline Ni, Mater. Sci. Eng. A. 494 (2008) 232–238.

[316]. M.C. Iordache, S.H. Whang, Z. Jiao, Z.M. Wang, Grain growth kinetics in nanostructured nickel, Nanostructured Mater. 11 (1999) 1343–1349.

[317]. G.D. Hibbard, J.L. Mccrea, G. Palumbo, K.T. Aust, U. Erb, An initial analysis of mechanisms leading to late stage abnormal grain growth in nanocrystalline Ni, Scr. Mater. 47 (2002) 83–87.

[318]. G. Sharma, J. Varshney, A.C. Bidaye, J.K. Chakravartty, Grain growth characteristics and its effect on deformation behavior in nanocrystalline Ni, Mater. Sci. Eng. A. 539 (2012) 324–329.

[319]. S.X. Mcfadden, R.S. Mishra, R.Z. Valiev, A.P. Zhilyaev, A.K. Mukherjee, Low-temperature superplasticity in nanostructured nickel and metal alloys, Nature. 398 (1999) 684–686.

[320]. C.C. Koch, R.O. Scattergood, M. Saber, H. Kotan, High temperature stabilization of nanocrystalline grain size: Thermodynamic versus kinetic strategies, J. Mater. Res. 28 (2013) 1785–1791.

[321]. V.M.S. Muthaiah, L.H. Babu, C.C. Koch, S. Mula, Feasibility of formation of nanocrystalline Fe-Cr-Y alloys: Mechanical properties and thermal stability, Mater. Charact. 114 (2016) 43–53.

[322]. L. Li, M. Saber, W. Xu, Y. Zhu, C.C. Koch, R.O. Scattergood, High-temperature grain size stabilization of nanocrystalline Fe – Cr alloys with Hf additions, Mater. Sci. Eng. A. 613 (2014) 289–295.

[323]. T. Roland, D. Retraint, K. Lu, J. Lu, Enhanced mechanical behavior of a nanocrystalline stainless steel and its thermal stability, Mater. Sci. Eng. A. 445–446 (2007) 281–288.

[324]. T. Chookajorn, H.A. Murdoch, C.A. Schuh, Design of Stable Nanocrystalline Alloys, Science 337 (2012) 951–955.

[325]. A. Khalajhedayati, T.J. Rupert, Disruption of Thermally-Stable Nanoscale Grain Structures by Strain Localization, Sci. Rep. (2015) 1–10.

[326]. B.G. Clark, K. Hattar, M.T. Marshall, T. Chookajorn, B.L. Boyce, C.A. Schuh, Thermal Stability Comparison of Nanocrystalline Fe-Based Binary Alloy Pairs, JOM. 68 (2016) 1625–1633.

[327]. R. Zheng, T. Bhattacharjee, A. Shibata, T. Sasaki, K. Hono, Simultaneously enhanced strength and ductility of Mg-Zn-Zr-Ca alloy with fully recrystallized ultra fi ne grained structures, Scr. Mater. 131 (2017) 1–5.

[328]. M. Lewandowska, K.J. Kurzydyowski, Thermal stability of a nanostructured aluminium alloy, Mater. Charact. 55 (2005) 395–401.

[329]. W. Chen, Q. Sun, L. Xiao, J. Sun, Thermal stability of bulk nanocrystalline Ti – 10V – 2Fe – 3Al alloy, Mater. Sci. Eng. A. 536 (2012) 223–230.

[330]. S.J. Li, Y.W. Zhang, B.B. Sun, Y.L. Hao, R. Yang, Thermal stability and mechanical properties of nanostructured Ti–24Nb–4Zr–7.9Sn alloy, Mater. Sci. Eng. A. 480 (2008) 101–108.

[331]. K. Park, Y. Kim, J.G. Lee, D.H. Shin, Thermal stability and mechanical properties of ultrafine grained low carbon steel, Mater. Sci. Eng. A. 293 (2000) 165–172.

[332]. K.A. Darling, B.K. Vanleeuwen, C.C. Koch, R.O. Scattergood, Thermal stability of nanocrystalline Fe – Zr alloys, Mater. Sci. Eng. A. 527 (2010) 3572–3580.

[333]. G.G. Maier, E.G. Astafurova, H.J. Maier, E. V Naydenkin, G.I. Raab, P.D. Odessky, S. V Dobatkin, Annealing behavior of ultra-fine-grained structure in low-carbon steel produced by equal channel angular pressing, Mater. Sci. Eng. A. 581 (2013) 104–107.

[334]. T.J. Rupert, The role of complexions in metallic nano-grain stability and deformation, Curr. Opin. Solid State Mater. Sci. 20 (2016) 257–267.

[335]. J. Ding, D. Neffati, Q. Li, R. Su, J. Li, S. Xue, Z. Shang, Y. Zhang, H. Wang, Y. Kulkarni, X. Zhang, Thick grain boundary induced strengthening in nanocrystalline Ni alloy, Nanoscale. 11 (2019) 23449–23458.

[336]. J. Humphreys, G.S. Rohrer, A. Rollett, Recrystallization and related annealing phenomena., 2017.

[337]. Z.Q. Gao, B. Fultz, Inter-dependence of grain growth, Nb segregtion, and chemcial ordering in Fe-Si-Nb nanocrystals, Nanostructured Mater. 4 (1994) 939–947.

[338]. E. Shapiro, R. Wurschum, H.E. Schaefer, H. Ehrhardt, C.E. Krill, R. Birringer, Structural stability and high-temperature positron lifetime study of mechanically alloyed nanocrystalline Pd-Zr, Mater. Sci. Forum. 343–346 (2000) 726–731.

[339]. C.E. Krill, R. Klein, S. Janes, R. Birringer, Thermodynamic stabilization of grain boundaries in nanocrystalline alloys, Mater. Sci. Forum. 179–181 (1995) 443–448.

[340]. G.A. Rao, M. Kumar, M. Srinivas, D.S. Sarma, Effect of standard heat treatment on the microstructure and mechanical properties of hot isostatically pressed superalloy Inconel 718, Mater. Sci. Eng. A. 355 (2003) 114–125.

[341]. Y.H. Rong, S.P. Chen, G.X. Hu, M. Gao, R.P. Wei, Prediction and characterization of variant electron diffraction patterns for γ″ and δ precipitates in an Inconel 718 alloy, Metall. Mater. Trans. A. 30A (1999) 2297–2303.

[342]. Y.F. Han, P. Deb, C. Chaturvedi, Coarsening behavior of γ″- and γ′-particles in Inconel alloy 718, Met. Sci. 16 (1982) 555–561.

[343]. T. Connolley, P.A.S. Reed, M.J. Starink, Short crack initiation and growth at 600 8C in notched specimens of Inconel718, Mater. Sci. Eng. A. 340 (2003) 139–154.

[344]. R. Li, M. Yao, W. Liu, X. He, Effects of cold rolling on precipitates in Inconel 718 alloy, J. Mater. Eng. Perform. 11 (2002) 504–508.

[345]. J.L. Zhang, Q.Y. Guo, Y.C. Liu, L.M. Yu, H.J. Li, Effect of cold rolling and first precipitates on the coarsening behavior of γ″-phases in Inconel 718 alloy, Int. J. Miner. Metall. Mater. 23 (2016) 1087–1096.

[346]. R.P. Singh, J.M. Hyzak, T.E. Howson, R.R. Biederman, Recrystallization behavior of cold rolled alloy 718, Superalloys 718, 625 Var. Deriv. (1991) 205–215.

[347]. T. Alam, M. Chaturvedi, S.P. Ringer, J.M. Cairney, Precipitation and clustering in the early stages of ageing in Inconel 718, Mater. Sci. Eng. A. 527 (2010) 7770–7774.

[348]. N. Zhou, D.C. Lv, H.L. Zhang, D. McAllister, F. Zhang, M.J. Mills, Y. Wang, Computer simulation of phase transformation and plastic deformation in IN718 superalloy: Microstructural evolution during precipitation, Acta Mater. 65 (2014) 270–286.

[349]. Z.N. Bi, J.X. Dong, M.C. Zhang, L. Zheng, X.S. Xie, Mechanism of α-Cr precipitation and crystallographic relationships between α-Cr and δ phases in Inconel 718 alloy after long-time thermal exposure, Int. J. Miner. Metall. Mater. 17 (2010) 312–317.

[350]. I. Kirman, D.H. Warrington, The precipitation of Ni3Nb phases in a Ni-Fe-Cr-Nb alloy, Metall. Trans. 1 (1970) 2667–2675.

[351]. H.L. Qin, Z.N. Bi, H.Y. Yu, G. Feng, H. Du, J, J. Zhang, Influence of stress on γ″ precipitation behavior in Inconel 718 during aging, J. Alloys Compd. 740 (2018) 997–1006.

[352]. L.M. Suave, J. Cormier, P. Villechaise, A. Soula, Z. Hervier, D. Bertheau, J. Laigo, Microstructural evolutions during thermal aging of alloy 625: Impact of temperature and forming process, Metall. Mater. Trans. A Phys. Metall. Mater. Sci. 45 (2014) 2963–2982.

[353]. R.W. Kozar, A. Suzuki, W.W. Milligan, J.J. Schirra, M.F. Savage, T.M. Pollock, Strengthening mechanisms in polycrystalline multimodal nickel-base superalloys, Metall. Mater. Trans. A Phys. Metall. Mater. Sci. 40 (2009) 1588–1603.

[354]. F. Wallow, E. Nembach, Synergisms of grain boundary and γ′-particle strengthening in nickel-base superalloys, Scr. Mater. 34 (1996) 499–505.

[355]. L.J. Huang, L. Geng, H.X. Peng, B. Kaveendran, High temperature tensile properties of in situ TiBw/Ti6Al4V composites with a novel network reinforcement architecture, Mater. Sci. Eng. A. 534 (2012) 688–692.

[356]. H.L. Cox, The elasticity and strength of paper and other fibrous materials, Br. J. Appl. Phys. 3 (1952) 72–79.

[357]. V.C. Nardone, K.M. Prewo, On the strength of discontinuous silicon carbide reinforced aluminum composites, Scr. Metall. 20 (1986) 43–48.

[358]. S. Xue, Q. Li, Z. Fan, H. Wang, Y. Zhang, J. Ding, H. Wang, X. Zhang, Strengthening mechanisms and deformability of nanotwinned AlMg alloys, J. Mater. Res. 33 (2018) 3739–3749.

[359]. V. V. Popov, E.N. Popova, A. V. Stolbovskiy, V.P. Pilyugin, Thermal stability of nanocrystalline structure in niobium processed by high pressure torsion at cryogenic temperatures, Mater. Sci. Eng. A. 528 (2011) 1491–1496.

[360]. H. Jiang, Y.T. Zhu, D.P. Butt, I. V. Alexandrov, T.C. Lowe, Microstructural evolution, microhardness and thermal stability of HPT-processed Cu, Mater. Sci. Eng. A. 290 (2000) 128–138.

[361]. X. Zhou, X. Li, K. Lu, Size Dependence of Grain Boundary Migration in Metals under Mechanical Loading, Phys. Rev. Lett. 122 (2019) 1–6.

[362]. M. Sundararaman, P. Mukhopadhyay, S. Banerjee, Deformation behavior of γ″ strengthened Inconel 718, Acta Metall. 36 (1988) 847–864.

[363]. L. Xiao, D.L. Chen, M.C. Chaturvedi, Shearing of γ″ precipitates and formation of planar slip bands in Inconel 718 during cyclic deformation, Scr. Mater. 52 (2005) 603–607.

[364]. L. Xiao, D.L. Chen, M.C. Chaturvedi, Cyclic deformation mechanisms of precipitation-hardened Inconel 718 superalloy, Mater. Sci. Eng. A. 483–484 (2008) 369–372.

[365]. D.W. Worthem, I.M. Robertson, F.A. Leckie, D.F. Socie, C.J. Altstetter, Inhomogeneous deformation in Inconel 718 during monotonic and cyclic loadings, Metall. Trans. A, Phys. Metall. Mater. Sci. 21 A (1990) 3215–3220.

[366]. M. Clavel, A. Pineau, Frequency and wave-form effects on the fatigue crack growth behavior of alloy 718 at 298 K and 823 K., Met. Trans A. 9 A (1978) 471–480.

[367]. M.F. Merrick, Effect of Heat Treatment on the Structure and Properties of Extruded, Metall. Trans. A. 7 (1976) 505–514.

[368]. Y. Ji, Y. Lou, M. Qu, J.D. Rowatt, F. Zhang, T.W. Simpson, L.Q. Chen, Predicting coherency loss of γ″ precipitates in IN718 superalloy, Metall. Mater. Trans. A 47A (2016) 3235–3247.

[369]. Y. Zhang, N.R. Tao, K. Lu, Mechanical properties and rolling behaviors of nano-grained copper with embedded nano-twin bundles, Acta Mater. 56 (2008) 2429–2440.

[370]. J. Rittner, D. Seidman, K. Merkle, Grain-boundary dissociation by the emission of stacking faults, Phys. Rev. B - Condens. Matter Mater. Phys. 53 (1996) R4241–R4244.

[371]. M. Legros, B.R. Elliott, M.N. Rittner, J.R. Weertman, K.J. Hemker, Microsample tensile testing of nanocrystalline metals, Philos. Mag. A Phys. 80 (2000) 1017–1026.